Microscopic Modelling of Correlated Low-dimensional Systems

Dissertation
zur Erlangung des Doktorgrades
der Naturwissenschaften

vorgelegt beim Fachbereich Physik
der Johann Wolfgang Goethe-Universität
in Frankfurt am Main

von
Lady-Andrea Salguero
aus Kolumbien

Frankfurt, 2009
D30

vom Fachbereich Physik der
Johann Wolfgang Goethe-Universität als Dissertation angenommen

Dekan:	Prof. Dr. Dirk-Hermann Rischke
Gutachter:	Prof. Dr. Maria-Roser Valentí Prof. Dr. Michael Lang
Datum der Disputation:	21 January 2009

Abstract

The characterization of microscopic properties in correlated low-dimensional materials is a challenging problem due to the effects of dimensionality and the interplay between the many different lattice and electronic degrees of freedom. Competition between these factors gives rise to interesting and exotic magnetic phenomena. An understanding of how these phenomena are driven by these degrees of freedom can be used for rational design of new materials, to control and manipulate these degrees of freedom in order to obtain desired properties. In this work, we study these effects in materials with small exchange interaction between the magnetic ions such as metal-organic and inorganic dilute compounds. We overcome the difficulties in studying these kind of materials by combining classical and quantum mechanical ab initio methods and many-body theory methods in an effective theoretical approach. To treat metal-organic compounds we elaborate a novel two-step methodology which allows one to include quantum effects while reducing the computational cost. We show that our approach is an effective procedure, leading at each step, to additional insights into the essential features of the phenomena and materials under study.

Our investigation is divided into two parts, the first one concerning the exploration of the fundamental physical properties of novel Cu(II) hydroquinone-based compounds. We have studied two representatives of this family, a polymeric system Cu(II)-2,5-bis(pyrazol-1-yl)-1,4-dihydroxybenzene (CuCCP) and a coupled system $Cu_2S_2F_6N_8O_{12}$ (TK91). The second part concerns the study of magnetic phenomena associated with the interplay between different energy scales and dimensionality in zero-, one- and two-dimensional compounds.

In the zero-dimensional case, we have performed a comprehensive study of $Cu_4OCl_6L_4$ with L=diallylcyanamide=N≡C-N-(CH_2-CH=CH_2)$_2$ ($Cu_4OCl_6daca_4$). Interpretations of the magnetic properties for this tetrameric compound have been controversial and inconsistent. From our studies, we conclude that the common models usually applied to this and other representatives in the same family of cluster systems fail to provide a consistent description of their low temperature magnetic properties and we thus postulate that in such systems it is necessary to take into account quantum fluctuations due to possible frustrated behavior.

In the one-dimensional case, we studied polymeric Fe(II)-triazole compounds, which are of special relevance due to the possibility of inducing a spin transition between low and high spin state by applying a external perturbation. A long standing problem has been a satisfactory microscopic explanation of this large cooperative phenomenon. A lack of X-ray data has been one mitigating reason for the absence of microscopic studies. In this work, we present a novel approach to the understanding of the microscopic mechanism of spin crossover in such systems and show that in these kind of compounds magnetic exchange between high spin Fe(II) centers plays an important role.

The correct description of the underlying physics in many materials is often hindered by the presence of anisotropies. To illustrate this difficulty, we have studied a two dimensional dilute compound $K_2V_3O_8$ which exhibits an unusual spin reorientation effect when applying magnetic fields. While this effect can be understood when considering anisotropies in the system, it is not sufficient to reproduce experimental observations. Based on our studies of the electronic and magnetic properties in this system, we predict an extra exchange interaction and the presence of an additional magnetic moment at the non-magnetic V site. This sheds a new light into the controversial recent experimental data for the magnetic properties of this material.

Contents

List of Figures

List of Tables

List of Abbreviations

1D	one-dimensional
2D	two-dimensional
3D	three dimensional
AFM	Antiferromagnetic
APW	Augmented Plane Waves
APW+lo	Augmented Plane Waves plus localized orbitals
ASA	Atomic Sphere Approximation
DFT	Density Functional Theory
DM	Dzyaloshinskii-Moriya
DOS	Density of States
FBZ	First Brillouin Zone
FM	Ferromagnetic
FP-LAPW	Full Potential Linearized Augmented Plane Waves
GGA	Generalized Gradient Approximation
HS	High Spin
LDA	Local Density Approximation
LS	Low Spin
LSDA	Local Spin Density Approximation
MOFs	Metal-organic Frameworks
MTO	Muffin Tin Orbitals
NMTO	order-N Muffin Tin Orbitals
PAW	Projector Augmented Wave
SC	Spin crossover
SO	spin-orbit

Dedicated to Fernando-Andres Salguero

Chapter 1

Introduction

Low dimensional quantum spin systems containing transition metal ions have been a subject of intensive research in the last few decades in solid state theory as they allow a direct comparison of experimental observations with theoretical predictions. Their many lattice and electronic (orbital, charge and spin) degrees of freedom are coupled by effective interactions such as hopping, Coulomb repulsion and Hund's rule coupling. When some of these interactions are of similar magnitude, competing phases may exist. Low dimensional spin systems refer to those materials where the magnetic interaction between the magnetic ions extend to less than three dimensions. Such arrangement resemble sheets (two dimensional), chains (one dimensional) or clusters (zero dimensional) with their short dimensions on the scale of atoms. As one or more dimensions are restricted, confinement effects play an important role, giving rise to a variety of extremely interesting and unusual quantum-mechanical phenomena. The theoretical study of such phenomena has been however hindered by the large characteristic energy scales found in many materials. For instance, inorganic cuprates have exchange constants of the order of $J \sim 1500$ K [60]. In order to study magnetic-field induced transitions, the applied magnetic field has to overcome the saturation field which for these materials is on the order of 3800 T. Experimentally it is possible to reduce the energy scales in model materials by introducing defects, substituting components or doping with non-magnetic ions (dilution). The recent discovery of low dimensional metal-organic compounds and dilute compounds with metal-metal exchange couplings on the order of few meV have brought renewed focus, both by experimentalists and theoreticians, to these materials [98], [119].

Metal-organic compounds formed by transition metal centers bridged with organic ligands are being intensively discussed in the context of new molecule-based magnets and electronic materials [54],[95]. They constitute a class of tunable materials in part due to their modular nature. The modular set-up has the advantage of allowing the modification of relevant subunits chemically without changing the subsequent crystal engineering. Substitution of organic groups and ligands in these systems plays the role of doping in the search for materials with the desired magnetic interaction strengths and charge carrier concentrations. These ideas are pursued from a theoretical point of view in the first part of this work. For instance, systematic changes in existing metal-organic materials are introduced in order to achieve desirable electronic or magnetic properties in the modified new structures. Such study allows for a gradual understanding of the properties of these low-dimensional systems and could provide a guide to systematic synthesis in the laboratory.

However, metal-organic compounds generally contain a large number of atoms in the unit cell and a very low symmetry, making the computational study of its electronic and magnetic properties, under different conditions, very demanding. Moreover, since an accurate determination of hydrogen positions with X-ray diffractometry is very difficult, usually the available structure data are poorly determined, often leading to unstable quantum mechanical calculations. In some cases the crystal structures are not even known, due to the absence of single crystals suitable for an X-ray structure analysis. Therefore, theoretical studies on these compounds have been restricted to classical approaches. The nature of the organic component in these materials plays an important role for the properties of the metal centers, making it necessary to take into account such contributions when attempting to investigate the ground state properties. One method that takes into account the effects of all the material constituents is first principles Density Functional Theory (DFT). This approach uses the knowledge of atomic constituents and their arrangement within the compound in order to calculate the many-body description of the ground state. This deceivingly simple concept is quite powerful and has dramatically influenced the understanding of the microscopic behavior of matter due to its accuracy complementing or even augmenting experimental observations. Since first principles or ab initio methods combine fundamental predictive power with atomic resolution, they provide a quantitatively accurate first step in the study and characterization of new materials, describing with unprecedent control molecular architectures exactly at those scales (hundreds to thousands of atoms) where most of the promising properties are to be engineered.

DFT provides information about the electronic structure and hence the properties of materials. An understanding of these properties allow us to design and model novel systems with desired properties. First principles simulations give a unique connection between microscopic and macroscopic properties which, when combined with experimental tools, can deliver insight and deeper understanding of the relation between the atomic arrangement and the observed phenomena.

To perform controlled ab initio calculations on reliable structures, we elaborate on a novel two-step approach, which combines classical with quantum-mechanical methods, to systematically prepare model structures for metal-organic or polymeric coordination compound systems and relax them to their equilibrium configuration. This procedure allows not only to study the ground state properties of compounds but also to modify their constituents. We show that this procedure is very effective, having the advantage of including quantum effects while diminishing the computational effort and increasing the accuracy. Neglecting these quantum effects can suppress interesting properties and can give rise to wrong conclusions. Our theoretical procedure has been successfully applied to different kind of complex metal-organic materials in this work.

Within the class of metal-organic compounds, we are particularly interested in hydroquinone-derived linkers connecting Cu^{2+} ions. The advantage of using hydroquinone linkers, is that they can be chemically modified in a way that influences the coordination geometry of the Cu^{2+} ions while keeping the magnetic exchange at a moderate strength. We studied the influence of organic linkers in the magnetic correlation between the metal centers in two representatives of a family of hydroquinone-based low-dimensional quantum-spin systems, namely Cu^{2+}-2,5-bis(pyrazol-1-yl)-1,4-dihydroxybenzene (CuCCP) which behaves as 1D spin chain system and a coupled-dimer system TK91. Additionally we have introduced theoretically, systematic changes to the CuCCP polymer in order to achieve desirable electronic and magnetic properties in the modified new structures. This study allows for a gradual understanding of the properties of these systems and provides a guide to systematic synthesis in the laboratory.

We have also extended our study to investigate microscopically not only the influence of the components and the dimensionality but also the effects of the geometrical arrangement and the interplay between different energy scales in the magnetic phenomena observed in zero-, one- and two-dimensional materials. For this purpose, we considered three different systems containing $3d$ transition metal ions which have a small magnetic interaction parameter between the magnetic centers, presenting very interesting properties when one apply an external perturbation such as a magnetic field or changes in the pressure or temperature. The $Cu_4OCl_6daca_4$ system shows characteristics of a quasi zero-dimensional material whose magnetic building blocks are almost isolated tetrahedra of Cu ions surrounded by an octahedra of Cl atoms. Due to this geometric arrangement, it is possible to obtain different ground state properties depending on the electronic state of the metal ions and the nature of their magnetic interaction. This compound and members of the same family of compounds exhibit anomalous magnetic behavior at low temperatures that cannot be accounted for by simple Heisenberg isotropic exchange. Our calculations provide a route to understand the experimental data collected for $Cu_4OCl_6daca_4$ compound; this allow us to compare our results with several scenarios proposed in the literature which attempt to explain the anomalous low temperature behavior of the magnetization. We show that these previous works fail to explain the experimental observations.

One intensively debated class of materials which have potential applications as optical switches, sensors or memory devices are the spin-crossover polymer systems, which involve transition metal ions linked by organic ligands. These systems show a sharp transition triggered by variation of temperature, pressure or by light irradiation between a low-spin (LS) state and a metastable high-spin (HS) state, which in many cases is accompanied by a change in color and a thermal hysteresis loop. These are signals of the large magnitude of the interactions between the active sites or cooperativity of the system. The origin of this transition and its cooperativity has been mainly discussed in the framework of elastic models, and only recently the possible role of magnetic exchange was suggested. However, there has been to date no conclusive microscopic study where all important interactions are incorporated and hence the origin of the large cooperativity has not been completely settled. The main difficulty in performing ab initio calculations for these kind of materials lies in the lack of accurate crystal structures. In the present work, we overcome the inavailability of structural data by predicting a crystallographic structure for a one-dimensional Fe(II) spin-crossover crystal using known experimental constraints and the two step procedure we have developed. We analyse the LS-HS phase transition and show, contrary to common belief, that there exists an interplay between magnetic exchange and elastic properties that is responsible for the large cooperativity in these systems. We corroborate the quality of our designed structure by comparing with magnetic experiments performed on a real sample.

One particularly appealing material is $K_2V_3O_8$, which behaves as an ideal 2D Heisenberg antiferromagnet. Although it does not have any organic component, it exhibits a very small nearest neighbor exchange constant due to its dilute character. The term 'dilute' refers to materials formed by transition ions surrounded by non-magnetic transition ions such as Zn^{2+} ($3d^{10}$) or V^{5+} ($3d^0$) and well separated from the next transition magnetic metal ion. $K_2V_3O_8$ presents an unusual spin reorientation effect when applying magnetic field. This effect can be understood when including anisotropies in the Hamiltonian which describes the system. We show, however, that the proposed Hamiltonian fails to explain the experimental observations. By studying the electronic and magnetic properties of this compound, we show that our results present a new view over the controversy arising from recent experimental results.

Our methodology and results on all the above mentioned compounds provide a new perspective on the parameters underlying the traditional theoretical approaches, making our study not only essential to understand future experimental results, but interesting in their own right.

This thesis is organized as follows: the first part of Chapter 2 is dedicated to the density functional theory and to the basis sets used for solving the DFT Hamiltonian utilized in this work, namely the FP-LAPW and LMTO/NMTO methods. The second part of Chapter 2 is dedicated to review the effective models employed in our study. Because electronic properties are given in the reciprocal space, we provide in Chapter 3 the different Brillouin zones associated to all of the unit cells for the studied compounds. In Chapter 4 we introduce the concept of metal-organic framework and the current state of art in this field. This is followed by a description of the compounds studied and the significant questions we address in this thesis. In Chapter 5 we present our methodological procedure and our findings. Finally in Chapter 6 we give a brief summary and overlook.

Chapter 2

Method

Our understanding of the electronic structure of matter is based upon theoretical methods of quantum mechanics and statistical mechanics. In general, the quantum mechanical methods attempt to obtain the properties of a system by calculating the characteristic Hamiltonian. However due to the complex character of the problem of matter, it has been necesary to use approximations that had evolved in a great variety of methods and theories, like the Density Functional Theory (DFT). These methods have a range of validity, due precisely, to the approximations done. In order to have a deep understanding of complex systems and related phenomena and in designing new compounds, it is often neccesary a combination of several methods, each being focused to deal with one specific aspect. In this work, *ab initio* DFT has been combined with many-body methods, in order to study the magnetic and electronic properties of low-dimensional systems. The goal of this chapter is to present the main ideas and concepts of the methods used in this work. In the first section we present an overview about the complexity of describing many-body interacting systems and the simplifications of this problems given by the DFT. The second section is dedicated to the description of the Density Functional Theory as well as the basis-set used for solving the DFT equations. An overview about classical ab initio and molecular dynamics is presented at the end of the second section. In the last section the effective models are introduced.

2.1 Describing the properties of matter

The microscopic description of the physical and chemical properties of matter is a complex problem. In general, one has to deal with a collection of interacting atoms, which may also be affected by an external perturbation like magnetic or electric fields. This ensemble of particles may be in the gas, solid, liquid or even amorphous phase. In all cases the system can be described, in a first approximation, by a number of nuclei and electrons interacting through the Coulomb interaction. Formally, the Hamiltonian of such a system is written in the following general form [63] :

$$\hat{H} = -\sum_i \frac{\hbar^2}{2m_e}\nabla_i^2 - \sum_I \frac{\hbar^2}{2M_I}\nabla_I^2 + \frac{e^2}{2}\sum_{j\neq i}\frac{1}{|r_i - r_j|} + \frac{e^2}{2}\sum_{J\neq I}\frac{Z_I Z_J}{|\mathbf{R}_I - \mathbf{R}_J|} - e^2\sum_{I,i}\frac{Z_I}{|\mathbf{R}_I - r_i|} \tag{2.1}$$

where $\mathbf{r} = \mathbf{r}_i, i = 1..N$, is a set of N electronic coordinates and $\mathbf{R} = \mathbf{R}_I, I = 1...\tilde{N}$, is a set of $\tilde{N}$ nuclear coordinates. m$_e$, Z_I and M_I are the electron mass, the nuclear charges and masses respectively. The first two terms in Eq. (2.1) are the electronic and nuclear kinetic energies, the next two terms are the electron-electron and nuclei-nuclei Coulomb interactions, the last term is the electrostatic Coulomb interaction between nuclei and electrons. Here we neglect relativistic effects which would add extra terms in this Hamiltonian like the spin-orbit coupling. Electrons are fermions, therefore the total electronic wave function must be antisymmetric with respect to exchange of two electrons. Strictly speaking, the atomic nuclei, composed by protons and neutrons, can be of bosonic or fermionic nature depending on whether the number of protons plus the number of neutrons is an even or odd number[1]. All the ingredients are perfectly known and, in principle, the properties of the many-body problem can be derived by solving the many-body stationary Schrödinger equation:

$$\hat{H}\Psi_i(\mathbf{r},\mathbf{R}) = E_i\Psi_i(\mathbf{r},\mathbf{R}) \tag{2.2}$$

Where Ψ is the wave function of the many body system. In practice, this problem is almost impossible to treat in a full quantum mechanical framework. Only in few cases a complete analytic solution is available, and numerical solutions are also limited to a very small number of particles. There are several features that contribute to this difficulty. First, this is a multicomponent many-body system, where each component obeys a particular statistics. Second, the complete wave function cannot be easily factorized because of the Coulomb interaction, therefore, in general, one has to deal with (3Ñ+3N) spatial coupled degrees of freedom. The usual way of minimizing the degrees of freedom in the many body problem, is neglecting the kinetic energy of the nuclei in Eq. (2.1). This approximation is justified by the fact that the ratio of mass $m_e/M_I \approx 1/2000 \ll 1$, therefore the movement of the nuclei is much slower than that of the electrons. Thus, we can consider the electronic

---

[1] In solid state is common to define the nuclei as the atomic nuclei of protons and neutrons plus the core electrons in filled shells

system at any time in equilibrium with the corresponding configuration of the nuclei. This is the so called *adiabatic approximation* or *Born-Oppenheimer approximation* [17] which is reasonable for most low energy excitations [2]. This approximation allows us to rewrite the Hamiltonian (2.1) in the following way:

$$\hat{H} = \hat{T} + \hat{V}_{ext} + \hat{U} \tag{2.3}$$

where

$$\hat{T} = \sum_{i}^{N} -\frac{\hbar^2}{2m_e}\nabla_i^2 \tag{2.4}$$

is the kinetic energy operator,

$$\hat{U} = \frac{e^2}{2}\sum_{j \neq i}\frac{1}{|r_i - r_j|} \tag{2.5}$$

is the electron-electron Coulomb potential operator and

$$\hat{V}_{ext} = \sum_{i}^{N} v_{ext}(\mathbf{r}_i) \tag{2.6}$$

is the external potential operator, which in this case, represents the Coulomb interaction between electrons and nuclei, however it can also represent the action of a external electrostatic or magnetic potential applied to the system under study. The many-body Schrödinger equation (2.2), written with the Hamiltonian (2.1) will allow us to obtain, in principle, the ground state energy and the wave function associated to the many body problem. However, even with this approximation, the quantum many body problem obtained is still difficult to solve and the wave function Ψ, associated to this equation, is still very complicated. The wave function is the central quantity in quantum chemistry and physics because it contains all the information about the particular state of the system under study. However, it cannot be proved experimentally. Also, because it depends on the positions and therefore on the number of electrons on the system (for real materials $N \sim 10^{24}$), any wave function will soon reach an unmanageable size [62]. This not only makes a computational treatment very difficult -if not impossible- but also reduces the possibility of a descriptive understanding. Hence, one may wonder whether the complicated wave function is really needed for obtaining the energy and the physical and chemical properties of interest of the many body

---

[2] In cases where the electron-phonon coupling is strong or the phonon energies are high, this approximation is inappropriate

system. A quantity with less degrees of freedom can provide all the useful information and be chosen as the central variable. This is indeed the case and the main subject of density functional theory.

2.2 Density Functional Theory (DFT)

Since its introduction by Hohenberg-Kohn and Kohn-Sham in the 1960s [47], [64] density functional theory (DFT) has evolved into a powerful tool that is widely used in condensed matter theory, computational materials science and quantum chemistry for the calculation of electronic, magnetic and structural properties of molecules and solids. The method has been remarkably successful in predicting, reproducing and explaining a wide variety of physical and chemical properties materials.
The formulation of the two theorems of Hohenberg and Kohn is as follows:

- **Theorem I:** *For any system of interacting particles in an external potential* $V_{ext}(\mathbf{r})$*, the potential* $V_{ext}(\mathbf{r})$ *is determined uniquely, except for a constant, by the ground state particle density* $\rho_0(\mathbf{r})$*.*

  An immediate consequence is that the ground state expectation value of any observable is a unique functional of the exact ground state electron density. *Therefore all properties of the system are completely determined given only the ground state density* $\rho_0(\mathbf{r})$*.*

- **Theorem II:** *A functional for the energy* $E[\rho]$ *in terms of the density* $\rho(\mathbf{r})$ *is defined:*

  $$E[\rho(\mathbf{r})] = \int \upsilon_{ext}(\mathbf{r})\rho(\mathbf{r})\,d\mathbf{r} + F[\rho(\mathbf{r})] \tag{2.7}$$

  where,

  $$F[\rho(\mathbf{r})] =< \phi|T + V_{ee}|\phi > \tag{2.8}$$

  the Hohenberg-Kohn density functional $F[\rho(\mathbf{r})]$ *is* **universal** *for any many-electron systems.* $E[\rho(\mathbf{r})]$ *reaches its* **minimal** *value for the ground state density corresponding to* V_{ext}*.*

The functional $E[\rho]$ alone is sufficient to determine the exact ground state energy and density. Unfortunately, the universal functional $F[\rho(\mathbf{r})]$ is not known and the theorems provide no guidance for constructing the functionals. Therefore, these theorems alone do not allow to solve the problem of finding the ground state properties of a system. The *ansatz* given by Kohn and Sham in 1965 [64], provide a way to make these theorems useful, calculating approximate ground state functionals for real systems of many electrons. The *ansatz* of Kohn-Sham *assumes* that the ground state density of the original interacting system is equal to that of some chosen non-interacting system. This leads to independent-particle equations for the non-interacting system that can be considered exactly soluble, with all the difficult many-body terms incorporated into an *exchange-correlation functional of the density.* By solving the equations one finds the ground state density and energy of the original interacting system with the accuracy limited only by the approximations in the exchange-correlation functional.

Following this idea, the density functional $F[\rho(\mathbf{r})]$ for the interacting system is written as a sum of the kinetic energies of a non-interacting electron gas $T_s[\rho]$ with the same density $\rho(\mathbf{r})$ as the original one, and additional terms that describe the inter-particle interactions

$$F[\rho] = T_s[\rho] + V_H[\rho] + E_{xc}[\rho] \tag{2.9}$$

where $V_H[\rho]$ is the classical Coulomb energy is given by (often referred as Hartree term)

$$V_H[\rho] = \frac{e^2}{2}\int\int \frac{\rho(\mathbf{r})\rho(\mathbf{r}')}{|\mathbf{r}-\mathbf{r}'|}\,d\mathbf{r}\,d\mathbf{r}' \tag{2.10}$$

and $E_{xc}[\rho]$ is the so-called *exchange-correlation energy* and contains all many-body effects not described by the other terms. In other words, $E_{xc}[\rho]$ describes the difference between the real system and the effective non-interacting system (including the correction for the kinetic energy and the Coulomb interactions):

$$E_{xc}[\rho] = \{T[\rho] + V_{ee}[\rho]\} - \{T_s[\rho] + V_H[\rho]\} \tag{2.11}$$

The difference is usually expected to be small, and $E_{xc}[\rho]$ principally contains the correction of $V_H[\rho]$ arising from the correlations between electrons. By imposing that the energy functional $E[\rho(\mathbf{r})]$ for the interacting problem must be minimized by the same electron density $\rho(\mathbf{r})$ that minimizes the energy $E_s[\rho(\mathbf{r})]$ of the non-interacting electron gas, it is possible to extract the *effective Kohn-Sham potential* V_{KS} from Eq. (2.9),

$$\left(-\frac{1}{2}\nabla^2 + V_{KS}\right)\phi_i(\mathbf{r}) = \varepsilon_i\phi_i(\mathbf{r}) \tag{2.12}$$

which is a single particle equation with an effective potential V_{KS},

$$V_{KS}(\mathbf{r}) = \upsilon_{ext}(\mathbf{r}) + e^2\int\frac{\rho(\mathbf{r}')}{|\mathbf{r}-\mathbf{r}'|}d\mathbf{r}' + \upsilon_{xc}(\mathbf{r}) \tag{2.13}$$

With the Kohn-Sham potential V_{KS}, the effective Hamiltonian describes a non-interacting system, since all interactions have been included in V_{KS}. The *exchange-correlation potential* is the variational derivative of the exchange correlation energy functional:

$$\upsilon_{xc}(\mathbf{r}) = \frac{\delta E_{xc}\left[\rho(\mathbf{r})\right]}{\delta\rho(\mathbf{r})} \tag{2.14}$$

The Kohn-Sham energies ε_i have been introduced as Lagrange multipliers to ensure the orthonormality of the the wave functions ϕ_i.

$$\int\phi_i(\mathbf{r})\phi_j(\mathbf{r})d\mathbf{r} = \delta_{ij} \tag{2.15}$$

the density is obtained from the $\phi_i(\mathbf{r})$,

$$\rho(\mathbf{r}) = \sum_{\mathbf{i=1}}^{\mathbf{N}}|\phi_{\mathbf{i}}|^{\mathbf{2}} \tag{2.16}$$

The wave function $\phi_i(\mathbf{r})$ appearing in the Kohn-Sham equations describe one-particle electronic orbitals for the auxiliary non-interacting gas; they are the eigenstates of the fictitious single electron non-interacting problem and should not be considered as wave functions for the electrons of the real system. Also the ε_i in the Kohn-Sham equation do not have the meaning of energy. It is only the total energy and the electronic density $\rho(\mathbf{r})$ that have a physical meaning. However, usually the Kohn-Sham energy levels give a good description of band structure of the real crystalline solids.

Self-consistency

Notice in Eq. (2.13) that the Kohn-Sham potential V_{KS} depends on the density $\rho(\mathbf{r})$ which in turn, depends on the single-particle wave functions ϕ_i. At the same time, the ϕ_i are obtained by solving Eq. (2.12). Therefore, we are dealing with a *self-consistent problem.* The procedure for solving this self-consistent problem is to guess some starting density ρ_0

and to use it for solving the eigenvalue problem (2.12), which gives a set of ϕ_1. With this set of wavefunctions a density ρ_1 is derived from the expression (2.16). This new density ρ_1 is used as an input density, to solve the eigenvalue problem, which will yield an output density ρ_2, and so on till the output density is the same as the input density. This final density is used to calculate the ground state properties of the system under study.

In practice, the starting density is obtained from the superposition of the densities for every atom in the compound treated as a free atom. From the output density calculated in every self-consistent calculation, the total energy and the charge distance between the last two iterations are also calculated. These are monitored in every cycle till the difference in charge distance or total energy in the last two or three iterations is less than a parameter $\alpha \sim 10^{-6}$, which can be modified accordingly with the desired precision for the calculations.

2.2.1 Approximations to the Exchange-Correlation energy functional

Although the exchange correlation energy functional, $\mathrm{E}_{xc}[\rho(\mathbf{r})]$, is well defined as a concept, it is not known precisely, and therefore an approximate expression is necessary, to obtain the ground state energy $E[\rho(r)]$. Many efforts have been made to elaborate very exact expressions for the exchange-correlation energy functional and therefore exist in the literature many versions of it. We introduce here only the approximations that have been used in this work:[3].

The *local density approximation* (LDA) has been for a long time the most widely used approximation to the exchange-correlation energy functional. *The main idea is to consider the general inhomogeneous electronic systems as locally homogeneous, and then to use the exchange-correlation energy per electron of a homogeneous electron gas* ϵ_{xc} for which there are very good approximations and also exact numerical results [77].

$$E_{xc}[\rho] = \int \rho(\mathbf{r})\epsilon_{xc}(\rho(\mathbf{r}))\, d\mathbf{r} \tag{2.17}$$

where ϵ_{xc} is the exchange-correlation energy per electron of a uniformly interacting electron gas of the same density, ρ. The LDA is strictly valid only if $\rho(\mathbf{r})$ is varying slowly, and many extensions exist which give improved accuracy for systems with localized electrons. For the LDA calculations performed in this work, we used the most recent and accurate fit to the Monte-Carlo simulations of Ceperley and Alder by Perdew and Wang [92].

---

[3] The choice of the approximation depends on how good it describes the properties under study, in our case magnetic properties in low-dimensional metal-organic/inorganic materials.

In magnetic systems or, in general, in systems where open electronic shells are involved, better approximations to the exchange-correlation functional can be obtained by introducing the two spins densities, $\rho_{\uparrow}(\mathbf{r})$ and $\rho_{\downarrow}(\mathbf{r})$, such that $\rho(\mathbf{r}) = \rho_{\uparrow}(\mathbf{r}) + \rho_{\downarrow}(\mathbf{r})$, and $(\zeta(\mathbf{r}) = \rho_{\uparrow}(\mathbf{r}) - \rho_{\downarrow}(\mathbf{r}))/\rho(\mathbf{r})$ is the magnetization density. The non-interacting kinetic energy splits trivially into spin-up and a spin-down contributions, and the external and Hartree potentials depend on the fully density $\rho(\mathbf{r})$, but the approximate exchange-correlation functional will depend on both spin densities independently, $E_{xc} = E_{xc}[\rho_{\uparrow}(\mathbf{r}), \rho_{\downarrow}(\mathbf{r})]$. The density, given by Eq. (2.16) contains a double summation, over the spin states and over the number of electrons in each spin state. These latter have to be determined according to the single-particle eigenvalues, by asking for the lowest $N = N_{\uparrow} + N_{\downarrow}$ to be occupied.

The equivalent of the LDA in spin-polarized systems is the *local spin density approximation* (LSDA), which basically consists of replacing the exchange-correlation energy density with a spin-polarized expression:

$$E_{xc}^{LSDA}[\rho_{\uparrow}(\mathbf{r}), \rho_{\downarrow}(\mathbf{r})] = \int [\rho_{\uparrow}(\mathbf{r}) + \rho_{\downarrow}(\mathbf{r})] \epsilon_{xc}^{h}[\rho_{\uparrow}(\mathbf{r}), \rho_{\downarrow}(\mathbf{r})] d\mathbf{r} \tag{2.18}$$

obtained for instance, by interpolating between the fully-polarized and fully-unpolarized exchange-correlation energy densities using an appropriate expression that depends on $\zeta(\mathbf{r})$.

To extend the local density approximation to systems with more significant non-homogeneous densities, several techniques have been proposed. The most successful one is the *generalized gradient approximation* (GGA), where the real $E_{xc}[\rho(\mathbf{r})]$ is expressed as a functional of the density $\rho(\mathbf{r})$ and its gradient $\nabla\rho(\mathbf{r})$:

$$E_{xc}[\rho] = \int \rho(\mathbf{r}) \epsilon_{xc}(\rho(\mathbf{r}))\, d\mathbf{r} + \int F_{xc}[\rho, |\nabla\rho|]\, d\mathbf{r} \tag{2.19}$$

where F_{xc} is a correction.

The GGA formalism gives a better description of inhomogeneous systems, like transition metals, and it significantly improves the binding and atomic energies, it improves bond lengths, angles, predicting good results also in the cases where LDA fails. It improves energetics, geometries and dynamical properties of water, ice and water clusters. *GGA accounts specifically for density gradients that are neglected in pure LDA*. For the GGA calculations performed in this work, the Perdew-Burke-Ernzerhof (PBE96) [93] parameterization for the exchange-correlation functional was used. This functional improves the description of hydrogen-bonded systems.

2.2.2 Orbital-dependent functionals: LDA+U method

The LDA approximation has proved to be very efficient for extended systems, such as large molecules and solids. But it fails when calculating the ground state properties of strongly correlated materials. Such systems usually contain transition metal or rare-earth metal ions with partially filled d (or f) shells. When applying a one-electron method with an orbital-independent potential like in the LDA, to transition metal compounds, one has as a result a partially filled d band with metallic type electronic structure and itinerant d electrons. This is definitely a wrong answer for the late-transition-metal oxides and rare-earth metal compounds where d (f) electrons are well localized and there is a considerable energy separation between occupied and unoccupied sub-bands (the lower Hubbard band and the upper Hubbard band in a model Hamiltonian approach (the Hubbard model will be explained in detail in Section 2.4)). There have been different attempts to improve on the LDA in order to take into account strong electron-electron correlations, the most popular one the LDA+U scheme.
The main idea of the LDA+U method is to separate electrons into two subsystems, localized d or f electrons for which the Coulomb $d-d$ ($f-f$) *interaction should be taken into account by the Hubbard term* $\frac{1}{2}U\sum_{i\neq j} n_i n_j$ *in a model Hamiltonian and delocalized s and p electrons which could be described by using an orbital-independent one electron potential (LDA).* There are three variants of this method, all with the common idea of introducing an orbitally dependent potential, for the chosen d or f set of electron states, to LDA potentials. Here we introduced two of them, which are the ones we have implemented in this work.

- **LDA+U (AMF)**: In this version, introduced by Czyzyk and Sawatzky [31] as 'Around the Mean Field' (AMF) method, the additional potential which mimics the Hubbard term, is zero when averaged over the chosen set of states. The center of gravity of the state $|l, m_l, m_s = +1/2\rangle$ is preserved as well as the center of gravity of the state $|l, m_l, m_s = -1/2\rangle$ *i.e.*, average exchange splitting is the same as in LSDA. The orbital-dependent potential is written as

$$V_{m\sigma}^{AMF} = V_{LDA} + \sum_{m'} U(n_{m'-\sigma} - n_0) + \sum_{m\neq m'} (U-J)(n_{m'\sigma} - n_0) \tag{2.20}$$

where n_0 is the average occupancy of the d (f) orbital, $n_{m\sigma}$ are spin -(σ) and orbital-(m) dependent occupancies. The U and J parameters, are the average on-site Coulomb and exchange interactions in the considered shell, respectively. This scheme is based on the suggestion that LDA corresponds to the homogeneous solution of the Hartree-Fock equations with averaged occupancy for all d orbitals.

- **LDA+U (SIC)**: In this version, introduced by Anisimov *et al.* [10], the LDA interaction is subtracted and replaced by a Hartree-Fock form for the electron-electron interaction in the spherically symmetric atom. This has the advantage that the self-interaction of the electrons is approximatively removed, hence it is usually referred to as the self-interaction corrected (SIC) LDA+U method. The orbital-dependent one-electron potential is written as:

$$V_{m\sigma}^{SIC} = V_{LDA} + \sum_{m'} (U_{mm'} - U_{eff}) n_{m-\sigma} + \sum_{m \neq m'} (U_{mm'} - J_{mm'} - U_{eff}) n_{m\sigma}$$

$$+U_{eff}(\frac{1}{2} - n_{m\sigma}) - \frac{1}{4} J \qquad (2.21)$$

where $U_{eff} = U - \frac{1}{2}J$, and the matrices $U_{mm'}$ are used instead of the scalar value U.

The difference between the two versions is clearly seen if the density matrix is diagonal and the terms proportional to J are neglected, *i.e.*, only the Hartree term is considered. The additional potentials V_m^{AMF} and V_m^{SIC} are then

$$V_m^{AMF} = U(n_0 - n_m), \qquad V_m^{SIC} = U(1/2 - n_m) \qquad (2.22)$$

The LDA+U(SIC) scheme is usually more appropriate for fully localized electrons, while the LDA+U(AMF) scheme might be better for weakly correlated systems.

2.2.3 Solving the DFT equations: The LAPW and LMTO methods

In order to solve the Kohn-Sham equation, several approaches have been elaborated. There are no fundamental disagreements: all agree when applied carefully and taken to convergence. In fact, each of the approaches leads to instructive, complementary ways to understand electronic structure and each can be developed into a general framework for accurate calculations. Each method has its advantages and its pitfalls. In this work we used the Atomic Sphere methods, which are the most general methods for the solution of the Kohn-Sham equations, namely the LAPW and LMTO-NMTO methods. *They are the* *linearized form of the augmentation plane wave PAW and muffin tin orbitals MTO methods respectively.* The disadvantage of augmentation is that the basis functions are energy dependent, so that matching conditions must be satisfied separately for each eigenstate and its eigenenergy. This leads to non-linear equations that make such methods complicated. *Linearization*[4] is achieved by defining augmentation functions as linear combinations of a radial function $\psi(E_\nu, r)$ and its derivative $\dot{\psi}(E_\nu, r)$ evaluated at a chosen fixed energy E_ν. In essence, $\psi(E_\nu, r)$ and $\dot{\psi}(E_\nu, r)$ form a basis adapted to a particular system that is suitable for calculation of all states in an energy "window". This has other advantages, e.g. it facilitates construction of full potential methods not feasible in the original APW and MTO methods.

APW and LAPW

The *augmented plane waves method* (APW), introduced by Slater [104], expands the eigenstates of an independent-particle Schrödinger equation in terms of basis functions, its shape depending on the region. The unit cell is divided in two regions: (I) spheres S_α of radius R_α around the atoms, such sphere is called *muffin tin sphere* and the (II) space between the spheres or the *interstitial region.* This is illustrated in Figure 2.1. In the region around each atom the potential is represented as a spherical potential, therefore the basis set in this region will be expanded in terms of spherical harmonics. In the interstitial region, between the atoms the potential is considered smooth and the electrons in this region are described by plane waves.

In this situation the basis set is defined in terms of plane waves in the interstitial region and spherical harmonics inside the sphere in the following way :

$$\phi_{\mathbf{k}}(\mathbf{r}) = \begin{cases} \frac{1}{\sqrt{V}} e^{i(\mathbf{k}+\mathbf{K})\cdot\mathbf{r}} & r > R_\alpha \\ \sum_{\ell,m} A_{\ell m}^{\alpha,\mathbf{k}+\mathbf{K}} u_\ell^\alpha(r,E) Y_m^\ell(\hat{\mathbf{r}}) & r < R_\alpha \end{cases} \tag{2.23}$$

where $\mathbf{k}+\mathbf{K}$ are vectors defined in the reciprocal space, r and $\hat{\mathbf{r}}$ are referred to an origin τ_α for each atom α in the unit cell and V is the volume of the unit cell. The Y_m^ℓ are spherical harmonics. The coefficients $A_{\ell m}^{\alpha,\mathbf{k}+\mathbf{K}}$ are defined in such a way that the functions outside and inside the sphere should match over the entire surface of the sphere S_α. The $u_\ell^\alpha(r,E)$ are the solutions to the radial part of the Schrödinger equation for a free atom α, and this

---

[4] Suggested by O.K. Andersen in 1975 [3]

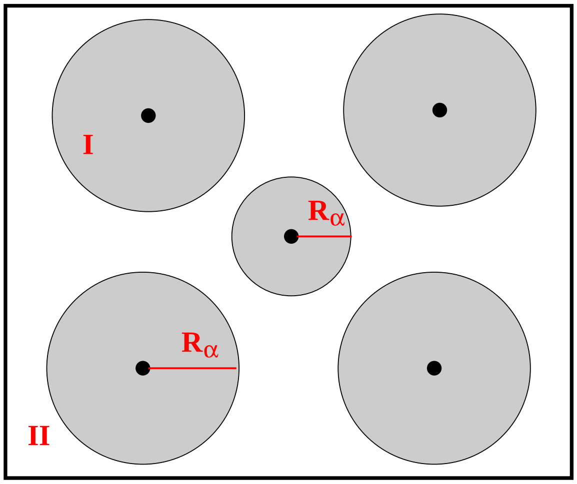

Figure 2.1: Schematic representation of the division of the unit cell done in APW/LAPW method.

at the energy E. The requirement that the plane waves continue smoothly into the sphere of radius R$_\alpha$ fixes the expansion in spherical harmonics since a $Y_m^{\ell_{max}}$ has at most $2\ell_{max}$ zeros around the sphere or $\ell_{max}/(\pi R_\alpha)$ nodes per unit of length, for a given ℓ_{max}. In order to have a plane wave that matches with this, there should be plane waves with at least a similar number of nodes per unit of length available, therefore the plane wave expansion should have a cut-off K_{max} which satisfies the condition $R_\alpha K_{max} = \ell_{max}$. This allows to determine a good ℓ_{max} for a given K_{max}.

This approximation allows for dramatic simplifications, since the wavefunctions can be represented in terms of the eigenstates in each region, reducing the entire problem into a matching or boundary condition problem. The disadvantage is the difficulty of matching the functions and solving the resulting non-linear equations in this basis.

Its linearized version, suggested by Andersen [3], the *linearized augmented plane waves* method LAPW, including the full potential generalization[5] FP-LAPW, is the most accurate and general method for electronic structure at the present time. The calculations can be done for structures of arbitrary symmetry with no bias if the basis is extended to convergence. This method takes into account all the core states, so that it allows to describe effects like nuclear magnetic resonance chemical shifts, electric field gradients at the nucleus

---

[5] The *full potential generalization* consists in including the matrix elements of the full non-spherical potential ΔV in the sphere and the full spatially varying potential in the interstitial. The basis functions are still the same LAPW (or LMTO), which are derived from a spherical approximation to the full potential.

and relativistic effects. The LAPW method expresses the basis set inside the sphere not only in terms of the radial solution of the Schrödinger equation but also includes its first derivative with respect to the energy:

$$\phi_{\mathbf{k}} = \sum_{lm} [A^{\alpha,\mathbf{k}+\mathbf{K}}_{lm,\mathbf{k}} u^{\alpha}_{l}(r, E_l) + B^{\alpha,\mathbf{k}+\mathbf{K}}_{lm,\mathbf{k}} \dot{u}^{\alpha}_{l}(r, E_l)] Y_{lm}(\hat{\mathbf{r}}) \tag{2.24}$$

where $u_l(r, E_l)$ is the regular solution at the origin of the radial Schrödinger equation for energy E_l and the spherical part of the potential inside sphere S_α; $\dot{u}^{\alpha}_{l}(r, E_l)$ is the energy derivative of u^{α}_{l} evaluated at the same energy E_l. A linear combination of these two functions constitute the linearization of the radial function; both coefficients A^{α}_{lm} and $\mathrm{B}^{\alpha,}_{lm}$ are determined by requiring that this basis function matches in value and slope each plane wave the corresponding basis function of the interstitial region. *Each plane wave is augmented by an atomic-like function in every atomic sphere.*

In APW the accuracy of the plane wave basis set was determined by K_{max}. For the LAPW basis set, it is not incorrect to use the same criterion. However, a better quantity to judge the accuracy in the LAPW is the product $R^{min}_{\alpha} K_{max}$, between the smallest atomic sphere radius R^{min}_{α} and K_{max}. In general, $R_{mt}K_{max} = 6 - 9$ are reasonable values. Systems containing C and H atoms are a special case because the muffin tin spheres of this atoms are usually very small, therefore the calculation needs a much smaller cutoff value. A cutoff value of $3 - 4$ give good results for this kind of systems.

The APW+lo method

Sjöstedt et. al. [103] have shown that the standard LAPW method is not the most efficient way to linearize Slater's APW method. It can be made more efficient when one uses the standard APW basis with the $u^{\alpha}_{l}(r, E_l)$ at a fixed energy E_l in order to keep the linear eigenvalue problem. Then, a new local orbital (lo) is added inside the muffin tin sphere to have enough variational flexibility in the radial basis functions:

$$\phi^{lm}_{\alpha,lo} = \sum_{lm} [A^{\alpha,lo}_{lm} u^{\alpha}_{\ell}(r, E_l) + B^{\alpha,lo}_{lm} \dot{u}^{\alpha}_{l}(r, E_l)] Y_{lm}(\hat{\mathbf{r}}) \tag{2.25}$$

The two coefficients $A^{\alpha,lo}_{lm}$ and $B^{\alpha,lo}_{lm}$ are determined by normalization, and by requiring that the local orbital has zero value at the muffin tin boundary (not zero slope). Hence, both the APW and the local orbital are continuous at the sphere boundary, but for both their first derivative is discontinuous. Using this approach means that per atom $2\ell + 1$ orbitals are added to the basis set. This makes the basis considerably larger than the LAPW basis set. This is compensated by the fact that a lower $R_{\alpha}^{min}K_{max}$ is needed for accurate results[6]. A mixed LAPW/APW+lo mixed basis set can be used for different atoms and even different ℓ-values for the same atom. In general, APW+lo is used for describing those orbitals which converge most slowly with the number of plane waves (like *d*- or *f*-orbitals) or the atoms with a small sphere size, and the rest with ordinary LAPW's.

MTO and LMTO

Muffin tin orbitals (MTO) form a basis of localized augmented orbitals introduced by Andersen [2] in 1971. It describes the electronic states in a small number of meaningful orbitals that can be accurate because the MTOs are generated from the Kohn-Sham Hamiltonian itself. An MTO can be understood in terms of a single atomic sphere with a flat potential in all space outside the sphere. It is defined to be a localized basis function continuous in value and derivative at the sphere boundary. The MTO basis functions are given by

$$||\chi_{RL}^{\alpha}(E)\rangle = |K_{RL}^{0}\rangle + |\chi_{RL}^{\alpha}(E)\rangle^{i} \tag{2.26}$$

where $|K_{RL}^{0}\rangle$ is defined inside the sphere and $|\chi_{RL}^{\alpha}(E)\rangle^{i}$ in the interstitial region.

$$|K_{RL}^{0}\rangle = |\psi_{RL}(E)\rangle N_{RL}^{\alpha}(E) + \sum_{R'L'} |J_{R'L'}^{\alpha}\rangle [P_{R'L'}^{\alpha}(E)\delta_{R'L',RL} - S_{R'L',RL}^{\alpha}] \tag{2.27}$$

where $|\psi_{RL}(E)\rangle$ are the solutions of the radial Schrödinger equation inside a muffin tin sphere, for certain energy E and angular momentum ℓ. $|K_{RL}^{0}\rangle$ fulfill the conditions of matching continuously and smoothly the angular momentum components at the surface of the sphere. $S_{R'L',RL}$ are the structure factors which depend only on the lattice structure and are characterized by an energy $\kappa^2(E - V_0)$. For $\kappa = 0$, the wavefunction in the interstitial region, is equivalent to the electrostatic potential due to a multi-pole moment and therefore satisfies the Laplace equation. The $N(E)$ and $P(E)$ are the normalization function and the potential function respectively, which are chosen in such a way that make the join smooth. They are defined in terms of the logarithmic derivative of the spherical Bessel J and Neumann functions K. α is the screening constant, which is introduced due to

---

[6] the reduction of RK$_{max}$ leads to smaller basis sets and thus the computational time is drastically reduced, all this with the same efficiency as with only LAPW basis set

the fact that the functions (2.26) are build up from screened Neumann functions, which add them a localized character. The Eq. (2.26) is the wavefunction at the origin of the sphere expressed as the sum of a 'head function' $|K^0_{RL}\rangle$ in that sphere plus the 'tails' from neighboring spheres $|\chi^\alpha_{RL}(E)\rangle^i$.

The solution can now be found for an eigenstate as a linear combination of the Bloch MTOs:

$$||\Psi(E)\rangle = \sum_{RL} |\chi^\alpha_{RL}(E)\rangle [N^\alpha_{RL}]^{-1} u_{RL}(E) \tag{2.28}$$

since the first term on the right-hand side of (2.27) is already a solution inside the atomic sphere, $||\Psi(E)\rangle$ can be an eigenfunction only if the linear combination of the last terms on the right-hand side of (2.27) vanishes, this is called 'tail cancelation'. This condition is expressed as

$$\sum_{RL} (P^\alpha_{R'L'}(E)\delta_{R'L',RL} - S^\alpha_{R'L',RL})[N^\alpha_{RL}]^{-1} u_{RL}(E) = 0 \tag{2.29}$$

this expression has the form of a KKR-type equation[7], but here $S_{LL'}$ does not depend on the energy.

Its linearized form, the LMTO basis [4], is written in terms of the solutions of the radial Schrödinger equation $|\psi_{RL}(E)\rangle$ and its derivative with respect to the energy $|\dot{\psi}_{RL}(E)\rangle$, by differentiating the MTO basis Eq. (2.26),

$$||\dot{\chi}^\alpha_{RL}(E)\rangle = |\dot{\psi}(E)\rangle N^\alpha_{RL}(E) + |J^\alpha_{RL}\rangle \dot{P}^\alpha_{RL}(E) \tag{2.30}$$

this implies, that for certain energy $E = E_\nu$

$$|J^\alpha_{RL}\rangle\rangle - |\dot{\chi}^\alpha_{RL}(E)\rangle N^\alpha_{RL}(E_\nu)[\dot{P}^\alpha_{RL}(E_\nu)]^{-1} \tag{2.31}$$

then, the LMTO basis is constructed as,

$$||\chi^\alpha_{RL}(E)\rangle = |\psi(E_\nu)\rangle N^\alpha_{RL}(E_\nu)$$

$$-\sum_{R'L'} |\dot{\psi}(E)\rangle N^\alpha_{RL}(E)[\dot{P}^\alpha_{RL}(E_\nu)]^{-1}[P^\alpha_{R'L'}(E_\nu)\delta_{R'L',RL} - S^\alpha_{R'L',RL}] + |\chi^\alpha_{RL}(E)\rangle^i \tag{2.32}$$

---

[7] KKR is a method developed by Korringa, Kohn and Rostoker, also called 'multiple-scattering theory'. It is a refined method for calculating energy band structures, which finds the stationary values of the inverse transition matrix T rather than the Hamiltonian.

The simplest version of MTO equations results when replacing the muffin tin spheres by space filling spheres, this is justified by the fact that if there is only a short distance between the spheres, as in a close-packed solid, the wavefunction will be nearly correct because it has the correct value and slope at the sphere boundary. This is associated with the *atomic sphere approximation* (ASA), in which the Wigner-Seitz sphere around each atom is replaced by a sphere as shown schematically in Fig. 2.2. It is evident that for closed-packed cases the distances between spheres are indeed short.

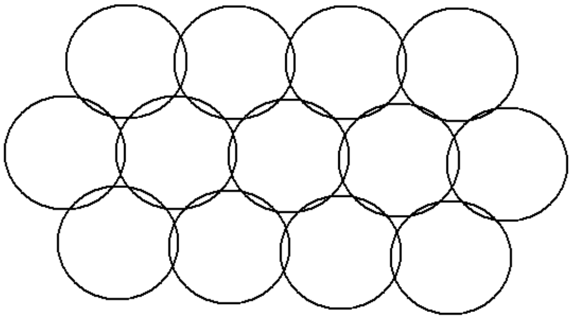

Figure 2.2: Atomic Sphere Approximation (ASA) in which the muffin tin spheres are chosen to have the same volume as the Wigner-Seitz cell, which leads to overlapping spheres [77].

Within the ASA approximation, the LMTOs are written as

$$||\chi^{\alpha}_{RL}(E)\rangle[N^{\alpha}_{RL}]^{-1} = |\psi(E_{\nu})\rangle - \sum_{R'L'} h^{\alpha}_{R'L'}|\dot{\psi}(E)\rangle \tag{2.33}$$

where,

$$h^{\alpha} = -(\dot{P}^{\alpha})^{-1/2}[P^{\alpha} - S^{\alpha}](\dot{P}^{\alpha})^{-1/2} \tag{2.34}$$

Eq. (2.33) *expresses the tail of an LMTO (function outside a sphere) extending into another sphere in terms of functions centered on that sphere.* Defining a function φ, $|\phi_{RL}(E_{\nu})\rangle = N(E)N^{-1}|\varphi(E)\rangle$, so that $|\phi\rangle = |\varphi\rangle$ and $|\dot{\phi}\rangle = \dot{\phi} + o|\phi\rangle$, this gives

$$||\chi\rangle = (I + ho)\phi + h\dot{\phi} \tag{2.35}$$

where I is the identity matrix. Finally, by orthogonalizing the LMTOs $||\tilde{\chi}\rangle = (I+ho)^{-1}||\chi\rangle$, gives the Hamiltonian form (neglecting few small terms)

$$H = E_{\nu} + h(I + ho)^{-1} = E_{\nu} + h - hoh - ... \tag{2.36}$$

The basis function defined in this way leads to an eigenvalue problem that is easier to solve than the non-linear equations given by the MTOs. The advantage of using the ASA approximation is that it removes the inconsistencies in the fact that the basis is complete to 1-th order inside the sphere while it is only complete to 0-th order in the interstital. With the ASA aproximation is possible to expand the Hamiltonian in an orthogonal representation as a power series in the two-centered tight-binding Hamiltonian h [5]:

$$\langle\tilde{\chi}|(H - E_\nu)|\tilde{\chi}\rangle = h - hoh + ... \tag{2.37}$$

this is the principle for the *ab initio tight-binding* (the tight-binding approach will be explained in the next section). This transformation of the equations leads to very simple expressions for the on-site terms and coupling between sites in terms of ψ and $\dot{\psi}$, providing an orthonormal minimal basis tight-binding formulation in which there are only two-center terms, with all Hamiltonian matrix elements determined from the underlying Kohn-Sham differential equation. The disadvantage is that all the terms are highly environment dependent, *i.e.* each matrix element depends in detail upon the type and position of the neighboring atoms.

Downfolding

In many cases the physics of the systems is contained in a few orbitals. The *downfolding* technique [100] provides a useful way to derive few-orbital Hamiltonians starting from a complicated full LDA or GGA Hamiltonian by integrating out degrees of freedom which are not of interest. The downfolded orbitals are provided by the tails of the LMTOs. They are selected by changing the order of the rows and columns in the KKR equation (Eq. (2.29)) in such a way that they are grouped into low sets (LMTO's that keep the basis) and intermediate sets (LMTO's downfolded), this leaves:

$$\begin{pmatrix} P^\alpha_{ll} - \mathbf{S}^\alpha_{ll} & -S^\alpha_{li} \\ -S^\alpha_{il} & P^\alpha_{ii} - \mathbf{S}^\alpha_{ii} \end{pmatrix} \begin{pmatrix} (N^\alpha_l)^{-1}\mathbf{u}_l \\ (N^\alpha_i)^{-1}\mathbf{u}_i \end{pmatrix} = \begin{pmatrix} 0 \\ 0 \end{pmatrix} \tag{2.38}$$

now the u_i are eliminated from the lower equation

$$[N^\alpha_i]^{-1}u_i = [P^\alpha_{ii} - S^\alpha_{ii}]^{-1}S^\alpha_{il}[N^\alpha_l]^{-1}u_l \tag{2.39}$$

This gives in the upper equation

$$(P^{\alpha}_{ll} - S^{\alpha}_{ll} - S^{\alpha}_{li}(P^{\alpha}_{ii} - S^{\alpha}_{ii})^{-1}S^{\alpha}_{il})(N^{\alpha}_{l})^{-1}u_l = 0 \tag{2.40}$$

when linearizing and solving this equation, the downfolded bands are obtained. This method has proved to be extremely successful for systems such as high-Tc cuprates [110] or low-dimensional inorganic quantum spin systems [111].

2.2.4 NMTO

The order-N muffin tin orbital (NMTO) (also known as third-generation MTOs) method provides a formalism more consistent than MTO and LMTO, in which the interstitial region is treated more accurately. The NMTO method treats the sphere and the interstitial equally by working with MTO-type functions $\psi_L(E_n, \mathbf{r}-\mathbf{R})$ localized around site $\mathbf{R}$ and calculated at fixed energies E_n both inside the sphere and in the interstitial (assumed to have a flat muffin tin potential). The NMTO basis function is then defined to be a linear combination of N, such functions evaluated at N energies [6], [8]

$$\chi^{NMTO}_{\mathbf{R},L}(\epsilon, \mathbf{r}) = \sum_{n=0}^{N} \sum_{\mathbf{R}'L'} \psi_{L'}(E_n, \mathbf{r}-\mathbf{R}') L^{N}_{nL'\mathbf{R}',L\mathbf{R}}(\epsilon, \mathbf{r}) \tag{2.41}$$

where $L^N_n(\epsilon)$ is the transformation matrix that includes the idea of screening (mixing states on different sites) and a linear combination of states evaluated at N fixed energies. The basic idea is then, instead of using one MTO with one fixed energy ($N = 1$) ϵ, N-energies ($N > 1$) $\epsilon_0, ..., \epsilon_N$ are used to construct the MTO, which then have errors proportional to $(\epsilon_i - \epsilon_0), ..., (\epsilon_i - \epsilon_N)$. This is analogous to using Lagrange or Newton interpolation and is far more practical.

Other important characteristics of these approach:

- The NMTO's are uniquely suited in materials with many bands and it provides a quantitative description of a one-electron mean-field theory with a minimal basis.
- The NMTO basis is a minimal set spanning all states in a *wide* energy range
- The energy selective and localized nature of NMTO basis makes the NMTO set *flexible* and may be chosen as *truly minimal* (=span selected bands with as few basis functions as there are bands.)

- If these bands are isolated, the NMTO set spans the Hilbert space of the Wannier functions and the orthonormalized NMTOs are the *Wannier functions.*
- Even if the bands overlap with other bands, it is possible to pick out those few bands and their corresponding Wannier-like functions with NMTO method.
- The NMTO method can thus be used for direct generation of *Wannier or Wannier-like functions*

Wannier Functions

Strictly speaking, the Wannier functions are the Fourier transform of Bloch functions $\psi(\mathbf{k},\mathbf{r})$ [76],

$$\phi(\mathbf{R},\mathbf{r}) = \frac{1}{\sqrt{N}}\sum_{\mathbf{k}} e^{-i\mathbf{k}\cdot\mathbf{R}}\psi(\mathbf{k},\mathbf{r}) \qquad (2.42)$$

The summation is over all **k**-vectors in a Brillouin zone. This functions at different sites or with different band indices are orthogonal. Since the complete set of Bloch functions can be written as linear combinations of the Wannier functions, the Wannier functions form a complete orthogonal set. They therefore offer an alternative basis for an exact description of the independent electron levels in a crystal potential. Because the Wannier functions are localized about individual points in the lattice, *i.e.*, when $\mathbf{r}$ is larger than some length one the atomic scale, $\phi(\mathbf{r})$ will be negligibly small, this functions offer an ideal tool for discussing phenomena in which the spatial localization of electrons plays an important role, as for example in magnetic phenomena.

2.2.5 Advantages and disadvantages: LAPW vs. LMTO

In this work the ground state properties were calculated with both LAPW and LMTO basis sets. The LMTO calculations were compared with the LAPW ones, which is necessary in order to ensure the fiability of the results. The necessity of confronting these two methods is related to the fact that the studied compounds are open-shell systems. This section is dedicated to the review the advantages and disadvantages of both LAPW and LMTO basis sets, in order to give an explanation about the necessity of combining different approaches in order to obtain reliable results. The FP-LAPW is one of the most efficient and accurate method for electronic structure at the present time, the ground state properties calculated within this basis set, the total energy, band structure, density of states, atomic forces, between others are very accurate and compare quite well with experimental results. However, the accuracy comes at a price, it is necessary to use a large basis set of plane waves and high angular momentum functions which in turn means that the potentials must be represented accurately to twice the cutoffs in wavevectors and angular moments used for the wavefunctions. The need of high angular momenta is required in order to match the spherical and plane waves at the sphere boundary. Thus, calculations with this method will be in general demanding. As a result, these calculations are slower than with other methods of less precision. In the case of open shell systems, many more plane waves will be necessary in order to fill the spaces between the spheres, making the calculations computationally very demanding[8].

On the other hand, the LMTO method makes use of a few basis functions for calculating the ground state properties which can be accurate for close-packed systems when using the ASA approximation. However, this approximation fails for open structures where the interstitial region is large. Within the ASA approximation, the LMTO method is extremely fast because it uses a minimal basis where only wavefunctions with ℓ corresponding to the actual electronic states involved are needed. This is in contrast to the LAPW method where is necessary to have high ℓ in order to fulfill the continuity requirements. The price for this speed and efficiency, is that the interstitial region is not treated accurately. Open structures can be treated only with correction terms or by using ‘empty spheres’. The choice of empty spheres is problematic in general cases [77]. Finally, there is no way to achieve full convergence as there is in the LAPW method. Thus the approximations in the LMTO approach are difficult to control and care is needed to ensure robust results.

The results of the electronic properties in this work, are presented within the FP-LAPW scheme because it gives the most accurate results. The LMTO calculations, which are cross-checked with the LAPW calculations, are necessary as an input for the NMTO calculations, which gives results for the magnetic properties of the systems. The comparison between

---

[8] Of course, this is a neccesary but not a sufficient condition for judging whether a calculation is demanding or not, because the lower the symmetry and the higher the number of C-H bondings make the calculations very demanding. The symmetries reduce the k-space where the numerical problem is solved, higher symmetries allow a bigger reduction in the number of k-points in the k-space or in our case the Brillouin zone. Also, the C-H bond lengths are usually small, which affect the size of the muffin tin radii of these atoms, which have to be choosen small. The matrix size to be solved is inversely related to the smallest muffin tin radii, i.e, the small the muffin tin radii the bigger the matrix size, which increases the computational requirements.

LAPW and LMTO is then neccesary in order to obtain the correct description of the electronic and magnetic properties.

2.2.6 Obtaining physical quantities with DFT

In order to determine the charge density and other quantities, it is necessary to evaluate sums over the occupied states, which for crystals become integrals over the Brillouin zone (The Brillouin zone will be presented in more detail in the next chapter.) These integrals are necessarily calculated numerically using wavefunctions and eigenvalues at a finite number of k-points in the zone. The quantities we are interested in, in our work are:

- *Charge Density:* is calculated from the eigenvalues of the solved self-consistent problem as

  $$Q = \int_V |\Psi(\mathbf{r})|^2 d\mathbf{r} \tag{2.43}$$

  which gives the probability of finding an electron in a given volume V (in the 3D case) or surface S (in the 2D case).

- *Band structure:* Once the Kohn-Sham orbitals are represented on a basis set (e.g. LAPW, LMTO), we proceed to solve the self-consistent problem, Eq. (2.12)-(2.16), in order to calculate the total energy. The resulting self-consistent solution in the k space gives a set of eigenvalues $\varepsilon_{\mathbf{k}}$ for each $\mathbf{k}$-point in the Brillouin zone (The Brillouin zone will be introduced in the next chapter), which form the Kohn-Sham band structure in a solid. *The dispersion of the energy levels as a function of* $\mathbf{k}$ *gives the band structure of a system.* This band structure is often assumed to approximate the true band structure of the interacting system. How closely the Kohn-Sham band structure approximates the true band structure, depends not only on the choice of the functional, but also on whether the system has spin-polarization or it is highly correlated.

- *Density of states:* When solving the self-consistent Kohn-Sham equations for a crystal lattice we get a set of n energy values ϵ_n or eigenvalue spectrum, because we are dealing with a problem with *periodic boundary conditions.* A very useful quantity obtained from the eigenvalue spectrum is,

$$g(\epsilon) = \frac{2}{V_{BZ}} \sum_{n} \int \delta(\epsilon - \epsilon_{\mathbf{k}}^{n}) d\mathbf{k} \tag{2.44}$$

The function $g(\epsilon)$ is called the *Density of states* DOS, which is the number of states per unit of energy. δ is the *Dirac delta function*, $\mathbf{k}$ is any vector in the first Brillouin zone that corresponds to a plane wave that is commensurate with the macroscopic crystal. V_{BZ} is the volume of the first Brillouin zone, and the integral is over the first Brillouin zone. The factor 2 is included to account explicitly for (degenerate) spin.

2.3 An overview on classical ab initio and molecular dynamics

Part of this work was developed as interdisciplinary projects between experimentalist and theoreticians from the chemistry and physics areas. Due to the complexity and diversity of the studied compounds, it was necessary in some cases, to develop a procedure which combine different approaches. This will be presented in Section 5.1. This procedure includes ab initio classical techniques and molecular dynamics relaxation. This section is dedicated to present the general ideas about these methods.

2.3.1 The DREIDING force field methods

A *force field* is a mathematical function which returns the energy of a system as a function of the conformation of the system. The idea is to consider a molecule as a collection of atoms held together by elastic forces, these forces can be written in terms of potential energy functions of various structural features such as bond lengths, bond angle, non-bonded interactions and so on. The force field is a combination of these potential energy terms. Force field methods were developed with the philosophy of carrying out simulations for describing molecular structures and properties in an accurate way within a reasonable amount of computational time and applicable to a large variety of systems. Different force field methods have been developed, every one for specific materials, in this work we have used the simple generic DREIDING force field [80], which is useful for predicting structures and dynamics of organic, biological and main-group inorganic molecules. It writes the force field of a system based on simple hybridization considerations. It needs only 4 input parameters namely, the atom type (N, B, etc.), the hybridization or geometry (1=linear (sp^1), 2=trigonal (sp^2), 3=tetrahedral (sp^3)), the oxidation state and the number of implicit hydrogens. Then, the force field is written as

$$E = E_{val} + E_{nb} \tag{2.45}$$

where E_{val} and E_{nb} contains the valence interactions and the non-bonded interaction terms respectively. In DREIDING the valence interactions consist of

$$E_{val} = E_B + E_A + E_T + E_I \tag{2.46}$$

where E$_B$ (two-body) is the bond stretch term, which is described either as a simple harmonic oscillator or as a Morse function, E$_A$ (three-body) is the bond-angle bend, E$_T$ (four-body) dihedral angle torsion and E$_I$ (four-body) inversion terms, while the non-bondend interactions consist of the van der Waals or dispersion (E$_{vdw}$), electrostatic (E$_Q$) and explicit hydrogen bonds (E$_{hb}$) terms,

$$E_{nb} = E_{vdw} + E_Q + E_{hb} \tag{2.47}$$

2.3.2 Car-Parinello molecular dynamics

The formulation introduced by Car and Parrinello [24], minimizes the Kohn-Sham functional (Eq. (2.7)) considering as parameters the nuclear coordinates R_I and the electronic degrees of freedom, expresed as independent particle Kohn-Sham orbitals ψ_i.

$$L = \sum_i \frac{1}{2}\mu \int d^3r|\dot{\psi}_i|^2 + \sum_I \frac{1}{2} M_I \dot{R}_I^2 - E[\psi_i, \mathbf{R}_I] + \Lambda_{ij}[\int d^3r \psi_i \psi_j - \delta_{ij}] \tag{2.48}$$

In Eq. (2.48) the dot indicates time derivative, M_I are the physical ionic masses, and μ is an arbitrary parameter of appropiate units. This Lagrangean generates a dynamics for the parameters ψ_i and R_I through the equations of motion:

$$\mu\psi_i(\mathbf{r},t) = -\frac{\delta E}{\delta\psi_i^*(\mathbf{r},t)} + \sum_{ik} \psi_k(\mathbf{r},t) \tag{2.49}$$

$$M_I R_I = -\nabla_{R_I} E = \mathbf{F}_I \tag{2.50}$$

Which have the form of motion of classical objects given by the newtonian equations for acceleration in terms of forces, subject to the constrain of orthogonality in the case of electrons. Thus, the Car-Parrinello approach allows to perform calculations for the nuclei treated classically and the electronic degrees of freedom, minimizing the energy of the electrons and solving the equation of motion for the nuclei simultaneously (*i.e* the atoms relax into their minimum energy configuration while the electron density is being refined). In the Kohn-Sham scheme it is necessary to solve the electronic degrees of freedom iteratively for a given atomic configuration and then move the atoms towards their minimum energy configuration guided by the calculated forces acting upon them.

2.4 Effective models

2.4.1 Tight-binding and Hubbard Hamiltonian

In the previous section it was discussed, that the LDA/GGA fails for systems with strong on-site Coulomb correlations. In section 2.2.2, LDA+U was shown as a possible improvement on LDA while retaining an effective single-particle scheme. Another way to take into account the correlations that are poorly described by LDA is sketched in the following. For the low energy physics, in most systems, only a small number of orbitals is relevant. These orbitals can be extracted from a LDA calculation and its energy can be parameterized by fitting a tight-binding model. A general tight-binding Hamiltonian can be written in the form

$$\hat{H}_{TB} = \sum_{i,\sigma} \varepsilon_i (c^\dagger_{i,\sigma} c_{i,\sigma}) + \sum_{\langle ij \rangle,\sigma} t_{ij} (c^\dagger_{i,\sigma} c_{j,\sigma} + h.c) \tag{2.51}$$

where $c^\dagger_{i,\sigma}$ and $c_{i,\sigma}$ are creation or annihilation operators for an particle at site i or j, respectively, for sake of simplicity, additional orbital indices are suppressed. The summation $\langle ij \rangle$ is over bonds connecting sites i and j, and ε_i is the so-called *on-site energy* of the orbital i.

The Hamiltonian of the correlated system can be constructed by adding terms guessed on the basis of physical intuition and adapted to the considered compound and problem. For the simplest case of only one band, the sum over the on-site energies is a constant, and the Hamiltonian is written as

$$\hat{H} = \sum_{\langle ij \rangle,\sigma} t_{ij} (c^\dagger_{i,\sigma} c_{j,\sigma} + h.c) + U \sum_i \hat{n}_{i,\uparrow} \hat{n}_{i,\downarrow}, \qquad \hat{n}_{i,\sigma} = c^\dagger_{i,\sigma} c_{i,\sigma} \tag{2.52}$$

this Hamiltonian is known as the *Hubbard Hamiltonian* [48]. The terms t_{ij}, usually called *hopping terms*, represents the kinetic energy; it transfers an electron at the ith site to the jth site without changing spin direction. U describes the Coulomb repulsion of two particles at the same site i in addition to the mean field repulsion contained in the tight binding approach. If more than one band is required for a proper description of the system, the Hamiltonian (2.52) can be expanded easily [122]:

$$\hat{H} = \sum_{i,\sigma} \varepsilon_i (c^\dagger_{i,\sigma} c_{i,\sigma}) + \sum_{\langle ij \rangle,\sigma} t_{ij} (c^\dagger_{i,\sigma} c_{j,\sigma} + h.c) + U \sum_i \hat{n}_{i,\uparrow} \hat{n}_{i,\downarrow} + \sum_{\langle ij \rangle,\sigma} V_{ij} \hat{n}_i \hat{n}_i \tag{2.53}$$

in Eq. (2.53), the on-site Coulomb repulsion U_i is generalized to be orbital dependent and an intersite Coulomb interaction V_{ij} is added.

2.4.2 Spin Hamiltonians

Direct exchange

The effective interaction between two spins located at i and j are described by the *Heisenberg Hamiltonian*:

$$H = -2\sum_{i,j} J_{ij}\mathbf{S}_i \cdot \mathbf{S}_j \tag{2.54}$$

where $\mathbf{S}_{i(j)}$ is the spin operator of the electron at site $i(j)$ and the coefficients J_{ij} are two-atom *exchange integrals.* The exchange interaction originates from a quantum exchange term of the Coulomb interaction between d electrons so that it has the coupling strength of the Coulomb interaction. The Hamiltonian (2.54) describes the *isotropic exchange coupling* in a system of N atoms with spins $S_1, S_2, ..., S_N$ without orbital degeneracy. The single-spin Hamiltonian model takes into account effective crystal field symmetry of the cluster.

Superexchange and magnetic anisotropy

Effective exchange interactions between spins on transition metal ions via oxygen or other ligands are referred as superexchange interactions. A microscopic basis for superexchange between magnetic ions was first given by P. Anderson [9]. His calculation started from a Hubbard Hamiltonian, Eq. (2.52), in which there is one electron per site in the limit of large Coulomb interaction U. In this limit, the hopping elements is neglected and each electron (hole) may be characterized by its spin. When the kinetic energy, described by the hopping term, is included perturbatively, one finds a spin Hamiltonian, which neglecting high order terms in the perturbation, is written as

$$H = J_{ij}\mathbf{S}_i \cdot \mathbf{S}_j \tag{2.55}$$

this is an isotropic exchange interaction between nearest-neighbor spins, with $\mathrm{J}_{ij} = 4t_{ij}^2/\mathrm{U}$. Moriya [85] used Anderson formalism to study the effect of spin-orbit interactions on superexchange between magnetic ions. The Hamiltonian expressing the spin-orbit interaction is given by

$$H_{SO} = \lambda(\mathbf{L} \cdot \mathbf{S}) \tag{2.56}$$

the coefficient λ is the *spin-orbit coefficient.* L and S are the orbital and spin momenta operators respectively. In the case of d electrons, the spin-orbit term is usually small compared with the crystal field terms, therefore it is usually treated as a perturbation. Applying perturbation theory till second order in the hopping perturbation, Moriya showed that for sufficiently low symmetry the most general effective spin Hamiltonian for two spin-1/2 magnetic ions is of the form

$$H = \sum_{ij}(J_{ij}\mathbf{S}_i \cdot \mathbf{S}_j + \mathbf{D}_{ij}[\mathbf{S}_i \times \mathbf{S}_j] + \mathbf{S}_i \cdot A_{ij} \cdot \mathbf{S}_j) \tag{2.57}$$

where A_{ij} is a symmetric 3×3 tensor. The first term represents the isotropic symmetric exchange, the second and third terms represent the antisymmetric and symmetric anisotropies, respectively. The antisymmetric interaction was pointed out phenomenologically by Dzyaloshinsky [37] and the microscopic derivation was done by Moriya. Therefore this interaction is called the *Dzyaloshinsky- Moriya antisymmetric exchange.* The vector $\mathbf{D}$ does not vanish in the general case, except when the crystal field surrounding the magnetic ion has inversion symmetry with respect to the center between two magnetic ions. The rules concerning the direction of the vector $\mathbf{D}$, obtained by Moriya, are as follows: be AB the line segment connecting the two spins, and C the midpoint of that line segment,

1. when there is a mirror plane perpendicular to AB through C: $\mathbf{D} \perp AB$
2. when there is a mirror plane m including AB: $\mathbf{D} \perp m$
3. when there is a two-fold rotation axis perpendicular to AB through C: $\mathbf{D}\perp$ two-fold rotation axis
4. when there is a n-fold rotation ($n > 2$) axis along AB: $\mathbf{D}||AB$

By this interaction, the spins of sublattices aligned antiparallel to each other due to the exchange interaction cant by a small angle θ and posses a ferromagnetic component perpendicular to the spin axis of the antiferromagnet. The canting angle θ is given by $\theta = D_z/(2|J|)$. The $\mathbf{D}_{ij}$ vector and the A_{ij} are related to the J parameter by

$$|D_{ij}| \sim (\Delta g/g)J, \qquad |A_{ij}| \sim (\Delta g/g)^2 J \tag{2.58}$$

where Δg is a shift in the value of the free-electron gyromagnetic ratio g due to the spin-orbit interaction.

Chapter 3

Crystal structures of the studied compounds

The materials studied in this work are described as bulk materials with a well-defined crystal structure. A crystal is an ordered state of matter in which the positions of the nuclei are repeated periodically in space. The crystal is completely specified by the type and positions of the nuclei in one unit (primitive unit cell), and the rules that describe the repetition (translations). The set of translations which generates the entire periodic crystal by repeating the basis, is a lattice of points in space called the Bravais lattice. The crystalline order is described by its symmetry operations. The set of translations with the addition operation forms a group. In addition there may be other point operations that leave the crystal invariant, such as rotations, reflections, and inversions. The knowledge of the crystal lattice parameters, with the basis set or atomic positions are requirements for performing ab initio calculations. In this chapter, we present a brief description of the Bravais lattices corresponding to the studied compounds in this thesis and we present the corresponding First Brillouin Zone FBZ for the equivalent cell in the reciprocal space. The FBZ is the primitive cell in the k-space which contains the symmetries of the Bravais lattice associated to it. On this Zone one can define high symmetry points which determine the irreducible zone. These symmetry points define the paths for studying the band structure on compounds.

3.1 Triclinic

This is the Bravais lattice generated by three primitive vectors with no special relationships to one another, and is therefore the Bravais lattice with minimal symmetry. It is noted by P1 and the only operation that contains is the identity. When within this group, the system has invariance under an inversion in a lattice point and the identity, it is denoted as $\bar{P}_1$ [109]. A triclinic unit cell is characterized by having no constrains for the magnitude of the primitive vectors and the angles between them, *i.e.*, $a \neq b \neq c$ and $\alpha \neq \beta \neq \gamma$ (see Figure 3.1). The volume of a unit cell can be calculated by evaluating $\mathbf{a} \cdot \mathbf{b} \times \mathbf{c}$, where **a**, **b** and **c** are the lattice vectors. The volume of a triclinic lattice is calculated as, $V = abc\sqrt{1 - \cos^2\alpha - \cos^2\beta - \cos^2\gamma + 2\cos\alpha\cos\beta\cos\gamma}$. The first Brillouin zone for this lattice is depicted in Figure 3.2. In it high symmetry points are also shown.

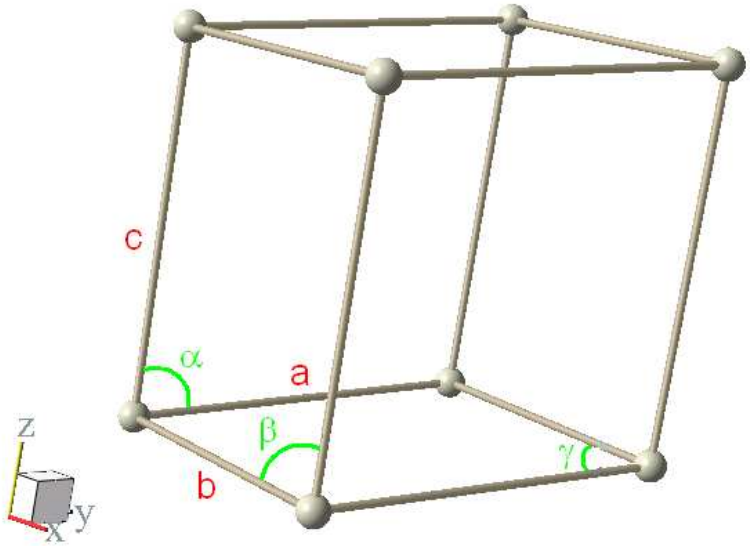

Figure 3.1: Representation of a Triclinic unit cell.

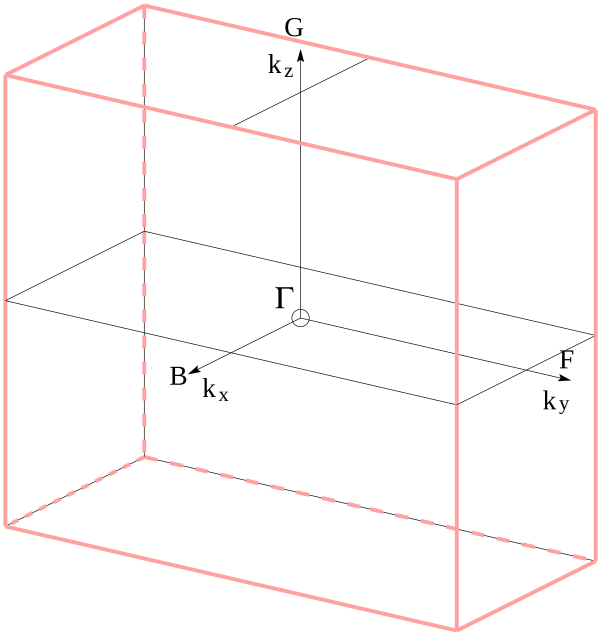

Figure 3.2: The Brillouin zone for a triclinic lattice. In it are shown high symmetry points: $\Gamma = (0, 0, 0)$, F=$(0, 1/2, 0)$, B=$(1/2, 0, 0)$ and G=$(0, 0, 1/2)$, in units of (π/a, π/b, π/c)

3.2 Monoclinic

This lattice is generated by requiring that one of the three primitive vectors be perpendicular to the plane of the other two which are inclined toward each other at an oblique angle, *i.e.*, $\alpha = \beta = 90 \neq \gamma$. There are no constraints for the magnitude of the primitive vectors $a \neq b \neq c$. The monoclinic lattices can be defined as, primitive monoclinic lattice (P) where the lattice positions are on the cell corners only, and a monoclinic lattice type (C) which is a primitive lattice (P) with a lattice point at the centers of the basis faces. In our study we have worked with a monoclinic lattice of type P, which is shown in Figure 3.3. The volume of this unit cell is defined as $V = abc \sin\gamma$. The Brillouin zone and some high symmetry points for this monoclinic lattice are shown in Figure 3.4.

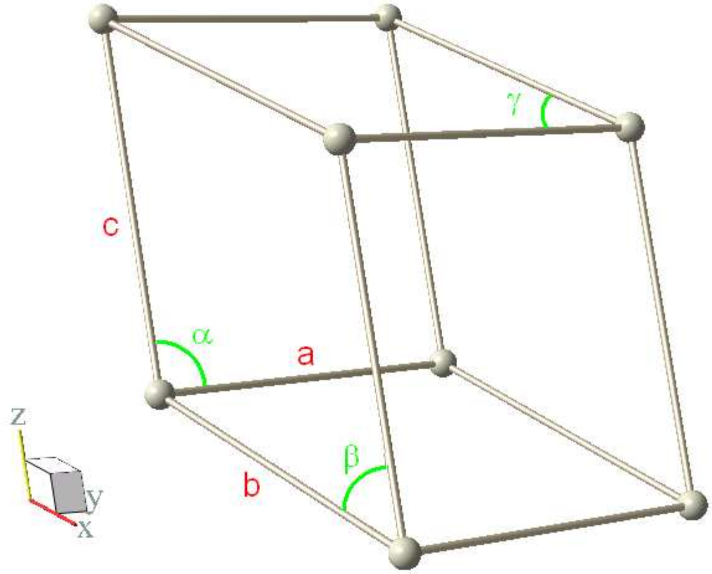

Figure 3.3: Representation of a primitive monoclinic unit cell.

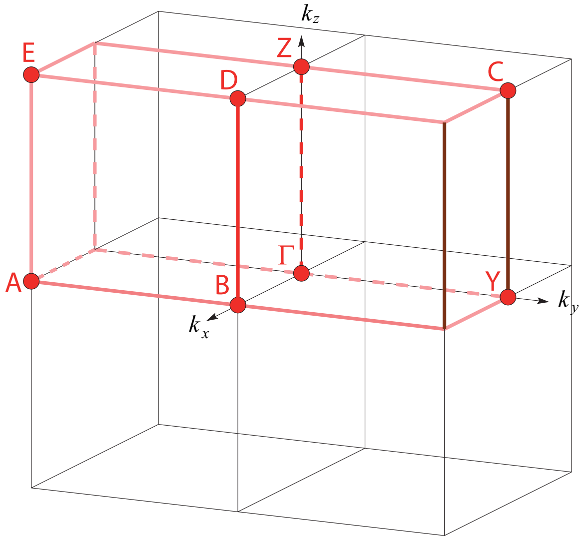

Figure 3.4: The first Brillouin zone for a monoclinic lattice. The high symmetry points chosen in this work are: $\Gamma = (0, 0, 0)$, Y=$(0, 1/2, 0)$, B=$(1/2, 0, 0)$ and Z=$(0, 0, 1/2)$, in units of $(\pi/a,\ \pi/b,\ \pi/c)$.

3.3 Tetragonal

This Bravais lattice is generated by requiring that three primitive vectors be perpendicular to each other and one of them can have a different length than the other two, *i.e.*, $\alpha = \beta = \gamma = 90^\circ$ and $a = b \neq c$. This unit cell will have a square basal plane. With this characteristics, one defines two kinds of tetragonal lattices, a primitive tetragonal lattice (P) in which the lattice points are at the cell corners only, and the body centered tetragonal lattice (I) which contains one additional lattice point at the center of the cell. In our study we have worked with a primitive tetragonal lattice of type P, it is shown in Figure 3.5. The volume of this lattice is given by $V = a^2c$. The First Brillouin Zone is shown in Figure 3.6.

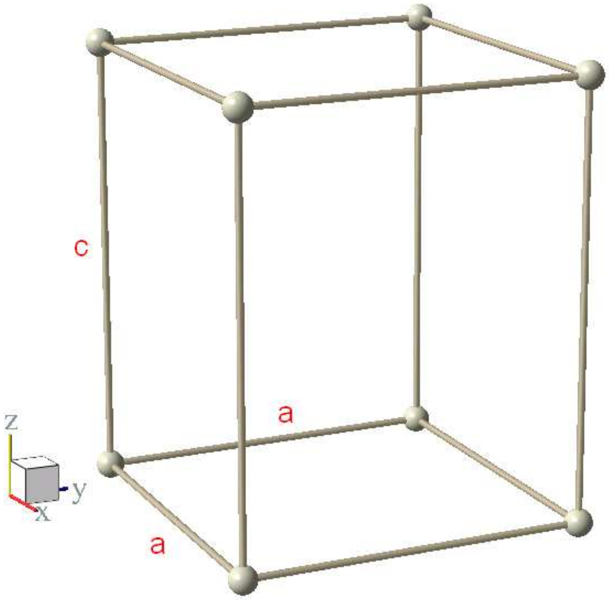

Figure 3.5: Representation of a primitive tetragonal unit cell.

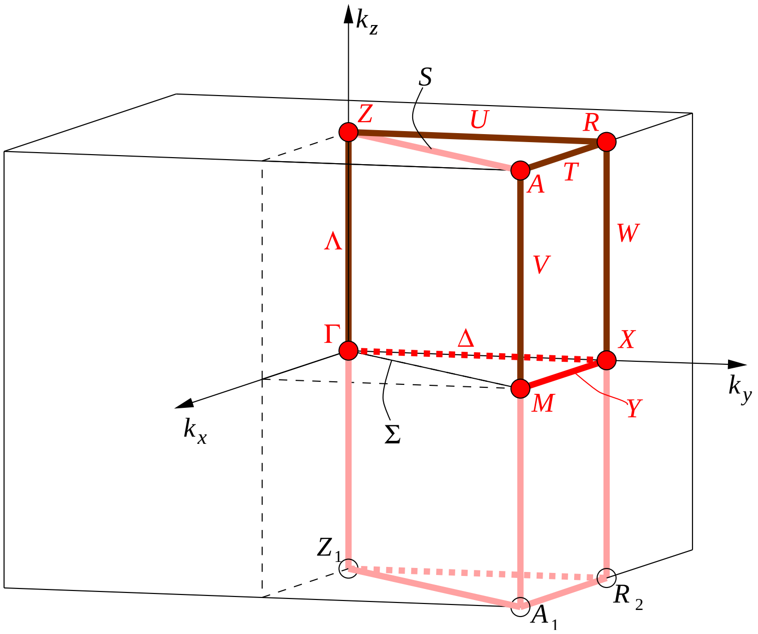

Figure 3.6: Schematic representation of the first Brillouin zone of a primitive tetragonal cell. The high symmetry points chosen in this work are $\Gamma = (0,0,0)$, Z=$(0,0,1/2)$, R=$(0,1/2,1,2)$, A=$(1/2,1/2,1/2)$, X=$(0,1/2,0)$, M=$(1/2,1/2,0)$ and X=$(0,1/2,0)$, in units of (π/a, π/b, π/c).

Chapter 4

Low dimensional spin systems

Low dimensional correlated systems show a wide variety of physically interesting and unusual properties, which depend not only on the dimensionality of the network but also on the nature of their components. In this chapter we present the materials we have investigated. Although our study is not limited to metal-organic frameworks, we review in the first section their importance focusing on their magnetic properties which are not usually exploited due to the difficulties associated to them. The second section is dedicated to Cu(II)-hydroquinone based materials. We show the advantages of linking Cu ions with quinoid linkers and motivate the study of two representatives of this family of compounds, namely, a polymeric chain and a dimer-like system. In the following sections we present materials with different dimensionality in which, competing interactions are present, giving rise to interesting magnetic phenomena. We introduce the structural properties for every of them and review experimental data. We describe the different magnetic phenomena that arise in these materials and review proposed scenarios that have attempted to explain the microscopic mechanisms for these phenomena. Finally, our methodology to describe the underlying physics in these systems and further goals are presented.

4.1 Metal-organic frameworks

Over the last decade, metal-organic frameworks (MOFs) also known as coordination polymers, have emerged as an important class of new materials which has attracted great interest. These materials are synthesized in a self-assembly process in which metal vertices are connected by organic linkers which do not involve direct metal-carbon bonding. Potential applications of MOFs include molecular magnetism, materials for adsorption applications (gas separation and gas storage) and heterogeneous catalysis. Because of the predictability of the synthetic routes to MOFs and the nearly infinite number of possible variations, molecular modelling is an attractive tool to further study the properties of these materials and screen new structures before they are synthesized. This approach will ultimately lead to developing a design strategy for MOFs with properties tailored towards specific applications by choosing the *appropriate building blocks.* So far, molecular modelling has been applied for example to the following areas [86], [11],[45], [79]:

- Structure predictions from individual building blocks
- Nucleation and growth of MOF crystals
- Ab initio predictions of vibrational frequencies and magnetic properties (molecular magnets)
- Investigating the stability of MOFs upon water uptake
- Optimization of interaction between MOFs and hydrogen molecules and prediction of adsorption equilibria

As molecular magnets, in order to achieve optimally functioning systems, it is of advantage to use ideas that have long been exploited heavily in the fine tuning of the properties of inorganic crystals. For example, charge and spin densities are routinely being adjusted in semiconductors and high-T_c superconductors by doping or by substituting the transition metals with neighbors in the periodic table. The interest in metal-organic materials is partly due to their modular nature: The extensive experience of organic synthetic chemistry can be used for the assembly of the molecular constituents of the metal-organic crystal. Thus, substitution of organic groups and formation of ligands can play the role of doping in the search for materials with desired magnetic interaction strengths and charge carrier concentrations. This modular setup has the great advantage that functionalities are decoupled, thus allowing to modify relevant subunits chemically while not changing the subsequent crystal engineering. Therefore, *metal-organic frameworks are promising candidates for the development of new materials for technological applications.* Organic molecules mediating metal interactions has also the advantage that it can produce rather moderate to weak coupling constants which allows experimentally to access regions of quantum criticality[1]. Magnetic field-induced or pressure-induced transitions are then possible to realize under

---

[1] The idea of criticality comes from phase transitions associated to quantum fluctuations. A quantum critical point occurs when the phase transition temperature of a material is suppressed to absolute zero.

easily accessible conditions. This is not the case for many of the inorganic materials, where often high magnetic fields or high pressures are needed to induce a quantum phase transition.

Due to these characteristics intense efforts have been dedicated to synthesize metal-organic materials that had led to a vast variety of these kind of compounds which exhibit also a wide variety of interesting phenomena, ranging from quantum criticality [106], spin transition [54] and magnetic ordering at room temperature [49] between others.

However, most of the metal-organic compounds generally contain a large number of atoms in the unit cell and a very low symmetry (usually triclinic or monoclinic), making the first principles study of the electronic and magnetic properties of these systems computationally very demanding. Moreover, since and accurate determination of hydrogen positions with X-ray diffractometry is very difficult, usually the available structure data are poorly determined, implying unstable quantum mechanical calculations. In some cases, the crystal structures are not even known, due to the absence of single crystals suitable for an X-rays structure analysis.

In order to overcome these shortcomings, this study was developed in a two-step approach which allowed to perform accurate ab initio density functional theory (DFT) calculations on reliable model structures for metal-organic compounds. The expression ‘ab initio prediction of crystal structures’ is also used in the sense of ‘a priori prediction’, *i.e.* predictions without reference to diffraction data. If experimental data are known, e.g. from crystal data of analogous structures, this knowledge should of course be used as far as possible in order to generate reliable model structures and to calculate solid-state properties. This procedure is explained in detail in Section 5.1. Additionally some of the metal-organic compounds we have studied allow the possibility of studying spin transitions as in the Fe(II)-triazole and magnetic frustration as in the $Cu_4OCl_6daca_4$.

4.2 1,4-hydroquinone ligands bridging Cu(II)-ions

With the goal of exploring new classes of molecule-based quantum magnets upon variations in their chemical and/or physical properties, a series of novel low-dimensional metal-organic compounds have been synthesized and characterized in the experimental groups of Prof. Mattias Wagner from the chemistry department and Prof. Michael Lang from the physics department of the Johann Wolfgang Goethe-Frankfurt University. These compounds are based on Cu(II) atoms and hydroquinone-derived linkers [117], [35], [118]. The 1,4-hydroquinone molecule belongs to the group of quinoid linkers ($p-$benzoquinone, $o-$benzoquinone, hydroquinone), which are based on a non-aromatic six-membered carbon ring. In particular, the hydroquinone with chemical formula $C_6H_4(OH)_2$, it has two hydroxyl (OH) groups bonded to a benzene ring as shown in Figure 4.1(b). The $o-$benzoquinone is one of the two isomers of quinone, the other being $p-$benzoquinone, which is a form of quinoid, is produced on oxidation of hydroquinone (Fig. 4.1). Their chemical formula is $C_6H_4O_2$ [13].

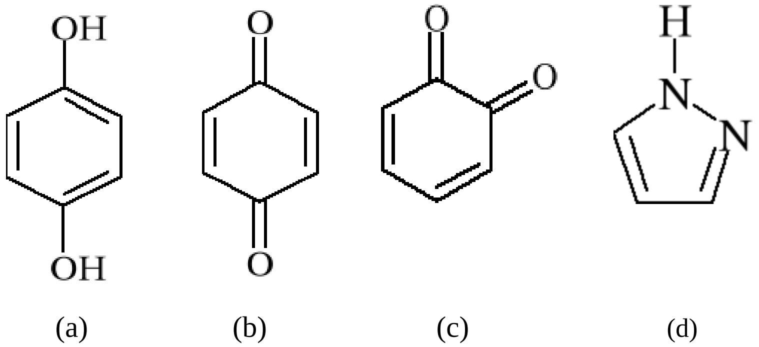

Figure 4.1: Quinoid linkers: (a) hydroquinone, (b) $p-$benzoquinone, (c) $o-$benzoquinone. The figure (d) shows a pyrazole ring, which together with the hydroquinone, is one of the constituents of CuCCP.

Quinoid linkers are particularly attractive, because their redox activity[2] is preserved after they have been attached to the metal ions. They tend to differ in their molecular structures as well as in their metal-ligand orbital interactions and therefore they allow to influence the magnetic properties of the bulk material using electrochemical methods. For these reasons, ligands built from a hydroquinone core appears to be a promising bridging unit for the gene-

---

[2] The redox process consists of electron transfer only and occurs stepwise with an intermediate radical ion of considerable thermodynamic stability

ration of polymeric metal-containing materials. Other di-nuclear transition metal complexes based on quinoid centers have been reported in the literature [16], [58]. Quinone linkers are known to mediate a magnetic exchange between Cu(II) ions of moderate strength, i.e 10 K [61]. Most importantly, the hydroquinone linker can be chemically modified maintaining the magnetic exchange between the Cu(II) ions at a moderate strength. Additionally, the synthesized compounds contain Cu^{2+} bridged by these hydroquinone molecules. The advantage of Cu^{2+} lies in the fact, that a square planar coordination sphere is preferred over an octahedral one, which minimizes the chance of unwanted interchain crosslink formation. Experimentally, a series of low-dimensional hydroquinone-based quantum-spin systems have been synthesized[117], which includes an isolated Cu(II) dimer (TK102), coupled-dimers systems (TK91, TK251) and Cu(II)-2,5-bis(pyrazol-1-yl)-1,4-dihydroxybenzene (known as CuCCP), which constitutes a 1D uniform antiferromagnetic $S = 1/2$ Heisenberg spin chain system. The aim of the present work is to study the electronic and magnetic properties of two representatives of this family of compounds namely, the 1D chain CuCCP and the Cu-dimer TK91, focusing on the influence of the bridging molecules over the metal centers. The crystal structure of the salt TK91 is rather similar to the structure of the salt TK251. The basic difference is in the coordinated molecules, O_3SCF_3 in the TK91 and BF_4 in TK251. However we choose the TK91 over the TK215 because the former was obtained as crystals and the later as powder.

The CuCCP compound offers the possibility of studying the physics of 1D systems and due to its modular nature, it allows to introduce modifications to the system in a straightforward manner. Its study gives important information to understand the microscopic properties of TK91, because the magnetic building blocks of TK91 are CuCCP polymers connected each other in the unit cell, which could give origin to 2D or 3D networks.

4.2.1 CuCCP

Dinnebier *et al.* reported the synthesis, magnetic structure and crystal structure determination of Cu(II)-2,5-bis(pyrazol-1-yl)-1,4-dihydroxybenzene compound obtained by layering a solution of 2,5-bis(pyrazol-1-yl)-1,4-dihydroxybenzene in CH_2Cl_2 with a solution of $CuBr_2$ in concentrated aqueous ammonia [35]. Its formula is $CuC_{12}N_4O_2H_8$, with one Cu-atom per unit cell. The system, known also as CuCCP, crystallizes in the triclinic space group $P\bar{1}$ with 27 atoms per unit cell and a=5.1723(5) Å, b=7.9587(9) Å, c=8.2298(11) Å, α=118.221(6)°, β=91.520(9)° and γ=100.148(8)°. It tends to form independent polymeric chains consisting of deprotonated 2,5-bis(pyrazol-1-yl)-1,4-dihydroxybenzene molecules bridged by Cu(II) ions with a $3d^9$ configuration, which corresponds to a local spin 1/2 (Fig. 4.3). Experimentally the susceptibility behavior shows that the system is a quasi one-dimensional antiferromagnetic spin system (J<0) with a nearest neighbor coupling constant of $J/k_B \sim$ 20 K.

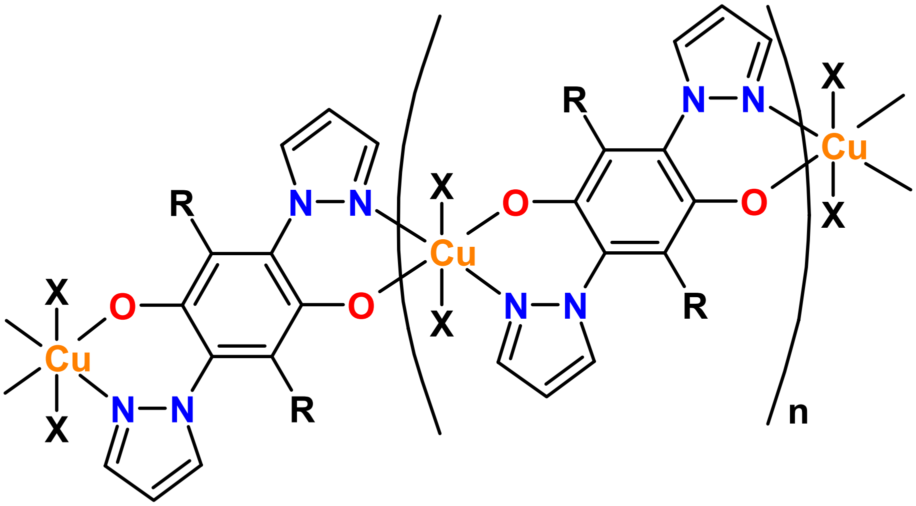

Figure 4.2: Polymeric unit of Cu(II)-2,5-bis(pyrazol-1-yl)-1,4-dihydroxybenzene (CuCCP) (X=$\emptyset$, R=H). We will consider the substitutions R=CN and R=NH_2 and the ligands X=H_2O and X=NH_3.

The chain axes are oriented along the *c*-axis of the crystal and the copper ions are located at $(1/2, 1/2, 1/2)$ and the center of the six-membered ring at $(1/2, 1/2, 0)$, which are both situated on centers of symmetry of the space group $P\bar{1}$. The chains are arranged in stacks along the *a*-axis of the crystal. The Cu–Cu distance along the approximate *a*-axis is about 5.169(1) Å, while along the *b*-axis is 7.961(1) Å and along the *c*-axis is 8.226(1) Å. The closest contact between hydrogen atoms of neighboring chains is approximately to 1.89 Å.

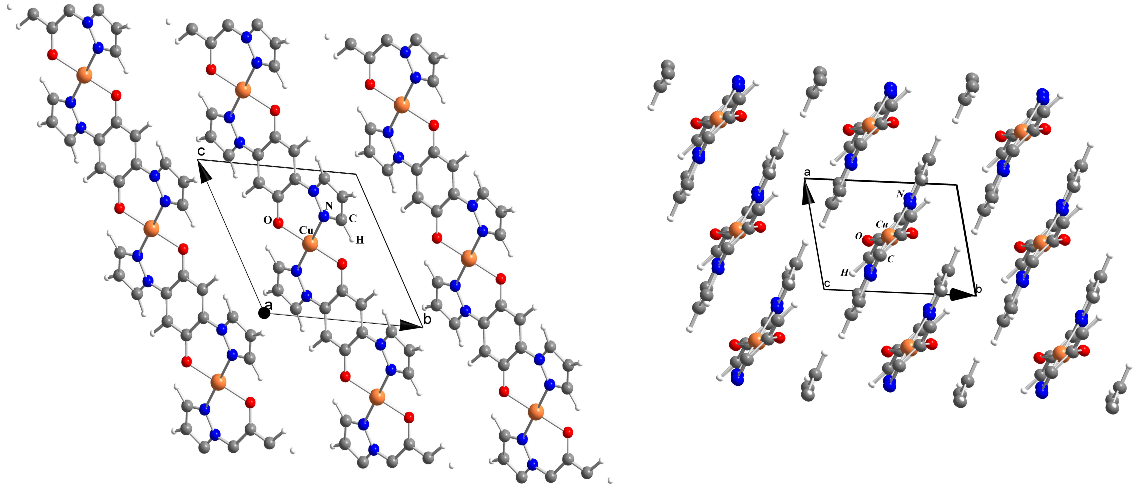

(a) (b)

Figure 4.3: (a) CuCCP is arranged as chains along the *c*-axis, (b) along *a*- and *b*-axis it is arranged in stacks

The Cu(II) ions in this compounds are coordinated in an almost square planar fashion by two pyrazolyl nitrogen atoms and two oxygen atoms of the deprotonated dihydroxybenzene groups. The pyrazole molecule constitutes a five membered ring composed of three carbon atoms and two nitrogen atoms in adjacent positions, with chemical formula $C_3H_4N_2$ [13] (Figure 4.1(d)). Assuming that the metal is located in the center of a cartesian coordinated system, its $3d$ orbitals will be oriented as shown in Figure 4.4. If the ligand atoms are located in the equatorial axis in a square planar fashion, the $3d^9$ electrons of the Cu^{2+} ions are splitted in the way showed in Figure 4.5. The states d_{xy}, d_{z^2}, d_{xz}, d_{yz} are full occupied except for $d_{x^2-y^2}$ which is half-occupied.

The crystal structure of CuCCP, was determined from X-ray powder diffraction data; consequently the overall structure and the arrangement of the chains are reliable, but the individual atomic positions have an accuracy of only about 0.3 Å; hence the information about bond lengths and angles is limited. We will show in Section 5.2.1 that the inaccuracy of this crystal structure determination leads to instabilities in the ab initio quantum mechanical calculations. Therefore, in order to achieve accurate DFT calculations we have, initially, optimized the geometric structure of CuCCP compound with a combination of classical and quantum mechanical methods, this will be shown is Section 5.1.

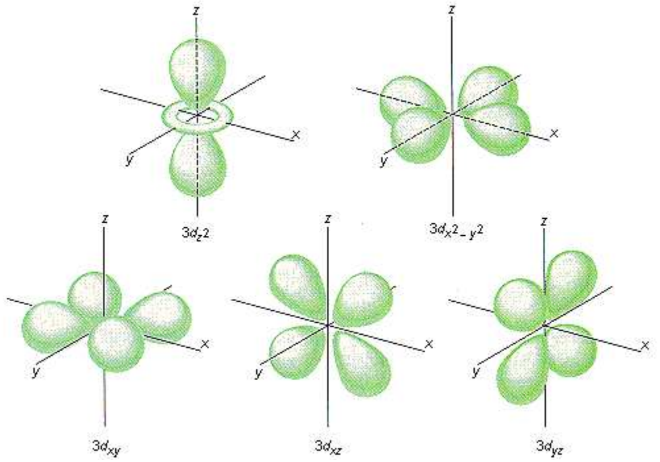

Figure 4.4: Orientation of the $3d$ orbitals in a local coordinated system, where the metal ions is located in the center of it.

The Cu–Cu interaction in CuCCP compound depends on the electronic nature of the linker. Its properties can be tuned smoothly and predictably by changing the substitution pattern R (see Figure 4.2) of the central carbon ring (hydroquinone), or by introduction of additional ligands X in the apical axis of the Cu(II) ions. Following this scheme, *i.e.* by introducing synthetically feasible substitutions in the hydroquinone ring or by adding ligands, we intend to modify the properties of the crystal in three ways: i) Change of effective dimensionality: The one-dimensional nature of the original compound can thus be made more two-dimensional or more three-dimensional, allowing for a controlled investigation of the crossover between dimensionalities. ii) Change of effective, intra-chain interaction: By influencing the charge density in the polymeric chain, substituents and ligands can be used to tune the magnitude of magnetic interactions between the Cu(II) centers in the spin chain. iii) Change of co-ordination and valence: Possible tuning of the valency of the Cu(II) ions by changing the ligand co-ordination, may induce changes in the transport properties along the one-dimensional chain by moving away from the Mott insulator at a half-filled Cu $3d_{x^2-y^2}$ orbital.

With the above ideas in mind, we first considered two possible H replacements in the hydroquinone: an NH_2 group, which acts as electron donating group, and a CN group, which acts as electron withdrawing group. Furthermore, extensive crystallization trials showed that crystallites of the Cu(II) polymer always contain lattice defects in high concentration. In many compounds, the Cu(II) ions are coordinated by six nitrogen or oxygen atoms

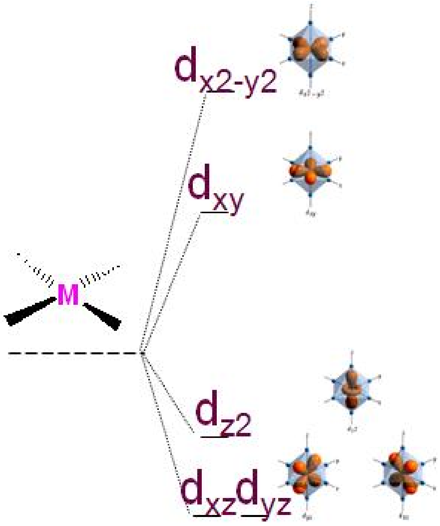

Figure 4.5: Splitting of the $3d$ states in a square planar configuration. M denotes transition metal ion.

instead of four ligands. The Cu(II) polymer is experimentally crystallized in a mixture of water and ammonia solvents, and it is likely that H_2O or NH_3 molecules are built into the crystal lattice. We have, therefore also considered the introduction of additional ligands like H_2O or NH_3 at the Cu(II) ions in this simulation study.

4.2.2 TK91

The compound known as TK91 crystallizes in the triclinic space group $\bar{P}1$, without inversion center, the unit cell parameters a=8.0083(12) Å, b=12.3677(14) Å and c=13.1673(19) Å, α=63.661(14)°, β=88.820(13)° and γ=77.488(11)° with its chemical formula $Cu_2S_2F_6N_8O_{12}C_{36}H_{48}$ (for the sake of simplicity, we refer to it as TK91) [65]. The name of the compound name makes reference to Tonia Kretz who synthesized it, in the group of Prof. Matthias Wagner from the chemistry department of the Johann Wolfgang Goethe-Frankfurt University. The basic structure of TK91 are polymeric chains as the CuCCP polymer (introduced in Section 4.2.1) connected to each other as shown in Figure 4.6.

The Cu-Cu atoms are bridged by hydroquinone rings and the polymer is directed along the a-axis. The cation is centrosymmetric and has a crystallographic inversion center at the midpoint of the hydroquinone ring. O atoms belonging to the next polymer and to the DMF

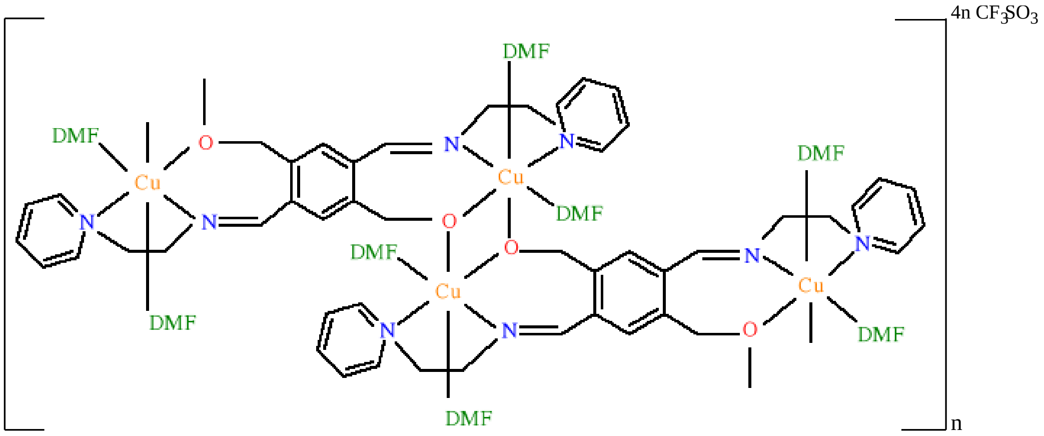

Figure 4.6: Schematic representation of the polymeric unit of $Cu_2S_2F_6N_8O_{12}C_{36}H_{48}$ (TK91).

(DMF correspond to CF_3SO_3) coordinate the Cu ions in the apical positions. Therefore the Cu atom has a distorted octahedral coordination. The Cu-N1, Cu-N2, Cu-O1 and Cu-O2 bonds are short equatorial bonds and there are two long axial Cu-O bonds: a Cu-O3 (DMF) bond of 2.5652(16) Å and a Cu-O1 bond of 2.4344(13) Å to a neighboring dimer (the Cu environment is shown in detail in Figure 4.7(b) below). As a result of these Cu-O contacts in the O apical positions, the nearest neighbor Cu-Cu ions form dimer-like structures, with a Cu-Cu distance of ∼ 3.27 Å, which is the shortest intermolecular Cu-Cu distance in the compound. The distances and angles are shown in Table 4.1.

Table 4.1: Bond lengths and angles in TK91

Distances	(Å)	Angles	(deg)
Cu-O1 (plane)	1.9197(12)	O1-Cu-N1	90.85(6)
Cu-N1	1.9653(16)	O1-Cu-O2	88.07(5)
Cu-O2	2.001(14)	N1-Cu-O2	175.04(6)
Cu-N2	2.0754(15)	O1-Cu-N2	175.61(6)
Cu-O1 (apical)	2.4344(13)	N1-Cu-N2	93.51(6)
Cu-O3	2.5652(16)	O2-Cu-N2	87.55(6)

Figure 4.7 show the compound in different view-planes. The Cu environment has been plotted with a polyhedra in order to make more visible the position of the Cu-Cu dimers in the compound. The Cu-Cu distance along the polymer, which is directed along the *a*-axis of the unit cell, is ∼ 8.36 Å, along the *c*-axis the Cu-Cu distance is ∼ 13.16 Å. The cations and

anions in this compound, are connected by intermolecular C-H...O and C-H...F hydrogen bonds. In fact, TK91 has 13 different C-H...O contacts with H...O distances between 2.51 Å and 2.75 Å and three different C-H...F contacts with H...F distances between 2.34 Å and 2.75 Å.

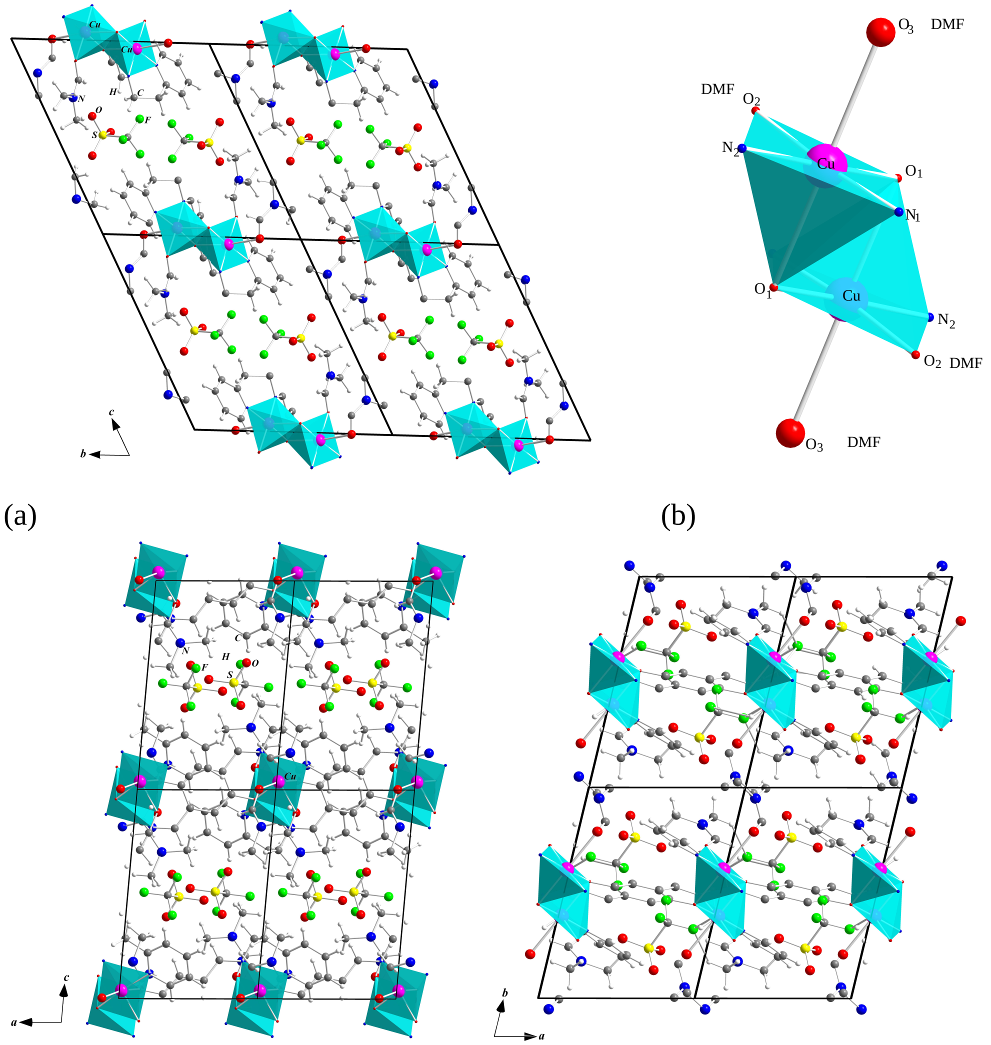

(a) (b)

(a) (b)

Figure 4.7: (above) (a) *bc*-viewplane of TK91 compound, (b) the Cu environment is shown in detail. (below) (a) *ac*- and (b) *ab*-viewplane of TK91 compound.

Experimental reports and motivation

First fits of susceptibility measurements to an isolated-dimer model could qualitatively reproduce the experimental observations and prove the existence of a spin gap due to the singlet-triplet excitation spectrum on a dimer system [107]. Nevertheless such an isolated dimer model was not able to reproduce the field dependence of the magnetic heat data at H> 4T, as shown in Figure 4.8. The deviation from the isolated-dimer model can be attributed to non-zero interdimer interactions.

Depending on the magnitude of these interdimer interactions and on the 2D or 3D character of the network, different interesting phases in the compound could develop. Our goal is then, to find through ab initio quantum mechanical calculations, the underlying interaction network in TK91 which may define it as a weakly coupled 2D or 3D dimer system. Our results will be compared to the ones obtained for CuCCP, in order to understand the nature of the chemical bonding and interaction pathes in TK91.

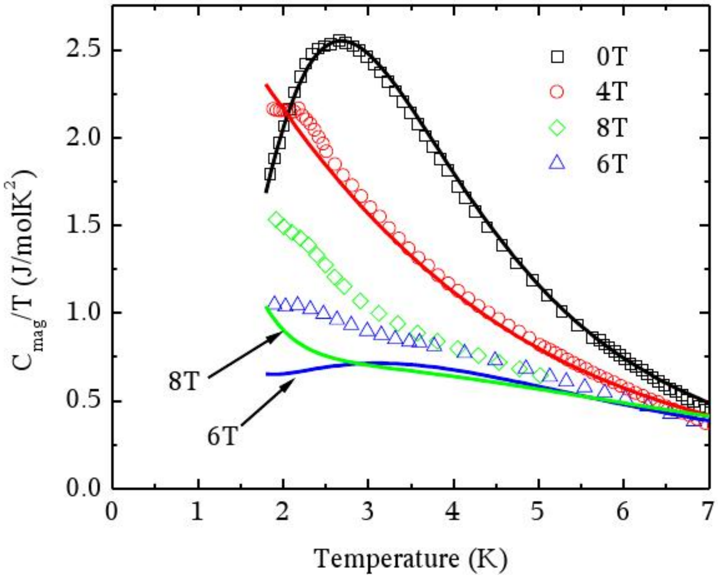

Figure 4.8: C_{mag}/T vs T at different applied magnetic fields in units of Tesla. Calculated values for an isolated-dimer model with $J_1/k_B = 9.6$ K and g= 2.1 are shown by solid lines. Figure taken from reference [107].

4.3 Competing interactions in low dimensional systems

4.3.1 'Zero-dimensional' system with frustration

In order to give an overview about the complexity of this problem, we introduce in the first part of this section the experimental observations by our collaborator Dr. Oksana Zaharko and her group from the Laboratory of Neutron Scattering, ETHZ & PSI in Switzerland. In the second part, a brief description of the different proposed scenarios and at the end a brief explanation of our goal is presented.

Geometric Structure of $Cu_4OCl_6daca_4$

O. Zaharko *et al.* [123] have obtained single crystals of $Cu_4OCl_6daca_4$ and have performed extensive characterization of this compound by means of synchrotron X-ray diffraction, magnetization, specific heat and inelastic neutron scattering measurements in the temperature interval 80 K-340 K.

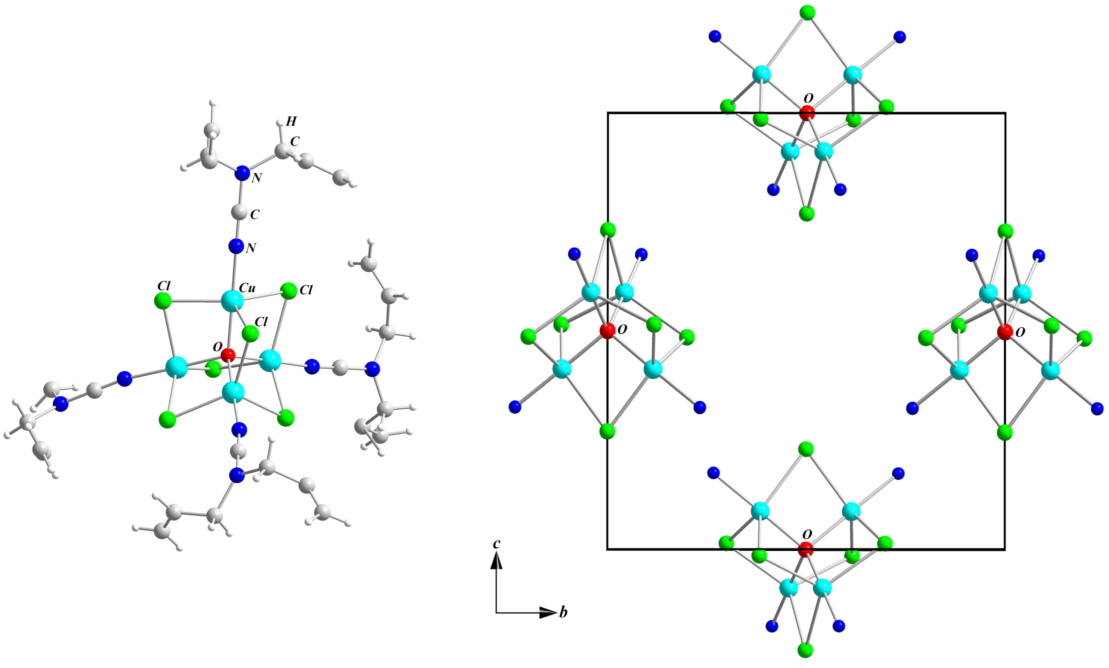

(a) (b)

Figure 4.9: (a) Magnetic unit of the system.(b) The *bc* projection of the $Cu_4OCl_6daca_4$ clusters in the unit cell. For simplicity only the Cu clusters without the organic molecules are shown.

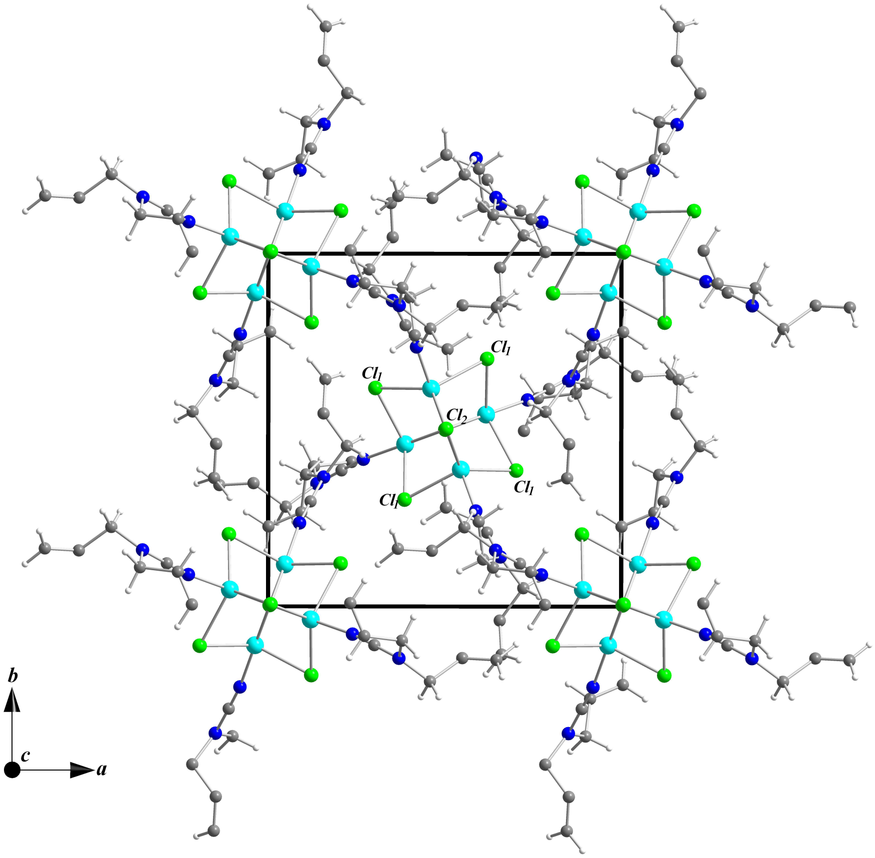

Figure 4.10: *ab*-plane view of the arrangement of $Cu_4OCl_6daca_4$ clusters within the unit cell. The Cu atoms are represented by turquoise spheres, Cl atoms in green, N atoms in blue, C atoms in grey and H atoms in white. The O atoms are located behind Cl2 atoms and therefore are not visible.

The structure spans a tetragonal structure with space group $\bar{P}42_1c$ in the whole studied temperature range. Figures 4.9 and 4.10 show the arrangement of the atoms within the unit cell in this compound. There are two $Cu_4OCl_6daca_4$ molecules per unit cell and they are slightly twisted around the z axis (which is parallel to the c-axis). The oxygen is in the center of the molecule, surrounded by a tetrahedron of Cu^{2+} ions with two different Cu-Cu distances as seen in Table 4.2. The tetrahedron is enclosed by a distorted octahedron of chlorine ions with four Cl atoms in the square base (which will be labelled as Cl1) and two Cl in the apexes (which will be labelled Cl2). Each copper has trigonal bipyramidal coordination: three Cl^- ions form the triangular base of the bipyramid, while the central O^{2-} ion and a terminal ligand L are located in apical positions. The exchange paths Cu-O-

Table 4.2: Characteristic intracluster distances (d_{intra} (Å)) and angles (in degrees (°)) for $Cu_4OCl_6daca_4$ at T=80 K and T=340 K. Also shown a comparison of the distances between the centers of the molecules in the unit cell (d_{inter}).

d_{intra} (Å)	T=80 K	T=340 K
Cu-Cu	3.079(2)	3.088(4)
Cu-Cu	3.118(2)	3.107(5)
Cu-O	1.901(1)	1.899(3)
Cu-N1	1.933(1)	1.937(3)
Cu-Cl1	2.369(3)	2.389(9)
Cu-Cl2	2.380(3)	2.416(9)
d_{inter} (Å)		
d_{100}	12.604(3)	12.565(1)
d_{001}	12.730(5)	13.768(2)
d_{111}	10.952(3)	11.239(1)
Angles (°)		
Cu-O-Cu	110.158(6)	108.804(2)
Cu-O-Cu	108.106(6)	109.805(2)
N-Cu-O	179.01(4)	178.181(1)
Cu-Cl1-Cu	80.465(1)	80.462(3)
Cu-Cl2-Cu	80.592(1)	80.535(3)
Cl1-Cu-Cl1	117.973(1)	118.804(3)
Cl1-Cu-Cl2	111.849(9)	120.001(3)

Cu are identical, while the two Cu-Cl1-Cu and Cu-Cl2-Cu paths through the chlorine ions slightly differ (see Table 4.2). Such geometry implies a D_{2d} symmetry.

The X-ray synchrotron powder (XPD) and single crystal (XSCD) diffraction experiments indicate that there is a structural transition in the 230 K-280 K temperature range. The volume of the compound expands in 7% with the increment in the temperature. The lattice parameters at T=80 K are a=12.604(9) Å, c=12.730(4) Å and at T=340 K a=12.532(8) Å, c=14.046(9) Å. The transition is not related to the $Cu_4OCl_6daca_4$ core, but rather to the organic part of the molecule. The branched ligands ($N{=}C{-}N(CH_2{-}CH{=}CH_2)_2$) fold and distances between the clusters decrease. The atomic positions in the $Cu_4OCl_6daca_4$ cluster itself change very little (Table 4.2). The only noticeable change in the $Cu_4Cl_6N_4$ core is the shift of the Cl_1 ions by 0.2487 Å while for Cu and Cl_2 the shift is only 0.0462 Å and 0.0282 Å respectively. Although the change in the core is small, it could influence the electronic structure (and accordingly the density distribution) of the whole cluster.

Low temperature behavior and motivation

Experimental curves of the magnetization per Cu ion as a function of temperature for all members of the Cu-daca family of compounds present a bump in the low temperature region similar as the one observed in Cu-daca shown in Figure 4.11 [123].

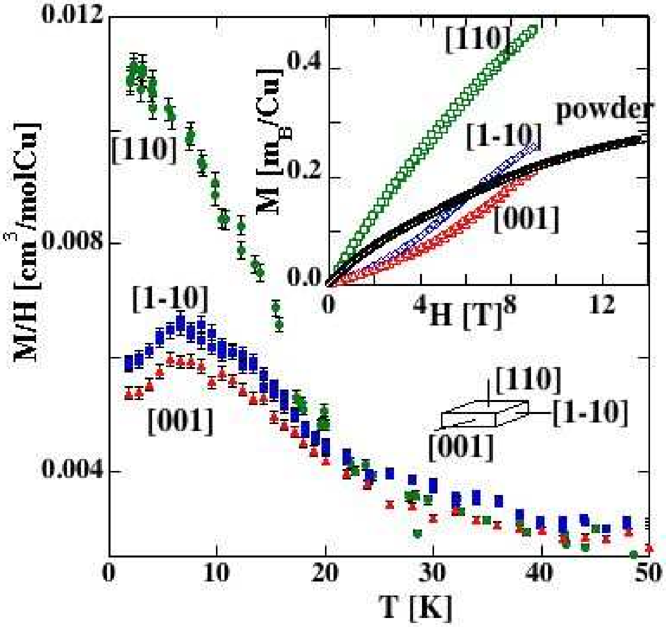

Figure 4.11: Temperature dependence of dc-magnetization (M/H) of a single crystal of $Cu_4OCl_6daca_4$ measured with magnetic field H=0.2 T applied along three crystallographic directions: [110] (green circles), [001] (red triangles) and [1-10] (blue squares), corresponding to short, middle and long edges of the crystal. Inset: Field dependence of dc-magnetization of single crystal and powder $Cu_4OCl_6daca_4$ at 1.8 K. Obtained by O. Zaharko [123].

This anomalous behavior cannot be modelled by simple isotropic Heisenberg Hamiltonian (introduced in Section 2.4.2). Different attempts to explain these characteristics include:

1. Modifications to the isotropic Heisenberg spin Hamiltonian, following two routes:

    - The first one, developed by Dickinson *et al.* [34] assumed an antiferromagnetic intracluster and a ferromagnetic intercluster exchange interaction. The difficulty with this model is that in order to agree with the experimental observations, the intercluster interaction is assumed to be rather strong (of the order of magnitude as the intracluster exchange interaction, in this work estimated as J $\sim$ 11 K) which is unlikely to be the case, since the intercluster distances are large, around 10 Å.

- The second approach proposed by Lines *et al.* [72] includes in the Hamiltonian antisymmetric and anisotropic terms, with the proposed Hamiltonian having the form:

$$H = H_{iso}+H_{as}+H_{an} = \sum_{i,j} J_{ij}\mathbf{S}_i\mathbf{S}_j+\sum_{i,j}\mathbf{D}_{ij}(\mathbf{S}_i\times\mathbf{S}_j)+\sum_{i,j}\sum_{\alpha=x,y,z} J_{ij}^{\alpha}\mathbf{S}_i^{\alpha}\mathbf{S}_j^{\alpha} \quad (4.1)$$

  where H_{iso} is the isotropic Heisenberg Hamiltonian, H_{as} is the antisymmetric and H_{an} the anisotropic terms. In order to fit the experimental results, the authors had to assume an orbital degenerate ground state for the Cu ions to obtain a good agreement with the experimental observations. However, situations where orbital effects are important for magnetic exchange in copper complexes are extremely rare.

2. Another mechanism that might be realized in $Cu_4OCl_6daca_4$ is a resonating mixed valence state with extra electron(s)/hole(s) delocalized over the whole cluster and this delocalization is temperature dependent. If this mechanism is realized, the hopping of electron/hole should be considered as a dominant term in the Hamiltonian, while magnetic exchange is a second order effect. It is shown [18] that for the d^9-d^9-d^8-d^8 tetramers electron transfer would lead not to a ferromagnetic spin alignment as would happen in dimers, but to a 'quasi' symmetrical energy spectrum with degenerate ground states. Presence of only one crystallographically independent Cu site supports such a mechanism. If the localization of a hole/electron on one Cu ion would take place, there would be a structural distortion, bond lengths would differ, etc. However, such a transfer is in contradiction with X-ray and specific heat data - the entropy released up to 10 K is small (in the case of additional degrees of freedom - orbital, hopping -entropy should be enhanced) and there is almost no change of interatomic distances in the cluster as the temperature is lowered.

All these proposed scenarios had failed to some degree, to explain the anomalous behavior of the magnetization at low temperatures. Our goal is to characterize the compound and to study its ground state properties in order to explain the experimental observations. In order to pursue this goal, this work combine experimental and theoretical efforts. Our strategy is the following: substantial experimental data have been collected on $Cu_4OCl_6L_4$ with L=diallylcyanamide=N≡ $C - N - (CH_2 - CH = CH_2)_2$ which have been confronted with ab initio calculations for the compound in both T=80 K and T=340 K regimes. Our results are compared with the experimental observations, which allow us to accept or reject the proposed models. Based on the experimental observations, we propose a model for the ground state properties of the compound. This will be presented in Section 5.3.1. Additionally, due to the tetrahedral configuration of the Cu atoms which is a characteristic geometry in frustrated materials, the frustration phenomena in this material is studied.

4.3.2 Spin-Crossover in One-dimensional chains

In general, early transition metal atoms with an electronic configuration $3d^4$-$3d^7$, immerse in an octahedrally coordinated ligand field can exist in either High-Spin (HS) or Low-Spin (LS) configuration depending on the nature of the ligand field. In some cases it is possible to drive the system from one of these spin states to the another by applying an external perturbation. This phenomenon known as *spin crossover* is one of the most spectacular examples of molecular bistability [52]. A molecular system is said to be bistable when it may be observed in two different electronic states within a given external perturbation range. Usually, one of the two states is the stable one, the another is a metastable state. The concept of molecular bistability concerns the molecular system and the perturbation in an indissociable way. *A system is said to be bistable with respect to a certain perturbation.* This section is devoted to Fe(II)-triazole based compounds, which usually experience a change in their spin state when an external perturbation such as light irradiation, changes of temperature or pressure, are applied to them. Different kinds of spin transition compounds exist in literature, mononuclear [70], binuclear [94], trinuclear [112], forming 1D, 2D and 3D networks [33], [69], [113], [78]. Our work is concerned with polymeric chains due to their relevance for technological applications. In the first part of this section the basic components of polymeric compounds as well as the spin transition mechanism are presented followed by a discussion on the responses shown by these kind of compounds when experiencing a spin transition, and the advantage of polymeric compounds in comparison to 2D and 3D networks. The different attempts to explain the microscopic mechanism of the spin-crossover in these compounds and their difficulties, as well as our novel approach are discussed in the

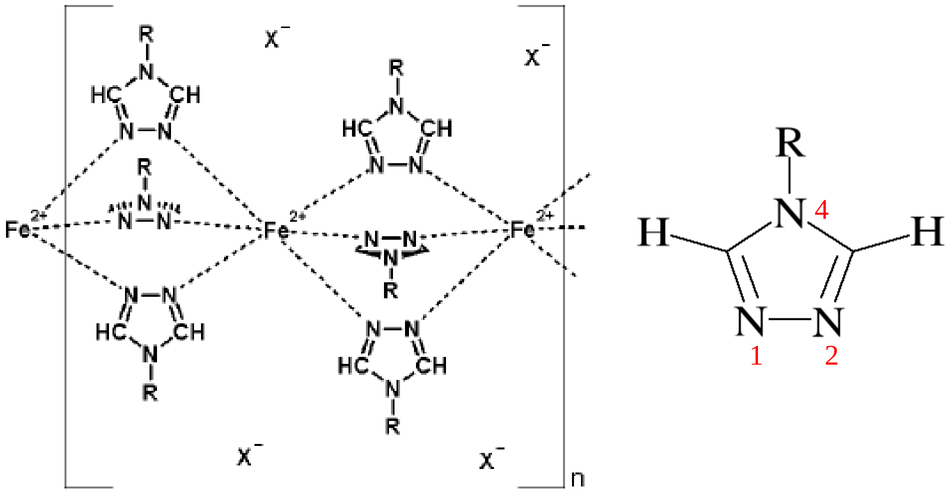

(a) (b)

Figure 4.12: (a) Chain structure of the compounds [Fe(Rtrz)$_3$]A$_2$ as deduced from EXAFS techniques [55], [12]. R represent the substituents and X the usually complicated counterions. (b) triazole molecule

second section. Finally, we introduce our novel theoretical methodology which allow to study systematically the electronic properties of polymeric Fe(II)-triazole compounds in every step of the spin transition and to investigate the role of the magnetic interactions in the spin-crossover phenomena, which has not been taken into account to date.

Basic units of polymeric Fe(II)-triazole compounds

The basic structure of polymeric Fe(II)-triazole based compounds is illustrated in Figure 4.12(a). Its general formula is [Fe(Rtrz)$_3$]A$_2$ $\cdot$ xH$_2$O where Rtrz=4-R-1,2,4-triazole and A$^-$ stands for anions or counterions and xH$_2$O stands for non-coordinated water molecules. In the figure, the substituents and the anions, which are usually large molecules or long polymeric chains, have been reduced for simplicity, to molecules R and A respectively, in order to show in detail the characteristic arrangement of Fe ions and the triazole molecules. It is composed of Fe^{2+} ions with electronic configuration $3d^6$, immersed in an octahedral environment formed by six N^{2-} ions belonging to triazole rings. The 4-R-1,2,4-triazole molecules (along the text we will refer to this molecule as triazole) are carbon rings, with N substituted nitrogen atoms in the positions 1,2 and 4 (see Figure 4.12(b)). The N atoms in positions 1 and 2 coordinate with the Fe ions. In this environment the Fe $3d$ orbitals split as shown in Figure 4.13 where it is assumed that the Fe is located in the center of a coordinated system with the N ions in the axis.

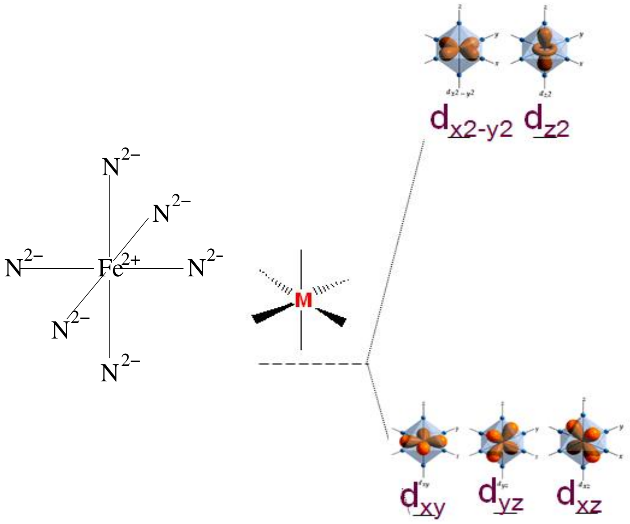

Figure 4.13: Splitting of the $3d$ electrons in an octahedral environment. M stands for transtion metal ion.

Because the orbitals $d_{x^2-y^2}$ and d_{z^2} of the Fe^{2+} ion point directly toward the N^{2-} ions, its energy increases much more than the energy of the other three d_{xy}, d_{xz}, d_{yz} orbitals, as is shown in Figure 4.13. The crystal field of the six N^{2-} ions therefore splits the degeneracy of the five $3d$ orbitals. By convention, the set of orbitals composed by d_{xy}, d_{xz}, d_{yz} in an octahedral complex are called the t_{2g} orbitals, the set of composed by $d_{x^2-y^2}$ and d_{z^2} orbitals, on the other hand, are called e_g orbitals. The difference between the energies of t_{2g} and e_g orbitals in an octahedral complex is represented by the symbol Δ and denotes the *crystal field splitting*. In weak ligand fields the ground state is HS where the spin multiplicity is a maximum, the d electrons being distributed over the t_{2g} and e_g sets, in the case of Fe, the HS state is $(t_{2g})^4(e_g)^2$, whereas strong crystal ligand fields stabilize the LS state with minimum multiplicity, the t_{2g} being completely occupied, as shown in Fig. 4.14. The interplay between the Hund's rules, on-site Coulomb repulsion and the energy associated to the crystal field splitting determine the spin state of the system. In the case of the compound we are concerned with, the application of an external perturbation could drive the system from one spin state to the other, this situation is illustrated in Fig. 4.14.

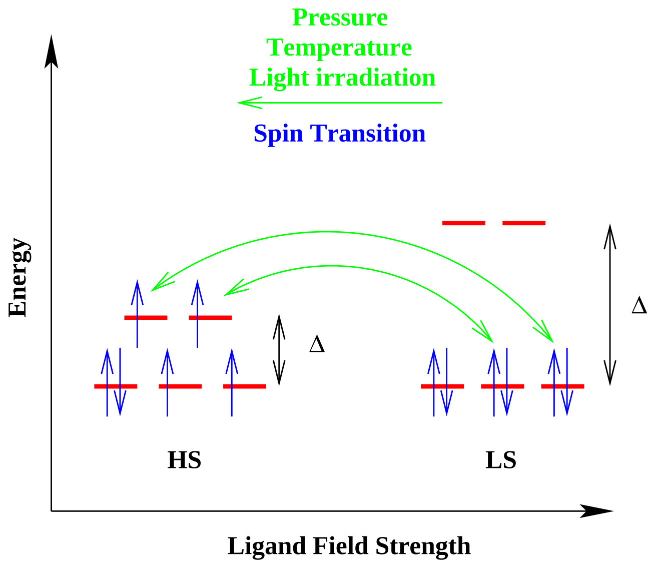

Figure 4.14: Electronic configuration for a d^6 iron, in the LS and the HS state. Δ stands for the crystal field splitting. With the application of a external perturbation is possible to drive the system to a spin transition.

Cooperativity

The spin crossover phenomena was observed for the first time in the 30s but only since the last three decades many experimental and theoretical efforts have been oriented to this effect. The reason for its attractiveness are the characteristics associated with the spin transition, namely, a change in color when going from one state to the another state and thermal hysteresis effects making these kind of compounds suitable candidates as active elements of memory devices. As an example, we show in Figure 4.15 the typical plots, when hysteresis is present, of the dependence of the magnetic susceptibility times the temperature χT *vs.* T for a HS to LS crossover of a representative of the Fe(II)-triazole family.

The existence of hysteresis confers a memory effect on the system because the state of the system at certain temperature depends on its history and therefore, from a technological point of view, it is desirable that the SC compound present a spin transition with a large and abrupt hysteresis when both, warming and cooling the sample. The presence of an hysteresis loop originates entirely from cooperative effects if there is not a change in the crystallographic phase. The loop width is related with the strength of the cooperative interactions. *The cooperativity is related to the magnitude of the interactions between active sites.*

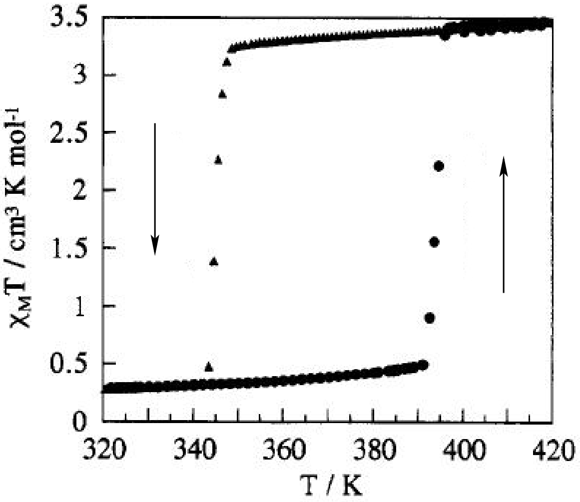

Figure 4.15: χT versus T plots in the warming and cooling modes for $[Fe(Htrz)_2(trz)](BF_4)$. Experimental curve taken from reference [66]

The first known SC compounds were mononuclear systems, in which the sharpness of the transition and the occurrence of thermal hysteresis have been linked to first-order crystallographic phase transitions [46], or to intermolecular interactions. These intermolecular interactions are very weak, usually driven by *van der Waals forces*. In many cases uncoordinated solvent molecules composed by hydrogen are present, which bounds to the crystal lattice. These hydrogen bonds may enhance the intermolecular interactions but still are insufficient to produce strong cooperativity. One may expect that direct chemical bonding could lead to an increase of the interactions between the active sites. Therefore, in polymeric spin transition compounds one should expect that the interaction is propagated through the entire crystal increasing the cooperative effects [52].

Keeping this idea in mind, intensive experimental studies have been devoted to the synthesis of polymeric spin-crossover compounds. Monomers [70], binuclear [125] and trinuclear [112] systems have been obtained, but only very few polymeric compounds have been reported so far [121], [66], [55], [82]. The most attractive members of polymers, which fulfill the criteria mentioned above, are the linear chain compounds of the general formula $[Fe(Rtrz)_3]A_2 \cdot xH_2O$ where Rtrz=4-R-1,2,4-triazole and A^- stands for anions or counterions and xH_2O stands for non-coordinated water molecules. For instance, the polymeric compounds $[Fe(Htrz)_2(trz)](BF_4)$ and $[Fe(NH_2trz)_3](NO_3)_2$ (Rtrz = 4-R-1,2,4-triazole) show a very abrupt transition with a hysteresis loop and the later presents a well-pronounced thermochromism between the purple color in the LS state and the white color in the HS state [53], [66].

Two essential characteristics are common to all synthesized Fe-based SC compounds: the anions are not coordinated to the metal center and the Fe^{2+} ions are directly linked by triple N atoms occupying the positions 1 and 2 in triazole molecules. These bridges are thought to be the origin of the observed cooperativity phenomenon in these materials. Another important point regarding linear $[Fe(Rtrz)_3]$ chains, is that they seem to remain the best candidates for technological applications, because of the richness of possible substituents, and the large range of spin-transition features accessible, due to the strong influence of the anion used and the substituent. Experimentally it has been shown that the nature of the substituent does not affect strongly the donor strength of the triazole molecule and its effect is directly related with the transition temperature and reduces the cooperativity of the transition only in the case when the size of the substitutents is so long that it reduces the length of the Fe-triazole chains. The most important effect of the counterions is on the transition temperature [99].

Attempts to understand the microscopic mechanism of the spin transition

It is important to note, that *the spin transition is accompanied by a change in the metal-ligands which causes a volume expansion of the molecules, of around* $\sim 10\%$ [121], which is related to the increase in the Fe-N distance when increasing the temperature. This experimental fact has been the starting point for theories which attempted to explain the cooperative phenomena in SC compounds. The transition has been attributed to coupling to lattice vibrations, [127], cooperative Jahn-Teller type of interaction of the HS ions [56] and elastic interaction between HS and LS ions via an image pressure that arises from the stress-free boundary condition [90]. But the coupling parameters within those models were either difficult to estimate or gave rise to disagreements and contradictions with the experimental observations. H. Spiering *et al.* [115], [105] extended the image pressure model deriving a phenomenological *ansatz* for the Gibbs free energy of the compounds. This model considers each spin-crossover center as a point defect and explains to a certain extent the spin crossover behavior in monomeric compounds. All the models mentioned above have been the basis for the quantitative description of the spin transition in terms of elastic effects.

A currently way of describing the spin transition is by a two-state Ising-like model, initially proposed by Wajnflasz and Pick [114]. In this model, the HS and LS microscopic states of the molecule are associated, respectively, with the eigenvalues +1 and -1 of the fictitious spin operator s with their respective degeneracies g_+ and g_-.

$$H = -J' \sum_{i \neq j} s_i s_j + \left(\Delta - \frac{k_B T}{2} \ln g \right) \sum_i s_i \tag{4.2}$$

$g = g_+/g_-$ is the degeneracy ratio and Δ the ligand field energy (such that the LS state is the ground state at 0 K). The sum $\sum_{i \neq j}$ is over the interaction neighbors and J', which is not an exchange magnetic coupling, represents the case when an attractive force (*i.e.*, a ferroelastic interaction) acts between neighboring sites in the same state (LS-LS or HS-HS) and a repulsive force acts between those in different states (LS-HS), which leads to bistability of the LS and HS states. A most realistic treatment, which includes a spin-phonon interaction, leads to obtaining a similar Hamiltonian as Eq. (4.2) with effective parameters J' and Δ, which depend on the distortions of the molecules at sites i, j [87]. Thus, J' and Δ are considered as effective parameters that have an elastic origin. This model has been widely used in trying to explain the SC phenomena, in fact the general trend for the models that have been elaborated up to now in order to explain the spin crossover (SC) mechanism have been mapped to 1D Ising-like equations. Despite of the drastic simplifications of this two-level system, it has been successfully applied to SC compounds with two-step spin crossover behavior [21] and explains consistently the change from a smooth transition to a first order transition for spin conversion between LS and HS states as a function of the parameters of the models [114],[88].

Further works have associated the SC phenomena to the interplay between long range and short range elastic interactions[71], [59], to the interaction between phonons and the electronic state of the system [19] and only recently magnetic interactions where considered in the Ising-like model, associating the SC phenomena to a possible interplay between the elastic interaction and the magnetic ordering [20]. These different theories in common, that cannot be applied successfully to all SC Fe(II)-triazole based compounds. This is so in part, due to the great variety of different kind of counterions which can influence dramatically the hysteresis behavior and hence the cooperativity in these materials. Also, a microscopic study where all important interactions are considered is still missing and the origin of the cooperativity has not been completely settled. In order to overcome this issue, we have focused on the study of the electronic and magnetic properties of the fundamental blocks of this family of compounds, namely the Fe ions bridged by triazole ligands by replacing the complicated and usually long conterions and substituents to minimal units. This has the advantage of focusing our study on the effect of the triazole molecules on the electronic state of Fe(II) atoms, which are the basic components in all Fe(II)-triazole based compounds, while minimizing the computational costs without affecting the accuracy of the calculations.

Building our model compound

To our knowledge, the only attempt to study the electronic properties of 1D Fe(II)-triazole compounds used the extended Hückel method [57], which in general produces orbital energy trends quite well but it does not include explicit electron-electron interactions and all the quantum effects which are possible to introduce within DFT theory. In order to perform DFT ab initio calculations on Fe(II) SC compounds, it is necessary to obtain reliable structural data. One of the major difficulties in studying Fe(II)-triazole chains is the lack of accurate crystallographic data, as it cannot be crystalized sufficiently well. X-ray structural analysis have been limited to molecular compounds, e.g. trimers containing three Fe(II) ions connected by six triazole ligands and six terminal water molecules [41]. Apart from a preliminary indexing of the chain-like structures $[Fe(Htrz)_2(trz)](BF_4)$ and $[Fe(Htrz)_3](BF_4)_2.H_2O$ (Htrz = 1,2,4-4H-triazole; trz = 1,2,4-triazolato) [82], no structural data have been published so far. For analogous polymeric Cu(II) compounds the structure was confirmed by single crystal X-ray analysis [36], [43][3].

In the present work, we overcome the unavailability of reliable structural data by constructing, based on the above mentioned data, hypothetical polymer crystals. This has been possible by applying the novel two-step procedure we elaborated in order to study the ground state properties of metal-organic compounds (it will be introduced in Section 5.1). Due to the fact that usually Fe(II)-triazole compounds are very large and present a very low symmetry, for an affordable all-electron calculation we have simplified the units, as replacing the long polymeric substituents R and counterions X (see Figure 4.12) by the smallest possible molecules. We could completely eliminate them, however they are necessary to ensure the neutrality of the unit cell. The replacement of units is supported by the experimental fact that the type and size of the counter ions has an effect mainly in the

---

[3] Although single crystals of Cu(II)-triazole based compounds have been obtained, they do not show spin-crossover behavior

temperature at which the transition takes place [99]. It is not our objective to study the effect of the counterions, nor to make studies regarding temperature changes but the role of the basic units, the Fe ions linked by the triazole ligands, in the microscopic mechanism of cooperativity. Therefore, the introduction of small substituents and counterions that allow to keep high symmetry in the system adjust to our goal. We have also replaced the usually slightly distorted Fe-N octahedron, by a perfect one in which all the N-Fe-N bonds make right angles and the Fe-N distances are the same. In this way we can visualize how powerful is our scheme, which allow to manipulate the structures in a desired way.

The methodology followed to build the model polymers and the resulting structures will be shown in Section 5.3.2. Initially we built our Fe(II)-triazole polymer with Fe-N distances $d_{Fe-N} \sim 2.0$ Å and $d_{Fe-N} \sim 2.2$ Å, which are the usual average Fe-N distances for LS state and HS state found in the literature [66], [38]. Within two-step approach we have varied these distances in such a way that we can consider intermediate distances values. This has the advantage of being able to follow the track of the transition between the two spin states. Thus we considered $d_{Fe-N} \sim 2.05$, 2.10 and 2.15 Å distances. Later we built also structures with $d_{Fe-N} \sim 2.08$, 2.09 and 2.12 Å in order to determine whether the transition is abrupt or not, and whether is possible to find an intermediate state between the LS-HS states.

This is a novel procedure which allow to investigate the role of the electronic properties on the spin-crossover including the effect of the magnetic interactions which has not been totally explored in these kind of materials so far.

4.3.3 Magnetic anisotropies in a 2D-system

Quantum antiferromagnets in the presence of external magnetic fields exhibit a variety of unusual quantum-mechanical phenomena of interest. Modern experimental technology allows precise measurements in the regime of field strengths comparable to the characteristic exchange constant of a system. This has made possible the observations of condensation of triplet excitations in a variety of chain, ladder and weakly coupled dimer compounds, magnetization plateaux in frustrated magnets and other interesting effects [126], [51], [26]. It turns out that in many cases experimental data deviates significantly from the theoretical predictions based on the pure isotropic Heisenberg model in external field. Such deviations are due to anisotropies, most notably Dzyaloshinskii-Moriya (DM) anisotropies, which are usually small and often neglected from zero-field considerations. Not only can such anisotropies induce qualitatively different effects, but also the strength of such effects seems to be significantly amplified when applying magnetic fields to the system. It is complementary in our study, to consider the effect of anisotropies in low-dimensional correlated systems. Nowadays, many compounds contain anisotropies which give rise to interesting phenomena in the presence of magnetic fields. Therefore, we have studied a 2D Heisenberg antiferromagnetic compound such as $K_2V_3O_8$ which presents also characteristics of a dilute system. It contains in the basal plane of the unit cell, two mutually perpendicular DM vectors which provides unusual spin reorientation effects with the applied magnetic fields. Due to its dilute character it has a relatively small value of the nearest neighbors exchange interaction J $\sim$ 12.6 K which could compete with other degrees of freedom in the system, such as the DM interactions, lattice degrees of freedom etc. This system is therefore a good candidate to study the interplay of these interactions, which has the advantage of having a high symmetry in comparison to the above mentioned metal-organic compounds.

Many experimental studies have been done on this compound, which show properties that have caused controversy and still nowadays is a topic of debate. With the goal of giving new insights into this debate, we study its geometric, electronic and magnetic properties by taking into account the many degrees of freedom involved in the system, which have been neglected in many approaches in the literature. Furthermore, our methodological approach allows to introduce other degrees of freedom which turn out to play an important role in the ground state properties of the system. In this section the $K_2V_3O_8$ compound is introduced. Its structural characteristics are given followed by some experimental observations and the specific goal of our study.

$\mathbf{K_2V_3O_8}$

$K_2V_3O_8$ belongs to the family of fresonite-type vanadium oxides $A_2V_3O_8$ (A=K, Rb, NH_4), which are tetragonal antiferromagnets [73]. It consists of slabs of corner-sharing VO_5 (magnetic V^{4+}) square pyramids and VO_4 (non-magnetic V^{5+}) tetrahedra, with K ions lying between each layer as shown in Figure 4.16. The role of the alkali-metal ion is to separate the magnetic layers, therefore this compound presents characteristics of a 2D system. At room temperature, $K_2V_3O_8$ crystallizes in the tetragonal space group P4*bm* with lattice parameters a=8.87 Å, c=5.215 Å, $\alpha = \beta = \gamma = 90°$.

The crystal structure has two different V sites, one V^{4+} per formula unit (along the text it

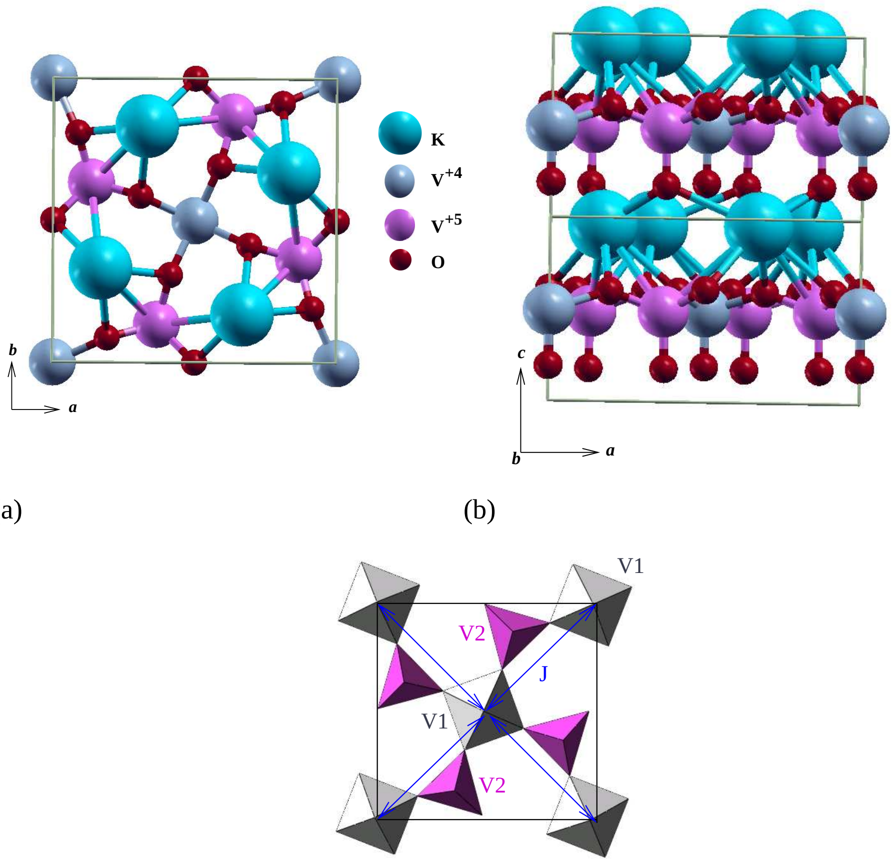

(a) (b)

Figure 4.16: (above)(a) Basal plane view of the unit cell of $K_2V_3O_8$. (b) Projection of the crystal structure along the *c*-axis. (below) $V^{4+}O_5$ (V1) pyramids in grey linked by non-mag netic $V^{5+}O_4$ (V2) tetrahedra shown in cyan. The intralayer coupling between S=1/2 V1 ions is shown by blue arrows.

will be denoted as V1) and two V^{5+} per formula unit (it will be denoted as V2). The VO_5 square pyramid is regular with the vanadium ion displaced from the basal plane towards the apex oxygen. The V1-O bond length is 1.945 Å, O being one of the four equivalent oxygen ions forming the base of the pyramid. The distance from V1 to the apex oxygen is much shorter, only 1.581 Å indicating the formation of a vanadyl bond. Between the family of fresonite-type vanadium oxides the vanadyl bond length in $K_2V_3O_8$ is the shortest one [73]. This system has been described as a S=1/2 2D Heisenberg antiferromagnet with coupling constant J=12.6 K and a g value of 1.89 [75]. It has a very small anisotropy with g experimental values of g_c=1.922 and g_{ab}=1.972 [96]. It orders magnetically at $T_N \sim 4$ K and experiences a structural phase transition at around 110 K, driven by a distortion of the apical oxygen of the pyramids and a distortion of the unit cell along the b direction [29]. Additionally it experiences a weaker relaxation near 60 K. The structure we have worked with is the one at room temperature [28].

Figure 4.17 shows the experimental susceptibility measured on single crystals of $K_2V_3O_8$. The curve shows a relatively broad maximum in the susceptibility below $\sim$ 15 K, indicating short-range magnetic correlations [73]. As seen in the figure, the susceptibility is the same for $H||c$ axis and $H \perp c$-axis at 'high' temperatures (above $T \sim 15$ K). This isotropic response implies that the vanadium magnetic moment is insensitive to its environment; it does not feel the modified surroundings arising from the 110 K structural distortion [29].

This compound presents a startling and unexpected spin reorientation effect. Specifically it has been found that a magnetic field applied in the plane of the square lattice causes a continuous rotation of the spins from a zero field orientation normal to the plane to an in-plane orientation normal to the field direction. This behavior is quite distinct from other, more conventional spin reorientations, such as spin-flop transitions, and suggests a novel competition between interactions in $K_2V_3O_8$. It has been claimed that this effect can be understood qualitatively in terms of the Heisenberg model incorporating Dzyaloshinskii-Moriya interactions [75]. Typically, only the antisymmetric term of the DM interaction is relevant, but the novel behavior in $K_2V_3O_8$ relies heavily on the inclusion of the symmetric component of the DM interaction (see Section 2.4.2).

M. D. Lumsden *et al.* have postulated [75] a two-spin, mean-field Hamiltonian as

$$H = 8J\vec{S}_1 \cdot \vec{S}_2 + 8D_z(\vec{S}_1 \times \vec{S}_2)_z + 8E_z S_{1z} S_{2z} - g\mu_B \vec{H} \cdot (\vec{S}_1 + \vec{S}_2) \tag{4.3}$$

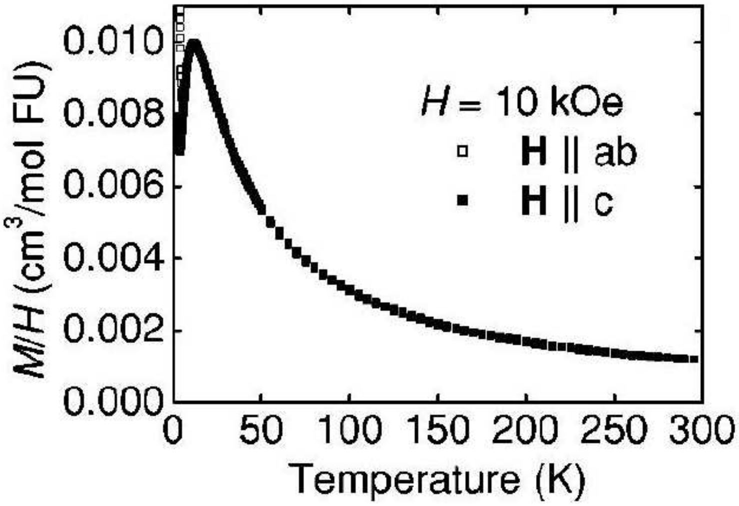

Figure 4.17: Experimental magnetic susceptibility applied parallel to the *ab*-plane direction (solid squares) and to the *c*-axis (open squares). Figure taken from Ref. [29]

The factor of 8 comes from the four near neighbors and two sublattices. E_z represents an additional *c*-axis anisotropy. The applied field required to induce both the basal plane spin reorientation and the *c*-axis spin flop transition has been experimentally estimated as $E_z/J \sim 0.0012$ and $D_z/J \sim 0.04$ (E_z and D_z are given in units of J) [75]. Using both triple-axis and time-of-flight inelastic neutron scattering, a small gap of 72 ± 9 μ eV at the antiferromagnetic zone center is found and the nearest-neighbor exchange constant is determined to be 1.08 ± 0.03 meV [74]. A finite ferromagnetic interplanar coupling along the crystallographic *c*-axis was measured, with a resulting magnitude of ~ -0.0036 ± 0.0006 meV. Detailed inelastic neutron scattering measurements and analysis of the zero magnetic excitation spectrum of $K_2V_3O_8$ reveals the presence of two modes in the excitation spectrum in the immediate vicinity of the zone boundary (Figure 4.18).

These features have not been found in other compounds and cannot be described by the Hamiltonian postulated for this compound. The fact that these modes vanish upon increasing the temperature, indicates that both are of magnetic origin, ruling out the possibility of a low-lying phonon mode interacting with the spin waves. To date, a consistent explanation for the peculiar zone boundary properties of $K_2V_3O_8$ has not been given, however there are a number of possible explanations to be discussed:

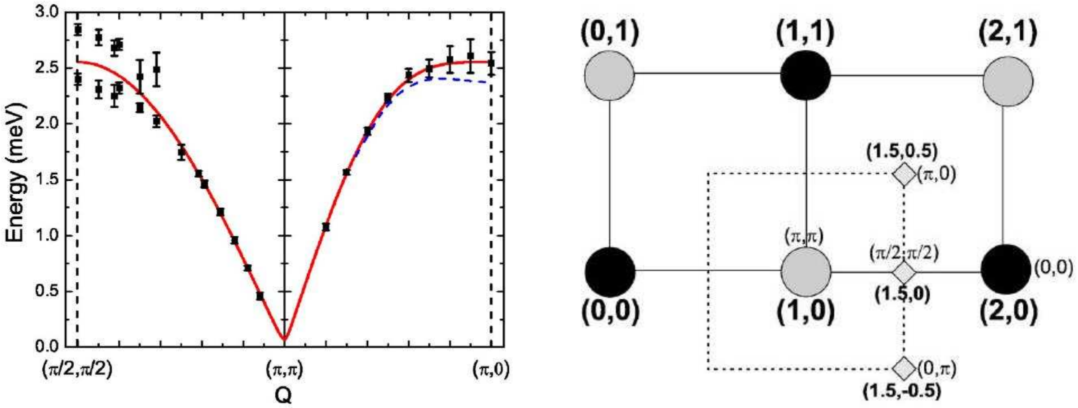

Figure 4.18: (left) Full triple-axis measured dispersion obtained from Ref. [74]. The solid line corresponds to a fit to linear spin-wave theory for data near the zone center. The dashed line represents the quantum corrections to the dispersion. (right) Reciprocal space diagram for $K_2V_3O_8$. Structural Bragg reflections are indicated by black circles and magnetic reflections by gray circles. Some high symmetry zone boundary points are indicated by gray diamonds. The dashed lines show the antiferromagnetic zone boundary around the (1,0) zone center.

1. **Additional couplings in the Hamiltonian:** Compounds like La_2CuO_4 present a double mode in the dispersion relation which shows evidence for substantial interactions beyond the nearest-neighbor term and has been explained by introducing additional coupling terms to its Hamiltonian [30]. It has been then found, that longer-range interactions in this compounds manifest themselves most simply at the zone boundary. Although the dispersion relation in La_2CuO_4 is quite different from the one found in $K_2V_3O_8$, we cannot exclude the possibility of long range interaction in this compound.

2. **Influence of orbital degrees of freedom:** Because this compound presents orbital anisotropies which couples the spin and orbital degrees of freedom, it is natural to think that it could influence the dispersion spectra of the system. A. Joshi *et al.* [50] developed a wave theory for spin systems with orbital degeneracy and investigated the elementary excitations of square lattices obtaining the energy dispersion for the cases with pure spin, pure orbital and spin-orbital modes, assuming a system with twofold orbital degeneracy. These calculations show that the orbital anisotropy splits the spin-orbital modes into two-fold degenerate branches and the wave spectra presents

similar characteristics to the ones observed for $K_2V_3O_8$. This scenario requires an understanding of the crystal-field ground state together with the approximate energies for the lowest excitations from this ground state.

3. Other possible explanations have been proposed as considering the compound as a diluted 2D antiferromagnet [108], [124] or the fact that fresonite structures are typically sensitive to displacive structural phase transitions [28] resulting in incommesurately modulated structures which affect the interactions between nearest-neighbor spin via a long-wavelength modulation of the superexchange interactions, as in the case of the isostructural compound $Rb_2V_3O_8$ [116].

In order to present a new view on the controversy about the double mode observed in the dispersion relation of this compound and to bring some information about the mechanisms discussed above, we have combined ab initio calculations and many body theory methods to calculate the ground state properties of the compound taking into account the many degrees of freedom involved such as, Spin-Orbit coupling effects that give rise to anisotropies in the system, lattice degrees of freedom and on-site Coulomb interaction. Our first ab initio calculations did not allow a study of the compound with the inclusion of spin polarization and big forces between the atoms were obtained specially in the vanadyl bond. We have optimized the volume and the atomic positions for different magnetic configurations within the FP-LAPW basis set. From this we obtained a suitable structure for DFT studies. Our calculations allow us to obtain the crystal field splitting and the magnetic and electronic properties of this compound with and without the inclusion of Spin-Orbit coupling. These results allow us also to study the magnetocrystalline anisotropy of the compound. To our knowledge, no other calculation of magnetocrystalline anisotropy has ever been reported for any vanadate-base material. Our novel theoretical approach consists in the combination of these results together with results obtained from many-body methods: by applying second-order perturbation theory to the three-band Hubbard Hamiltonian for this system we have obtained analytically the DM vector $\mathbf{D}$ and the spin-orbit coupling parameter. We show that the proposed Hamiltonian found in the literature does not fit the experimental susceptibility and specific heat. Our results allow us to propose a slightly different model Hamiltonian which matches the experimental observations.

Chapter 5

Results and Discussion

5.1 Preparation of reliable structures for ab initio calculations

In the absence of diffraction data, a method much used to *a priori* predict crystal structures, is the force field technique [102], [84]. While such calculations are computationally fast, they rely on a classical *ansatz* and therefore miss all possible quantum mechanical effects, which are important for the description of the electronic structure. Quantum mechanical methods, on the other side, are computationally much more demanding, and they are in this study, used for local optimization of the geometry after global optimization with force field methods. In order to study the ground state properties of CuCCP and the compounds derived of it, we have developed an effective way of designing reliable crystal structures which shares the advantages of both methods namely, fast calculations with classical force field methods and subsequent accurate quantum mechanical description with DFT ab initio methods. Our procedure can be summarized in two steps:

1. Creation of a rough structure on the basis of crystallographic databases [25]. If no crystal structures of similar compounds are known, a hypothetical crystal structure is constructed having the highest possible symmetry, a small number of atoms per unit cell and a sensible arrangement of the individual fragments. The crystal structure - atomic positions, cell parameters - is optimized by force field methods, while keeping the original symmetries. In this case, we have used the Cerius^2 program package [27] with a modified Dreiding force field [80]; atomic charges were calculated

by the Gasteiger and Marsili method [44]. This structure is used as an input for the molecular dynamics method in order to improve the relaxation of the geometry [24]. The Car-Parrinello ab initio molecular dynamics calculations [24] are performed with a projector augmented wave (PAW) basis set [15] (both methods were introduced in Chapter 2).

After the relaxation of the structures, the forces are calculated with the FP-LAPW method in order to obtain the best possible equilibrium structure even for demanding transition metal complexes. We have performed non-spin polarized DFT calculations - in contrast to spin-polarized ones - for the structure relaxation since the energy associated with magnetism is much smaller than the cohesion energy and therefore, possible changes on the atomic positions due to the magnetic energy can be assumed to be negligible.

2. Once the reliable structures are obtained, we proceed to calculate and analyze the electronic and magnetic properties with the FP-LAPW basis as implemented in the Wien2k code [14]. Within this basis, calculations are done with both LDA and GGA approximations in order to test these energy functionals. The choice of muffin-tin radii r_{mt}, number of *k*-points in the irreducible FBZ and plane-wave cutoffs RK_{max} were carefully tested for every compound. Finally, in order to extract the effective microscopic Hamiltonian, the Cu-Cu hopping integrals were derived within the *Nth* order muffin tin orbital (NMTO) *downfolding* technique [6] [8] (see Chapter 2) as implemented in the Stuttgart code [7]. Such estimates of the effective hopping integrals are useful to define the underlying low-energy magnetic model. More precisely, the one-electron effective Cu-Cu hopping integral t, can be related to the Cu-Cu magnetic exchange coupling interaction J via a second-order perturbative treatment within the framework a many-body Hubbard model. Assuming that these couplings are antiferromagnetic and neglecting ferromagnetic contributions, J can be estimated as $J_{AFM} \approx 4t^2/U_{eff}$ where U_{eff} is the effective onsite Coulomb repulsion on the magnetic ion site.

With this novel stepwise approach it has been possible to study complicated coordination polymers, being also an effective procedure to obtain reliable structures for accurate quantum mechanical analysis.

Due to the already discussed, characteristics of the metal-organic compounds, which make them quite difficult to handle, the first step of our theoretical methodology has been developed as a combination of efforts between different theoretical groups: the classical calculations were done together with Christian Buchsbaum and Prof. Martin Schmidt (Institute for inorganic and analytic chemistry, JWG-Frankfurt University) and the geometry relaxations with molecular dynamics have been done by Harald Jeschke (Institute for theoretical physics, JWG-Frankfurt University). This combined effort was applied only for the cases of CuCCP and Fe(II)-triazole compounds due to the very demanding computational effort require and the many derivatives of these compounds we have obtained.

5.2 New class of quantum magnets based on 1,4-hydroquinone ligands

5.2.1 Geometry relaxation of CuCCP

A first DFT analysis of the forces between the atoms shows that experimentally determined CuCCP structure is still very unstable with forces of the order of 100mRyd per a_B or more for some atoms. As an example of the unstable results arising from the non-relaxed structures, we show in Fig. 5.1 (a) the FP-LAPW density of states DOS within LDA approximation for the experimental polymer structure CuCCP. In it is noticeable the pronounced peak at the Fermi level, the presence of which is a consequence of the structural instability of the experimental structure (forces bigger than $100 \sim$ mRyd/a_B for some atoms). Calculations with the GGA exchange correlation functional show very similar results for the relaxed structure, therefore we show here only the LDA results. The hydrogen atom contribution to the DOS has not been included because is not visible at this scale.

The pronounced peak disappears in the relaxed structure (see Fig. 5.1 (b)), and one can observe characteristic quasi-one-dimensional van Hove singularities near the band edges around the Fermi level. As a consequence of the relaxation, the bands between -4 eV and -2 eV join together and the bands under -4 eV are shifted upwards in energy. Other characteristics like the number of individual peaks in the structure without relaxation are reduced in the relaxed one. The occupation of the states around the Fermi level does not change after the relaxation. At the structural level, after the relaxation there were only differences in the values of the length bonds of the components, the final obtained values coincide with the standard ones found in the literature [1].

Electronic and magnetic properties

The following results were obtained with the FP-LAPW method. We have considered muffin tin values of 1.8, 1.3, 1,2, 1.1 and 0.79 u.a for Cu, O, N, C and H atoms respectively. 91 k-points in the irreducible FBZ has been used and a RK_{max}=3.8, which is reasonable for systems containing hydrogen atoms. The calculations were done with both GGA and LDA approximations for the exchange-correlation energy functionals. Both of them gave us similar results, therefore we show in this section only the results obtained with the GGA approximation.

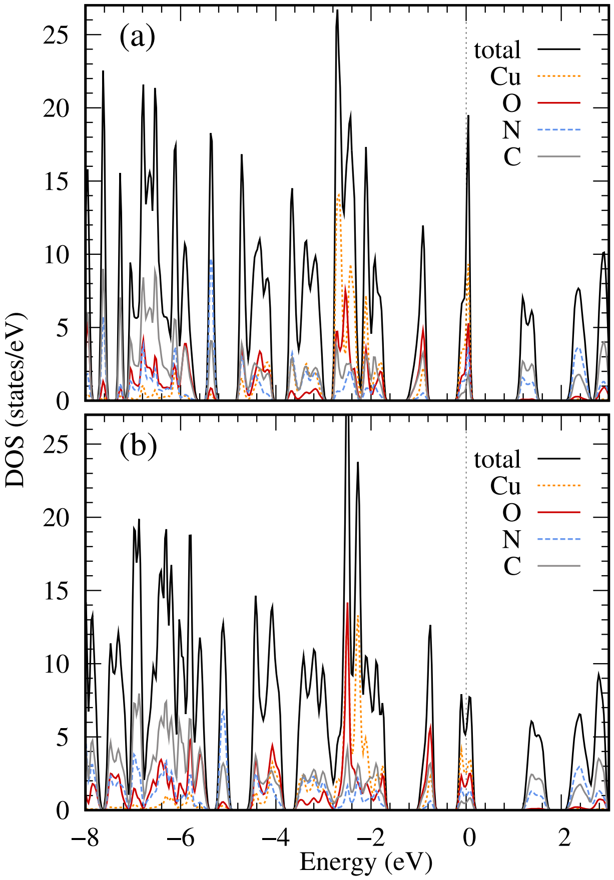

Figure 5.1: Comparison between the total and partial DOS obtained for (a) the polymer without relaxation (experimental structure) CuCCP and (b) the relaxed CuCCP polymer.

Figure 5.2 shows the orbital resolved Density of States (DOS) for the relaxed CuCCP. The Fermi level has been adjusted to zero. In the unit cell there are two inequivalent N atoms belonging to the pyrazole ring. In the DOS plot we identify them as N2 and N1, being N2 the one coordinating directly with the Cu ions. In this range of energy four regions are differenciated:

1. The region between -3.6 eV and -1.8 eV is governed by *p* orbitals of the O, N and C atoms and the Cu 3*d* states. There is a small amount of N *s* and C *s* states in this region, which is not possible to see in the plot due to the scale.

2. The region with a peak around -0.8 eV well separated from the other remaining states in the valence band. This peak contain contributions from Cu d_{xy} (as shown by the band character in Fig. 5.3), O *p* and C *p* states and it is well separated from the other

regions.

3. The region corresponding to the DOS around the Fermi level has a predominant Cu $d_{x^2-y^2}$ character. It contains a significant contribution from O p and N2 p states, indicating important hybridization between these and the Cu d states. The presence of C p and N2 s states in this region is a sign of the bonding nature of the organic bridges which interconnect the Cu atoms.

4. The peak in the conduction region is well separated from the Fermi level. It is mainly formed by C p states, with very small contribution from the N p and H s states.

The H s states in the compound contribute mainly in a range of energy lower than -1.6 eV in the valence region.

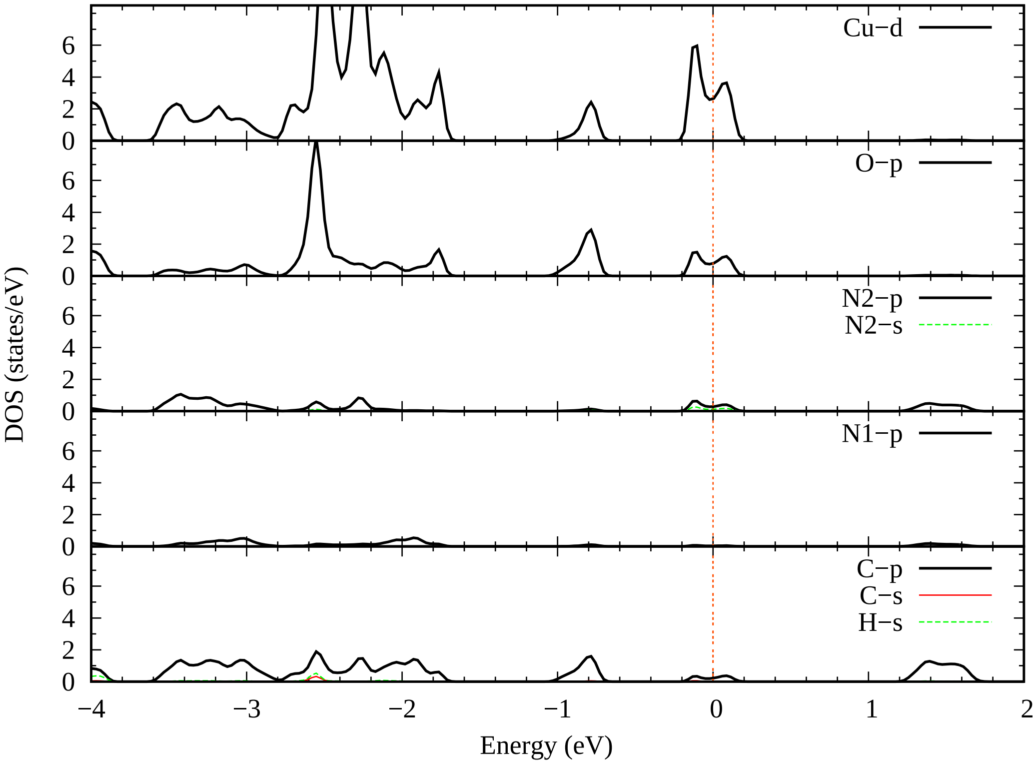

Figure 5.2: Orbital resolved DOS for the relaxed structure CuCCP. The contribution of the Cu s/O s/N1 s states are smaller than 0.1 % in this region and therefore are not shown.

In Fig. 5.3 the band structure for the relaxed CuCCP is shown, with the Cu d band character denoted by bars on the side of the picture. The band character is calculated in the local coordinate frame of Cu which is defined with the local z direction pointing from the Cu to out-of-plane N atom in the next layer and the y direction pointing from the Cu to in-plane O atom. Cu is in a $3d^9$ configuration, with all d bands occupied except for the last band which is half-filled. Both LDA and GGA predict a metallic behavior for this system.

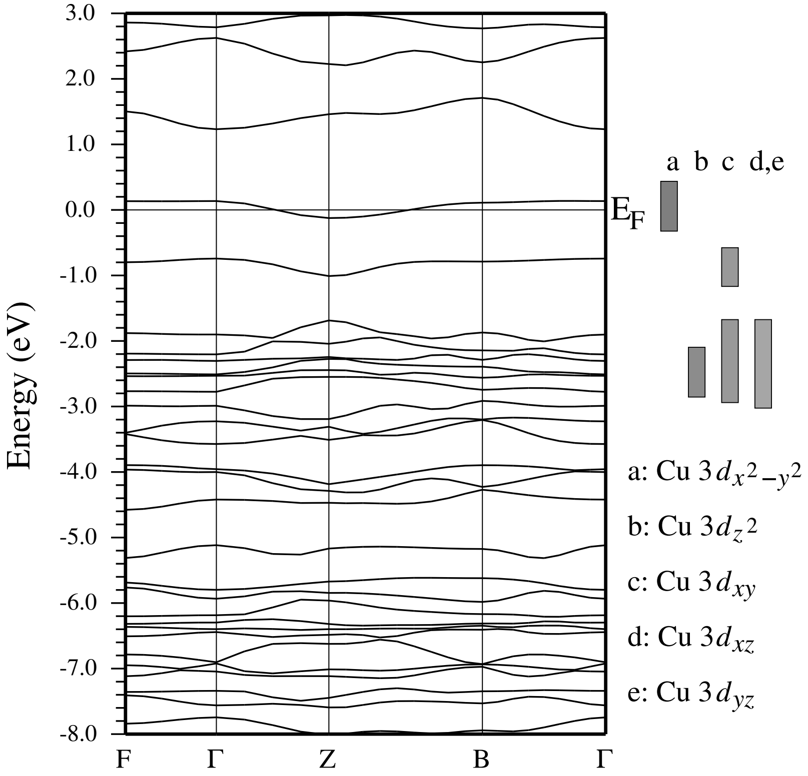

Figure 5.3: Band structure for the relaxed Cu(II) polymer CuCCP in the GGA approximation along the path [22] F$(0,1,0)$-Γ$(0,0,0)$-Z$(0,0,1)$-B$(0.99,-0.13,0)$-Γ$(0,0,0)$ in units of π/a, π/b, π/c. The bars indicate the dominant band character in the local coordinate frame of Cu (see text for explanation).

Since the O-Cu-N angle in the CuO_2N_2 plane is not exactly 90°, the various Cu d degrees of freedom defined with respect to the local coordinate frame mentioned above show slight admixtures. The arrangement of the Cu d states shown in the plot is the expected from the usual splitting of $3d$ states in a square planar coordination as shown in chapter 4. In particular, the Cu $d_{x^2-y^2}$ band crossing the Fermi level contains also small contributions from Cu d_{yz} due to the distorted geometry. The gap between the Cu $d_{x^2-y^2}$ state and the next one, Cu d_{xy} is around 1 eV. From the dispersion of the Cu d band at the Fermi level we confirm the one-dimensional character of the structure. The paths F-Γ (parallel to the crystallographic b-direction) and B-Γ (parallel to the crystallographic a-direction) which correspond to the inter-chain paths are almost dispersionless and the intrachain Γ-Z-B (parallel to the c-direction) path shows a cosine-like behavior. An initial tight-binding fitting to the band around the Fermi level gives a hopping interaction between the Cu-Cu ions along the chain (corresponding to the Γ-Z path in the band structure) of ~ 79 meV. This one-electron hopping integral can be related to the Cu-Cu magnetic exchange coupling interaction J via a second-order perturbative treatment starting with a many-body Hubbard-like model. Calculations for the CuCCP in different magnetic configurations have shown that the ground state of this polymer is antiferromagnetic. For antiferromagnetic coupling and neglecting ferromagnetic contributions, we can use the estimate $J_{AFM} \approx 4t_3^2/U_{eff}$ where U_{eff} is the effective onsite Coulomb repulsion on the Cu site. We consider for U_{eff} typical values for Cu oxides [68] $U_{eff} \approx 4-6$ eV. By choosing $U_{eff} = 5$ eV[1], we obtain nearest-neighbor coupling of $J_{AFM} \approx 58$ K which is somewhat larger than the experimental estimate [118] J$\sim$ 21.5 K obtained by fitting susceptibility data to an effective nearest neighbor Heisenberg model, but remains of the same order of magnitude. A more detailed calculation with massive downfolding procedure, by keeping only the Cu $d_{x^2-y^2}$ degrees of freedom active and integrating out all the rest within the NMTO framework, allows to obtain different hopping values corresponding to the directions shown in Figure 5.4. These values were calculated by B. Rahaman and T. Saha-Dasgupta from the S.N. Bose National Center for Basic Sciences, India.

The largest hopping integral $t_3 = 79$ meV which is directed along the chain (see Fig. 5.4), agrees with the prior estimate from the FP-LAPW bands. All other hoppings correspond to interchain Cu-Cu interactions and are almost an order of magnitude smaller: t_1= 4 meV and t_2= 8 meV correspond to the paths along a- and b-lattice directions respectively (Cu-Cu distance $\sim$ 8 Å). The t_7=5 meV and t_8=3 meV hoppings correspond to Cu-Cu distances bigger than 8 Å which are comparable with the intrachain Cu-Cu interactions t_1 and t_2. Due to the very small value of the intrachain hopping integrals in comparison with the one along the chain, we still can argue that the compound has a quasi one-dimensional character. A very useful tool to understand the obtained t hopping values is the charge density plot obtained with the FP-LAPW method. It will be introduced when analyzed the charge density for the CuCCP with substitutions in the following section.

---

[1] This is however, a very rough estimate since the Cu in this compound is surrounded by two O and two N atoms and the interaction between metallic centers along the chain is via a complicated organic linker.

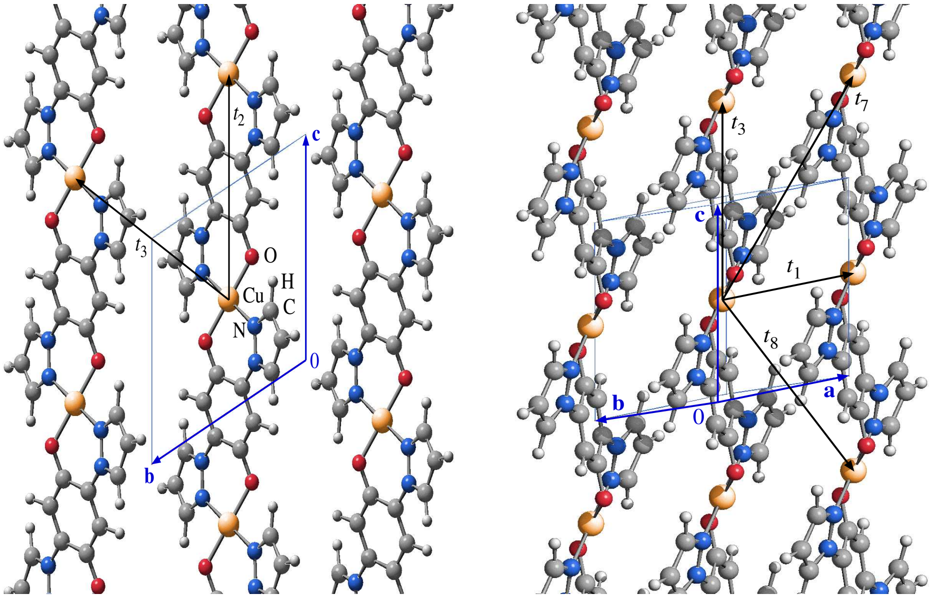

Figure 5.4: Cu-Cu interaction paths t_i, where the index $i = 1, 2, 3, 7, 8$ denotes the ith neighbor.

Spin-polarized calculations open a gap around the Fermi level as shown in Fig. 5.5. The Cu d states are splitted in a lower occupied Hubbard band and an upper unoccupied Hubbard band and the system is described as a *Mott-Hubbard insulator*.

The energy gap around the Fermi level is approximately 0.8 eV . The spin-polarization splits also the contributions due to N, O and C atoms in order to keep the hybridizations between Cu d states with N p and O p states but the ranges of energies, in comparison to the non-spin polarized calculation (Fig. 5.2) remain almost unchanged except for the splitting of the bands above and under the Fermi level. The cosinus-like character of the Cu-Cu $d_{x^2-y^2}$ band is kept in the spin-polarized case as shown in Figure 5.6. We obtain a total magnetic moment per unit cell of 2 μ_B, which correspond to two copper ions with S=1/2. Inclusion of on-site electronic correlation with both LDA+U(AMF) and SIC schemes (see Chapter 2) widens the gap between the Cu d upper and lower bands around the Fermi level with a value proportional to the magnitude of the U parameter.

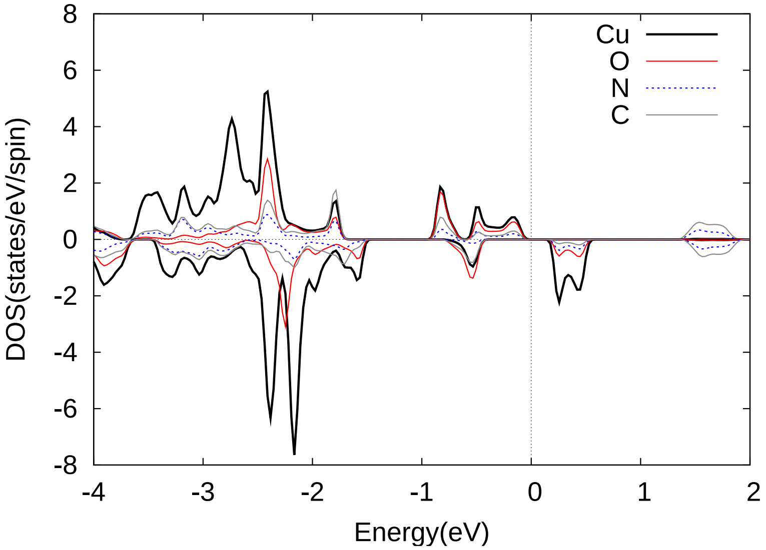

Figure 5.5: Partial spin-polarized DOS for the relaxed CuCCP compound. In it the contribution from spin up (upper panel) and spin down (lower panel) are shown. For simplicity the total density of states have been removed.

5.2.2 Cu(II)-NH_2 and Cu(II)-CN polymers

In order to construct the first set of model structures, the H atoms in the hydroquinone were replaced by aminophenol (NH_2) and cyanophenol (CN) groups, in the following these new structures will be referred as Cu(II)-NH_2 and Cu(II)-CN compounds respectively. The symmetry and cell parameters were kept unchanged with respect to the unsubstituted Cu polymer system CuCCP and relaxing only the atomic positions of the light atoms. These molecules were introduced with the constrain that the center of inversion in the center of the hydroquinone ring must be preserved, then the structures were relaxed until the forces on the atoms were sufficiently small to ensure stability of the quantum mechanical calculations, following the procedure described in Section 5.1. The Appendix A contains the relaxed structural data. Figure 5.7 shows the obtained structure Cu(II)-NH_2. After the final relaxation, the H atoms belonging to the substituted amino group are tilted out of the plane defined by the benzene rings, on the opposite, the cyano-group did not show any distortion or tilting with respect to the hydroquinone ring in the Cu(II)-CN compound. In order to account quantitatively the structural changes that the polymers undergoes under the various substitutions, we define the angle between the vector perpendicular to the CuO_2N_2 plane and the vector perpendicular to the benzene ring (see Fig. 4.2) as the tilting

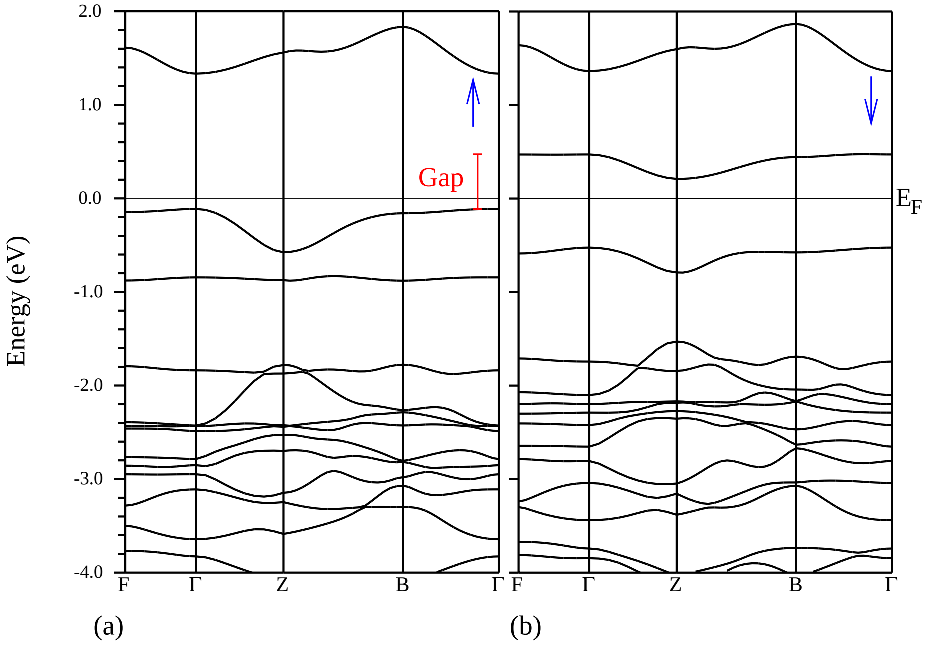

(a) (b)

Figure 5.6: Band structure for CuCCP in the spin-polarized calculation. (a) spin up and (b) spin down.

angle ϑ. The substitution of H by NH_2 or CN in the hydroquinone rings induces a tilting from ϑ=34.9° in CuCCP to ϑ=37.3° in Cu(II)-NH_2 and ϑ=36.3° in Cu(II)-CN.

We have used the same muffin tin radii, RK_{max}, number of k-points in the irreducible FBZ and exchange-correlation functionals used in the case of CuCCP, in order to confront the obtained electronic and magnetic properties of the modified structures with the original one. In Figs. 5.8 (a) and (b) we present the FP-LAPW orbital resolved DOS for the Cu(II)-NH_2 and the Cu(II)-CN within the GGA approximation. It shows the contribution to the total DOS of Cu, O, N, C atoms and the groups NH_2 and CN.

One can observe a modification of the detailed shape of the DOS for Cu, O, N and C between Figs. 5.8 (a) and 5.8 (b) and the DOS for the CuCCP:

- The bands, that in the CuCCP compound where located between -2 eV and -4 eV are now extended above -2 eV and further below -4 eV. The gap between these bands and the next one nearer to the Fermi level diminishes in 0.1 eV.

- The contribution of the N states to manyfold immediately under the one around the

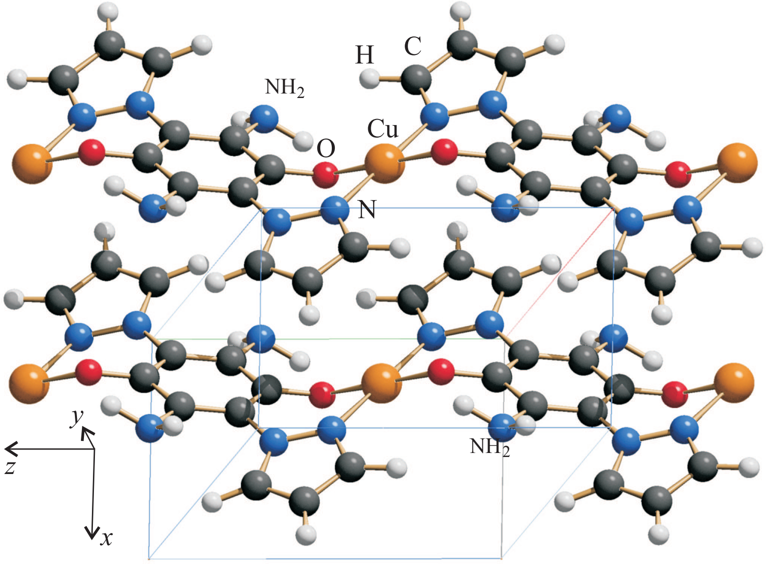

Figure 5.7: Four unit cells of CuCCP where two hydrogen atoms in the hydroquinone rings have been substituted by two amino groups. Notice the tilting of the hydrogen atoms belonging to the molecule NH_2.

Fermi level diminishes in both cases. The N atoms belonging to the NH_2 molecule contributes to this peak. The value of the gap between these peak and the one around the Fermi level remains the same in the case of the CN substitution but with the NH_2 substitution, it diminishes in 0.2 eV.

- The peak around the Fermi level in both cases contains also contribution mainly from the Cu d, O p and N p states, but the weight of the N p contribution in Cu(II)-CN in comparison to the CuCCP is smaller.
- The manyfolds in the conduction band, composed mainly by C p states, are closer to the Fermi level in Cu(II)-CN system than in the other two cases.

The most important feature is the different electronic nature of the NH_2 and CN groups. While the CN group contribution to the DOS lie in a low energy range into the valence band, the NH_2 group has appreciable contribution near the Fermi level, which indicates its involvement in the effective interaction paths between copper atoms as will seen more clearly in the study of the Wannier-like orbitals. The N s in both cases contributes to the band around the Fermi level, as in the CuCCP, which is a sign of the nature of the bonding. These characteristics reflect the donator and acceptor character of the substituted NH_2 and

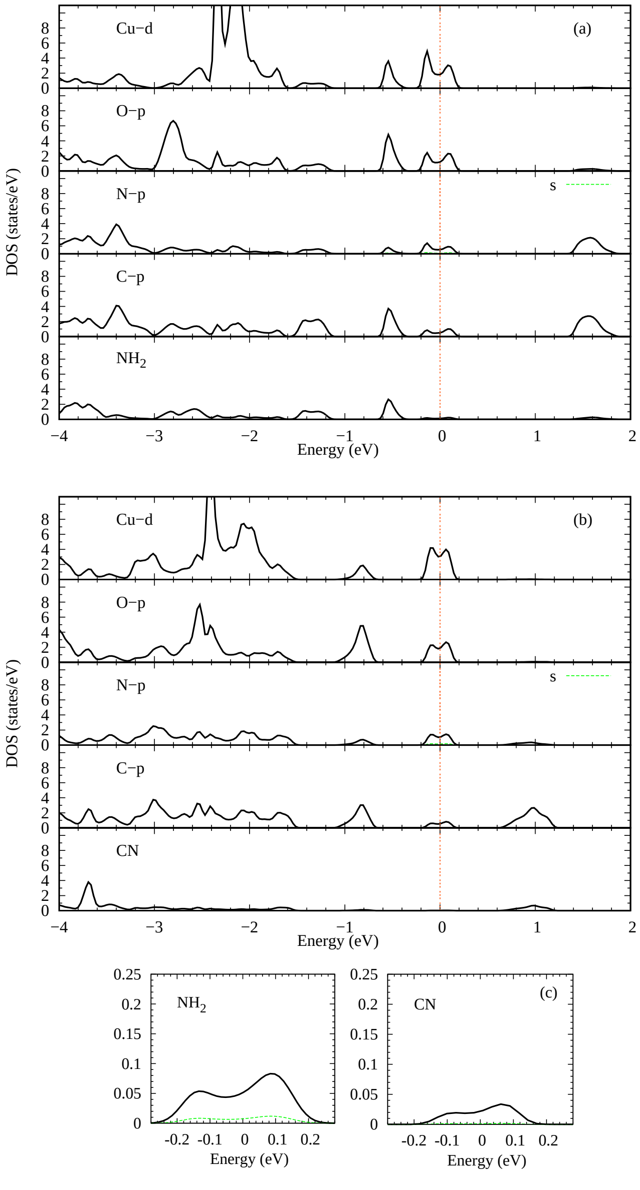

Figure 5.8: Orbital resolved DOS for (a) Cu(II)-NH_2 and (b) Cu(II)-CN; (c) comparison between the contribution of NH_2 and CN groups to the DOS at E_F in a blown up scale, the green line indicates the contribution of the N *s* states in this energy range.

Table 5.1: Comparison of the values (given in meV) for the Cu–Cu hopping integrals calculated with the NMTO downfolding method for the relaxed CuCCP, Cu(II)-NH_2 and Cu(II)-CN structures. The subscripts i= 1,2,3,7,8,12 denote the ith Cu–Cu nearest neighbors. Note that t_4, t_5, t_6 are missing since these values are less than one hundredth of 1 meV in the calculation. See Figure 5.4.

Path	CuCCP	Cu(II)-NH_2	Cu(II)-CN
t_1	4	9	22
t_2	8	3	0
t_3	79	88	68
t_7	5	1	9
t_8	3	8	8
t_{12}	0	0	9

CN respectively. Spin-polarized calculations as well as the inclusion of U correlations open a gap around the Fermi level for these compounds, as in the CuCCP case. Therefore, both compounds behave as a Mott insulator.

Figure 5.9 shows a comparison of the band structure for the relaxed CuCCP, Cu(II)-NH_2 and the Cu(II)-CN polymers in the energy range [-0.25 eV, 0.25 eV] where only the Cu $d_{x^2-y^2}$ dominated band is involved. Though the basic nature of the dispersion remains the same upon substitution, there are fine changes in details of the band dispersion induced by the substitutions. While the NH_2 seems to be the most effective substitution to increase the intrachain Cu–Cu interaction (the bandwidth widens along the Γ-Z-B path for the Cu(II)-NH_2 system), the CN substitution reduces this interaction (note the bandwidth narrowing along the Γ-Z-B path for the Cu(II)-CN system) but enhances certain interchain couplings. The almost dispersionless behavior along F-Γ and B-Γ in the CuCCP polymer becomes more dispersive with the introduction of the CN molecule. Description of such fine and subtle changes needs some quantitative measures which can be best described by the changes in effective Cu-Cu hoppings. This is shown in Table 5.1 which contains the hopping integrals obtained within the NMTO downfolding method. These values were obtained by B. Rahaman and T. Saha-Dasgupta from the S.N. Bose National Center for Basic Sciences, India.

Note that the t_1 hopping for the Cu(II)-CN system along the crystallographic a direction is enhanced by a factor of 4.5. Similarly, t_7 and t_8 hopping terms for the Cu(II)-CN system between neighboring Cu chains in the b direction (see Fig. 5.4) are almost 2-3 times larger compared to that of the CuCCP system. The long-ranged t_{12} hopping parameter between

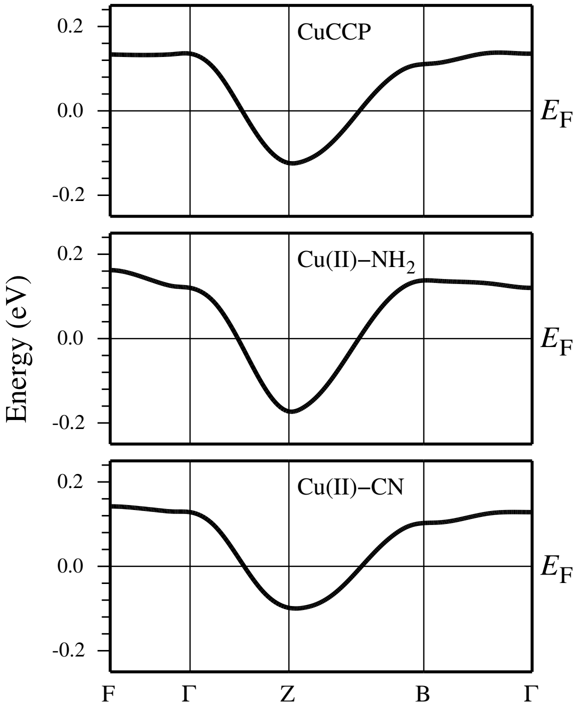

Figure 5.9: Comparison of the band around the Fermi level between (from top to bottom) the relaxed CuCCP, Cu(II)-NH$_2$ and Cu(II)-CN respectively. In all cases the same path in the irreducible FBZ described for CuCCP was used.

neighboring chains along the a axis also attains appreciable enhancement compared to a vanishing small value for the CuCCP system. Similarly, t_1 and t_8 are enhanced by factors $\approx$ 2-3 in Cu(II)-NH$_2$. Among all these hopping values, only t_2 shows the exception of being systematically decreased upon substitution. The predominant hopping t_3 is enhanced in Cu(II)-NH$_2$ system and reduced in Cu(II)-CN system as already predicted from bandwidth arguments.

A very helpful tool to understand the origin of the change in the hopping values discussed previously, is the charge density plot. Figure 5.10 shows the 3D charge density plots for the three Cu(II) models presented so far. The charge density has the expected Cu $d_{x^2-y^2}$ symmetry at the central Cu site, with the bigger concentration of charge around it (*i.e.*, in the Cu-O-N core). The shapes of the orbitals sitting at other sites correspond to the characteristic charge distribution of hybridized s and p orbitals of the various components of the polymers (known as π bonds). Note that the Cu d, O p and N p antibonding orbitals in the basic CuN$_2$O$_2$ square plaquette remain similar in all three cases but the orbital distribution in the hydroquinone ring is markedly different.

The changes are most prominent for the NH_2 substituted case with the orbitals attaining appreciable weight at the sites in the hydroquinone ring, which correspond to an increase in the overlap of the p orbitals lobes of the carbon atoms in the ring. To be noticed also is the occurrence of weight at the NH_2 assembly which is in accordance with the orbital resolved DOS study. This leads to an enhancement in both intra- and some interchain Cu–Cu interactions, caused by the larger overlap of the orbitals. The enhancement happens via two different routes: one is due to the different tilting of the benzene ring compared to the original compound and the other one is the opening of additional interaction paths via the NH_2 group which enhances the intrachain t_3 as well as interchain interactions t_1 and t_8 as can be seen in the quantitative estimates of the hopping interactions in Table 5.1. In the case of the CN substitution, there is not overlap of the carbon p lobes reducing the possibility of the presence of additional intrachain pathways, which is reflected in the reduced intrachain (t_3) hopping interaction. However the mechanism via the tilting of the hydroquinone ring is still operative which is seen in the enhancement of several interchain couplings, especially t_1.

The one-electron hopping integrals between Cu atoms in Table 5.1 can be related to the Cu-Cu magnetic exchange coupling interaction J via a second-order perturbative treatment starting with a many-body Hubbard-like model as done previously for CuCCP polymer. The J_{AFM} values estimated for Cu(II)-NH_2 are $J_{AFM} \approx 72$ K and for Cu(II)-CN is $J_{AFM} \approx 43$ K. Out of these estimates one can predict the trend of enhancing the Cu–Cu interaction through introduction of NH_2 while reducing it through introduction of CN groups. The introduction of CN groups on the other hand enhances some long-ranged interchain interaction paths which were absent in the CuCCP polymer.

5.2.3 Cu(II)-H_2O and Cu(II)-NH_3

The second set of modifications has been the introduction of two kinds of ligands, H_2O and NH_3, in the CuCCP polymer (see Figs. 5.11 and 5.12).

The goal with these models is to study the effect of H_2O and NH_3 satellites on the CuCCP structure as well as to search for possible routes to change the Cu coordination from planar to octahedral. In the original crystal structure the chains are quite densely stacked. The introduction of H_2O (or NH_3) molecules would either lead to unrealistically short inter-

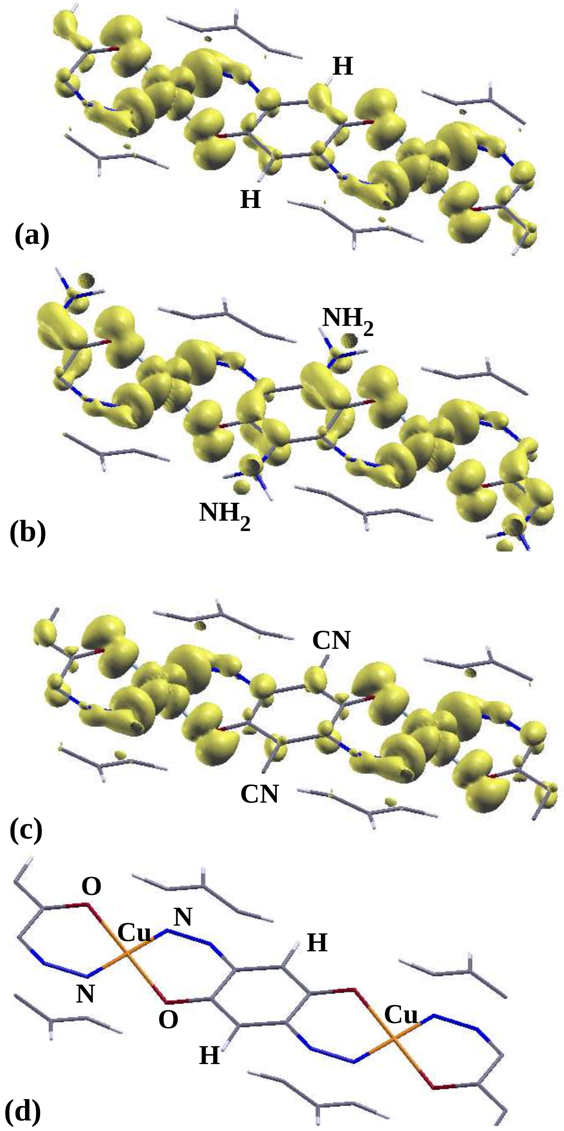

Figure 5.10: 3D charge density in the energy isovalue $\rho = 0.003\ e/\text{Å}^3$ for (a) relaxed CuCCP polymer, (b) Cu(II)-NH_2 polymer, and (c) Cu(II)-CN polymer; (d) indicates the atom positions common to (a)-(c). The N-C-C-C-H chain of atoms appearing above the chains belongs to the next layer.

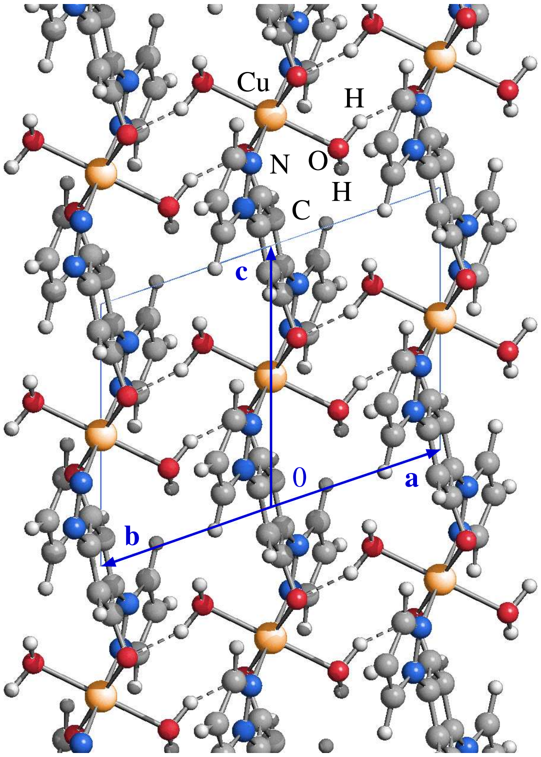

Figure 5.11: Crystal structure of the Cu(II) polymer with water ligands (Cu(II)-H_2O). Shown are also the unit cell (vectors a, b and c) and the hydrogen bonds (dashed lines).

molecular distances between the H_2O (NH_3) moieties and the neighboring chains, or to a considerable increase of the distances between the chains, resulting in an unrealistically loosely packed structure. Therefore the crystal structuctures of Cu(II)-H_2O and Cu(II)-NH_3 polymers were fully optimized, including an optimization of the lattice parameters. Moreover, in order to achieve a better packing of the Cu(II) polymer chains with a favourable lattice energy, the Cu(II) chains shifted in the optimization process both sideways as well as along the chain direction with respect to each other. In Table 5.2 is shown a comparison between the lattice parameters and the volume of the original structure CuCCP and the ones obtained for the modified structures. The resulting fractional positions are shown in Appendix A. In Table 5.3 are shown the Cu-Cu interchain (along c-axis) and intrachain (a- and b-axis) distances for CuCCP and the resulting ones for the relaxed Cu(II)-H_2O and Cu(II)-NH_3 polymers. In general, the change of packing is characterized by the increase of the Cu-Cu distance along the b-axis as well as in the volume.

The final obtained structures are characterized by Cu-O (O belonging to the H_2O molecule)

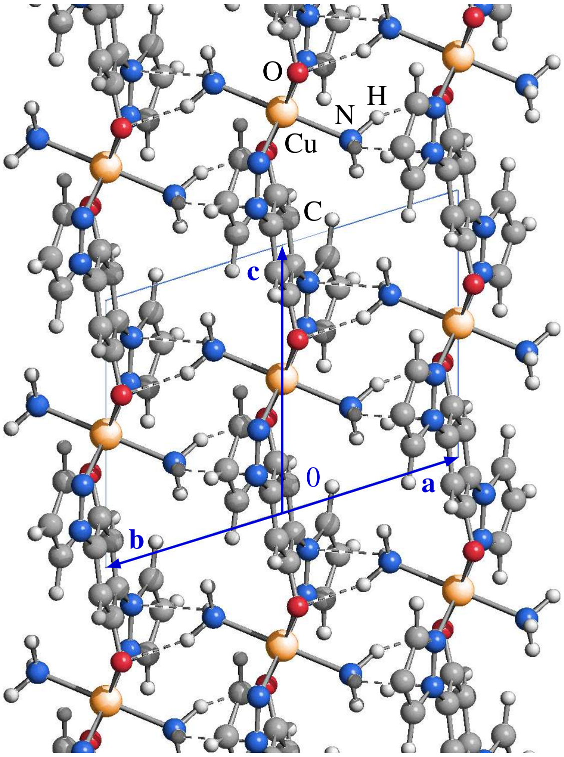

Figure 5.12: Crystal structure of the Cu(II) polymer with ammonia ligands (Cu(II)-NH_3). Shown are also the unit cell (vectors a, b and c) and the hydrogen bonds (dashed lines).

distances of d_{CuO}=2.17 Å while the Cu-O and Cu-N in-plane distances are d_{CuO}=1.99 Å and d_{CuN}=2.01 Å, respectively. This corresponds to a distorted octahedron elongated along the Cu-H_2O direction (see Fig. 5.11). For the case of the NH_3 ligands the Cu-N (N of the NH_3 molecule) distances are d_{CuN}=2.14 Å, while the Cu-O and Cu-N in-plane distances are d_{CuO}=2.02 Å and d_{CuN}=2.03 Å, also giving rise to an elongated octahedron along the Cu-NH_3 direction (see Fig. 5.12). The ligands close to the Cu(II) center also induce a tilting of the hydroquinone ring with respect to the CuO_2N_2 plane. From the initial angle of ϑ=34.9° in CuCCP, the tilting due to the H_2O ligand is quite significant, leading to a value ϑ=42.9 ° in Cu(II)-H_2O. The NH_3 molecule, instead, leads to a lowering of this angle to ϑ=31.8 ° in Cu(II)-NH_3.

For these calculations, within the FP-LAPW scheme, we have considered the same number of k-points in the irreducible FBZ, RK_{max} values and exchange-correlation functional as in the previous cases, however we had to use different muffin tin values due to changes in the lengths of bonds involving C and H. The muffin tin values considered are 1.8, 1.2, 1,2,

Table 5.2: Lattice parameters for the structure CuCCP and models CuCCP-H_2O and CuCCP-NH_3

Structure	a (Å)	b (Å)	c(Å)	$\alpha(°)$	$\beta(°)$	$\gamma(°)$	V(Å^3)
CuCCP exp	5.172	7.959	8.230	118.221	91.520	100.148	291.47
CuCCP-H_2O	5.234	11.249	8.072	117.611	68.822	127.155	330.43
CuCCP-NH_3	5.459	11.597	8.349	118.423	68.840	130.883	350.49

Table 5.3: Comparison of the Cu-Cu distances between CuCCP and models CuCCP-H_2O and CuCCP-NH_3.

Distance (Å)	CuCCP	CuCCP-H_2O	CuCCP-NH_3
Cu-Cu (intrachain, along *c*-axis)	8.229	8.072	8.349
Cu-Cu (interchain, stack along *a*-axis)	5.172	5.234	5.459
Cu-Cu (interchain, stack along *b*-axis)	7.958	11.249	11.596

1.1 and 0.66 u.a for Cu, O, N, C and H atoms respectively. In Figure (5.13) is shown the orbital resolved density of states for Cu(II)-H_2O and Cu(II)-NH_3 compounds within the GGA approximation, where the contribution to the total DOS of Cu *d*, O *p*, N *p*/*s*, C *p* and the molecules H_2O and NH_3 are shown in detail. The contribution to the DOS of O *s* and C *s* are less than 0.1 % and therefore are not shown in the plots. Figures 5.14 and 5.15 contain the band structure for the Cu(II)-H_2O and Cu(II)-NH_3 compounds respectively, with the Cu-3*d* band character shown by bars on the right side. The band characters are given on the local frame of Cu which is defined with the local *z*-direction pointing from the Cu to the H_2O molecule (or to the NH_3 molecule in the case of the Cu(II)-NH_3 polymer) and the *y*-direction pointing from the Cu to the in-plane O atom. In this case is not straightforward to compare the characteristics of the density of states with the one of the CuCCP polymer, because for these new compounds, the lattice parameters and therefore the packing has changed allowing for the inclusion of the new molecules.

The DOS, for both structures, is well defined in four regions as in the CuCCP case. The Cu contribution to the DOS form well localized peaks, located mainly in the upper part of the valence region under -1.8 eV. The main contribution from the rest of the atoms in this region is located under these Cu peaks, indicating a small hybridization of these Cu states with the rest of the atoms. Because this characteristic is similar in both compounds, this could be an effect derived from the new packing. A well isolated manyfold composed by Cu *d*, O *p* and C *p* is present in both cases at around -1 eV in Cu(II)-H_2O and at -0.8

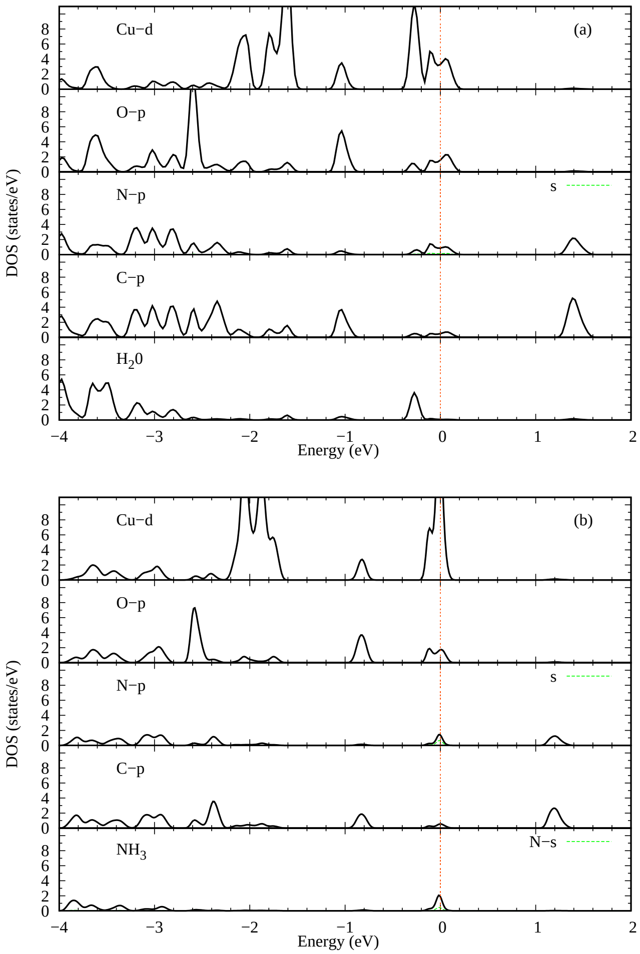

Figure 5.13: Orbital resolved DOS for (a) Cu(II)-H_2O and (b) Cu(II)-NH_3.

eV in Cu(II)-NH_3. We see from the band structure character (Figures 5.14 and 5.15), these Cu peaks correspond to Cu d_{xy}, d_{xz} and d_{yz} states. There is a well defined manyfold very close to the one around the Fermi level of mainly Cu d_{z^2} character, explaining the presence of a significant contribution of H_2O states in the same energy range in the DOS corresponding to Cu(II)-H_2O. This accounts for the interaction between H_2O and Cu d_{z^2} states along the apical position of the Cu atom considered as the z-axis in the local reference system of the Cu. In both polymers, all atoms (except the H_2O molecules in Cu(II)-H_2O) contribute to the peak around the Fermi level. The Cu $d_{x^2-y^2}$ state contribute to this manyfold accounting for hybridizations between Cu d and N p and O p states.

In the Cu(II)-NH_3 case, the Cu d_{z^2} states are so close to the Fermi level that it seems to overlap the peak localized around the Fermi level in the DOS plot, however as seen in the detailed plot of band structure, Figure 5.15(b), these manyfolds do not overlap. The overlapping seen in the DOS is due to the Gaussian broadening[2]. Interestingly, the contribution of N *p/s* states is smaller and more localized around the Fermi level in comparison to all the other cases. The NH_3 states have a considerable contribution to this manyfold.

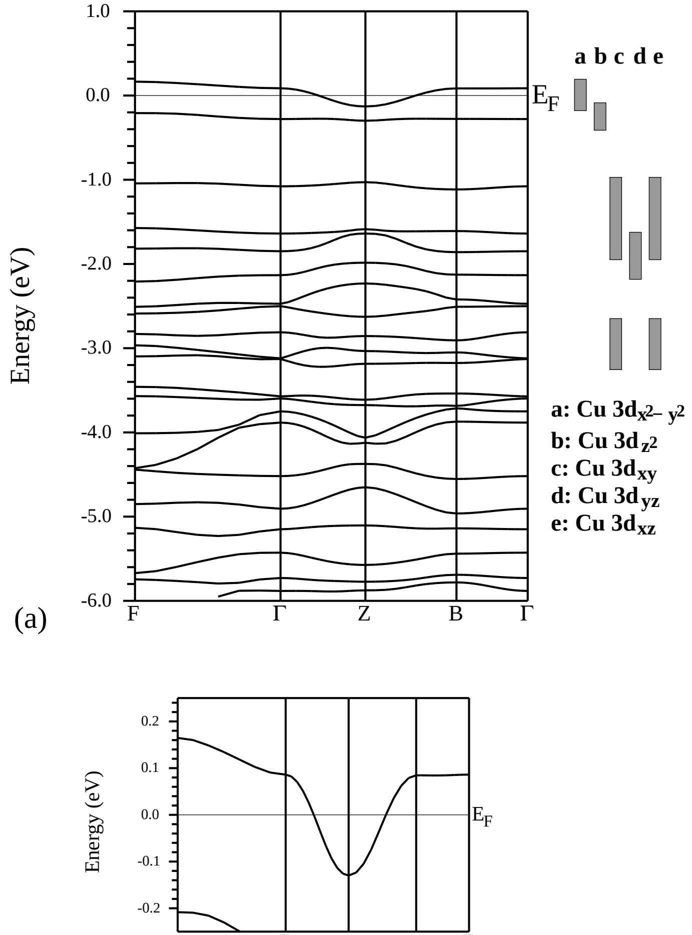

(a)

(b)

Figure 5.14: Band structure of Cu(II)-H_2O compound. (a) the bars indicate the dominant band character in the local coordinate frame of Cu (see text for explanation) (b) detailed plot of the band structure around the Fermi level.

---

[2] In practice a temperature or a gaussian broadening is added to the DOS in order to take into account the experimental broadening effects in spectral lines.

A more detailed analysis on the band structure of Cu(II)-H_2O polymer (Fig. 5.14) reveals it preserves the quasi 1D character present in the original CuCCP polymer. This is shown by the cosinus-like character of the band along the Γ-Z path (along the chain), which is seen in more detail in Figure 5.14(b). In this case (in fact in both compounds, as will be shown below), the inclusion of molecules in the apical positions changes the arrangement of the Cu 3d states, the Cu d_{z^2} goes up in energy closer to the Cu $d_{x^2-y^2}$ and the Cu d_{xy} states go down closer to the d_{xz} and d_{yz} states. This arrangement is similar to the splitting of 3d states into two sets in an octahedral configuration, t_{2g} and e_g states. In Cu(II)-H_2O polymer, the octahedral environment is rather distorted splitting further the t_{2g} and e_g states.

The most interesting effect is seen in the band structure of Cu(II)-NH_3 (see Fig. 5.15). The Cu d_{z^2} states are rather close to the $d_{x^2-y^2}$ states mixing in the band immediately below the Fermi level. This mixing explains the cosinus-like shape of this band along the Γ-Z path corresponding to the intrachain direction. The band around the Fermi level, formed by $d_{x^2-y^2}$ loose its cosinus-like behavior along the c-direction, which is the intrachain Cu-Cu interaction. This is compensated by an increment in the Cu-Cu interchain interactions, as shown by the non-flat dispersion of the bands along the interchain paths Γ-F and B-Γ. As explained above, in this case, the arrangement of the Cu 3d states indicates the successful change in coordination from planar to octahedral. Notice that in these two cases, the dispersion along the path F-Γ is not flat, opposite to what have been found in CuCCP, Cu(II)-NH_2 and Cu(II)-CN polymers, which could be also consequence of the change of packing in the new structures.

In order to quantify the effect of the H_2O and NH_3 ligands on the electronic properties of CuCCP, we show in Table 5.4 the values of the Cu–Cu hopping integrals calculated with the NMTO downfolding method where the hopping parameters for the original CuCCP have been included for comparison.

Note that the intrachain Cu–Cu coupling is reduced by a factor of 1.5-3.5 with the inclusion of both ligands. The reduction is especially significant with NH_3, which is associated with the mixing of Cu d_{z^2} and $d_{x^2-y^2}$ states near to the Fermi level and the almost flat dispersion along the intrachain Cu–Cu direction. The only Cu–Cu interchain path that is enhanced is t_1 which is between Cu in nearest neighbor chains (along F-Γ in the band structure) and has its origin in the hydrogen bonds between the H of the H_2O (NH_3) molecule and the O of the hydroquinone fragments in the chains. Relating the magnetic superexchange coupling

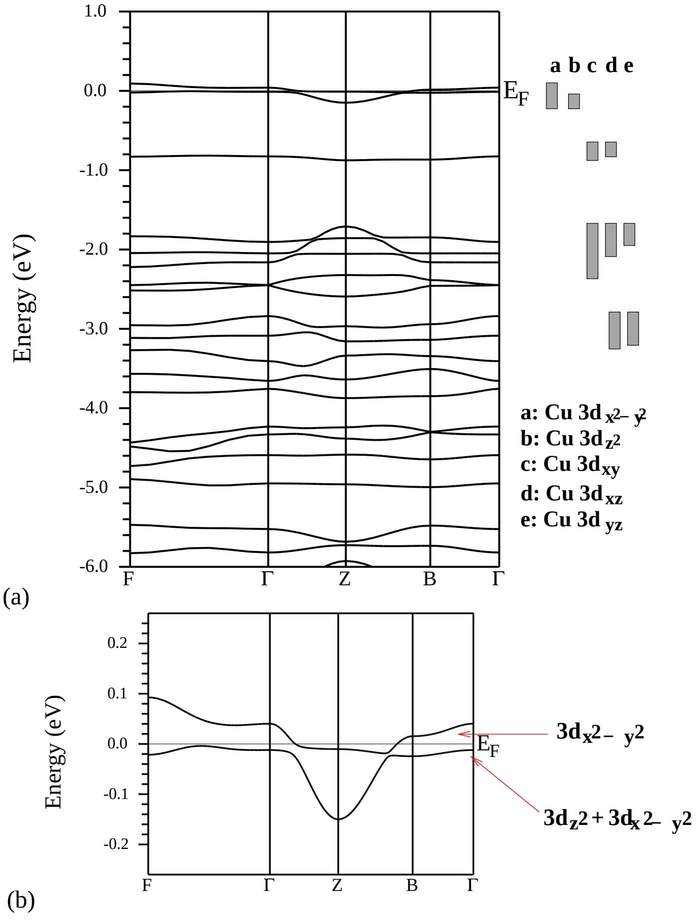

Figure 5.15: Band structure of Cu(II)-NH_3 compound. (a) the bars indicate the dominant band character in the local coordinate frame of Cu (see text for explanation.) (b) detailed plot of the band structure around the Fermi level.

Table 5.4: Values for the Cu–Cu hopping integrals calculated with the NMTO downfolding method for the relaxed CuCCP, Cu(II)-H_2O and Cu(II)-NH_3 structures. The values are given in meV. The subscripts $i = 1, 2, 3, 7, 8, 12$ denote the ith nearest neighbors. See Fig. 5.4.

Path	CuCCP	Cu(II)-H_2O	Cu(II)-NH_3
t_1	4	8	11
t_2	8	7	5
t_3	79	57	22
t_7	5	1	1
t_8	3	0	0
t_{12}	0	0	0

interaction J with the effective hopping interaction t via $J_{AFM} \approx 4t_3^2/U_{eff}$ as was done for the first substitutions, and using also $U_{eff} \sim 5$ eV, the nearest-neighbor coupling for the Cu(II)-H_2O is calculated to be $J_{AFM} \approx 28$ K and for Cu(II)-NH_3 to be $J_{AFM} \approx 4.2$ K. Thus we have obtained compounds with very small exchange constants which are suitable for studying physical phenomena in regions where the applied magnetic field overcome the J value.

Charge density calculations for this compounds for energies around the Fermi level showed a mix between the Cu $d_{x^2-y^2}$ and d_{z^2} states because they are so close, which is not correct as we see from the band structure. This problem is solved by using NMTO methods which are able to pick-up just the states that belong to the band around the Fermi level integrating out the other degrees of freedom, as explained in the Chapter 2. The Wannier orbital plots are shown in Fig. 5.16. From it we can observe that the distorted octahedral environment of the Cu in the Cu(II)-NH_3 structures induces very little mixing of the Cu d_{z^2} orbital to the predominant $d_{x^2-y^2}$. Also note the little contribution of weight in the hydroquinone ring, in both Cu(II)-NH_3 and Cu(II)-H_2O, in contrast to the previous discussed systems (see Fig. 5.10) which is a manifestation of the isolated nature of Cu in these structures. The inclusion of the H_2O and NH_3 satellites, does not change the Cu oxidation state of almost 2+ as observed in our calculations. While the GGA calculations give a metallic behavior with a half-filled predominantly Cu $d_{x^2-y^2}$ band, spin-polarized calculations and the inclusion of correlation effects with LDA+U drive the system to an insulating state. Therefore these systems keep the insulating nature manifested on CuCCP.

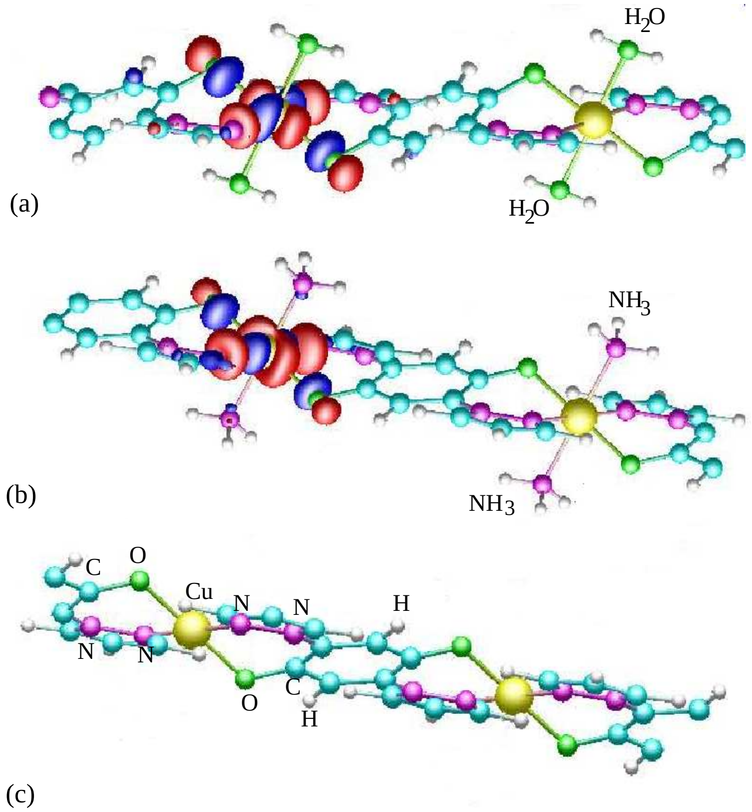

Figure 5.16: Cu Wannier functions for (a) the Cu(II)-H_2O and (b) Cu(II)-NH_3 systems, (c) indicates the atomic positions common to (a) and (b).

5.2.4 TK91

The following results have been obtained within the FP-LAPW method, for this calculations we have considered muffin tin values of 2.0, 1.2, 1,4, 1.0, 1.5, 1.5 and 0.79 u.a for Cu, O, N, C, S, F and H atoms respectively. 100 *k*-points in the irreducible FBZ has been used and a RK_{max} =3.44, which is reasonable for systems that contain hydrogen atoms. A combination of LAPW/APW+lo was used for the Cu states. The calculations were done with both GGA approximation for the exchange-correlation energy functionals because the main building blocks of this compounds are CuCCP-type polymers and for this polymers we got that both LDA and GGA give us similar results. Figure 5.20 shows the contribution of all atoms belonging to the compound to the Density of States (the S p states contribute in energy ranges lower than the energy range showed and therefore its contribution is not shown) and Figure 5.18 shows the contribution to the DOS for the atoms surrounding the Cu atom in TK91, which make an octahedra around it: O1, O2, O3 and (N1 + N2).

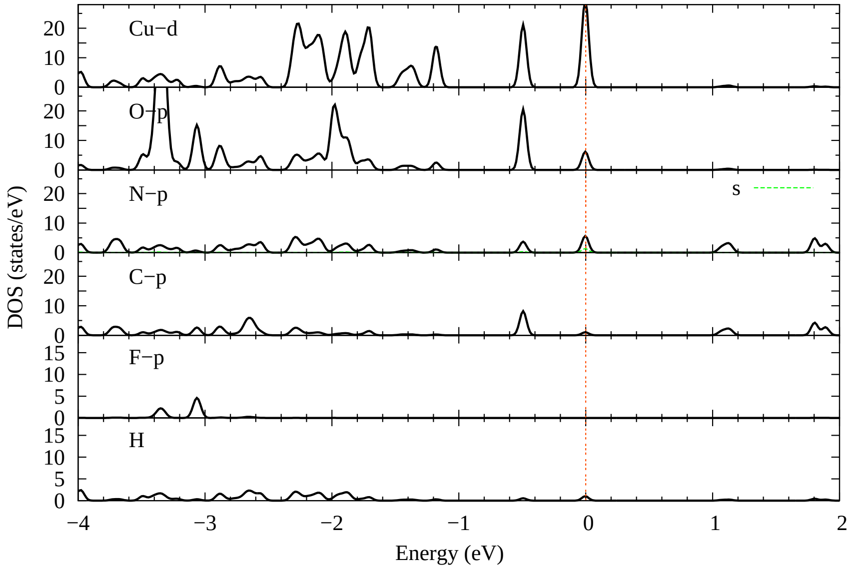

Figure 5.17: Partial density of states for TK91. The contribution from S s/p states in this energy region are less than 0.1 % and therefore in this scale is not possible to see it.

The region between -4 eV and -1 eV contains contribution from all atoms states, mainly from Cu d and O p. The Cu d atoms in this region have d_{xy}, d_{yz} and d_{xz} which are located between the axis that joins Cu and O and N atoms. The peak between -0.4 eV and -0.6 eV has a Cu d_{z^2} which hybridizes in that energy region mainly with O p states. This manyfold is separated in approximately 0.3 eV to the peak around the Fermi level. This peak has a Cu $d_{x^2-y^2}$ character with contributions from O p and N p and in smaller amount from C p. This is a sign of the bonding nature of the bridges between Cu-Cu. The states in the conduction region are well separated from the valence states and contain, in the energy range shown in the figure, contributions from N p and C p states. The general characteristics of the DOS for the Cu atoms are similar to the ones obtained for the CuCCP compound (Fig. 5.2). As expected, the presence of extra components in TK91 in comparison to CuCPP like for instance the apparent coupling of the chains, the DMF ligands, seem not to have a stronger influence on the intrinsic properties of Cu ions coupled by hydroquinone linkers. The most interesting feature is the lack of O3 p states around the Fermi level, as shown in Figure 5.18, which could be an indication of the isolated nature of the dimers because its completely filled states do not provide a route where the electrons can travel. Spin polarized calculations show the Cu ions in this compound have a S=1/2 and the density of states presents a gap around the Fermi level, in a similar way as in the CuCPP, revealing Mott insulator character of the compound.

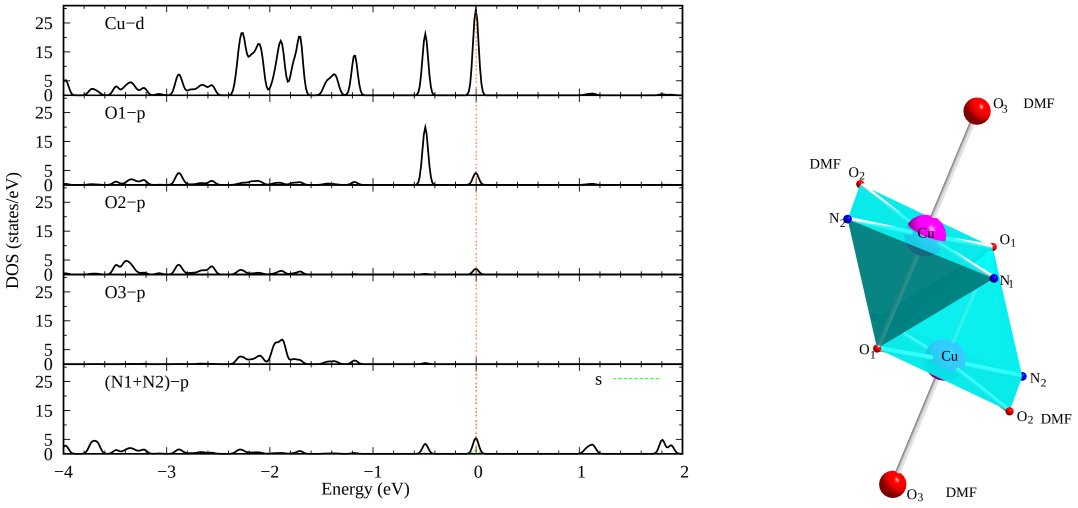

Figure 5.18: (left) Partial density of states from the atoms belonging to the Cu crystal field, (right) Cu crystal field.

The FP-LAPW bands shown in Figure 5.19, plotted only in the region around the Fermi level, reveal the weak quasi two dimensional character of the compound. The main Cu-Cu interaction is directed along the chains, with a flat band along the b-direction, which is

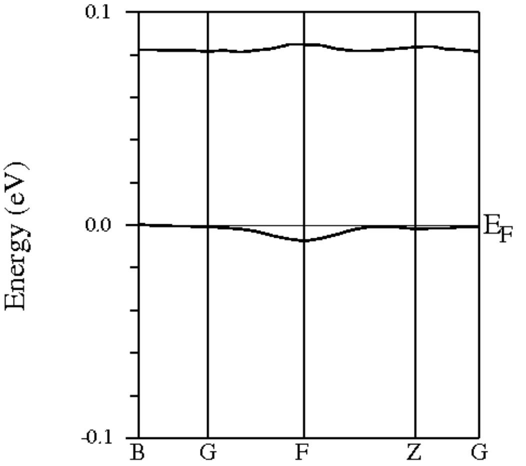

Figure 5.19: Band structure around the Fermi level for TK91 in the GGA approximation.

the direction where the nearest neighbor Cu-Cu are connected and a small dispersion along the c-direction, which is the direction of the longest Cu-Cu distance. The Table 5.5 shows the calculated hopping values corresponding to the different paths shown in Figure 5.20, obtained by fitting the band around the Fermi level with tight-binding.

Table 5.5: Values for the Cu–Cu hopping integrals given in eV. The subscripts i= 1,2,3,denote the ith Cu–Cu nearest neighbors. Also shown the Cu-Cu distances corresponding to these paths.

Path	d_{Cu-Cu}(Å)	t (eV)	J (K)
1 (along a-axis)	8.36	0.007	5.39
2 (along b-axis)	3.27	0	0
3 (along c-axis)	13.16	0.001	0.11

As in the case of CuCCP compound, the superexchange coupling interaction J values are related to the hopping parameters t via $J_{AFM} \approx 4t^2/U$. In this case we used U=4 eV. The coupling across the modified hydroquinone ligands is labelled J_1, the coupling across oxygen ions J_2 and the coupling across anion sheets J_3. The coupling constant obtained underestimate the experimental value $J_1/k_B = 9.4$ K, while the same value calculated with LMTO/NMTO (the estimation was performed by B. Rahaman and T. Saha-Dasgupta from the S.N. Bose National Center for Basic Sciences, India) overestimate it, $J_1 \sim 10$ K, however while LMTO/NMTO gives a 3D character to this compound, with J_2 and $J_3 \sim 1$ K we have found that this compound behave a as a quasi two dimensional compound with a weak

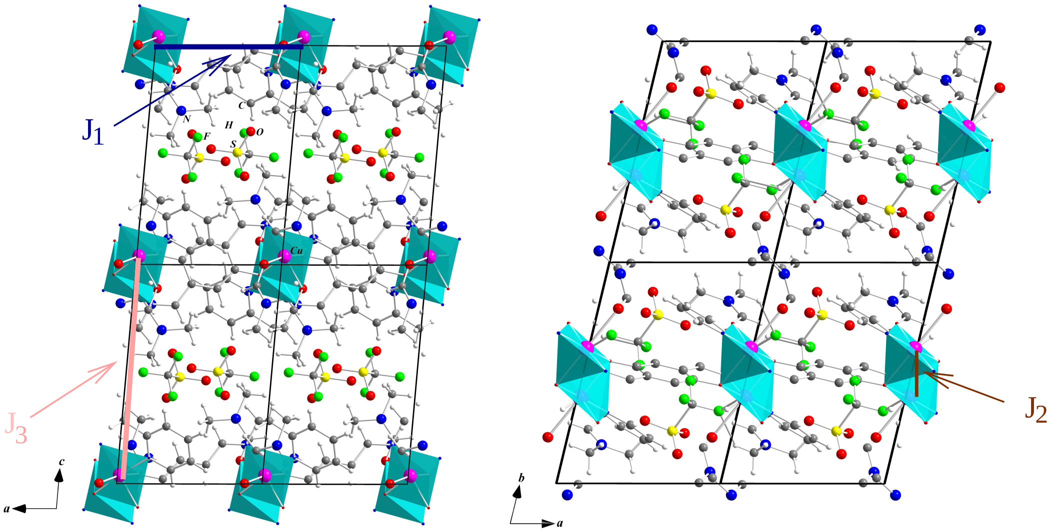

(a) (b)

Figure 5.20: Cu-Cu interaction paths in the TK91 compound.

coupling between the dimers, which is the behavior that is observed experimentally[3]. The discrepancy between this two methods is due mainly to the fact that LMTO is a reliable method for closed packed system, while in very open systems as TK91, small changes in the muffin-tin spheres can produce very different results in the results. Interestingly, the apparent obvious dimer unity, which is the one between nearest neighbor coppers depicted by polyhedra in Figure 5.20 is not such one, actually it is the dimer unit formed by copper atoms linked by the hydroquinone ring, which has a Cu-Cu distance of approximately 8 Å. It is also interesting the fact that there is an interaction between the Cu-Cu atoms which have a distance of $\sim$ 13 Å, in contrast with the zero interaction between the Cu-Cu atoms with the shortest distance in the material.

In order to understand this result, we have plotted the 3D charge density for the compound, which is shown in Figure 5.21(a),(b).

It shows the charge is concentrated mainly in the Cu-N-O plane, with almost no charge in the hydroquinone ring or in the region between the apparent Cu-Cu dimer. This charge contained in the plane of the Cu atoms is known as a delta bonding, which explains that bigger J is directed along the hydroquinone and the almost zero interaction between the nearest neighbor Cu atoms. Figure 5.21(c) shows the charge density for the CuCCP calculated with

---

[3] Very recent, the experimentalists confirmed the dimensionality of the compound

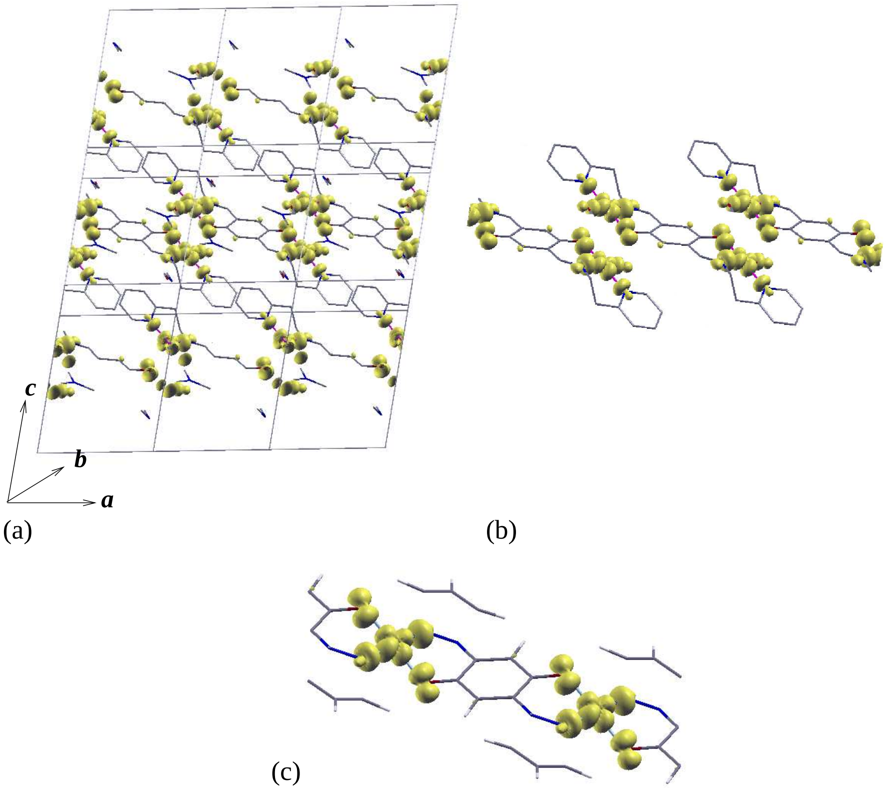

Figure 5.21: Charge density calculated for an isovalue ρ=0.008 $e/\text{Å}^3$ for TK91, (b) shows in more detail the charge density along the polymeric chains of the compound and (c) is the charge density of CuCCP for the same ρ value for comparison.

the same isovalue as for TK91. The very similar characteristics in both cases, indicates the strong influence of the hydroquinone on the Cu-Cu interactions and its tendency of preserve this behavior along different modifications to the structures. This constitutes a very interesting result which could be used when attempting to design materials with small J interactions concentrated in only one direction.

5.3 Magnetic phenomena in zero-, one- and two-dimensional compounds

5.3.1 $Cu_4OCl_6daca_4$

The electronic and magnetic properties have been calculated for the compound at T=80 K and T=340 K with the FP-LAPW basis set. In Table 5.6 the muffin tin radii selected the atoms in the compound are presented. Within the muffin tin chosen for Cu, the 4s states are excluded (the average radii for the wave functions belonging to these states is 2.7 u.a), thus these states lie in the interstitial region. We have used a mixed LAPW/APW+lo basis for the Cu atoms. The valence wave functions have been expanded up to ℓ=10. A number of 48 k-points in the irreducible FBZ and $RK_{max} \sim 3.41$ were necessary for achieving a good precision.

Table 5.6: Magnetic moment (μ(m_B/atom)) within the muffin-tin radii (r_{rmt}) and its % of the total moment. For the interstitial the moment is normalized per formula unit (f.u=$CuO_{0.25}Cl_{1.5}$ daca)

.

Atom	r_{mt}	μ	%
Cu	2.1	0.58350	58
O	1.4	0.44204	11
Cl1	1.6	0.08352	8.3
Cl2	1.6	0.09027	4.5
N1	1.2	0.14477	2.9
interstitial		0.14477	14

Figure 5.22 shows the orbital resolved density of states for the compound at T=80 K and T=340 K within the GGA approximation for the exchange correlation energy functional. Within the GGA approximation we obtain that the Cu d states are partially occupied and therefore the system is metallic. In general, we observe a very narrow and sharp contribution of Cu d and Cl p, N p and O p states in the manyfold around the Fermi level. This band is well separated from the rest of the valence and conduction states at both temperatures. These features indicate that these states strongly hybridize and that the system is almost zero dimensional, formed by well isolated tetrahedra. The band at the Fermi level is narrow with bandwidth less than 0.2 eV, indicating that there is almost no interaction between the tetrahedra. This could be an indication that the interaction between the tetrahedra is very

small or almost zero giving the compound a zero dimensional character.

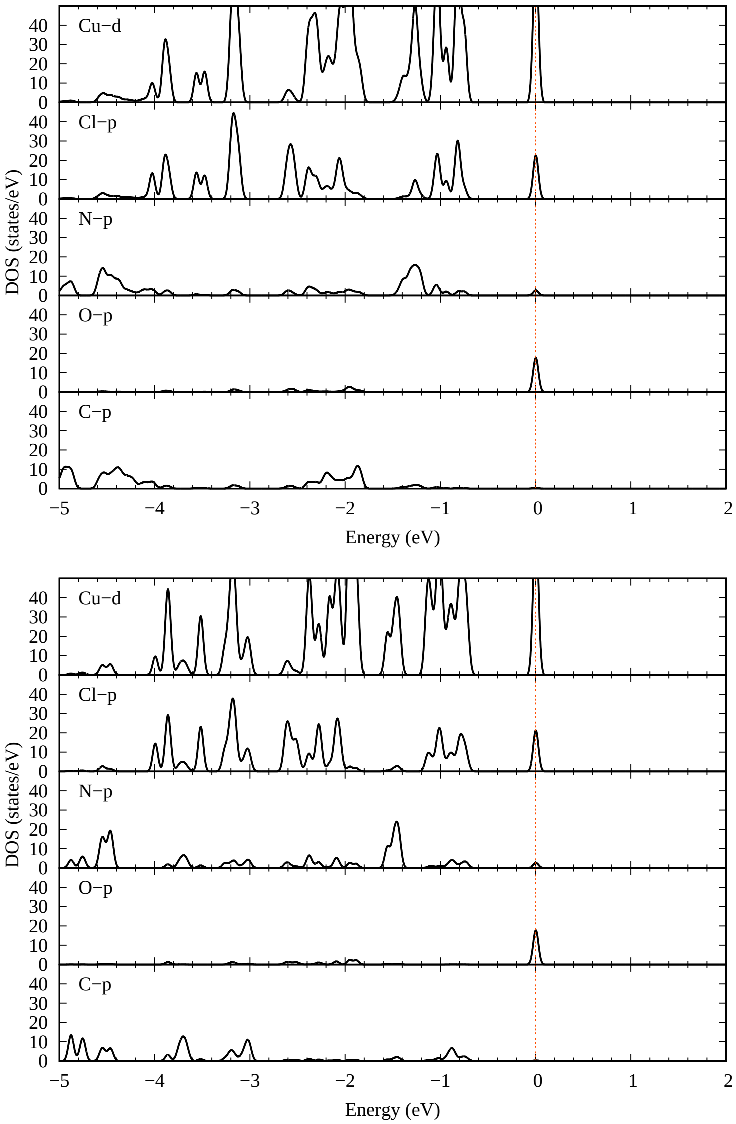

Figure 5.22: Orbital resolved DOS for Cu-daca compound at T=80K (above) and T=340 K (below).

By comparing both DOS plots, we see that with the change of temperature which, induces changes in the organic part of the compound, there is a redistribution of the states of the organic links in the valence region. This reorganization induces changes in the qualitative characteristics of the Cu *d* states, but the gap between the band around the Fermi level and the next occupied states as well as the occupation of these states, remains the same at both temperatures.

Spin polarized calculations open a small gap at the Fermi level for the compound at both temperatures T=80 K and T=340 K. Qualitatively they show the same characteristics therefore, we show only one case in Figure 5.23. In it the contribution of the Cu *d* states to the DOS for the majority (spin up) and minority (spin down) spin channels is presented. The integral under the DOS curve corresponding to the Cu *d* states confirms that the Cu^{2+} ions are in the $3d^9$ configuration. From the figure it follows that the occupation of the spin-up and spin-down Cu *d* states, which is obtained by calculating the area under the DOS curve, are very similar giving a small magnetic *d*-moment. Table 5.6 contains the magnetic moment at the cluster core inside the muffin tin radii. The unpaired Cu electron is strongly delocalized via hybridization mainly with oxygen and less strongly with chlorine and nitrogen. These results exclude a mixed valence state in this compound, which is one of the models proposed in an attempt to explain the experimental data (see Section 4.3.1).

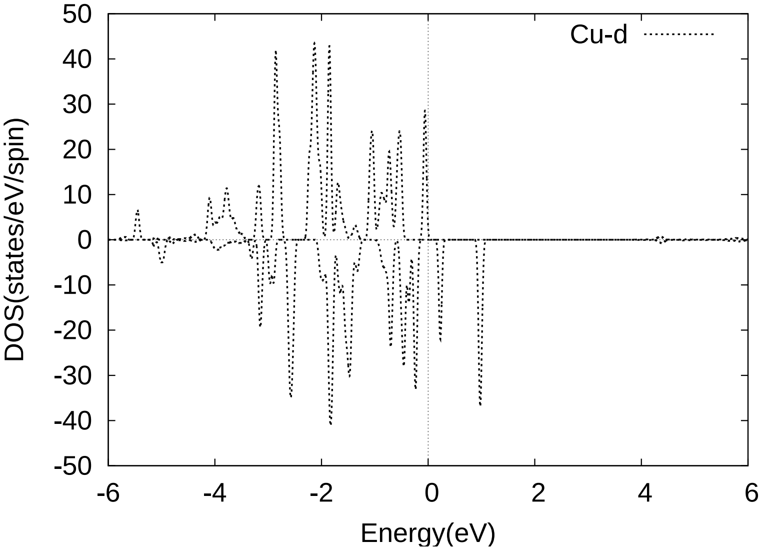

Figure 5.23: Spin polarized DOS at T=80 K. The upper panel corresponds to the contribution to the DOS of the majority channel, the lower panel the minority channel one.

Examination of the crystal field splitting (Figure 5.24) in the local reference frame of the $CuCl_3ON$ trigonal bipyramid, shows that the unpaired electron of the Cu^{2+} ion occupies the d_{z^2} singlet orbital with no angular momentum. The energy difference between this state and the next lowest one is around 900 meV, so the d_{z^2} orbital remains nondegenerate. With fact we reject the proposed model by Lines[72] who attempts to explain the anomalous behavior of the effective magnetic moment by considering orbital degeneracy.

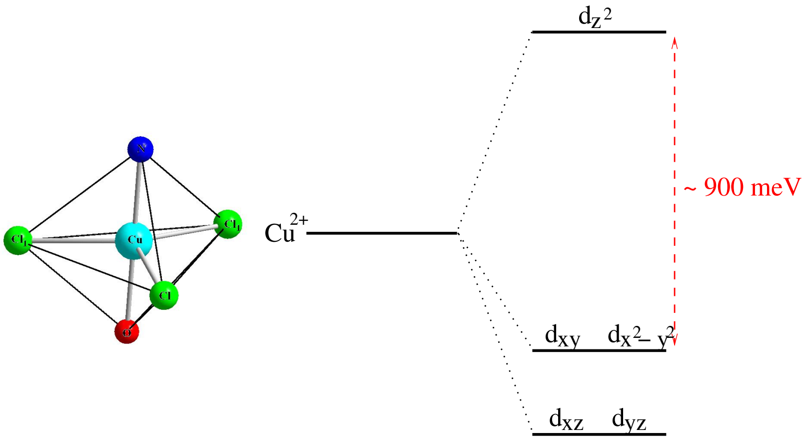

Figure 5.24: Crystal field splitting of Cu ions in the bipyramidal coordination given in $Cu_4OCl_6daca_4$.

The difference Fourier map through the N-O-N plane of the molecule (Fig. 5.25(a)) shows additional electron density near Cu atoms at T=80 K. The tiny peaks (0.38 and 0.31 $e/Å^3$) are displaced along z by 0.84(5) Å and 0.73(10) Å from Cu towards O and N respectively. At T=340 K (Fig. 5.25(b)) these peaks are less pronounced (0.24 $e/Å^3$). These difference electron density peaks near Cu and O, N, C positions evidence the delocalization of e-density in the O-Cu-N≡C bonds. No smearing of electron density near copper atoms or an increase of their anisotropic displacement parameters is observed implying the absence of a static and/or dynamic Jahn-Teller effect at T=80 K. The part (b) of the above mentioned figures show the projection on the plane spanned by N-O-Cl of the calculated charge density map of the band around the Fermi level which are agreement with the measured difference Fourier map from the T=80 K X-ray diffraction experiment shown in Figure 5.25. Its explain the additional electron density near Cu atoms, towards N and O described by the experimental report. The presence of charge between N and Cu indicates the covalent character of the bonding between them. The shape of the charge density in the Cu positions correspond to the d_z^2 shape-like. In this case the mixing between different atomic orbitals is relatively low, therefore is possible to distinguish the p states belonging to Cl, O and N. The charge density at both temperatures show similar characteristics because the magnetic core does not change with the change of temperature. This implies also, that the rearrangement of the organic components of the compound does not have or have very small effect on the electronic properties of the magnetic core.

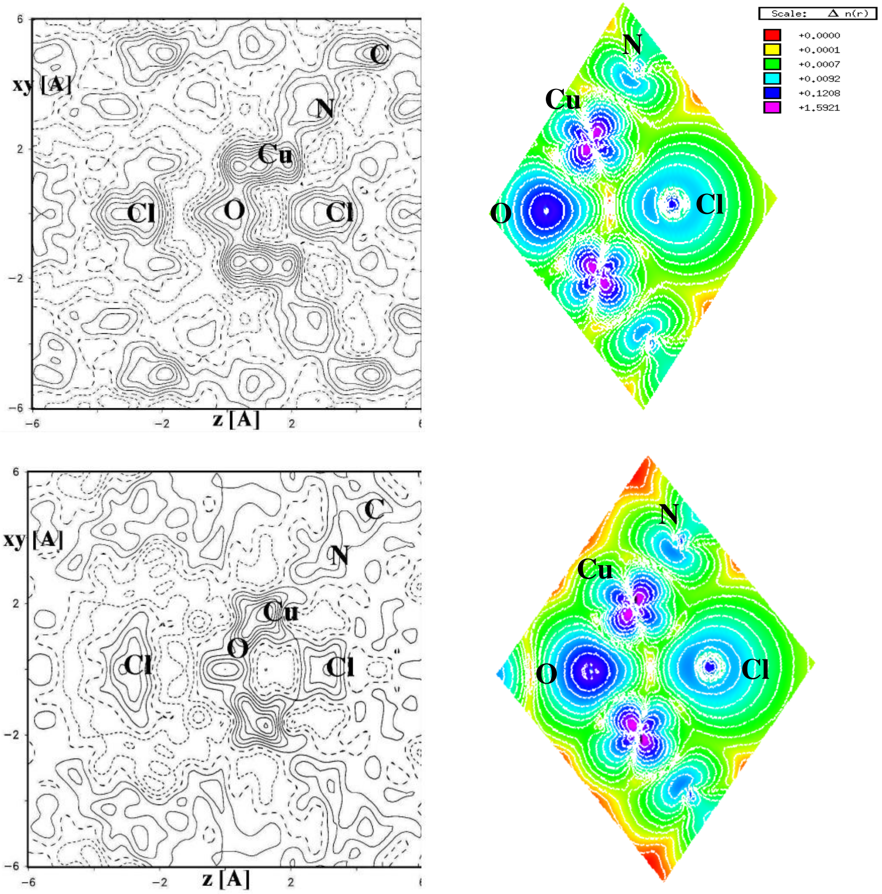

(a) **(b)**

Figure 5.25: Comparison between (a) the difference Fourier map of $Cu_4OCl_6daca_4$ from X-ray single data and (b) the 2D calculated charge density for the compound at T= 80 K (above) and at T= 340 K (below).

Figure 5.26 shows the 3D charge density for the compound at T=80 K, the one at T=340 K presents the same characteristics and therefore is not presented here. Both of them show the characteristic shape of the Cu d_{z^2}. The lobes are directed towards the O atom showing the strong interaction between these orbitals and the O p orbital. The presence of a charge in the Cl atom indicates its active role in the superexchange interaction between Cu-Cu by means of Cl atoms.

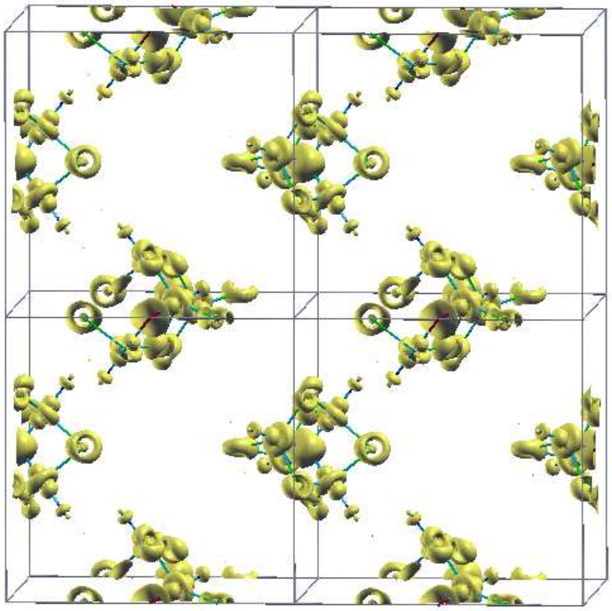

Figure 5.26: 3D charge density of $Cu_4OCl_6daca_4$ at T= 80 K, for a energy isovalue ρ=0.01 e/Å.

Inspection of the interatomic distances and angles as presented in Section 4.3.1 suggests the Cu-O-Cu magnetic exchange is antiferromagnetic (angle $\sim$ 108 °), while the Cu-Cl-Cu (angle $\sim$ 80 °) one is ferromagnetic. Therefore it will be reasonable to postulate an scenario were the intratetrahedral exchange couplings are not uniform. Such a picture is reinforced by a M/H calculation for a model comprising two types of clusters, (i) with isotropic AFM exchange J$\sim$ -20 K, (ii) with three AFM (J $\sim$ -20 K) and three FM ($J_{1j} \sim$ 20 K, j =2...4) couplings, and a small paramagnetic contribution. In such case the magnetic susceptibility (M/H) can be written as

$$\chi = \chi_1 + \chi_2 + \chi_3 \tag{5.1}$$

where χ_1 is the susceptibility of the isolated AFM clusters, χ_2 the susceptibility of the AFM/FM clusters coupled via an AFM intercluster exchange. χ_3 is the paramagnetic con-

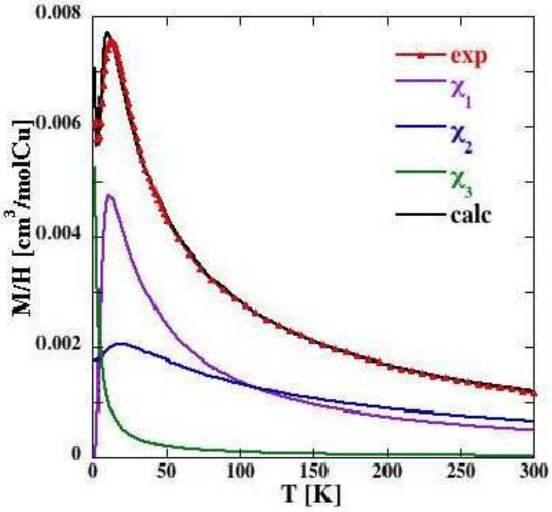

Figure 5.27: Calculated (black) and experimental (red) dc-magnetization (M/H) of the single crystal as well as the separate contributions of AFM clusters χ_1 (violet), of AFM/FM clusters χ_2 (blue) and the paramagnetic term χ_3 (green).

tribution. The best fit for the susceptibility is presented in Figure 5.27. It was obtaining by assuming that the crystal is composed of 1/3 of AFM clusters and 2/3 AFM/FM clusters. According to the fit, AFM/FM clusters are coupled by short range AFM intercluster exchange. Neglecting this exchange or introducing intercluster exchange between AFM clusters results in much worse fits. Surely such intercluster correlations is unrealistic for the ideal Cu-daca system, as the distances between the molecules are too large. Yet the presence of such interactions is feasible when numerous defects on grain boundaries are taken into account. These defects are formed while cooling (the quality of the samples decrease dramatically) and are extremely dependent on sample growth and on thermal treatment. Therefore, different single crystals have different χ_1, χ_2 and χ_3 contributions.

In order to support or reject this scenario, at the theoretical level, we have attempted to calculate the exchange paths within the tetrahedra, by considering different magnetic configurations, as the ones shown in Figure 5.28. However, due to the highly frustrated nature of the compound the magnetic momenta of the system kept oscilating as well as the difference charge density and total energy criteria in the self-consistent calculations.

Although our calculations had shed a light in the understanding of the experimental results observed, it is not possible to explain precisely the ground state properties of this compound and to postulate an scenario that explains the low temperature behaviour. This is due to

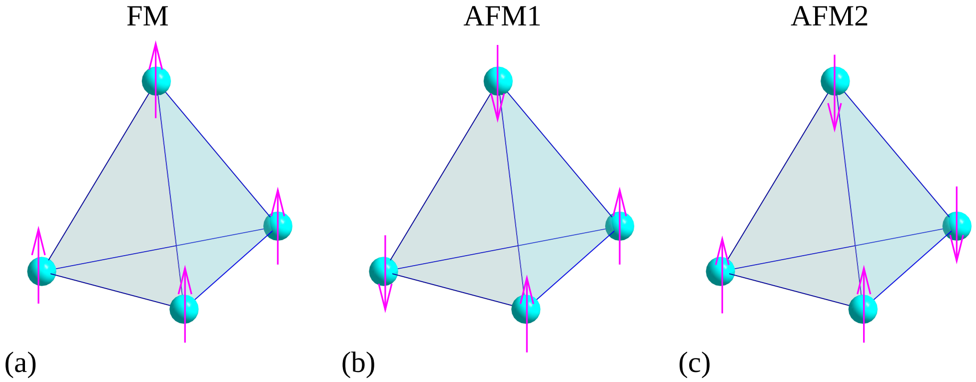

Figure 5.28: Classical scheme of the magnetic configurations considered: (a) ferromagnetic FM and antiferromagnetic (b) AFM1 and (c) AFM2.

the fact that the shape of the M/H curves change in different crystals of the same material making a precise theoretical study difficult. The problems in real samples are due to the isostructural order/disorder structural transition at T=282 K and to the high plasticity of the Cu^{2+} coordination sphere, the quality of the crystals become worse during cooling. This modifies the exchange interactions weakening the AFM Cu-O-Cu exchange in favor of the FM Cu-Cl-Cu one. Measurements of the bulk properties reveal that only part of the clusters retain the spin singlet ground state, another part has magnetic ground state and the ratio between these fractions is sample- and growth direction-dependent. Moreover, apparently there exists an AFM intertetrahedral exchange between the AFM/FM clusters and this exchange can be easily modified by applied magnetic field. These complications of the real samples, hinder answering the initial question which motivated our research. More experiments on that compound are being performed at the moment this thesis was written, in order to confirm/reject our postulated model. However, due to the highly frustrated character we have found in this compound, we can conclude that in order to describe the ground state properties of this compound it is necessary to include quantum fluctuations.

5.3.2 Fe(II)-triazole polymers

As it was discussed in Section 4.3.2 up to date it has not been possible to get an accurate X-ray structure determination of Fe(II) spin crossover polymer systems, which is an indispensable input for ab initio DFT calculations and therefore, to our knowledge, no reliable ab initio structures have been performed. With the two step method described in Section 5.1, which is a combination of classical and quantum mechanical methods, we obtained - based on known data for molecular Fe(II) spin crossover systems - optimized model polymer structures which can be used as input for ab initio DFT calculations.

Since we aim at understanding the HS-LS transition with accurate all-electron DFT calculations, which are computer intensive, we kept the essential features of the material and simplified those elements that make the calculation more intensive, like the usually long polymeric substituents R and the counterions X^-, which are reduced to R=CH_3 and X^-=F. The resulting chemical formula of the compound is $[Fe(CH_3trz)_3]F_2$ (CH_3trz=4-CH_3, -1,2,4-triazole), in the rest of the text we will name this structure Fe[CH_3trz]. The maximum possible crystal symmetry obtained was the monoclinic structure $P112_1/m$. The angles were kept fixed from the beginning to α=90°, β=90° and γ=90.1°.

For simplicity, it has been assumed a perfect octahedral environment for the Fe^{2+} ions. After building the structures and performing a classic relaxation with Force-Field methods, we proceeded to the quantum mechanical relaxation. In this step it was not possible a full relaxation of the compounds, therefore some constrains were applied, as keeping fixed the N-N bond length in the triazole molecule. This is justified by the fact that it has been adjusted to the experimental value d_{N-N}=1.38 Å and that the application of this procedures to previous structures had lead to the bonding values near to the experimental ones (as seen for the case of CuCCP in Section 5.2.1). One representative of the final structures are shown in Figure 5.29. In the top panel is shown the chain arrangement of the compound directed along the *c*-axis. In the bottom panel is shown the view in the *ab*-plane. The packing of the structure and the position of the non-coordinated anions are clearly seen in the figure.

The compound has two formula units per unit cell. The Fe^{2+} ions are located on crystallographic inversion centers, whereas all triazole units contain a crystallographic mirror plane between the neighboring nitrogen atoms. Initially it was chosen only the Fe-N distances (d_{Fe-N}) that correspond, experimentally, to the LS ($d_{Fe-N} \sim 2.0$ Å) and HS ($d_{Fe-N} \sim 2.2$

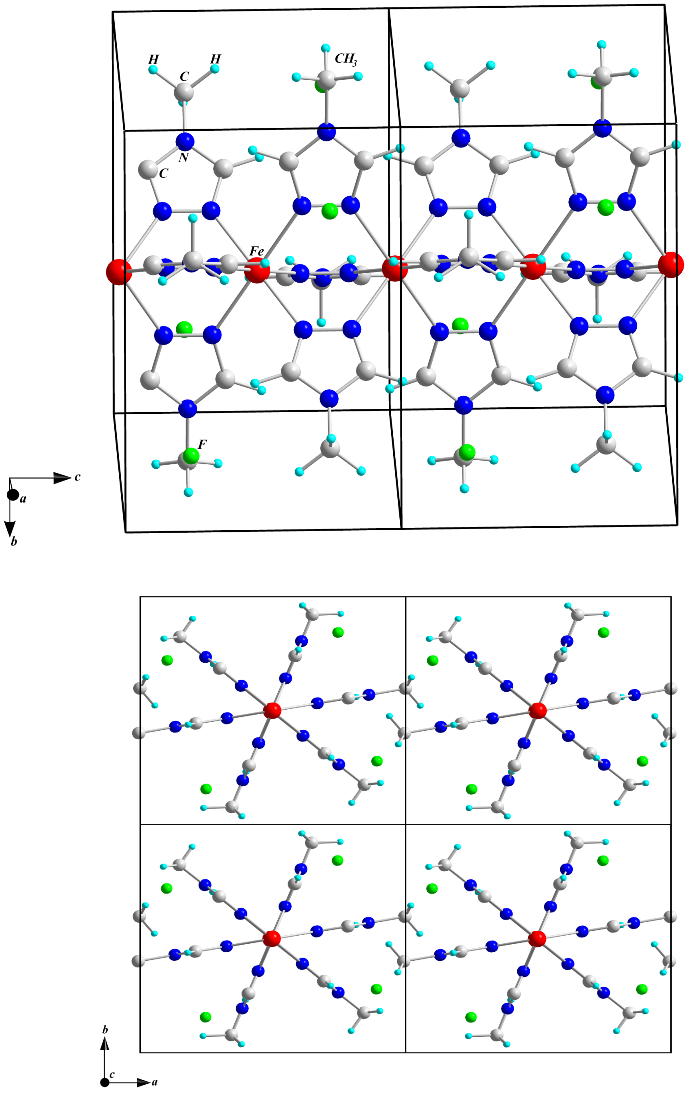

Figure 5.29: Schematic representation of our model polymer Fe[CH_3trz], (above) view along the c-axis, (below) view in the ab-plane.

Å) situation (the atomic positions for the resulting structures are shown in Appendix B), once we could reproduce the spin state in every compound we proceed to build structures between the LS and HS ones in order to study the electronic behavior along the transition. Therefore, by changing d_{Fe-N} in the LS structure, keeping all the characteristics described before, we have obtained structures with d_{Fe-N} =2.05 Å, 2.08 Å, 2.12 Å, 2.15 Å, and later structures with d_{Fe-N}= 2.09 Å and 2.10 Å were constructed. The resulting atomic positions of all these structures are shown in Appendix B. The change in d_{Fe-N} leads automatically to a change in the lattice parameters, particularly the relative change in the *c*-lattice parameter is larger than for the *a*- and *b*-lattice parameters. This means that the volume of the unit cell also increases linearly from V=963.45 Å for d_{Fe-N}=2.0 Å to V=1083.08 Å for d_{Fe-N}=2.2 Å as it is shown in Figure 5.30. Experimentally, the transition from LS to HS is accompanied with a dilatation of the crystal lattice [42]. Due to the change in volume, the Fe-Fe distances along the *a*-, *b*- and *c*-axis increases, the lattice parameters values are also shown in Table 5.7. The Fe-Fe distance for the d_{Fe-N}= 2.00 Å compound are 10.92 Å along *a*-axis, 11.96 Å along *b*-axis and 3.68 Å along *b*-axis. For the d_{Fe-N}= 2.20 Å compound, 11.25 Å along *a*-axis, 12.29 Å along *b*-axis and 3.92 Å along *c*-axis.

Table 5.7: Lattice parameters of the constructed Fe(II)-triazole structures

d_{Fe-N} (Å)	*a*	*b*	*c*
2.0	10.9205	11.9598	7.3766
2.05	11.0019	12.0414	7.4920
2.08	11.0509	12.0904	7.5613
2.09	11.0671	12.1067	7.5844
2.10	11.0834	12.1234	7.6075
2.12	11.1162	12.1558	7.6537
2.15	11.1650	12.2046	7.7230
2.2	11.2466	12.2861	7.8384

At this point, it is important to mention the energy scales that have some effect in- or contribute to- the phase transition,

- The crystal field splitting, which is the difference in energy between the e_g and t_{2g} states.
- The mean pairing energy which is accounted for by the Hund's exchange coupling parameter J_H.

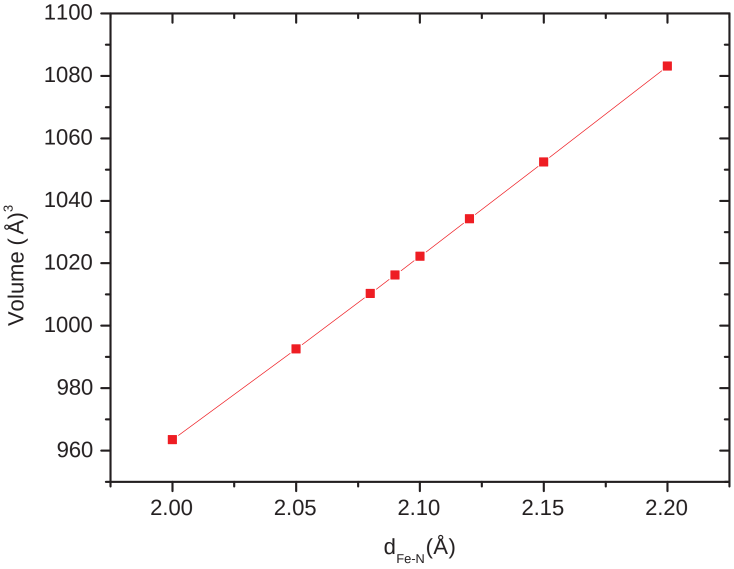

Figure 5.30: Volume *vs.* Fe-N distance in Fe[CH_3trz]

- The phononic excitations
- The short-range and/or long range elastic interaction parameters
- The exchange interaction J due to nearest neighbors superexchange between Fe(II) ions.

The competition between these energy scales determines the nature of the transition. In our calculations, the crystal field splitting energy is fixed by the way the model structures have been constructed. The role played by the phonons in driving the LS-HS transition in spin-crossover has been widely discussed in terms of the elastic models we presented in Chapter 4. In our calculations, the phononic degrees of freedom are frozen. The energy scale effects we want to investigate is the exchange interaction J due to nearest neighbors superexchange, the role of the electronic and magnetic degrees of freedom and their relation with the microscopic origin of cooperativity in the HS-LS transition.

Electronic and magnetic properties

In order to obtain a qualitative and quantitative description of the electrons ordering according to the difference in distance Fe-N, we use spin-polarized version of the GGA approximation which follows the Hund's rules. The band structure calculated along the path Γ(0,0,0)-Z(0,0,1/2) (it corresponds to the direction along the chain) and the total and partial Fe 3d contribution to the density of states for the models with distances d_{Fe-N}=2.0Å and d_{Fe-N}=2.2Å are shown in Figures 5.31 and 5.32. The Fermi energy E_f has been adjusted to zero and it is showed by a red line; the shaded area in the DOS indicates the contribution from d orbitals of the iron ions.

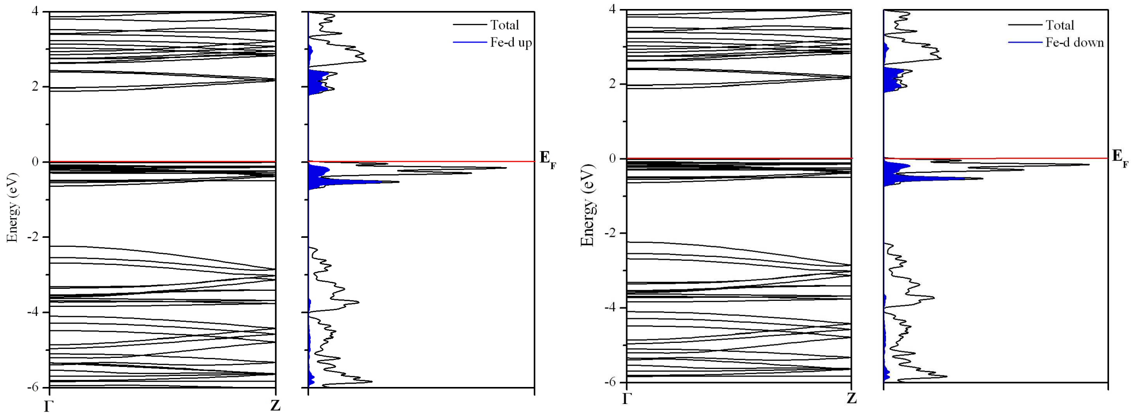

Figure 5.31: Band structure and density of states for our Fe(II)-triazole model with d_{Fe-N}=2.0Å

In the case of d_{Fe-N}=2.0Å the Fe 3d^6 states are occupied in both spin up and spin down cases, as shown in Figure 5.31, the triazole bridging ligand push the neighboring irons apart to ∼ 3.6 Å, consistent with the Fe-Fe experimental distances [121], and thus there is clearly no metal-metal bonding. The four bands with Fe d character above the Fermi level correspond to the 4 e_g states corresponding to the two iron atoms in the unit cell, they are almost degenerate. The number of Fe d states immediately under the Fermi level are not clear due to the presence of F states in the same energy range. This indicates the ionic interaction between these two atoms in the compound. However, due to the two Fe atoms in the unit cell, there should be six t_{2g} states. The e_g states are completely empty, the t_{2g} states are completely filled and are located, without taking into account the counterions, above the bands that come from the triazole ligands. The separation between e_g and t_{2g}

states is around 1.8 eV which is fairly consistent with the observed value of 2.4 eV for the spin transition compound described by Kröber *et al.* which has the general characteristics our models presents [67]. Our calculations indicate this compound has spin S=0.

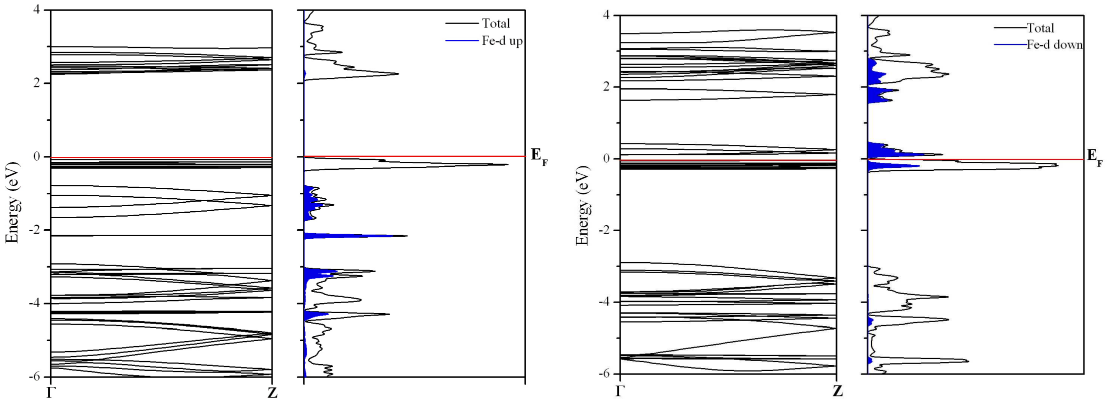

Figure 5.32: Band structure and density of states for our Fe(II)-triazole model with d_{Fe-N}=2.2Å

For the case d_{Fe-N}=2.2Å e_g states are not longer empty, the majority (spin up) contribution for all Fe *d* states is totally occupied and the minority (spin down) is partially occupied as seen in Figure 5.34, this is consistent with the Hund's rule which establish that the state of minimum energy is the one with the maximum spin state. The imbalance between up and down electron numbers is $n_\uparrow - n_\downarrow = 4$ which corresponds to the HS state S=2. In the DOS for the majority spin, the four e_g states are located between -2 eV and 0 eV and the t_{2g} states below -2.5 eV cannot be well distinguished from others. For the minority case, the bands nearer to the Fermi level are the $6t_{2g}$ states, although we find only two bands of this states above the Fermi level, there is one band doubly degenerate, the other two are completely occupied located under this level, but cannot be well distinguished from others. The bands above 1.8 eV correspond to the $4e_g$ states, they are well separated from the t_{2g} states around 1 eV which is fairly consistent with an observed value of 1.5 eV in the HS state [67]. The gap between occupied and unoccupied states is approximately 0.2 eV. The Fe *d* contribution to the DOS are broader than in the LS model and more extended in the energy range. This is an indication of the weaker ligand field around the Fe. The bands are almost flat in both cases, indicating the small correlation between Fe-Fe.

In order to account for hybridizations and the role the bridging molecules play in the spin state of the Fe ions, we have plotted in more detail the contribution of every atom of the models in Figure 5.33 for the model with d_{Fe-N}=2.00 Å and Figure 5.34 for the model with d_{Fe-N}= 2.20 $\AA$.

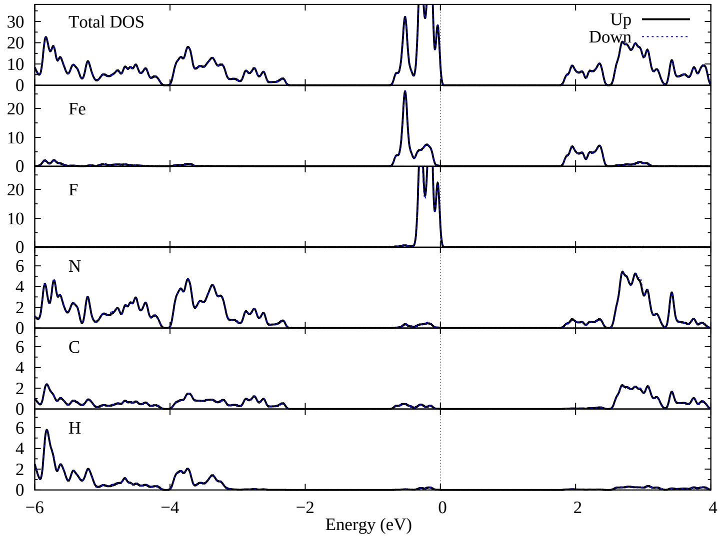

Figure 5.33: Total and partial density of states in the GGA spin polarized approximation of the structure with d_{Fe-N} = 2.0 Å. Both spin contributions have been plotted in the same panel to account for the matching of the contributions.

For d_{Fe-N}= 2.00 Å it is evident the perfect match between the spin up and spin down contributions from all atoms, which indicates the system has a zero total magnetic moment (LS state). In the valence region the N *p*, C *p* and H *s* states contribute mainly to the energy range below -2 eV with a very small contribution from Fe t_{2g} states. These states are mainly concentrated between -1 eV and the Fermi level, with a small contribution from N *p* and C *p* states, which indicates the small hybridization between these and the Fe *d* states. The F *p* states are highly localized in this energy range. The contribution from the counterions, F atoms, is not of relevance in this analysis because it was introduced to replace real physical counterions and to maintain the neutrality of the unit cell. However we could argue that the fact that their contribution to the DOS is located in the same energy range than the Fe ions accounts for the compensation to the Fe charge the F atoms introduce, revealing its ionic character. The states in the conduction region are well separated from the valence states, with a gap ~ 1.8 eV and it extends above 4 eV. The contribution of the Fe e_g in this region are concentrated from 1.8 eV to 2.2 eV approximately.

In contrast, for the compound with d_{Fe-N} = 2.2 Å, Figure 5.34 shows that the change in

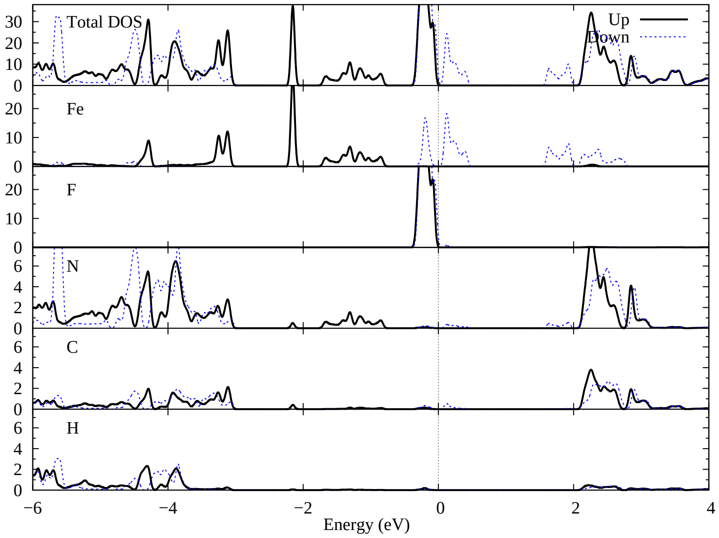

Figure 5.34: Total and partial density of states in the GGA spin polarized approximation of the structure with $d_{Fe-N} = 2.2$ Å. Both spin contributions have been plotted in the same panel.

the spin state of the metal atoms affects also the spin polarization of the states of the atoms belonging to the triazole molecule, having a bigger effect in the N p states. The change in the spin state affects also the distribution of the Fe 3d states in the DOS affecting the states of the rest of the atoms in the compound, which is reflected in the hybridizations. In this case, the states under the Fermi level split in four peaks of spin up and one peak of spin down, above the Fermi level, there are three peaks of spin down. This splitting of the Fe 3d states push the states that before were located around -2 eV further, lower in energy. Therefore, in this case, we distinguish more regions in the Total and partial DOS than in the LS case. The first region located from ∼ -3 eV, contains the contribution from Fe d, N p, C p and H s states. In this region, the N, C and H contributions are polarized, but specially N which shows a stronger polarization. The peaks around -1.9 eV and between -2.1 eV and -0.8 eV have Fe 3d nature, with a very small contribution from N p atoms, which evidence the hybridization between these states. The third region, located immediately below the Fermi energy is mainly composed of Fe d and F p states. Immediately above the Fermi level the main contribution comes from the Fe atoms with a very small presence of N and C states. The last region, located above 1.8 eV contains the contribution of all atoms, the contribution of the Fe states are lower in energy in this region in comparison with the N and C atoms. Due to the broadening of the N p states, which is bigger in this case in comparison with the LS model, the hybridization with this states increases.

From the analysis of the DOS for both LS and HS structures, we can give an important conclusion: when going from LS to HS, the Fe $3d$ states rearrange themselves in energy, this rearrangement push lower in energy the states of the triazole atoms, if this rearrangement is propagated through the whole chain, we could argue that this repulsion between states contribute also to the mechanism of cooperativity in this family of compounds.

Intermediate structures

In order to study the reorganization of the Fe $3d$ states with the crystal field and its effect

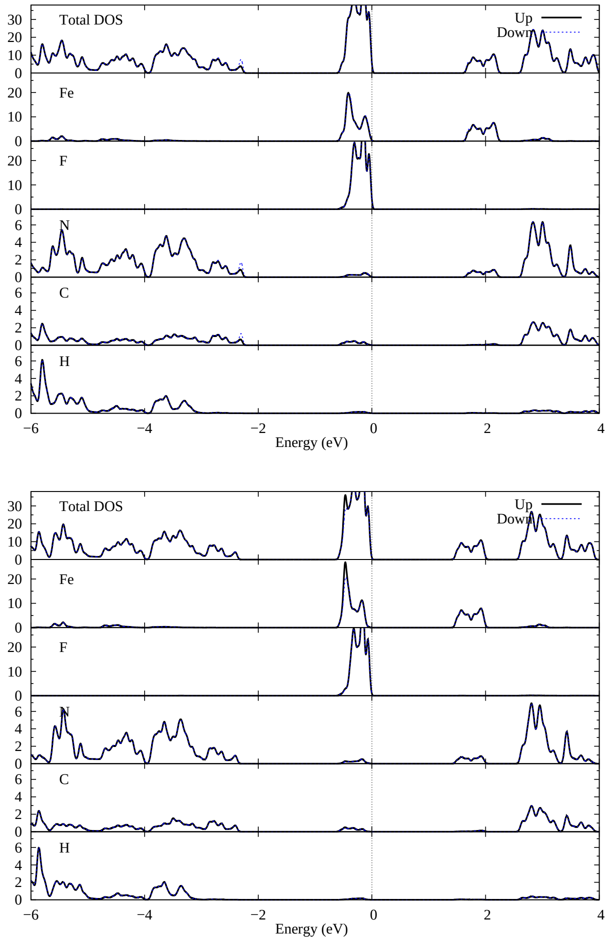

Figure 5.35: LS structures: (above) d_{Fe-N}= 2.05 Å, (below) d_{Fe-N}= 2.08 Å

on the states of the triazole molecules, we have built with our two-step procedure, structures with Fe-N distances between the ones for the LS and HS states. Thus, we have chosen the distances d$_{Fe-N}$= 2.5, 2.08, 2.12, 2.15 Å. Figures 5.35 and 5.36 show the total and partial density of states for these models with intermediate distances.

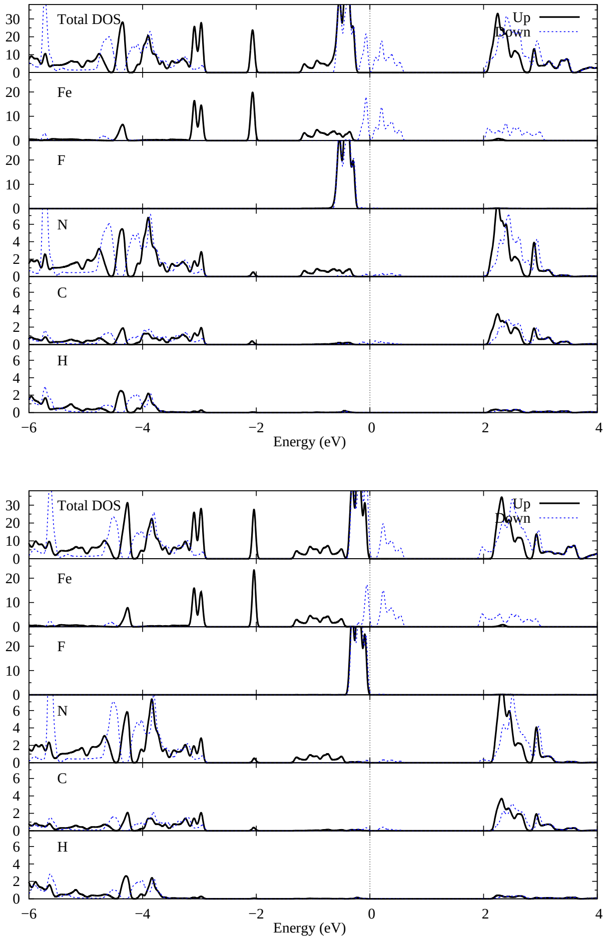

Figure 5.36: HS structures: (above) d$_{Fe-N}$= 2.12 Å, (below) d$_{Fe-N}$= 2.15 Å

The spin up and down density of states for the models with d$_{Fe-N}$= 2.05 Å and d$_{Fe-N}$= 2.08 Å (Figure 5.35) match perfectly indicating the diamagnetic character of these models. In general, the qualitative characteristics of the DOS for these compounds are rather similar to the DOS for the LS model with d$_{Fe-N}$= 2.00 Å. The DOS belonging to the models with distances d_{Fe-N}= 2.12 Å and d$_{Fe-N}$= 2.15 Å (Figure 5.36) show similar qualitative characteristics as the HS compound d$_{Fe-N}$= 2.20 Å. These compounds show also a total spin S=2 and similar reorganization of the triazole states in the transition to the HS state. In order to characterize the transition LS → HS, we have collected the Fe $3d$ contribution to the DOS from all built models in one graphic (see Fig. 5.37).

The upper part of every panel correspond to the spin up contribution, the lower part correspond to the spin down contribution. When d_{Fe-N}= 2.00 Å the compound is in the LS state, characterized by an equal distribution of Fe $3d$ spins, the t_{2g} states are fully occupied and the e_g fully empty and this situation remain so, with only a decrease in the distance between occupied and unoccupied states when increasing the Fe-N distance till d_{Fe-N}= 2.08 Å. A further increment in the Fe-N distance makes the Fe d states get closer, the t_{2g} set is moved toward the region above the Fermi level and two electrons from it jump to the upper e_g states, letting both states partially occupied and opening a gap that increases with the increasing in the Fe-N distance. The e_g spin-up subset is moved toward the region below the Fermi level. The empty e_g states still remain near the Fermi level. When going from 2.15 Å to 2.2 Å, the t_{2g} spin-down subset and the e_g spin up subset moves to ranges lower in energy in comparison to the later case. The energy gap between the t_{2g} and the e_g states is related to the magnitude of the crystal field splitting Δ which has been plotted in Figure 5.38. In it is also evident the decrease in the crystal field splitting when increasing the d_{Fe-N}, from Δ=2.66 eV when d_{Fe-N}= 2.00 Å to Δ=2.22 eV when d_{Fe-N}= 2.20 Å.

In order to find out whether the spin transition is abrupt or whether there is an intermediate state between LS and HS, we have built two more structures between the ones with Fe-N distances in the middle of d_{Fe-N}= 2.08 Å and d_{Fe-N}= 2.12 Å. A first structure with d_{Fe-N}= 2.10 Å is in the HS state with similar electronic characteristics as the other HS compounds. The second structure with d_{Fe-N}= 2.09 Å did not converge, oscillating neither in charge nor in energy, however, its spin state was showing a value near to S $\simeq$ 1.5 per Fe ion. This result indicates that the spin transition in homogeneous polymer systems is very sharp, as observed experimentally [54]. At this point we can conclude that by carefully preparing a series of model structures we have reproduced microscopically the LS-HS transition.

In order to quantify energetically the LS-HS transition, we have plotted the total energy obtained with the FP-LAPW method for every elaborated compound, Fig. 5.39. Notice that there is a discontinuous jump in the energy between the compounds with S=0 (LS) and the compounds with S=2 (HS). The relative electronic energy differences between HS

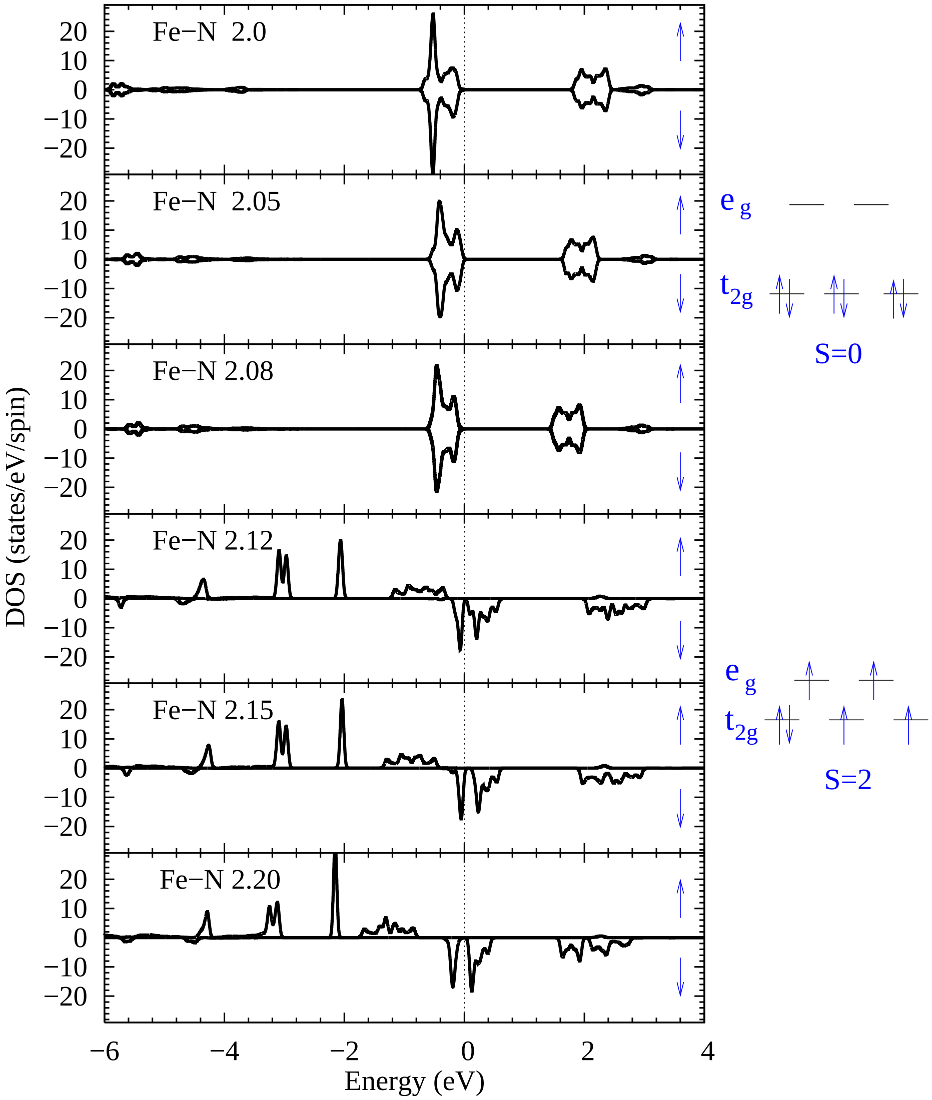

Figure 5.37: Spin resolved density of states for Fe 3*d* states for our Fe(II)-triazole model with different d_{Fe-N} distances. It is shown explicitly the spin up (upper panels) and spin down (lower panels) contributions. The first three structures in the upper part of the figure, correspond to the spin state S=0, the three last figures in the lower part correspond to the spin state S=2.

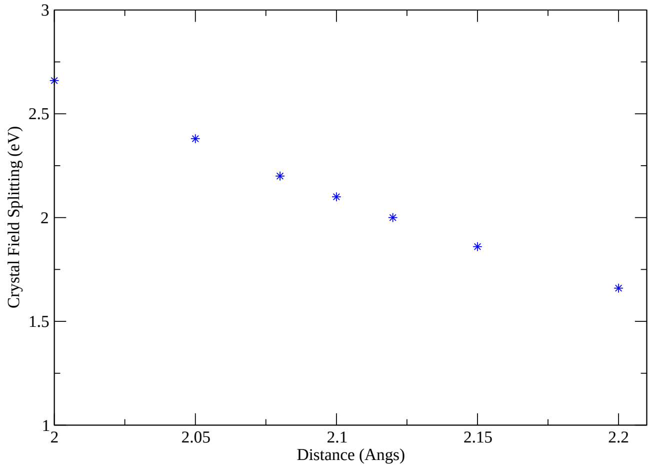

Figure 5.38: Crystal field splitting Δ *vs.* Fe-N distances.

and LS systems, given by $\frac{E^{(HS)_{el}}-E^{(LS)_{el}}}{E^{(HS)_{el}}}$ is about 10^{-5} which agrees with the relative energy estimates for spin crossover molecular systems [91]. The energy value for the compound with d_{Fe-N}= 2.09 Å was oscillating between the energies for d_{Fe-N}= 2.08 Å and d_{Fe-N}= 2.10 Å, but it is closer to the later.

Exchange interaction

Our ab initio calculations offer a unique opportunity to calculate exchange parameters otherwise inferred from fitting the eigenvalue spectrum of an appropriate spin interaction Hamiltonian to magnetization, specific heat and neutron scattering measurements. There are several ways to extract exchange parameters from the calculations. As seen for the case of CuCCP based compounds, tight-binding fitting of the bands around the Fermi level provide the hopping integrals corresponding to the interacting state Cu $d_{x^2-y^2}$ for calculating the J exchange parameter. However, in this case, every of the $3d^6$ states belonging to the one of the Fe atoms interact with the $3d^6$ states belonging to the another Fe atom in the unit cell, as a result we get a five times five matrix with the interaction values between these states. The various hopping elements t are shown in Table 5.8. In this case the NMTO method offers a unique opportunity to calculate these parameters because it allows to integrate out the other atoms degrees of freedom, which mixes with the Fe d states making not

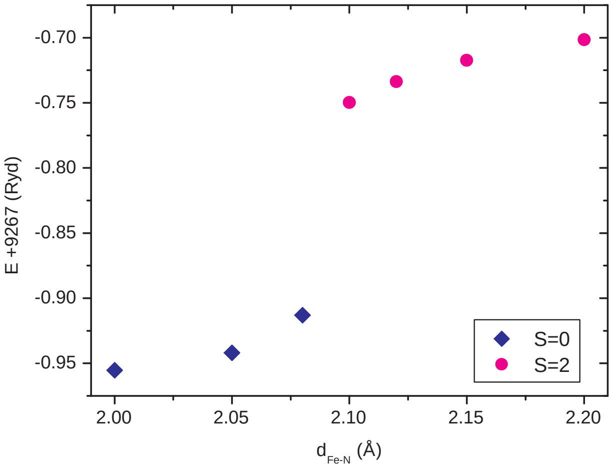

Figure 5.39: Ground state energies as function Fe-N distance, for the set of model structures obtained within GGA-sp in the FP-LAPW basis set.

possible to distinguish between Fe *d* states and the others (this situation was shown in the band structure plots). Therefore in this case, it was not possible to perform a tight-binding fitting.

In general, these hopping values range between 1 meV to 80 meV quantifying the strength of the various interaction paths between neighboring Fe *d* orbitals. In order to extract exchange parameters from our calculations we make use of total energy difference methods, which has a simple implementation in the case of a single exchange parameter. This method relies on mapping the ab initio Hamiltonian onto a spin model Hamiltonian that in our case is the Heisenberg Hamiltonian,

$$E^{TOT} = J \sum_{i=1}^{N} S_i \cdot S_j$$

which is the spin Hamiltonian between nearest neighbors Fe spins S_i. The J parameter is extracted from the ferromagnetic (FM) and antiferromagnetic (AFM) energies for two Fe ions in the unit cell of the Fe-triazole with d$_{Fe-N}$= 2.20 Å as

$$J = \frac{1}{16}(E_{FM}^{TOT} - E_{AFM}^{TOT}) \approx 2.1 meV = 24K \tag{5.2}$$

The results of our model calculations can now be compared with the magnetic properties ob-

Table 5.8: Hopping parameters obtained between the Fe $3d$ orbitals in our constructed models.

	Fe-N=2.00 Å					Fe-N=2.20 Å				
	xy	yz	$3z^2-1$	xz	x^2-y^2	xy	yz	$3z^2-1$	xz	x^2-y^2
xy	64	-45	4	38	18	-12	16	20	22	-1
yz	-45	16	-7	0	61	-16	15	-9	15	26
$3z^2-1$	4	-7	83	9	8	20	9	-48	11	0
xz	-38	0	9	56	-71	-22	15	-11	11	24
x^2-y^2	18	61	8	-71	-42	-1	-26	0	24	42
	Fe-N=2.05 Å					Fe-N=2.15 Å				
xy	27	-23	-31	31	-1	0	-12	-27	30	1
yz	18	-15	-19	-23	46	12	9	-18	-14	34
$3z^2-1$	-31	19	-61	-11	3	-27	18	-54	-9	0
xz	-31	-23	11	-37	45	-30	-14	9	-4	34
x^2-y^2	-1	-46	3	-45	-46	1	-34	0	-34	-45
	Fe-N=2.08 Å					Fe-N=2.12 Å				
xy	50	43	16	33	5	14	29	27	26	0
yz	-43	-39	-5	34	57	-29	-11	-12	22	35
$3z^2-1$	16	5	-43	1	1	27	12	-56	14	0
xz	-33	34	-1	-53	-52	-26	22	-14	-8	-34
x^2-y^2	5	-57	1	52	-29	0	-35	0	34	-46

tained on real samples of polymeric compounds. For this work, Volodymyr Pashchenko from Johann Wolfgang Goethe-Frankfurt University performed susceptibility χ measurements on the polymeric compound Fe[(hyetrz)$_3$](4-chlorophenylsulfonate)$_2\cdot$H$_2$O. In Figure 5.40 the χT has been plotted versus T. The sample shows hysteresis at T=80 K with a width of 20 K. Since this system consists of spin S=2 Fe chains with weak interchain interactions, the magnetic susceptibility have been analyzed in the frame of a spin S=2 Heisenberg chain model.

The susceptibility of an L-site chain is given by

$$\chi_L = \frac{g^2\mu_B^2}{k_B T}\frac{Tr[(\sum_{i=1}^{L} S_i^z)^2 e^{-\beta H}]}{Tr[e^{-\beta H}]} \tag{5.3}$$

where H is the Heisenberg Hamiltonian (introduced in Section 2.4), μ_B is the Bohr magneton, g is the gyromagnetic factor, k_B is the Boltzmann constant, T is temperature and S_i^z is the z-component of the spin on site i. In the thermodynamic limit, the bulk susceptibility at high temperatures can be obtained as a series expansion in $1/T$:

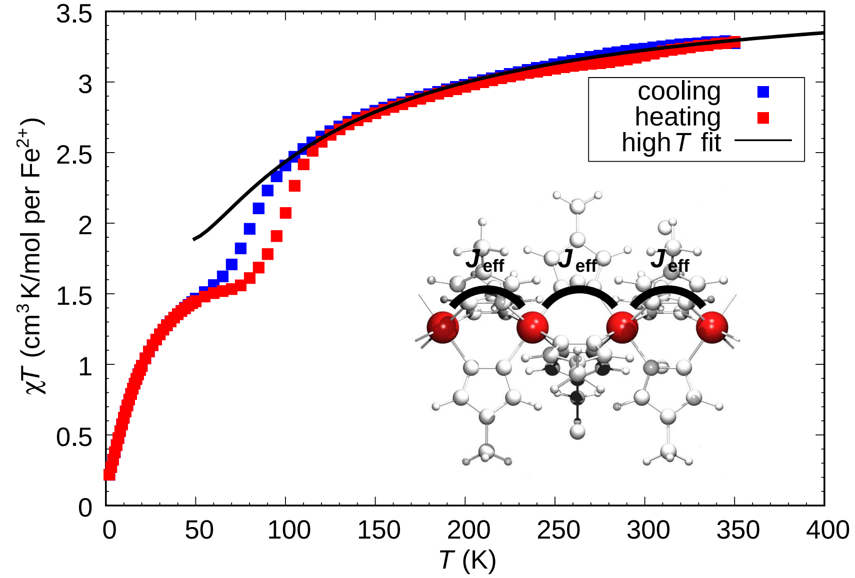

Figure 5.40: Magnetic susceptibility of Fe[(hyetrz)$_3$](4-chlorophenylsulfonate)$_2$·H$_2$O.

$$\frac{\chi J}{g^2\mu_B^2} = \frac{1}{3}[\frac{S(S+1)J}{k_BT}] - 8(\frac{J}{k_BT})^2 + 16(\frac{J}{k_BT})^3 + O((\frac{J}{k_BT})^4) \tag{5.4}$$

For $k_BT/J > S(S+1)$, Eq. 5.4 compares very well to quantum montecarlo data for spin $S = 2$ chains [120]. The fit of Eq. 5.4 to the measured susceptibility of Fig. 5.40 is best for g= 2.2 K and J= 11 K. The J values obtained from our ab initio calculations (J $\approx$ 24 K) are slightly larger than the J extracted from the susceptibility data (J= 11 K) on the real sample, but remain in the same order of magnitude. Considering that *i*) we performed the calculations in a model structure which was built with several approximations and *ii*) the experimental measurements are affected by the quality of the samples, we can conclude that the comparison is quite good and the designed structures are reliable.

An important topic is the analysis of the various energy scales that contribute to the cooperativity of the HS-LS transition in spin crossover systems. In our calculations we froze the elastic degrees of freedom and concentrated on the electronic and magnetic properties for which we have quantified the corresponding parameters. A comparison with the elastic coupling constants estimated from Ising-like models [19] (in such an approach, a material with a transition temperature of T=80 K would be described by elastic interactions of J$_{elastic}$ $\approx$ 20-30 K) shows that in one-dimensional Fe(II) triazole, the elastic coupling constants J$_{elastic}$ are of equal importance as the magnetic exchange for explaining the spin crossover transition, and the cooperativity should be understood as an interplay between elastic properties and magnetic exchange. Cooling from the HS to the LS transition, while the elastic coupling tends to drive the system to the LS state, the magnetic exchange tends to keep up the magnetic state for a larger temperature range (see Fig. 5.40). In comparison, in the heating process, the magnetic exchange is initially absent (LS) and therefore the elastic interaction initially drives the transition which has its on-set at a higher temperature than in the cooling process. The width of the transition between cooling and heating (hysteresis) is therefore enhanced by the magnetic interaction.

A fundamental difference between the polymeric systems we are dealing with in this work, and the molecular bi-, tri-, tetra-...nuclear Fe systems is the connectivity between the Fe(II) centers. While the molecular systems form isolated clusters of Fe(II) centers and therefore there is no strong connectivity between clusters, the polymers have important nearest neighbor interactions in the thermodynamic limit. This implies that for the polymers, the magnetic superexchange is not restricted to the cluster as in the molecular systems, but rather becomes important for the nature of the HS-LS phase transition. In the work of Desroches *et al.* [33] various estimates of the magnetic J for molecular systems have been given. The values range between 4-6 K. Our estimated values for the present polymers are larger, between 11-24 K and in the energy range of the elastic constants, what indicated as described above that the cooperativity in these SC systems is most likely enhanced by the exchange interactions.

5.3.3 $K_2V_3O_8$

This section is dedicated to the understanding of the ground state properties of the 2D spin 1/2 Heisenberg compound $K_2V_3O_8$, which were performed with the FP-LAPW method, which are analyzed and combined with many body methods. Our results are discussed in terms of the experimental observations and compared with the proposed mechanisms which were explained in Section 4.3.3.

Structure optimization

The calculations were done within the FP-LAPW basis set, a muffin tin radii of 2.0, 1.6 and 1.33 were use for K, V and O respectively. The convergence of the total energy was tested with respect to the k_{max} and number of k-points in the irreducible FBZ. The optimal values found were RK_{max}=7 and 99 k-points. A plane wave expansion cut off of 12 and a combination of LAPW/APW+lo basis set for the V atom were used.
For the optimization process the experimentally obtained atomic positions were used for the initial calculation and the free internal structural parameters were optimized using the calculated forces on the atoms in an iterative way. A first ab-initio calculation performed for the experimental atomic positions given in reference [40] showed big forces between the atoms, specially in the vanadyl bond, due probably to its small length. Additionally spin-polarized calculations did not converge. We have then performed optimization of the lattice parameters justified also, by a more recent determination of the atomic positions performed with neutron powder diffraction [28] which showed the sensitivity of the lattice parameters and atomic positions with temperature. The optimization was performed in two steps:

- **Unit cell optimization:** The unit cell parameters have been optimized varying the ratio c/a as a function of the energy, with both LDA and GGA in the non-spin polarized scheme. Within the LDA approximation, the minima obtained was for $c/a \sim 1.08\%$, in the GGA approximation $c/a \sim 1.3\%$ with respect to the ratio c/a from the experimental one. These results agree with the well known fact that the LDA approximation tends to underestimate the volume meanwhile GGA tends to overestimate it [23].

- **Atomic positions relaxation:** With the minima obtained when minimizing the c/a ratio we calculated and minimized the forces between the atoms. The relaxation of

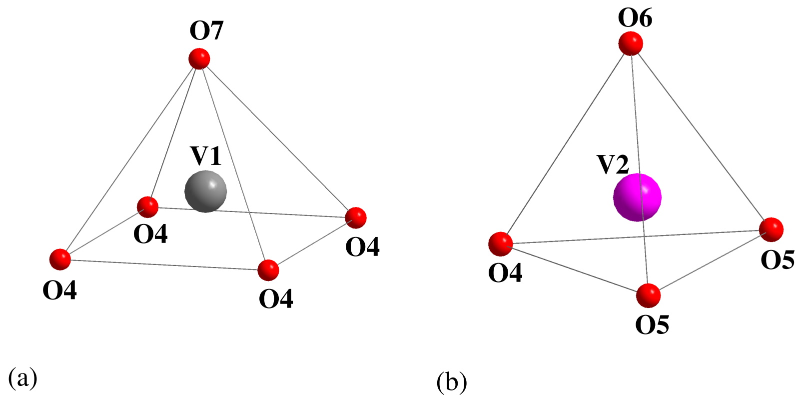

Figure 5.41: Building units of $K_2V_3O_8$. (a) VO_5-square pyramid. (b) VO_4 tetrahedra

> the O atoms was not enough, therefore it was neccesary to relax all the atoms in the unit cell. The forces were minimized with the constrain that the total energy and charge distance should be minimized also.

It is important to note that, in the search for the equilibrium positions the symmetry constrains of the space group were conserved. In the Table 5.9 are shown the experimental and obtained values for the distances and angles related with the V1-V2 environment (see Figure 5.41) in both LDA and GGA approximations. The positions obtained are showed in Appendix C.

We have obtained that the energy given by GGA approximation (E $\sim$ -18619.50078 Ryd) is lower than the one given by the LDA approximation (E $\sim$ -18569.87234 Ryd). Also, when calculating the compound in different magnetic configurations, we obtain better agreement with the experiment within the GGA approximation. Therefore, we use this approximation for our analysis in the rest of the work.

From Table 5.9 we notice that in all cases, the V1 ion is not located in the centre of the pyramid, but it is slightly displaced from the centre towards the O atom in the apical position. The displacement is smaller for the relaxed structure with the GGA approximation, which is compensated with the shortening of the distance V1-O4, which are the O atoms in the equatorial plane. In the opposite, the V-O distances for all the O atoms of the tetrahedron increases for the GGA relaxed structure in comparison with the experimental one. In summary, after the relaxation the pyramids shrink and the tetrahedras expand.

Our calculations within GGA approximation predict $K_2V_3O_8$ has a metallic character, which is opposite to the insulating trend found experimentally [97]. This is to be expected due to the inability of GGA to describe Mott insulators, as discussed in Chapter 2.

Table 5.9: Comparison between distances and angles in $K_2V_3O_8$ before and after the relaxation. The labelling of the atoms is according to Figure 5.41.

	Exp	Relaxed LDA	Relaxed GGA
Distance (Å)	Pyramid		
V_1-O_7	1.5817	1.5951	1.6103
V_1-O_4	1.9453	1.9029	1.9181
O_4-O_4	2.6508	2.6014	2.6025
O_4-O_7	2.8644	2.7783	2.8311
Angles (°)			
O_7-V_1-O_4	106.26	104.827	106.38
O_4-V_1-O_4	85.49	86.2449	85.43
Distance (Å)	Tetrahedron		
V_2-O_5	1.6278	1.6336	1.6464
V_2-O_4	1.6994	1.7251	1.7329
V_2-O_6	1.7943	1.8005	1.8126
O_6-O_4	2.8457	2.8593	2.8628
O_4-O_4	2.7839	2.8248	2.8113
Angles (°)			
O_5-V_2-O_4	110.54	110.29	111.19
O_4-V_2-O_4	108.87	109.91	108.41

In order to find the ground state, we have performed spin-polarized calculations for the compound in ferromagnetic (FM) and antiferromagnetic (AFM) configurations based on the relaxed structure. Because there are two magnetic vanadiums per unit cell, there is only one possible magnetic configuration within the unit cell , namely, one of them with spin up and the another with spin down in the AFM configuration, both spins are set up parallel to each other in the FM configuration. We have found that the AFM is the ground state with a difference in energy respect to the FM state of ~ 0.92 eV per formula unit. This result is in agreement with neutron scattering experiments [75] which show that V spins associated with the V1 sites, order antiferromagnetically at low temperature in a simple alternating nearest neighbor pattern within the 2D V-sheets. The energy for the antiferromagnetic configuration is 0.020 eV per formula unit below that of the non-spin polarized calculation, reflecting the Hund's coupling on the vanadyl V1-O1 ions. noindent The band structure for the antiferromagnetic ground state, calculated along selected high

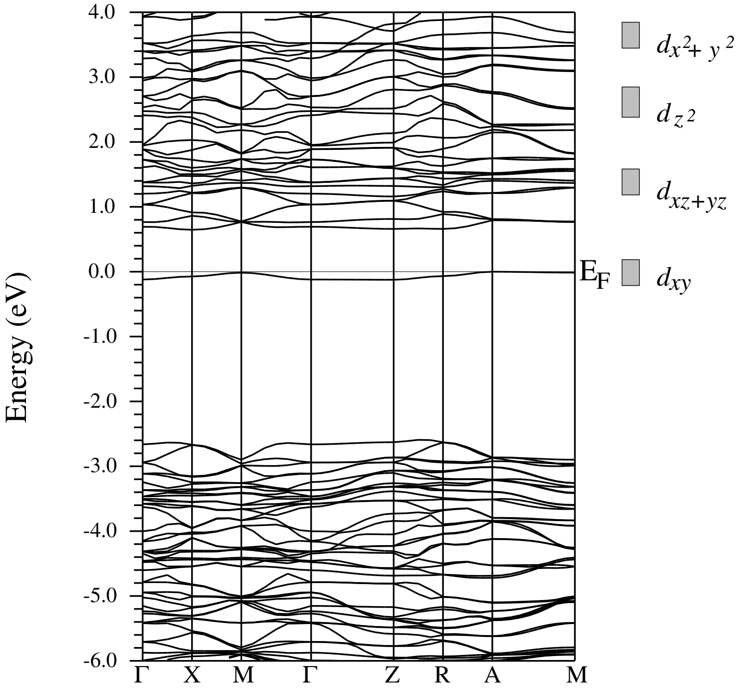

Figure 5.42: Band structure for $K_2V_3O_8$ in the AFM configuration. The bars indicate the dominant band character in the local coordina te frame of V1. The selected path correspond to Γ(0,0,0)-X(0,1/2,0)-M(1/2,1/2,0)-Γ-Z(0,0,1/2)-R(0,1/2, 1/2)-A(1/2, 1/2, 1/2)-M in units of $(\pi/a, \pi/b, \pi/c)$.

symmetry lines within the FBZ corresponding to the tetragonal lattice, is shown in Fig. 5.42. Projections of the density of states onto the V and the O LAPW spheres are shown in Fig. 5.43. Due to the scale of the oxygen contribution, they had to be drawn in a separate figure. The electronic structure shows a gap of $\sim$ 3 eV which separates a manifold of occupied O p derived bands from an occupied valence band manifold of V 3d states. The gap between the valence and the conduction bands is around 0.5 eV. There are two similar bands immediately above and under the Fermi level. These are the exchange split vanadyl majority and minority spin states which have V d_{xy} character. These are very flat bands, and show practically the same dispersion, reflecting the weak interaction of these split off states with the other orbitals. The hybridizations between V1 d and O p are mainly in the

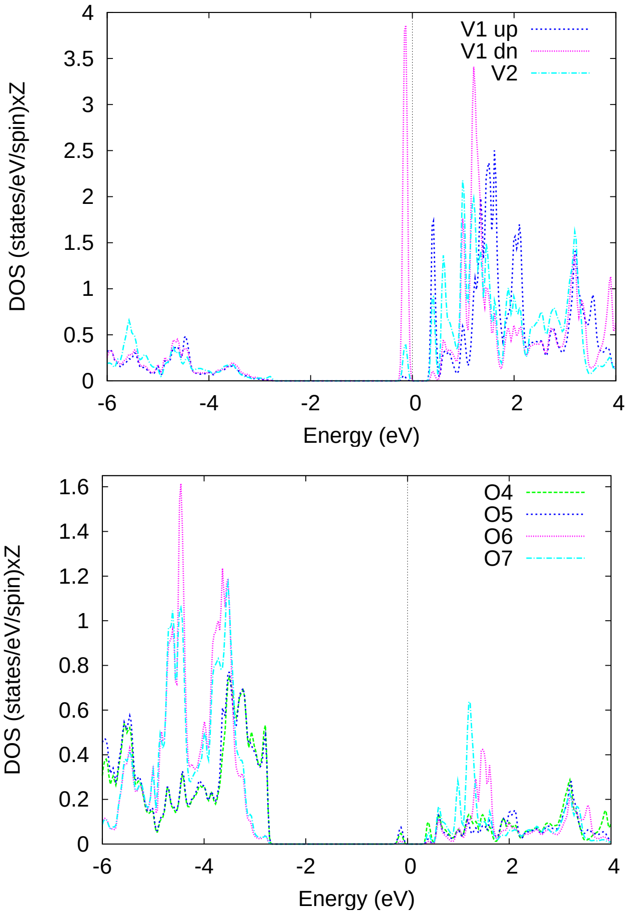

Figure 5.43: Orbital resolved DOS for the AFM configuration in the spin up channel for V atoms (above) and O atoms (below). The K contribution to the DOS in this energy range is very small and thus it have been omitted for simplicity.

conduction region, although there is a very small hybridization between these states in the band immediately under the Fermi level.

In Section 4.3.3 it was discussed the possibility of having orbital degeneracy in the V1 d states. This can be obtained from the results for the electronic properties of the compound from which we can derive the crystal field splitting of the magnetic vanadium atom. This is done by locating the V1 atom in the center of the ligand field formed by O atoms in a square pyramidal arrangement, with the vanadyl bond along the z axis and the O4 atoms in the xy plane of the reference system as shown in Figure 5.44(a).

Figure 5.44(b) shows the obtained crystal field splitting. The V^{+4} ion yields a splitting of the octahedral t_{2g} levels into a singlet (d_{xy}) and a doublet (d_{xz}, d_{yz}) and the octahedral e_g

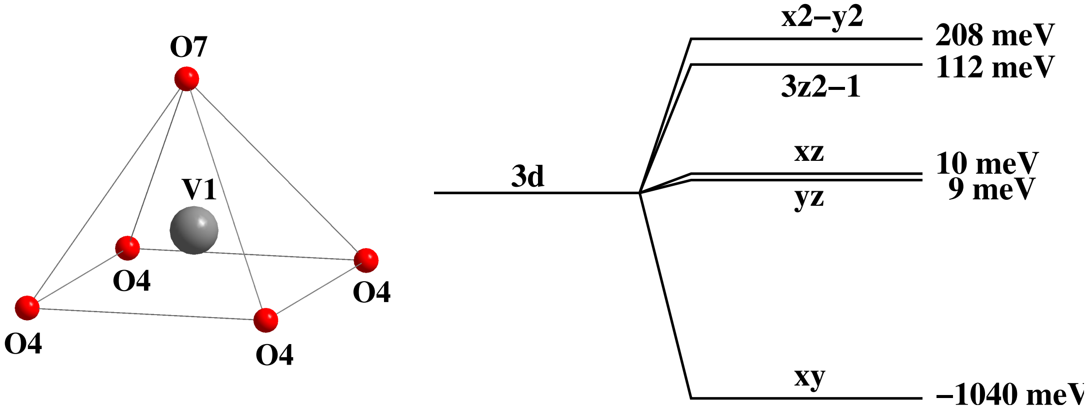

Figure 5.44: Crystal field splitting obtained from the GGA results, calculated in the local reference system of V1.

states into singlets ($d_{x^2-y^2}$ and d_{z^2}). Then the only possibility of an orbitally degenerate ground state would be the (d_{xz}, d_{yz}) doublet. In an ideal square pyramidal geometry, where the cation sits in the center of the square plane of the pyramid, this doublet is indeed the ground state. However, for $V^{4+}O_5$ square pyramids, the V^{4+} cation is significantly displaced from this square plane which lowers the energy of the d_{xy} singlet relative to that of the doublet. The d_{xy} is the ground state with a rather large splitting to the lowest excited state of approximately 1000 meV. The next unoccupied states d_{xz} and d_{yz}, have a small difference in energy of $\sim$ 1 meV, the octahedral e_g states which are much higher in energy, have a difference in energy between them of $\sim$ 96 meV. We observe then, that neither of the 3*d* orbitals are degenerate. This fact together with the large magnitude of the splitting between the ground state and the next excited state eliminates orbital effects from playing a significant role on the qualitative characteristics observed in the dispersion spectra. Therefore we rule out the possibility of the existence of a flat excitation mode generated by the mixing of the spin and orbital degrees of freedom in orbital degenerated square lattice systems, which is responsible for the double dispersion mode near to the AFM boundary in two-fold degenerated square lattices [50].

Superexchange parameters

Eliminating the second scenario proposed, we seek the possibility of additional exchange parameters in the compound. We have calculated the V1-V1 hopping terms along the directions shown in Figure 5.45. The obtained hopping values calculated within the downfolding

LMTO/NMTO method by B. Rahaman and T. Saha-Dasgupta from the S.N. Bose National Center for Basic Sciences, India, are shown in Table 5.10. The corresponding superexchange J values were calculated considering J $\sim$ 4t^2/U, with U $\sim$ 4-5 eV which are typical values for vanadyl compounds [83]. J_1 correspond to the weak ferromagnetic interaction between planes along the c direction, J_2 is the nearest neighbor interaction between V1, which is found very similar to the experimental value. The J_4 and J_3 are the second and third nearest neighbor interactions. Our calculation predict an interaction value, J_4 which have not been reported before and which, considered in the Hamiltonian of the compound, could shed some light into the controversy caused by the proposed Hamiltonian by M. D. Lumsen [75].

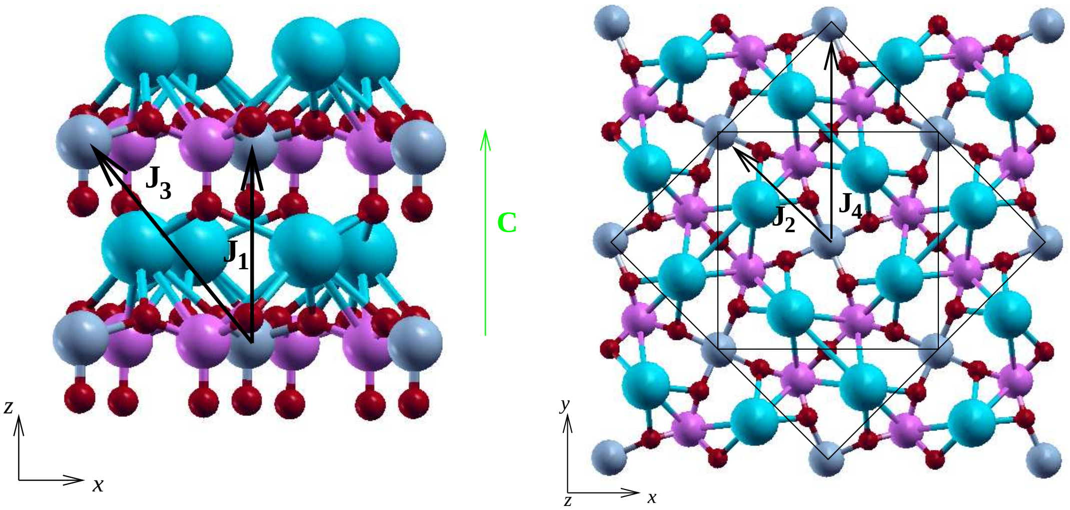

Figure 5.45: Chosen paths for the calculation of the J superexchange parameters in $K_2V_3O_8$.

Table 5.10: Comparison between the experimental and calculated hopping parameters for $K_2V_3O_8$. The label of the parameters correspond to the paths showed in Figure 5.45.

	d_{V1-V1} (Å)	Hopping t (meV)	Calculated J (K)	Experimental J (K)
J_1	5.215	3	0.079	0.040
J_2	6.272	37	12.05	12.6
J_3	8.157	0	0	-
J_4	8.870	14	1.72	-

In order to understand the obtained hopping parameters we have calculated the 3D charge density for this compound, which is shown in Figure 5.46. It has been calculated for the manyfold around the Fermi level in the GGA approximation. The charge density is concentrated in the V-O plane. There is not charge density in the K atom, and only a small quantity in the O5 atom site, which is located in the apical position of the VO_4 tetrahedra. This small charge is then responsible for the small ferromagnetic coupling between V-O planes. The charge density in the V1 site has a d_{xy} character which is perpendicular to the vanadyl bond. The fact that the occupied d orbital is in the V-O plane is also a cause for the very weak magnetic exchange along the c-direction, because there is no overlap between the occupied V1 d orbital and the O p orbitals of the O atom in the vanadyl bond. On the other hand, the d_{xy} orbital allows an obvious exchange path through the VO_4 tetrahedra to the next neighbor in the plane. The presence of a small amount of charge density in the non-magnetic vanadium site shows it plays an important role in the interaction between the magnetic vanadiums. This fact together with the charge density found in the O atoms that are within the V-O planes are responsible for the first nearest neighbors J_1 and the second nearest neighbors J_4 interactions.

Spin-orbit coupling (SO) effects

Before discussing whether the obtained second nearest neighbor superexchange interaction J, plays some significant role in the thermodynamic properties of $K_2V_3O_8$, it is mandatory to consider the spin-orbit (SO) interaction into the electronic and magnetic properties of the compound due to the presence of anisotropies manifested by Dzyaloshinskii-Moriya DM vectors.

In order to consider the DM interactions in this compound, we have to consider the projection of the crystal structure onto the tetragonal basal plane as shown in Figure 5.47. There is a plane of inversion symmetry between nearest neighbors magnetic vanadiums located along (110), represented by the dashed lines in Figure 5.47, resulting in DM vectors located in that inversion plane [85]. This gives a DM vector whose components are directed along the (110) and (001) directions which we will denote as $\mathbf{D}_{xy}$ and $\mathbf{D}_z$, respectively. The configuration of these vectors within the unit cell are shown in Figure 5.47.

In the following we will show our results on the effects of the anisotropy in the compound calculated within a density functional framework and complemented with a theoretical analysis based on a perturbative approach.

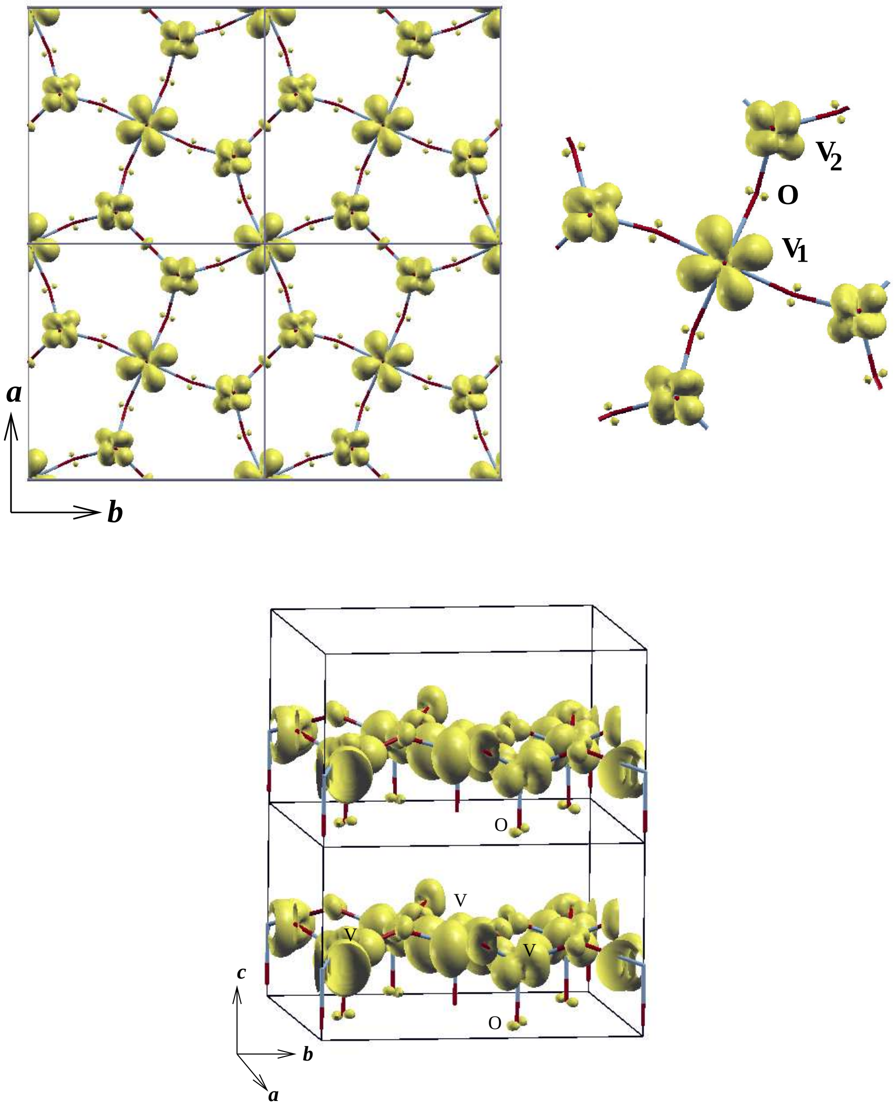

Figure 5.46: 3D charge density calculated in the GGA approximation. (above) the charge density is calculated for and isovalue ρ=0.005 $e/\text{Å}^3$, (below) the charge density is calculated with a smaller isovalue ρ=0.002 $e/\text{Å}^3$ in order to show the small charge around the O atoms which coordinate with the non-magnetic V atoms.

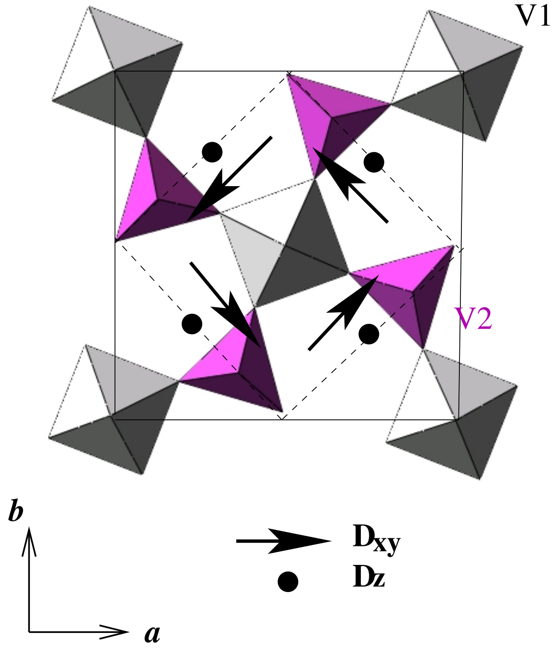

Figure 5.47: Components of the Dzyaloshinskii-Moriya vectors in the basal plane of $K_2V_3O_8$. Shown are the VO_4 square pyramids and the VO_5 tetrahedra.

SO effects studied within density functional theory

SO coupling effects are introduced in the DFT scheme as a variational effect [89]. We have applied this effect for the AFM configuration which is the ground state one, along different magnetization axis within the unit cell. The relative energies given with respect to the calculated ground state energy (Δ ENE=E-E_{AFM}), magnetic spin and orbital moments are shown in Table 5.11.

Inspection of the energy differences shows that the inclusion of so coupling with the magnetization directed along the *c*-axis lowers the energy with respect to the AFM state in 0.0011 eV, in contrast to the cases where the magnetization is directed in the basal plane of the unit cell, in which case the energy is higher. This indicates that the *c*-axis is the easy magnetization axis which agrees with experimental observations [75]. As a complementary study we can obtain with these energies the magnetocrystalline anisotropy of the system which is defined as the difference between the ground state energies due to rotation of the magnetic field (magnetization direction). Due to the relative smallness of the magnetocrystalline anisotropies, usually being in the range from a few μeV to a few meV per atom and

Table 5.11: Comparison between energies, spin and orbital magnetic moments of V1, calculated for the compound in the ground state, with and without spin-orbit coupling and on-site Coulomb repulsion U.

	Δ ENE (eV)	Spin moment (μ_B)	Orbital moment (μ_B)
AFM	0	-	-
AFM+so-c	-0.0011	0.5753	0.0169
AFM+so-ab	+0.0010	0.5571	0.0065
AFM+so-c U=2.5	0.1574	0.6311	0.0195
AFM+so-c U=3.5	0.2533	0.6637	0.0212
AFM+so-c U=4.5	0.3492	0.6944	0.0228
AFM+so-c U=5.5	0.4427	0.7214	0.0244

several orders of magnitude smaller than the total energies involved, their evaluation puts strong requirements on the accuracy of the numerical scheme involved. We have then doubled the number of k-points finding that the magnetocrystalline anisotropy changes only in 1×10^{-4} Ryd.

The energy difference $\Delta E = E[001] - E[100] = 0.51$ meV per formula unit, determines the magnetocrystalline anisotropy. In agreement with experimental results, the magnetic moments point along the crystallographic c direction perpendicular to the V-O planes [75]. We did not find any report on experimental or theoretical magnetocrystalline anisotropy for vanadium atoms so far, however it is a well known fact that LSDA calculations usually result in a semiquantitative agreement with experiment, *i.e.*, the correct order of magnitude and the correct easy axis is predicted although it tends to overestimate the value of the magnetocrystalline anisotropy [32] [81]. The table contains also the orbital magnetic moment on the V1 sites calculated for the different directions of the magnetization. The V1 orbital moment clearly shows a pronounced anisotropy, while the spin moment is nearly independent of the magnetization axis.

Figure 5.48(a) shows the band structure with the inclusion of spin-orbit effect from which we deduce that its effect is so small in this compound that is not visible in the band structure, when comparing it with respect to the one for the AFM state (Figure 5.42). However, when including the on-site Coulomb parameter within the LDA+U scheme (which was introduced in Section 2.2.2), some effects are visible as seen in Figure 5.48(b). In our calculation, we have chosen U=4.5 eV and J=0.9 eV which are typical values for Vanadium-based compounds [83].

From the figure we notice that the simultaneous inclusion of so coupling and U splits some

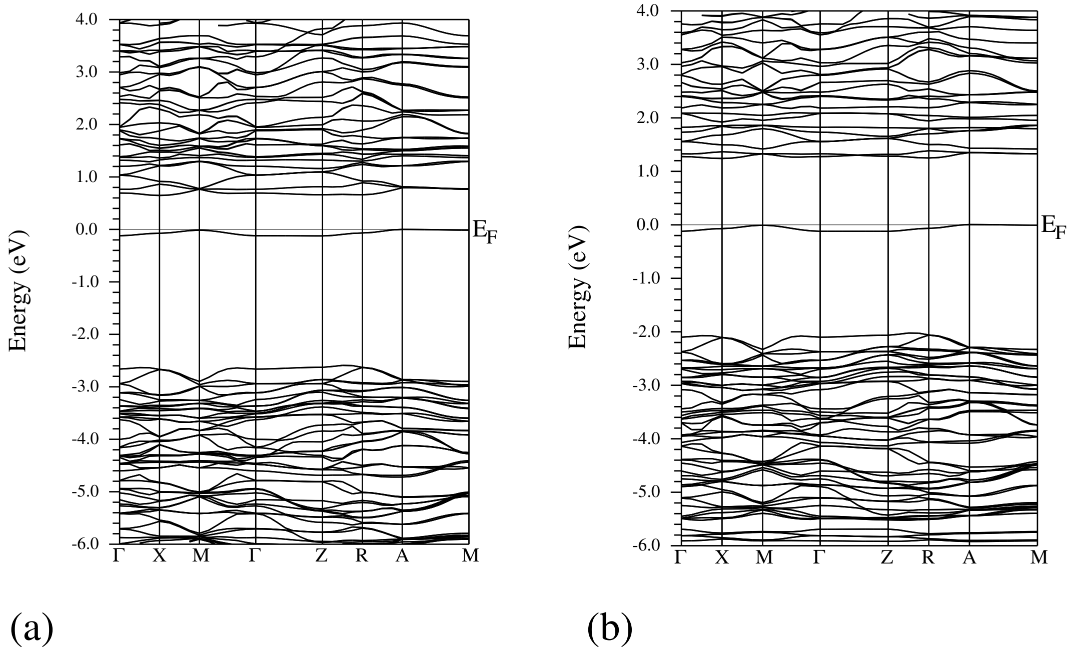

Figure 5.48: Band structure for the AFM configuration (a) with the inclusion of SO coupling along the crystallographic axis *c* and (b) with the inclusion of SO along the *c*-axis and the on-site Coulomb repulsion U (U=4.5 eV) simultaneously.

manyfolds in the band structure, but the splitting is very small, of the order of a few μeV. The main characteristic of the inclusion of the Coulomb repulsion is the broadening of the gap between the occupied and unoccupied states from 0.65 eV to 1.2 eV, which is the typical effect of the inclusion of an on-site term in the calculations.

We have also performed a systematic study of the variation of the spin and orbital moments in function of U included simultaneously with the so coupling along the *c*-axis. The results are shown in Table 5.11 for U values of 2.5, 3.5, 4.5 and 5.5 eV. The relative energies with respect to the ground state energy are also shown in Table 5.11. The increment of the energy is proporcional to the U value, which is expected because the total energy is proportional to the LDA+U potential (see Chapter 2). We have plotted the spin and orbital magnetic moments of V1 in function of U in order to see the dependency of these values with U (see Figure 5.49). The inclusion of U increases both orbital and spin moment and the increment is proporcional to the value of U. The orbital moment is increased by more than one order of magnitude which manifest the tendency of the one-site Coulomb term U of localizing the V1 $3d$ states. Because this localization, more charge is concentrated within the V1 muffin tin sphere, thus increasing the spin magnetic moment.

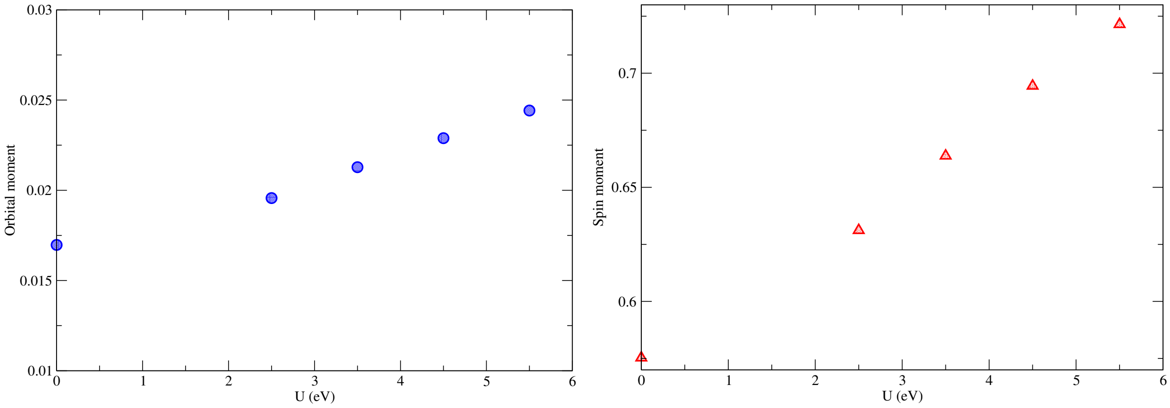

(a) (b)

Figure 5.49: Dependence of the spin and orbital magnetic moment of V1 (in units of μ_B) with U in the LDA+U calculation with inclusion of SO coupling.

Consideration of anisotropies within a perturbative approach

In order to calculate the DM vector one has to consider the spin-flop between the vanadiums along the path V1-O-V2-O-V1, for simplification we consider the interaction between V1-V1 by means of an effective t hopping between them, where the O-V2-O behaves as an atom with a hole, and this atom interacts with the V1. Therefore we consider that the hopping is between the d_{xy} electron of V^{+4} and the $2p$ orbitals of this 'pseudo-atom'. The Hamiltonian for this system, is a three-band Hubbard model in which there are two active sites in the V and one effective site between them. Every V1 atom interacts with the other by means of the V1-O-V2-O-V1 path along all x and y directions within the xy-plane (see Figure 5.45), then we consider only the spin-flop between V1-V1 along that path and no direct V-V interaction. The notation is the following: $d^{\dagger}_{i,\sigma}$ is the creation operator for spin-σ electrons in the V d_{xy} orbital on site i (i=1,2) and by $p^{\dagger}_{\sigma}$ the creation operator of spin-σ electrons in the p orbital of the 'pseudo-atom'.

The Hamiltonian is written:

$$H = H_0 + H_1 \tag{5.5}$$

$$H_0 = \epsilon_d \sum_{i\sigma} d^\dagger_{i\sigma} d_{i\sigma} + \epsilon_p \sum_{\sigma} p^\dagger_\sigma p_\sigma \sum_{\sigma} t_{dp} (d^\dagger_{1\sigma} + d^\dagger_{2\sigma}) p_\sigma + c.c.$$

$$+U \sum_i d^\dagger_{i\uparrow} d_{i\uparrow} d^\dagger_{i\downarrow} d_{i\downarrow} \tag{5.6}$$

$$H_1 = \sum_\sigma (t_\sigma d^\dagger_{1\sigma} d_{2\sigma} + t^\dagger_\sigma d^\dagger_{2\sigma} d_{1\sigma}) \tag{5.7}$$

t_{dp} denotes the charge transfer integral between the V d_{xy} and p orbitals in the bond, $t_\sigma = -t + i\sigma\lambda$ is the hopping of the electrons with spin $\sigma = \pm 1$ between the V d_{xy} orbitals in the bond. t_σ is diagonal in the spin quantum numbers because we have chosen the quantization axis for the spin to be along c, *i.e.* the main crystallographic axis. Here we have discarded the hopping between the O-V2-O.

For evaluating the D vector we have considered the process which describes a spin flip between two consecutive ions up to second order perturbation theory in H_1:

$$H^{(2)} = \langle \downarrow\uparrow | H_1 \frac{1}{H_0} H_1 | \uparrow\downarrow \rangle \tag{5.8}$$

$$| \uparrow\downarrow \rangle \equiv d^\dagger_{2\downarrow} d^\dagger_{1\uparrow} | 0 \rangle$$

$$t_\sigma = -t + i\lambda\sigma$$

In evaluating this term we obtain

$$H^{(2)} = \frac{4t^2}{H_0} + \frac{4i\lambda t}{H_0} \tag{5.9}$$

Assuming, $H_0 \sim U$,

$$Re(H^{(2)}) = J; Im(H^{(2)}) = D$$

We get an estimate of λ and D using:

$$D \sim (\Delta g / g) \, J$$

where g is the gyromagnetic ratio of the Vanadium ion and Δ g is the corresponding deviation from the free electron value. By considering the g values obtained from ESR measurements [96], experimental g=1.89, g for the free electron = 2.002319, the hopping value obtained from NMTO-downfolding t=-37 meV and the usual U value for vanadyl compounds U $\sim$ 5eV, we get: λ=2.146 meV, D=0.06264 meV = 0.058 J.

Experimentally has been determined the value $g_{ab} = 1,972$ [75],

$$\frac{D_{xy}}{J} = \frac{\Delta g}{g_{ab}} = 0,01537$$

with J= $1,0952$ meV, $D_{xy} = 0,01683$ meV and then from

$$D^2 = D_{xy}^2 + D_z^2$$

one obtain for $D_z = 0,06033$ meV.

Thermodynamic properties

In the last section we have found that the inclusion of SO coupling as a perturbation to the system allow us to obtain an estimate of the DM vectors. The value we have found agrees well with the estimate given by the experimental data [75]. Based on the argument that neutron diffraction measurements show that the magnetic unit cell contains two spins in both zero and nonzero fields, M. D. Lumsden *et al.* [75] proposed a two-spin mean field Hamiltonian based in the following,

$$H = \sum_{kl} \left\{ J_{kl} S_k \cdot S_l + D_{kl} \cdot (S_k \times S_l) + \frac{1}{2} S_k \cdot A_{kl} \cdot S_l \right\} \tag{5.10}$$

Where the first term represents the isotropic symmetric exchange, the second and third terms represent the antisymmetric ($D_{kl} = -D_{lk}$) and symmetric ($A_{kl} = A_{lk}$) anisotropies. Figure 5.50 (a) shows the spin arrangement they used, assuming a sum between spin pairs in the unit cell and then summing over four nearest neighbors and two sublattices (which are shown with different colors in the figure), they obtained the following expression:

$$H_{12} = 8JS_1S_2 + 8D_z(S_1 \times S_2)_z + 8E_zS_{1z}S_{2z} - g\mu_B H \cdot (S_1 + S_2) \tag{5.11}$$

which is the Hamiltonian for a dimer with anisotropic and antisymmetric terms. The expression $(\mathbf{S}_1 \times \mathbf{S}_2)_z$ is the z component of the vector cross product. By diagonalizing this two-spin Hamiltonian and using the expressions for the susceptibility per spin:

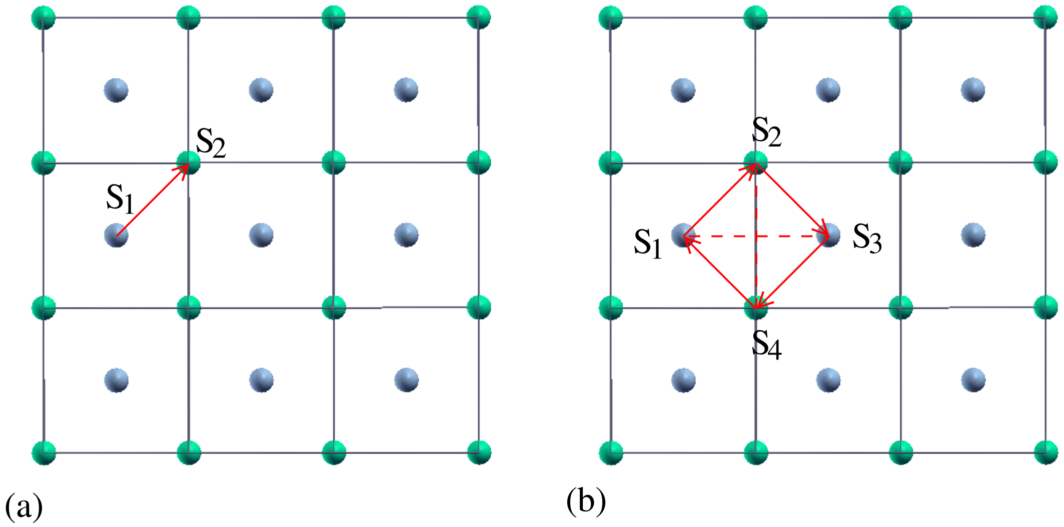

Figure 5.50: Schematic representation of the different spin configurations studied in (a) reference [75] and (b) our model. The spheres represent the magnetic vanadium atoms with different spins (represented by different colors)

$$\chi = \frac{\mu_B^2 g^2}{kT}[\langle(S^z)^2\rangle - \langle S^z\rangle^2] \tag{5.12}$$

(μ_B^2 and k denote the Bohr magneton and the Boltzmann constant respectively) where

$$\langle S^z\rangle = \frac{\sum_i S_i^z e^{-\beta E_i}}{\sum_i e^{-\beta E_i}} \tag{5.13}$$

where E_i are the eigenvalues obtained from the diagonalization of the Hamiltonian 5.11. The magnetic specific heat is determined as,

$$C_m = \frac{N_A k}{T^2}[\langle(E)^2\rangle - \langle E\rangle^2] \tag{5.14}$$

With these expressions we have then calculated the susceptibility and specific heat of the system based on the proposed Hamiltonian Eq. 5.11. But this Hamiltonian fails to fit the experimental observations as shown in Figure 5.51. In that figure we have also included other spin lattice models as an isolated dimer and a two-dimensional lattice. Notice that these two last models give even better agreement with the experimental observations than the proposed model from reference [75]. The fact that the 2D curve does not fit the experimental observations comes from the size effects that are significant in two dimensions.

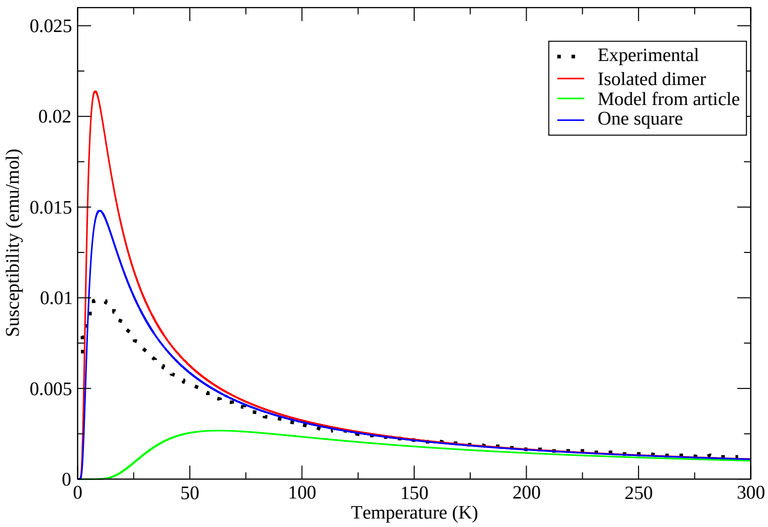

Figure 5.51: Comparison between the proposed model [75], an isolated dimer and a square lattice models with the experimental data.

Aditionally, G. Liu and J. E. Greedan [73] made susceptibility measurements for different members of the fresonite family. They fitted the experimental susceptibility to a linear chain, dimer and 2D system, concluding that only the last one give better agreement with the experimental observations. We have therefore, rewritten the Hamiltonian 5.10, taking into account a spin configuration as the one shown in Figure 5.50 (b), in which the vectors D_{xy} cancel out. Additionally, this spin configuration allow us to include the extra superexchange parameter between second nearest neighbors we found from our ab initio calculations, as the diagonals of the square lattice formed by the spins. This configuration gives better agreement with the experimental observations. Before showing our results, we would like to discuss an important issue namely, the finite size effects. This 2D spin configuration is significantly affected by finite size effects and by periodic boundary conditions. We had increased the number of lattices from one (with four spins) to four lattices in a leg arrangement (with four spins) to four lattices every one connected to other four lattices in a periodic arrangement, with and without the diagonal terms in the square lattice. These two last calculations were done by Dr. Yuzhong Zhang from the Institut for theoretical physics, JWG-Frankfurt University, with exact diagonalization techniques. Our results are summarized in Figures 5.52 and 5.53

Figure 5.52 shows the results for the comparison of finite size without DM interaction between N=1 × 4 which is a 4-site chain with a 4-site loop and N=4 × 4 which is a 4-leg

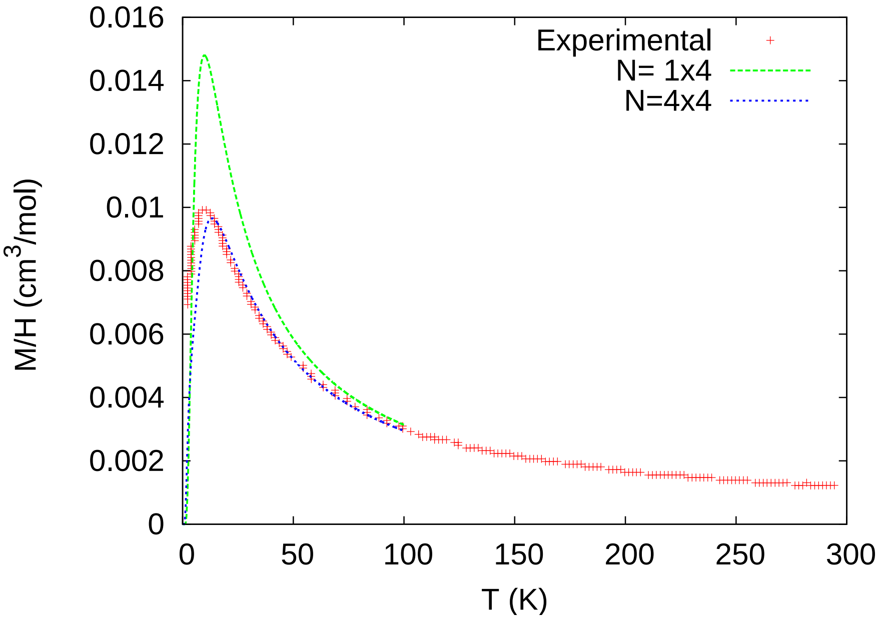

Figure 5.52: Susceptibility per site calculated with exact diagonalization for two different lattice sizes.

ladder with periodic boundary conditions and 4 sites per leg. For the 4-site spin system it was necessary to diagonalize a 16 × 16 matrix. These plots were generated for the experimental superexchange value J $\sim$ 12.6 K. It shows that an increase of the lattice size produce results that are much closer to the experimental value.

Figure 5.53 shows the susceptibility per spin for the case with (labelled frustrated) and without (labelled non-frustrated) the diagonal term. Because this diagonal exchange J_4 term is very small in comparison to the nearest neighbor term J_1, $J_4/J_1 \sim 0.14$ its effect on the characteristics of the susceptibility are very small, however it is evident that the extra term tends to shift the susceptibility curve to the left of the graphic.

At this point it is important to note down that we did not have direct access to the experimental data. We picked up the experimental points directly from the figures shown in reference [29] for the susceptibility and from reference [101] for the magnetic specific heat, therefore these experimental data are subject to inaccuracies. Our results show that the susceptibility is not very sensible to the size effects and presence or absence of extra terms in the Hamiltonian. We have also calculated the magnetic specific heat which is shown in Figure 5.54. The magnetic specific heat has been calculated for different size clusters, with

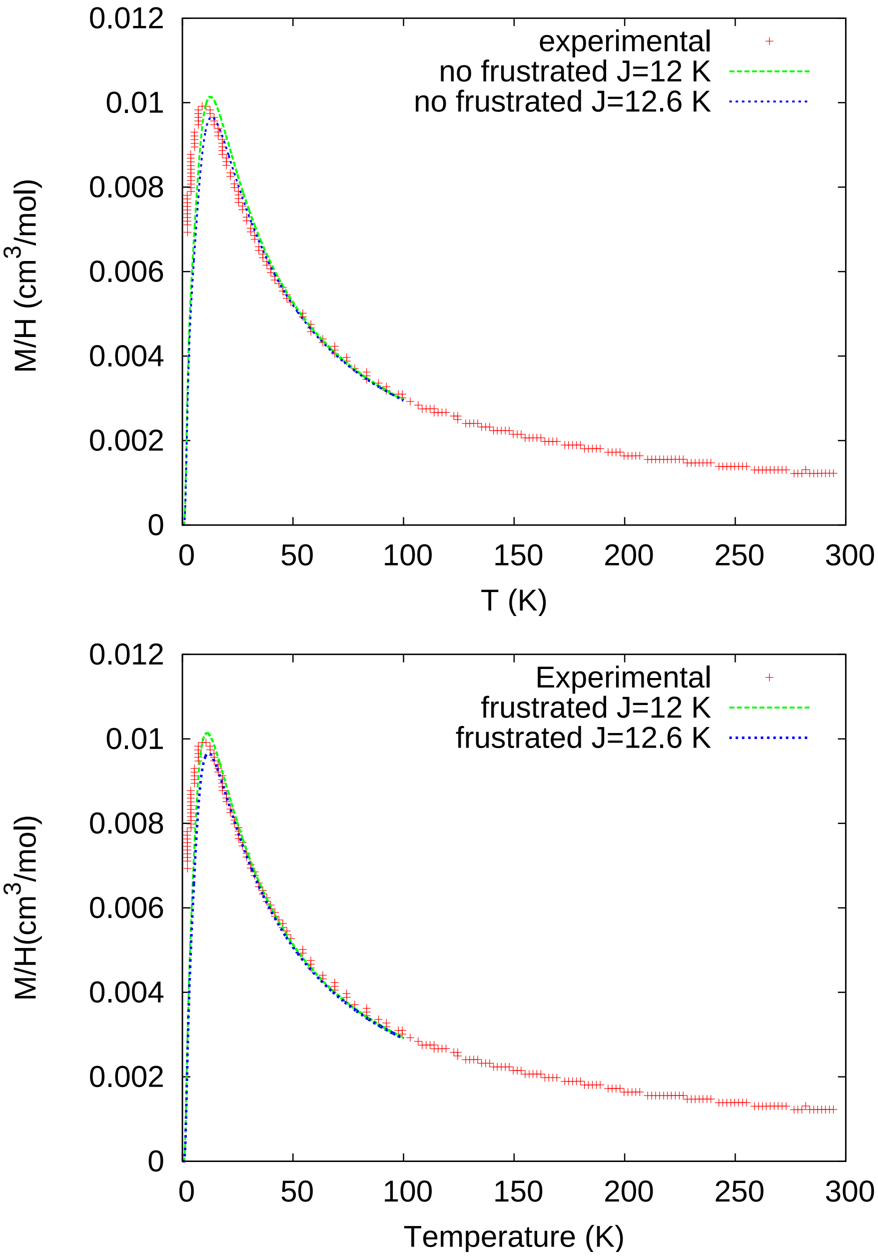

Figure 5.53: Susceptibility per spin calculated for the 2D square lattice without (upper panel) and with (lower panel) the extra superexchange term.

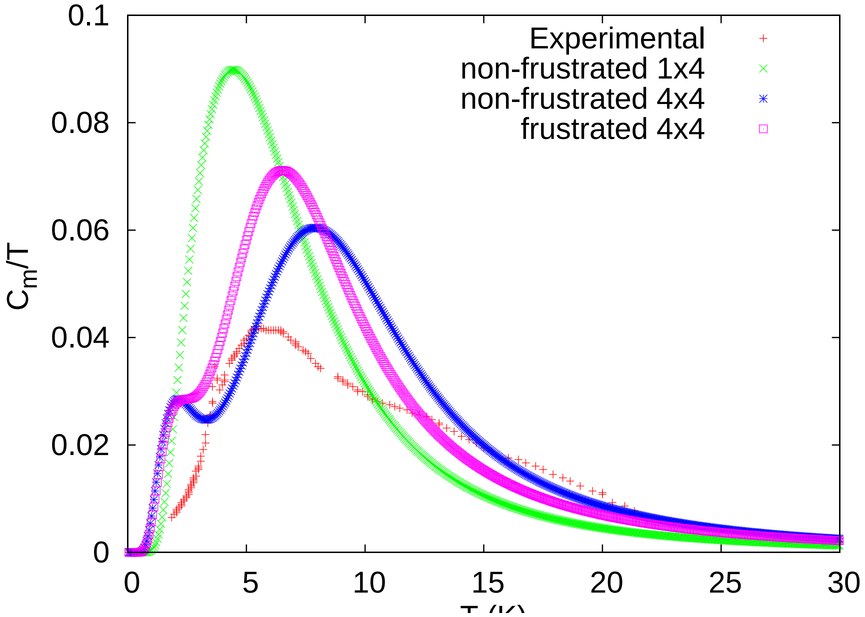

Figure 5.54: Comparison between theoretical and experimental specific heat results given in reference [101].

and without the J_4 term. Here the size effects and the effects of the introduction of extra terms are more evident. Increasing the cluster size reduces considerably the curve, also increasing the number of points shows characteristics like the extra peak located at around 3 K. The effect of the second nearest neighbor parameter is also to shift the curve to lower T values, however the small peak is located at the same positions in both cases.

None of the calculated curves fit the experimental results. In this case is much more difficult to obtain agreement between theory and experiment due to many reasons, namely, the way the data is obtained (experimentally, the magnetic contribution to the specific heat is not calculated directly. Instead, it is estimated by substracting a Debye lattice contribution from the total heat capacity) and experimental errors in the measurements which are taken into account when plotting these curves. Because we did not count with the experimental data we are not aware of the factor the experimentalists used for obtaining that curve and how they substracted the phonon contribution from the specific heat. However, characteristics like the position of the main peak and the extra small peak at low temperature are reproduced theoretically, specially for the case with the extra exchange parameter, giving an indication that it should be present in order to describe the ground state properties of this compound.

Further investigations in this field should consider exact diagonalization with bigger number of sites or Quantum Montecarlo calculations with our proposed model.

Chapter 6

Summary and Outlook

The theoretical characterization of low dimensional materials is a very rich and broad field. Ground state properties of materials are strongly influenced by the dimensionality and geometry of the network, as well as the environment in which its components, atoms or molecules are immersed. In this work, we have studied compounds with different dimensionalities, namely, zero-, one- and two-dimensional compounds which offer the opportunity to investigate the different magnetic phenomena associated to them. All studied compounds have in common that they contain transition metal ions and behave as Mott insulators, in which correlation effects are important, and that the exchange interaction J between the magnetic ions are relatively small, on the order of few eV. Due to the smallness of the coupling constants, those kind of systems are of particular interest as the application of moderate magnetic fields or pressure can drive the system into a phase transition.

In low dimensional structures the study of materials composed by metal ions bridged by organic linkers materials is a challenging problem. These materials are characterized by having a very low symmetry and a large number of atoms per unit cell, making their study computationally very demanding and hence previously limited to semiempirical approaches. We elaborated a novel stepwise approach in order to study complicated metal-organic materials and demonstrated that it is an effective procedure to obtain reliable structures for subsequent accurate quantum mechanical analyses. We note that an exclusive use of only one approach, namely ab initio molecular dynamics or FP-LAPW method, is very time-consuming while the combination of classical and quantum approaches speeds up the relaxation process considerably. We first employ a classical force field to create and relax plausible initial structures. In the second step, we proceed with ab initio molecular dynamics to relax these structures towards a stable configuration. Finally we extract the electronic properties with precise FP-LAPW methods which are combined with schemes such as the LMTO/NMTO method. Our calculations have shown that the combination of methods presented in this work is an efficient means to study properties of complex systems and that prescription employed in the present study provides a plausible route to manipulate properties related to general low-dimensional quantum spin systems.

In the search for low dimensional quantum spin systems with tunable properties, we shown that hydroquinone based materials offer, among others, the possibility to replace or modify constituents of the parent compound in a straightforward manner. We have chosen two members of a family of hydroquinone-based compounds, namely CuCCP and TK91, in order to study its ground state properties and the influence of substitutions and the dimensionality in these compounds. We have proposed and analyzed various chemical modifications to the Cu-based polymeric coordination compound CuCCP. Our goal has been to tune, in a controlled way, the magnetic interactions between Cu centers and to test the efficiency and feasibility of the combination of methods proposed here. We pursued two ways of modifying the original CuCCP structure: *i*) by changing the substitution pattern in the linker (hydroquinone) and 2) adding ligands to the system. Following the first scheme we considered two possible H substutions in the hydroquinone ring, namely an electron donating group (NH_2) and an electron withdrawing group (CN). For the second scheme, we considered structures with H_2O and NH_3 ligands. From our study we conclude that NH_2 substitution in the hydroquinone is the most effective means to enhance the intra-chain Cu-Cu interaction in CuCCP, while the CN substitution induces and enhances the inter-chain interactions in the system which are either absent or very weak in the original CuCCP compound. In contrast, the inclusion of H_2O and NH_3 ligands has the effect of isolating the Cu ions. The effects observed in this study are very small, mainly due to weak coupling constants in these kind of metal-organic materials.

We have shown that the compound known as TK91 behaves as a weakly-coupled two-dimensional spin 1/2 dimer system, with the strongest Cu-Cu interaction located along the polymeric hydroquinone-based chains and a weak interaction along the *c*-axis. The dimer unity is not such one formed by the nearest Cu-Cu atoms in the unit cell but the one formed by the Cu ions bridged by the hydroquinone linker and separated by a distance of about 8 Å. We showed that the microscopic parameters derived by our calculations are at the same order of magnitude as the ones obtained by fitting the experimental curves of

susceptibility and specific heat at zero magnetic field. Analysis of the electronic properties for this compound reveals the presence of a dd δ bonding contained in the plane of the O-Cu-N atoms within the chain, which concentrates the interaction between coppers along the polymeric chain. These characteristics together with a gap in the excitation spectra, make this compound one possible candidate for studies of quantum critical phenomena. At the time this thesis was being completed, a magnetic field induced Bose-Einstein condensation of magnons or a Kosterlitz-Thouless scenario were being discussed for this compound. However more experimental studies are necessary to confirm or reject these hypothesis. Presently, many experimental efforts are directed to this goal.
In general the hydroquinone molecule tends to strongly influence the magnetic interaction between the metal centers, keeping moderate values of the interaction between the metal centers and fixing the direction of the strongest interaction to the one influenced directly by this molecule.

The $Cu_4OCl_6daca_4$ system is comprised of very interesting magnetic units formed by Cu ions arranged in a tetrahedral way. Our calculations show that it is formed by an almost isolated Cu^{2+} S=1/2 tetrahedron. The unpaired electron is only partially localized in the Cu *d* states, transferred to the oxygen atom in the center of the tetrahedron and is then further delocalized around atomic cores within the molecule. Different scenarios were proposed in the literature, in an attempt to explain the anomalous behavior of the effective magnetic moment which has been observed experimentally. Our findings reject these previous scenarios, where the compound was considered as a valence mixed system as well as described by an isotropic Heisenberg model with large anisotropy and orbital degeneracy. Due to the geometry of the cluster, two exchange paths are possible, both antiferromagnetic Cu-O-Cu via the central oxygen atom and ferromagnetic Cu-Cl-Cu via the peripheral chlorine atoms. This, together with the fact that measurements of the bulk properties reveal that apparently there exists a very weak AFM inter-tetrahedral exchange between AFM/FM clusters, has lead us to propose a model which includes AFM/FM and very weak AFM inter-cluster correlations. Our DFT calculations of ferro- or antiferromagnetic intra-cluster interactions turned out to be quite unstable with respect to the sign of J, which is a sign of the highly frustrated behavior of the compound. The magnetic frustration together with the poor sample quality and the anisotropic sample growth make difficult to confirm or reject this scenario theoretically and experimentally. At the preparation of this thesis, additional experimental efforts were directed to obtain higher quality crystals and to study the interplay between electron delocalization and magnetic interaction in more detail.

In the case of Fe(II)-triazole, we have shown that by carefully preparing a series of model structures, we had successfully simulated the spin transition from LS to HS. This turned out to be an abrupt transition in the models structures we have elaborated. An advantage in these models is that the basic units of in this family of polymers are used for the calculations, while the usually varying counterions are replaced by small units that keep the unit cell neutral. Our calculations can therefore be extrapolated to any polymeric material. In our calculations the elastic degrees of freedom were frozen and we concentrated on the electronic and magnetic properties for which we quantified the corresponding parameters. We have shown that the magnetic interactions play an important role in the microscopic mechanism of the spin transition providing a new interpretation about the origin of the parameters underlying traditional theoretical approaches for polymeric spin-crossover materials. A next step in future investigations should concern the inclusion of lattice dynamics (phonons) in the ab initio calculations.

In the case of $K_2V_3O_8$ compound, we have shown that in order to obtain the correct ground state it is necessary to relax the forces between the structures, as it was shown in the case of the metal-organic compounds. However, in this case we did not need the two step procedure because the compound has a high symmetry and low number of atoms per unit cell. Although there are anisotropies present in the system they are small, and only influence the properties of the compounds when applying magnetic fields, as has been observed experimentally. Our calculations show that the system is well described by an antiferromagnetic 2D square lattice Heisenberg Hamiltonian with a nearest neighbor interaction of J $\sim$ 12 K and diagonal superexchange terms of J' $\sim$ 1.7 K. This last term has not been predicted or observed previously but it influences considerably the ground state properties, as shown by our calculations of susceptibility and specific heat and give better agreement with the experimental observations when including the diagonal terms. We have thus presented a new approach which provide an improved treatment of the ground state properties for this compound and rejects the scenarios of orbital degeneracy and two-spin models.

The present work shows that, in general, low dimensional materials composed of transition metal oxides with small exchange parameter comprise an extremely interesting class of materials due to the rich variety of magnetic phenomena they exhibit. Their lattice and electronic (orbital, charge and spin) degrees of freedom are coupled by effective interactions (electron-phonon coupling, hopping t, Coulomb repulsion U and Hund's rule coupling J) and, when some of these are of similar magnitude, competing phases may exist. We studied different representatives of these materials to examine how the interplay between these energy scales determines the ground state properties or different phenomena when applying a external perturbation and how these energy scales can be changed by introducing substitutions or changing the coordination of the metal center. Due to the different energy scales involved, we have shown that to correctly and completely describe these microscopic mechanisms it is necessary to combine different approaches, namely at the ab initio level, classical and quantum mechanical methods, as well as ab initio methods together with effective Hamiltonians. In doing so, we have managed not only to describe the structural, magnetic and electronic properties of these compounds but also to predict new structures. This can then provide a guide for synthesis in the laboratory and to design materials which exhibit novel microscopic behavior. Using the present results, further work could proceed along these lines: following our two-step approach, to study the effect of pressure and to perform further substitutions in hydroquinone-based compounds and to study the effect of electron-phonon coupling on Fe(II)-triazole compounds. In the case of $Cu_4OCl_6daca_4$, further studies at the theoretical level should consider different magnetic configurations in the tetrahedra within one unit cell and the influence of quantum fluctuations and molecular vibrations on the magnetic behavior at low temperatures. This should be followed by experimental efforts concerning the synthesis of improved samples. Additionally an experimental study of the interplay between electron delocalization and magnetic interactions our calculations have predicted is required. When this thesis was in preparation, there were already controversies regarding the zero-dimensional character of the compound and was identified as a molecular magnet. Further work we have elaborated on this issue reject this model [39]. Further progress in the understanding of the magnetic properties of $K_2V_3O_8$ should study the magnon dispersion relation with the proposed Hamiltonian and consider the role of the small weights found in the non-magnetic V positions on the spectra in our calculations.

Appendix A

Atomic coordinates for the relaxed CuCCP-based structures

Table A.1: Fractional atomic coordinates of nonequivalent atoms in the CuCCP relaxed structure. For the lattice parameters, see Table 5.2

Atom	x	y	z
Cu	0.50000000	0.50000000	0.50000000
O2	0.45807085	0.34945590	0.61867100
C3	0.47453250	0.42427727	0.79976209
C4	0.66964239	0.58689132	0.92934831
C5	0.03307743	0.77291193	0.67969033
C6	0.22055285	0.84552796	0.83633834
C7	0.10236956	0.77948528	0.94972154
C8	0.69708703	0.66146833	0.12029633
N9	0.85763836	0.67389511	0.86095005
N10	0.81088455	0.66923587	0.69559172
H11	0.17321893	0.79227770	0.08154772
H12	0.41931318	0.93171559	0.86071647
H13	0.04560064	0.78754151	0.55485514
H14	0.84710562	0.79189166	0.21212560

Table A.2: Fractional atomic positions of nonequivalent atoms in Cu(II)-NH_2 obtained after relaxation.

Atom	x	y	z
Cu	0.50000000	0.50000000	0.50000000
O	0.45952338	0.34384463	0.62047714
N1	0.87129861	0.67649196	0.85703667
N2	0.81592808	0.67403219	0.69273582
N3	0.89342131	0.81953377	0.25313235
C1	0.48379900	0.42607948	0.80332348
C2	0.68236558	0.58873536	0.92870320
C3	0.03998649	0.76736537	0.66677421
C4	0.23751744	0.83563448	0.81694695
C5	0.12514376	0.77281287	0.93447831
C6	0.70113966	0.66249861	0.12137891
H1	0.20669437	0.78002257	0.06146726
H2	0.43843580	0.91660682	0.83522646
H3	0.04936408	0.77481595	0.53807198
H4	0.82019516	0.86915420	0.37967013
H5	0.94873662	0.93065156	0.22239484

Table A.3: Fractional atomic positions of nonequivalent atoms in Cu(II)-CN obtained with the PAW method. For the lattice parameters, see Table 5.2 (same as CuCCP).

Atom	x	y	z
Cu	0.50000000	0.50000000	0.50000000
O2	0.45586047	0.34601917	0.61954812
C3	0.48225645	0.42521098	0.79980648
C4	0.67945058	0.58805578	0.92534823
C5	0.03840246	0.75931280	0.66201665
C6	0.23489475	0.83140998	0.81391636
C7	0.12391950	0.76942719	0.93099867
C8	0.69442255	0.66012194	0.11819527
C9	0.10296089	0.18115566	0.75982224
N10	0.86871330	0.67385342	0.85532789
N11	0.81516655	0.66763181	0.68801486
N12	0.91623888	0.05749851	0.67879026
H13	0.21036322	0.77929926	0.05704328
H14	0.43529131	0.91345668	0.83230517
H15	0.04931745	0.76810831	0.53464886

Table A.4: Fractional atomic positions of nonequivalent atoms in Cu(II)-H_2O obtained after relaxation. For the lattice parameters, see Table 5.2.

Atom	x	y	z
Cu	0.50000000	0.50000000	0.50000000
O1	0.54548630	0.39146013	0.61449576
O2	0.11104809	0.50997119	0.71612732
C1	0.50846703	0.44754970	0.80067207
C2	0.68032852	0.61183880	0.90724635
C3	0.05894527	0.84496851	0.61704992
C4	0.26950758	0.95163087	0.75697623
C5	0.15279255	0.87395244	0.88376263
C6	0.32801067	0.33993413	0.89980571
N1	0.88662263	0.72926141	0.81944391
N2	0.82847386	0.71119262	0.65595860
H1	0.23644016	0.90962503	0.01364916
H2	0.47761970	0.07047826	0.76570604
H3	0.05611367	0.85699006	0.49132676
H4	0.20991897	0.21421176	0.81558567
H5	0.02924495	0.44665601	0.79637256
H6	0.92725690	0.45505960	0.64249638

Table A.5: Fractional atomic positions of nonequivalent atoms in Cu(II)-NH_3 obtained with the PAW method. For the lattice parameters, see Table 5.2.

Atom	x	y	z
Cu	0.50000000	0.50000000	0.50000000
O2	0.46792628	0.37997535	0.62845458
C3	0.47857169	0.44435792	0.80643875
C4	0.67614669	0.61476778	0.91027186
C5	0.08811637	0.85402562	0.62829276
C6	0.28665702	0.97094387	0.77525302
C7	0.15203987	0.89487447	0.90229372
C8	0.69320820	0.66296774	0.09556227
N9	0.88608232	0.73995911	0.83090719
N10	0.84894377	0.71586082	0.66309812
H11	0.22284424	0.94017554	0.03735531
H12	0.49773965	0.09575630	0.78918445
H13	0.09716036	0.86012825	0.49969803
H14	0.83131748	0.79172500	0.17927696
N15	0.85868062	0.47014482	0.31230695
H16	0.76116972	0.35073628	0.28122641
H17	0.07885375	0.54072073	0.36734836
H18	0.90882562	0.48724318	0.19073394

Appendix B

Atomic coordinates for the obtained Fe[CH_3trz] structures

Table B.1: Fractional atomic positions of nonequivalent atoms for Fe-N distance 2.0 Å

Atom	x	y	z
Fe	0.50000000	0.50000000	0.50000000
F2	0.30651000	0.10168000	0.75000000
F3	0.93868000	0.32793000	0.75000000
N4	0.16504000	0.54583000	0.75000000
N5	0.62375000	0.21212000	0.75000000
N6	0.71102000	0.74188000	0.75000000
N7	0.35221000	0.52030000	0.65648000
N8	0.55467000	0.37294000	0.65653000
N9	0.59314000	0.60672000	0.65648000
C10	0.03247000	0.56372000	0.75000000
C11	0.67265000	0.09819000	0.75000000
C12	0.79450000	0.83758000	0.75000000
C13	0.23924000	0.53568000	0.60529000
C14	0.59632000	0.27586000	0.60517000
C15	0.66428000	0.68827000	0.60512000
H16	0.01352000	0.65232000	0.75000000
H17	0.59792000	0.03915000	0.75000000
H18	0.88791000	0.80811000	0.75000000
H19	0.99298000	0.52586000	0.63066000
H20	0.72817000	0.08549000	0.63125000
H21	0.77855000	0.88755000	0.63004000
H22	0.20647000	0.54127000	0.46751000
H23	0.68504000	0.71300000	0.46776000
H24	0.60842000	0.25000000	0.46615000

Table B.2: Fractional atomic positions of nonequivalent atoms for Fe-N distance 2.05 Å

Atom	x	y	z
Fe	0.50000000	0.50000000	0.50000000
F2	0.33132219	0.14087842	0.75000000
F3	0.88654614	0.37046367	0.75000000
N4	0.16518442	0.55712575	0.75000000
N5	0.62244295	0.20908205	0.75000000
N6	0.70705792	0.74724140	0.75000000
N7	0.34962994	0.52065997	0.65791993
N8	0.55561998	0.37064997	0.65796997
N9	0.59475995	0.60864996	0.65791993
C10	0.03537249	0.58303297	0.75000000
C11	0.65670021	0.09242721	0.75000000
C12	0.79093894	0.84131033	0.75000000
C13	0.23680430	0.54368581	0.60351494
C14	0.59601539	0.27229390	0.60622714
C15	0.66286124	0.69378071	0.60361488
H16	0.02299063	0.67390614	0.75000000
H17	0.57272218	0.04210771	0.75000000
H18	0.88551913	0.81098879	0.75000000
H19	0.99320883	0.54509254	0.63214722
H20	0.71127636	0.07527682	0.63004305
H21	0.77500994	0.88997817	0.62765063
H22	0.20317540	0.55910591	0.46488643
H23	0.67628193	0.72534100	0.46594206
H24	0.60689064	0.24497966	0.46888530

Table B.3: Fractional atomic positions of nonequivalent atoms for Fe-N distance 2.08 Å

Atom	x	y	z
Fe	0.50000000	0.50000000	0.50000000
F2	0.32569604	0.12482324	0.75000000
F3	0.90597412	0.35422893	0.75000000
N4	0.16337365	0.55327077	0.75000000
N5	0.62456975	0.20895069	0.75000000
N6	0.70882924	0.74717243	0.75000000
N7	0.34810995	0.52086995	0.65876991
N8	0.55617997	0.36929000	0.65882001
N9	0.59571997	0.60978997	0.65875999
C10	0.03296893	0.57384732	0.75000000
C11	0.66253189	0.09355855	0.75000000
C12	0.79263805	0.84090629	0.75000000
C13	0.23529819	0.54151314	0.60544464
C14	0.59756124	0.27166537	0.60752142
C15	0.66424277	0.69413955	0.60527798
H16	0.01613958	0.66369363	0.75000000
H17	0.58053636	0.04128601	0.75000000
H18	0.88667593	0.81042699	0.75000000
H19	0.99314260	0.53353434	0.63380905
H20	0.71738818	0.07813021	0.63107456
H21	0.77681666	0.88931125	0.62861733
H22	0.20211157	0.55612648	0.46906038
H23	0.67866896	0.72470740	0.46916039
H24	0.60888138	0.24448269	0.47145859

Table B.4: Fractional atomic positions of nonequivalent atoms for Fe-N distance 2.09 Å

Atom	x	y	z
Fe	0.50000000	0.50000000	0.50000000
F2	0.33342615	0.13990841	0.75000000
F3	0.88664544	0.36980824	0.75000000
N4	0.16409460	0.55652601	0.75000000
N5	0.6224853	0.20810188	0.75000000
N6	0.70733741	0.74821033	0.75000000
N7	0.34759995	0.52093997	0.65904002
N8	0.55636997	0.36883996	0.65908997
N9	0.59603999	0.61016996	0.65904002
C10	0.03458526	0.58042457	0.75000000
C11	0.65588576	0.09190211	0.75000000
C12	0.79084923	0.84170184	0.75000000
C13	0.23548675	0.54347097	0.60534668
C14	0.59629461	0.27104212	0.60795423
C15	0.66343796	0.69489771	0.60540921
H16	0.02053982	0.67059426	0.75000000
H17	0.57203560	0.04234526	0.75000000
H18	0.88484301	0.81145043	0.75000000
H19	0.99325272	0.54180423	0.63385046
H20	0.71003681	0.07460198	0.63148753
H21	0.77507611	0.89021801	0.62925016
H22	0.20245679	0.55845339	0.46830821
H23	0.67669669	0.72589580	0.46926277
H24	0.60702401	0.24389808	0.47222612

Table B.5: Fractional atomic positions of nonequivalent atoms for Fe-N distance 2.10 Å

Atom	x	y	z
Fe	0.50000000	0.50000000	0.50000000
F2	0.33214373	0.13554648	0.75000000
F3	0.89179173	0.36547926	0.75000000
N4	0.16356198	0.55551287	0.75000000
N5	0.62310722	0.20804256	0.75000000
N6	0.70779228	0.74825160	0.75000000
N7	0.34710001	0.52100999	0.65931991
N8	0.55655000	0.36839001	0.65936998
N9	0.59635994	0.61053997	0.65931991
C10	0.03391910	0.57794772	0.75000000
C11	0.65758597	0.09222540	0.75000000
C12	0.79122620	0.84165016	0.75000000
C13	0.23501999	0.54291125	0.60594812
C14	0.59675425	0.27082583	0.60837978
C15	0.66381732	0.69505583	0.60593469
H16	0.01866680	0.66781213	0.75000000
H17	0.57432274	0.04209292	0.75000000
H18	0.88505883	0.81139246	0.75000000
H19	0.99322986	0.53869431	0.63435898
H20	0.71182225	0.07543010	0.63183261
H21	0.77546391	0.89007871	0.62958243
H22	0.20209115	0.55772194	0.46963014
H23	0.67732501	0.72579452	0.47028904
H24	0.60761205	0.24373160	0.47306762

Table B.6: Fractional atomic positions of nonequivalent atoms for Fe-N distance 2.12 Å

Atom	x	y	z
Fe	0.50000000	0.50000000	0.50000000
F2	0.32939838	0.12713562	0.75000000
F3	0.90151882	0.35682543	0.75000000
N4	0.16254367	0.55356680	0.75000000
N5	0.62432921	0.20789738	0.75000000
N6	0.70884006	0.74826042	0.75000000
N7	0.34608995	0.52114998	0.65986999
N8	0.55691998	0.36749001	0.65992001
N9	0.59698992	0.61129994	0.65985993
C10	0.03271947	0.57318286	0.75000000
C11	0.66085857	0.09283636	0.75000000
C12	0.79217902	0.84143276	0.75000000
C13	0.23410802	0.54182359	0.60710461
C14	0.59766561	0.27038293	0.60921804
C15	0.66466288	0.69532491	0.60697001
H16	0.01514672	0.66242079	0.75000000
H17	0.57876223	0.04159434	0.75000000
H18	0.88567782	0.81112786	0.75000000
H19	0.99329727	0.53272393	0.63535508
H20	0.71523986	0.07700588	0.63251928
H21	0.77647911	0.88971605	0.63025437
H22	0.20143118	0.55617657	0.47205502
H23	0.67868579	0.72550467	0.47227742
H24	0.60876213	0.24337844	0.47472966

Table B.7: Fractional atomic positions of nonequivalent atoms for Fe-N distance 2.15 Å

Atom	x	y	z
Fe	0.50000000	0.50000000	0.50000000
F2	0.32765200	0.12029941	0.75000000
F3	0.90878319	0.34921868	0.75000000
N4	0.16142255	0.55196241	0.75000000
N5	0.62536825	0.20746089	0.75000000
N6	0.70997242	0.74846249	0.75000000
N7	0.34459997	0.52135998	0.66067990
N8	0.55746992	0.36615999	0.66071989
N9	0.59792993	0.61241999	0.66066993
C10	0.03172457	0.56907336	0.75000000
C11	0.66341986	0.09323065	0.75000000
C12	0.79310833	0.84125087	0.75000000
C13	0.23296589	0.54094204	0.60860758
C14	0.59852151	0.26961793	0.61045481
C15	0.66568120	0.69580994	0.60839730
H16	0.01213771	0.65757468	0.75000000
H17	0.58244523	0.04119841	0.75000000
H18	0.88615407	0.81096851	0.75000000
H19	0.99347664	0.52767148	0.63662199
H20	0.71780313	0.07819235	0.63356159
H21	0.77751275	0.88938796	0.63134750
H22	0.20070412	0.55467366	0.47496948
H23	0.68012573	0.72527073	0.47493916
H24	0.60976548	0.24274658	0.47715794

Table B.8: Fractional atomic positions of nonequivalent atoms for Fe-N distance 2.2 Å

Atom	x	y	z
Fe	0.50000000	0.50000000	0.50000000
F2	0.32896350	0.11707757	0.75000000
F3	0.91064062	0.34534154	0.75000000
N4	0.16006180	0.55117969	0.75000000
N5	0.62587650	0.20635497	0.75000000
N6	0.71089700	0.74932391	0.75000000
N7	0.34213995	0.52169995	0.66198999
N8	0.55837999	0.36394997	0.66203998
N9	0.59947993	0.61426993	0.66198999
C10	0.03102796	0.56652311	0.75000000
C11	0.66407900	0.09297989	0.75000000
C12	0.79355417	0.84143345	0.75000000
C13	0.23133010	0.54058401	0.61080274
C14	0.59917558	0.26814432	0.61247479
C15	0.66678671	0.69693206	0.61057526
H16	0.01011767	0.65415721	0.75000000
H17	0.58392072	0.04099757	0.75000000
H18	0.88591498	0.81132191	0.75000000
H19	0.99365318	0.52473736	0.63841087
H20	0.71815882	0.07824863	0.63529397
H21	0.77812308	0.88940423	0.63325687
H22	0.19968775	0.55363351	0.47907036
H23	0.68133525	0.72554207	0.47897265
H24	0.61036816	0.24149507	0.48108713

Appendix C

Atomic coordinates for the relaxed $K_2V_3O_8$ compound

The obtained lattice values after relaxing the c/a ratio in the GGA approximation are a=8.8542 Å and c=5.2908 Å.

Table C.1: Fractional atomic coordinates of nonequivalent atoms in the $K_2V_3O_8$ relaxed structure in the GGA approximation.

Atom	x	y	z
K	0.66907000	0.16907000	0.17283915
V1	0.00000000	0.00000000	0.63161551
V2	0.36602359	0.13397641	0.64335752
O1	0.00000000	0.00000000	0.93587594
O2	0.18878065	0.08677589	0.52936466
O3	0.36982000	0.13018000	0.95431334
O4	0.00000000	0.50000000	0.51391578

The obtained lattice values after relaxing the c/a ratio in the LDA approximation are a= 8.8606 Å and c= 5.2831 Å.

Table C.2: Fractional atomic coordinates of nonequivalent atoms in the $K_2V_3O_8$ relaxed structure in the LDA approximation.

Atom	x	y	z
K1	0.66907000	0.16907000	0.17407021
V1	0.00000000	0.00000000	0.62494906
V2	0.36607440	0.13392560	0.64170505
O1	0.00000000	0.00000000	0.92677612
O2	0.18907646	0.08556979	0.53280423
O3	0.36982000	0.13018000	0.95070083
O4	0.00000000	0.50000000	0.51854406

Bibliography

[1] F. H. Allen, O. Kennard, D. G. Watson, L. Brammer, A. G. Orpen, and R. Taylor. *J. Chem. Soc. Perkin Trans. II*, pages S1–S19, 1987.

[2] O. K. Andersen. *in Computational Methods in Band Theory.* Plenum, New York, 1971.

[3] O. K. Andersen. *Phys. Rev. B*, **12**:3060, 1975.

[4] O. K. Andersen and O. Jepsen. *Phys.Rev.Lett.*, **53**:2571, 1984.

[5] O. K. Andersen, O. Jepsen, and G. Krier. *Lecture Notes on Methods of Electronic Calculations.* World Scientific Publ. Co, Singapore, 1994.

[6] O. K. Andersen, T. Saha-Dasgupta, and S. Ezhov. *Bull. Mater. Sci.*, **26**:19, 2003.

[7] O. K. Andersen, T. Saha-Dasgupta, S. Ezhov, L. Tsetseris, O. Jepsen, R. W. Tank, C. Arcangeli, and G. Krier. *Psi-k Newsletter*, 45:86–119, (June 2001).

[8] O.K. Andersen and T. Saha-Dasgupta. *Phys. Rev. B*, **62**:R16219, 2000.

[9] P.W. Anderson. *Phys. Rev. B*, **115**:2, 1959.

[10] V. I. Anisimov, I. V. Solovyev, M. A. Korotin, M. T. Czyzyk, and G. A. Sawatzky. *Phys. Rev. B*, **48**:16929, 1993.

[11] I. A. Baburin, V. A. Blatov, L. Carlucci, G. Ciani, and D. M. Proserpio. *J. Sol. State Chem.*, **178**:2452, 2005.

[12] N. V. Bausk, S. B. Érenburg, L. G. Lavrenova, and L. N. Mazalov. *J. Str. Chem.*, **36**:925, 1995.

[13] H. Beyer, W. Walter, and W. Francke. *Lehrbuch der organischen Chemie.* ed. Hirzel Sttutgart, 2004.

[14] P. Blaha, K. Schwartz, G. K. H. Madsen, D. Kvasnicka, and J. Luitz. *WIEN2K, An Augmented Plane Wave + Local Orbitals Program for calculating crystal properties.* Technical Report ISBN 3-9501031-1-2, K. Schwarz, Techn. University Wien, Austria, 2001.

[15] P. E. Blöchl. *Phys. Rev. B*, **50**:17953, 1994.

[16] A. M. Bond, F. Marken, C. T. Williams, D. A. Beattie, T. E. Keyes, R. J. Forster, and J. G. Vos. *J. Phys. Chem. B*, **104**:1977, 2000.

[17] M. Born and R. Oppenheimer. *Ann. Phys.*, **84**:457, 1927.

[18] J. J. Borrás-Almenar, E. Coronado, B. S. Tsukerblat, and R. Georges. *In Molecular Magnetism: From molecular assemblies to the devices.* Eds. E. Coronado, NATO series. Kluwer Academic Publishers, 1996.

[19] K. Boukheddaden, S. Miyashita, and M. Nishino. *Phys. Rev. B*, **75**:094112, 2007.

[20] K. Boukheddaden, M. Nishino, S. Miyashita, and F. Varret. *Phys. Rev. B*, **72**:014467, 2005.

[21] A. Bousseksou, J. Nasser, J. Linares, K. Boukheddaden, and F. Varret. *J. Phys. I France*, **2**:1381, 1992.

[22] C. J. Bradley and A. P. Cracknell. *The Mathematical Theory of Symmetry in Solids: Representation Theory for Point Groups and Space Groups.* Oxford University Press, 1972.

[23] K. Burke. *The ABC of DFT.* Department of Chemistry, University of California, Irvine CA, 2007.

[24] R. Car and M. Parrinello. *Phys. Rev. Lett.*, **55**:2471, 1985.

[25] Cambridge Crystallographic Data Centre. Cambridge structural database. 2005.

[26] O. Cépas, K. Kakurai, L. P. Regnault, T. Ziman, J.P. Boucher, N. Aso, M. Nishi, H. Kageyama, and Y. Ueda. *Phys. Rev. Lett.*, 87:167205, 2001.

[27] Cerius2. *Version 4.9.* Accelrys Inc., Cambridge, UK, 2003.

[28] B. C. Chakoumakos, R. Custelcean, T. Kamiyama, K. Oikawa, B. C. Sales, and M. D. Lumsden. *J. Solid State Chem.*, **180**:812, 2007.

[29] J. Choi, Z. T. Zhu, J. L. Musfeldt, G. Ragghianti, D. Mandrus, B. C. Sales, and J. R. Thompson. *Phys.Rev.B*, **65**:054101, 2001.

[30] R. Coldea, S. M. Hayden, G. Aeppli, T. G. Perring, C. D. Frost, T. E. Mason, S.-W. Cheong, and Z. Fisk. *Phys. Rev. Lett.*, **86**:5377, 2001.

[31] M. T. Czyzyk and G. A. Sawatzky. *Phys. Rev. B*, **49**:14211, 1994.

[32] G. H. O. Daalderop, P. J. Kelly, and M. F. H. Schuurmans. *Phys. Rev. B*, **41**:11919, 1990.

[33] C. Desroches, G. Pilet, P. A. Szilágyi, G. Molnár, S. A. Borshch, A. Bousseksou, S. Parola, and D. Luneau. *Eur. J. Inorg. Chem.*, **2**:357, 2006.

[34] R. C. Dickinson, W. A. Baker, T. D. Black, and R. S. Rubins. *J. Chem. Phys.*, **79**:2609, 1983.

[35] R. Dinnebier, H. W. Lerner, L. Ding, K. Shankland, W. I. F. David, P. W. Stephens, and M. Wagner. *Z. Anorg. Allg. Chem.*, **628**:310, 2002.

[36] K. Drabent and Z. Ciunik. *Chem. Commun.*, **1254**:1254, 2001.

[37] I. Dzyaloshinskii. *J. Phys. Chem. Solids*, **4**:241, 1958.

[38] S. B. Erenburg, N. V. Bausk, V. A. Varnek, and L. G. Lavrenova. *J. Magn. Magn. Mater.*, **157**:595, 1996.

[39] A. Furrer. *Letter to Editor Phys. Rev. B*, 2008.

[40] P.J. Galy and A. Carpy. *Acta Cryst.*, **B31**:1794, 1975.

[41] Y. Garcia, P. Guionneau, G. Bravic, D. Chasseau, J. A. K. Howard, O. Kahn, V. Ksenofontov, S. Reiman, and P. Gütlich. *Eur. J. Inorg. Chem.*, page 1531, 2000.

[42] Y. Garcia, V. Ksenofontov, G. Levchenko, and P. Gütlich. *J. Mater. Chem.*, **10**:2274, 2000.

[43] Y. Garcia, P. J. van Koningsbruggen, G. Bravic, P. Guionneau, D. Chasseau, G. L. Cascarano, J. Moscovici, K. Lambert, A. Michalowicz, and O. Kahn. *Inorg. Chem.*, **36**:6357, 1997.

[44] J. Gasteiger and M. Marsili. *Tetrahedron*, **36**:3219, 1980.

[45] J. A. Greathouse and M.D. Allendorf. *J. Am. Chem. Soc.*, **128**:10678, 2006.

[46] P. Gütlich, A. Hauser, and H. Spiering. *Angew. Chem. Int.*, **33**:2024, 1994.

[47] P. Hohenberg and W. Kohn. *Phys. Rev.*, **136**:B864, 1964.

[48] J. Hubbard. *Electron Correlations in Narrow Energy Bands. IV. The Atomic Representation*, **285**:542, 1965.

[49] R. Jain, K. Kabir, J. B. Gilroy, K. A. R. Mitchell, K. Wong, and R. G. Hicks. *Nature*, **445**:291, 2007.

[50] A. Joshi, M. Ma, F. Mila, D. N. Shi, and F. C. Zhang. *Phys. Rev. B*, **60**:6584, 1999.

[51] H. Kageyama, K. Yoshimura, R. Stern, N. V. Mushnikov, K. Onizuka, M. Kato, K. Kosuge, C. P. Slichter, T. Goto, and Y. Ueda. *Phys. Rev. Lett*, **82**:3168, 1999.

[52] O. Kahn and E. Codjovi. *Phil. Trans.*, **354**:359, 1996.

[53] O. Kahn, E. Codjovi, Y. Garcia, P. J. van Koningsbruggen, R. Lapouyade, and L. Sommier. *ACS Symp. Series*, **20**:298, 1996.

[54] O. Kahn and C. Jay Martinez. *Science*, **279**:44, 1998.

[55] O. Kahn, L. Sommier, and E. Codjovi. *Chem. Mater.*, **9**:3199, 1997.

[56] T. Kambara. *J. Chem. Phys.*, **74**:4557, 1981.

[57] Y. Kazunari, H. Miyajima, and T. Yamabe. *J. Phys. Chem. B*, **101**:4383, 1997.

[58] T. E. Keyes, R. J. Forster, P. M. Jayaweera, C. G. Coates, J. J. McGarvey, and J. G. Vos. *Inorg. Chem.*, **37**:5925, 1998.

[59] D. I. Khomskii and U . Löw. *Phys. Rev. B*, **69**:184401, 2004.

[60] Y. J. Kim, A. Aharony, R. J. Birgeneau, F. C. Chou, O. Entin-Wohlman, R. W. Erwin, M. Greven, A. B. Harris, M. A. Kastner, I. Ya. Korenblit, Y. S. Lee, and G. Shirane. *Phys. Rev. Lett.*, **83**:852, 1999.

[61] H. Kobayashi, T. Haseda, E. Kanda, and S. Kanda. *J. Phys. Soc. Jpn.*, **18**:349, 1963.

[62] W. Koch and M. C. Holthausen. *A chemist's Guide to Density Functional Theory.* 2nd edition. Wiley-VCH, Weinheim Germany, 2001.

[63] J. Kohanoff. *Electronic Structure Calculations for Solids and Molecules: Theory and computational methods.* Cambridge university press, Cambridge UK, 2006.

[64] W. Kohn and L. J. Sham. *Phys. Rev.*, **140**:A1133, 1965.

[65] T. Kretz. Crystallographic data tk91, private communication. Technical report, Institute for inorganic and analytic chemistry, Frankfurt university, 2005.

[66] J. Kröber, J. P. Audière, R. Claude, E. Codjovi, O. Kahn, J. G. Haasnot, F. Grolière, F. Jay, A. Bousseksou, J. Linares, F. Varret, and A. Gonthier-Vassal. *Chem. Mater.*, **6**:1404, 1994.

[67] J. Kröber, E. Codjovi, O. Kahn, F. Groliere, and C. Jay. *J. Am. Chem. Soc.*, **115**:9810, 1993.

[68] R. Laskowski, P. Blaha, and K. Schwarz. *Phys. Rev. B*, **67**:0751021, 2003.

[69] G. Lemercier, N. Bréfuel, S. Shova, J. A. Wolny, F. Dahan, M. Verelst, H. Paulsen, A. X. Trautwein, and J. P. Tuchagues. *Chem. Eur. J.*, **12**:7421, 2006.

[70] J. F. Létard, P. Guionneau, E. Codjovi, O. Lavastre, G. Bravic, D. Chasseau, and O. Kahn. *J. Am. Chem. Soc.*, **119**:10861, 1997.

[71] J. Linares, H. Spiering, and F. Varret. *Eur. Phys. J. B*, **10**:271, 1999.

[72] M. E. Lines, A. P. Ginsberg, R. L. Martin, and R. C. Sherwood. *J. Chem. Phys.*, **57**:1, 1972.

[73] G. Liu and J. E. Greedan. *J. Solid State Chem.*, **114**:499, 1995.

[74] M. D. Lumsden, S. E. Nagler, B. C. Sales, D. A. Tennant, D. F. McMorrow, S. H. Lee, and S. Park. *Phys. Rev. B*, **74**:214424, 2006.

[75] M. D. Lumsden, B. C. Sales, D. Mandrus, S. E. Nagler, and J. R. Thompson. *Phys. Rev. Lett.*, **86**:159, 2001.

[76] O. Madelung. *Introduction to Solid-State Theory.* Springer Verlag, Berlin Heidelberg, Germany, 1981.

[77] R. M. Martin. *Electronic structure. Basic theory and practical methods.* Cambridge university press, Cambridge, United Kingdom, 2004.

[78] G. S. Matouzenko, G. Molnar, N. Bréfuel, M. Perrin, A. Bousseksou, and S. A. Borshch. *Chem. Mat.*, **15**:550, 2003.

[79] M. Mattesini, J. M. Soler, and F. Yndurain. *Phys. Rev. B*, **73**:094111, 2006.

[80] S. L. Mayo, B. D. Olafson, and W. A. Goddard III. *J. Phys. Chem.*, **94**:8897, 1990.

[81] D. Mertz, R. Hayn, I. Opahle, and H. Rosner. *Phys. Rev. B*, **72**:085133, 2005.

[82] A. Michalowicz, J. Moscovici, B. Ducourant, D. Cracco, and O. Kahn. *Chem. Mater.*, **7** :1833, 1995.

[83] T. Mizokawa and A. Fujimori. *Phys. Rev. B*, **54**:5368, 1996.

[84] W. T. M. Mooij, B. P. van Eijck, S. L. Price, P. Verwer, and J. Kroon. *J. Computat. Chem.*, **19**:459, 1998.

[85] T. Moriya. *Phys. Rev.*, **120**:91, 1960.

[86] U. Mueller, M. Schubert, F. Teich, H. Puetter, K. Schierle-Arndt, and J. Pastre. *J. Mat. Chem.*, **16**:626, 2006.

[87] J. Naser, K. Boukheddaden, and J. Linares. *Eur. Phys. J. B*, **39**:219, 2004.

[88] M. Nishino, S. Miyashita, and K. Boukheddaden. *J. Chem. Phys.*, **118**:4594, 2003.

[89] P. Novák. *Notes on Calculation of spin-orbit coupling.* Institute of Physics, Praha Czech Republic.

[90] S. Ohnishi and S. Sugano. *J. Phys. C: Solid State Phys.*, **14**:39, 1981.

[91] H. Paulsen and A. X. Trautwein. *Top. Curr. Chem.*, **235**:197, 2004.

[92] J. P. Perdew and Y. Wang. *Phys. Rev. B*, **45**:13244, 1992.

[93] J. P. Perdew and A. Zunger. *Phys. Rev. B*, **23**:5048, 1981.

[94] A. V. Postnikov, G. Bihlmayer, and S. Blügel. *Comp. Mat. Sc. Proceedings of the Second Conference of the Asian Consortium for Computational Materials Science ACCMS-2.*, **36**:91, 2006.

[95] A. V. Postnikov, J. Kortus, and M. R. Pederson. *Psi-k Newsletter*, page 127, 2004.

[96] M. Pouchard, E. ThPobald, and J. G. ThPobaId. *Bull. Soc. Chim. Belg.*, **97**:241, 1988.

[97] R. C. Rai, J. Cao, J. L. Musfeldt, D. J. Singh, X. Wei, R. Jin, Z. X. Zhou, B. C. Sales, and D. Mandrus. *Phys. Rev. B*, **73**:075112, 2006).

[98] H. M. Ronnow and D. F. McMorrow. *Phys. Rev. Lett.*, **87**:037202, 2001.

[99] O. Roubeau, J. M. Alcazar-Gomez, E. Balskus, J. J. A. Kolnaar, J. G. Haasnoot, and J. Reedijk. *New J. Chem.*, **25**:144, 2001.

[100] T. Saha-Dasgupta. 2000.

[101] B. C. Sales, M. D. Lumsden, S. E. Nagler, D. Mandrus, and R. Jin. *Phys. Rev. Lett.*, **88**:095901–1, 2002.

[102] M. U. Schmidt and U. Englert. *J. Chem. Soc., Dalton Trans.*, page 2077, 1996.

[103] E. Sjöstedt, L. Nordström, and D. J. Singh. *Solid State Commun.*, 114:15, 2000.

[104] J. C. Slater. *Phys.Rev. B*, **92**:603, 1937.

[105] H. Spiering and N. Willenbacher. *J. Phys.:Condens. Matter*, **1**:10089, 1989.

[106] M. B. Stone, C. Broholm, D. H. Reich, O. Tchernyshyov, P. Vorderwisch, and N. Harrison. *Phys. Rev. Lett.*, **96**:257203, 2006.

[107] Y. Tsui, A. Brühl, K. Removic-Langer, V. Pashchenko, B. Wolf, G. Donath, A. Pikul, T. Kretz, H.-W. Lerner, M. Wagner, A. Salguero, T. Saha-Dasgupta, B. Rahaman, R. Valenti, and M. Lang. *J. Mag. Mag. Mat.*, **310**:1319, 2007.

[108] Y. J. Uemura and R. J. Birgeneau. *Phys. Rev. B*, **36**:7024, 1987.

[109] N. W. Ashcroft und N. D. Mermin. *Solid State Physics.* 7 ed. Wiley, New York, 1996.

[110] R. Valentí, T. Saha-Dasgupta, J. V. Alvarez, K. Pozgajcic, and C. Gros. *Phys. Rev. Lett.*, **86**:5381, 2001.

[111] R. Valentí, T. Saha-Dasgupta, C. Gros, and H. Rosner. *Phys. Rev. B*, **67**:245110, 2003.

[112] G. Vos, R. A. G. de Graaff, J. G. Haasnoot, A. M. van der Kraan, P. de Vaal, and J. Reefjik. *Inorg. Chem.*, **23**:2905, 1984.

[113] W. Vreugdenhil, J. H. van Diemen, R. A. G. de Graaff, J. G. Haasnoot, J. Reedijk, A. M. van der Kraan, O. Kahn, and J. Zarembowitch. *Polyhedron*, **9**:2971, 1990.

[114] J. Wajnflasz. *Phys. Status Solidi*, **40**:537, 1970.

[115] N. Willenbacher and H. Spiering. *J. Phys. C: Solid State Phys.*, **21**:1423, 1988.

[116] R. L. Withers, T. Höche, Y. Liu, S. Esmaeilzadeh, R. Keding, and B. Sales. *J. Sol. Stat. Chem.*, **177**:3316, 2004.

[117] B. Wolf, A. Brühl, V. Pashchenko, K. Removic-Langer, T. Kretz, J.W. Bats, H.W. Lerner, M. Wagner, A. Salguero, T. Saha-Dasgupta, B. Rahaman, R. Valentí, and M. Lang. *C. R. Chimie*, **10**:109, 2007.

[118] B. Wolf, S. Zherlitsyn, B. Lüthi, N. Harrison, U. Löw, V. Pashchenko, M. Lang, G. Margraf, H.-W. Lerner, E. Dahlmann, F. Ritter, W. Assmus, and M. Wagner. *Phys. Rev. B*, **69**:092403, 2004.

[119] F. M. Woodward, A. S. Albrecht, C. M. Wynn, C. P. Landee, and M. M. Turnbull. *Phys. Rev. B*, **86**:159, 2001.

[120] S. Yamamoto. *Phys. Rev. B*, **53**:3364, 1996.

[121] T. Yokoyama, Y. Murakami, K. Kiguchi, T. Komatsu, and N. Kojima. *Phys. Rev. B*, **58**:14238, 1998.

[122] K. Yosida. *Theory of Magnetism.* Series in Solid-State Sciences 122. Springer-Verlag, Berlin Heidelberg, Germany, 1996.

[123] O. Zaharko, J. Mesot, L. A. Salguero, R. Valentí, M. Zibiri, M. Johnson, Y. Filinchuk, B. Klemke, K. Kiefer, M. Mys'kiv, T. Strassle, and M. Mutka. *Phys. Rev. B*, 77:224408, 2008.

[124] I. A. Zaliznyak. *Phys. Rev. B*, **68**:134451, 2003.

[125] S. Zein and S. A. Borshch. *J. Am. Chem. Soc.*, 127:16197, 2005.

[126] A. Zheludev, Z. Honda, Y. Chen, C. L. Broholm, K. Katsumata, and S. M. Shapiro. *Phys. Rev. Lett*, **88**:077206, 2002.

[127] R. Zimmermann and E. König. *J. Phys. Chem. Solids*, **38**:779, 1977.

Publications

1. B. Wolf, A. Brhl, V. Pashchenko, K. Removic-Langer, T. Kretz, J. W. Bats, H.-W. Lerner, M. Wagner, Andrea Salguero, T. Saha-Dasgupta, B. Rahaman, R. Valentí and M. Lang, *Modified 1,4-hydroquinone ligands bridging Cu(II) ions: Building blocks for a new class of quantum magnets*, Comptes Rendus Chimie **10**, 109 (2007).

2. H. O. Jeschke, L. A. Salguero, R. Valentí, C. Buchsbaum, M. U. Schmidt, and M. Wagner, *Classical and ab initio preparation of reliable structures for polymeric coordination compounds*, Comptes Rendus Chimie **10**, 82 (2007).

3. L. A. Salguero, H. O. Jeschke, B. Rahaman, T. Saha-Dasgupta, C. Buchsbaum, M. U. Schmidt, and R. Valentí, *Cu-based metalorganic systems: an ab initio study of the electronic structure*, New J. Phys. **9**, 26 (2007).

4. H. O. Jeschke, L. A. Salguero, B. Rahaman, C. Buchsbaum, V. Pashchenko, M. U. Schmidt, T. Saha-Dasgupta, and R. Valentí, *Microscopic modeling of a spin crossover transition*, New J. Phys. **9**, 448 (2007).

5. Y. Tsui, A. Bruehl, K. Removic-Langer, V. Pashchenko, B. Wolf, G. Donath, A. Pikul, T. Kretz, H.-W. Lerner, M. Wagner, A. Salguero, T. Saha-Dasgupta, B. Rahaman, R. Valenti, M. Lang, *Field-induced phase transition in a metalorganic spin-dimer system a potential model system to study Bose-Einstein condensation of magnons*, Journal of Magnetism and Magnetic Materials **310** , 1319 (2007).

6. O. Zaharko, J. Mesot, L.A. Salguero, R. Valentí, M. Zbiri, M. Johnson, Y. Filinchuk, B. Klemke, K. Kiefer, M. Mys'kiv, T. Strassle, H. Mutka, *Tetrahedra system Cu4OCl6daca4: magnetic exchange against molecular vibrations*, Phys. Rev. B **77**, 224437 (2008).

7. O. Zaharko, J. Mesot, Y. Zhang, L.A. Salguero, R. Valentí, M. Zbiri, M. Johnson, Y. Filinchuk, B. Klemke, K. Kiefer, M. Mys'kiv, T. Strassle, H. Mutka, *Reply to comment. Prof. Furrer on tetrahedra system*, Letter to editor Phys. Rev. B (submitted).

8. L.A. Salguero, B. Rahaman, T. Saha-Dasgupta, R. Valentí, *Microscopic properties of* $K_2V_3O_8$, (to be submitted to Phys. Rev. B).

Zusammenfasung

Niedrigdimensionale Quantenspinsysteme basierend auf Übergangsmetallionen standen in den letzten Jahrzehnten im Mittelpunkt intensiver Forschung. Die grosse Anzahl ihrer Freiheitsgrade (Orbital-, Ladungs- und Spinfreiheitsgrade) sind durch atomaren Überlapp sowie Wechselwirkungen wie Coulombabstossung und den daraus resultierenden Hundschen Regeln verknüpft. Konkurrierende Phasen treten auf, wenn einige dieser Wechselwirkungen von vergleichbarer Grösse sind. Der Begriff 'niedrigdimensionale Spinsysteme' bezieht sich auf Materialien, in denen sich die magnetischen Wechselwirkungen zwischen magnetischen Ionen im Wesentlichen auf Ebenen (zweidimensional), Ketten (eindimensional) oder Clustern (nulldimensional) beschränken. Confinement-Effekte spielen eine wichtige Rolle, die zu einer Vielzahl interessanter und ungewöhnlicher Quantenphänomene führen. Die experimentelle Untersuchung dieser Phänomene wird jedoch häufig durch die grossen charakteristischen Energieskalen vieler Materialien erschwert. So haben z.B. die anorganischen Kuprate Austauschkonstanten in der Grössenordnung von J $\sim$ 1500 K [60]. Um magnetfeldinduzierte Übergänge zu untersuchen, muß das angelegte Magnetfeld grösser als das Sättigungsfeld sein, das für diese Materialien in der Grössenordnung von 3800 T liegt. Experimentell können kleiner Energieskalen durch das Einbringen von Defekten, die Substitution von Komponenten oder durch Dotierung mit nichtmagnetischen Ionen (Verdünnung) erreicht werden. Die jüngsten Entdeckungen von niedrigdimensionalen metallorganischen Verbindungen mit Austauschkopplungen zwischen Metallen in der Grössenordnung einiger meV, hat diese Materialien wieder in den Mittelpunkt des Interesses von Experimentatoren und Theoretikern gerückt [98], [119].

Metallorganische Verbindungen, in denen Übergangsmetallzentren über organische Liganden gekoppelt sind, werden im Zusammenhang mit molekularen Magneten und elektronischen Materialien diskutiert [54],[95]. Ihre Eigenschaften lassen sich wegen ihres modularen Aufbaus verändern, ohne dass dabei der grundlegende Kristallaufbau verändert werden muß. Die Substitution organischer Gruppen oder Liganden kommt als mögliche Ladungsträger-Dotierung bei der Suche nach Materialien mit den gewünschten magnetischen Wechselwirkungen und Ladungsträgerkonzentrationen eine wichtige Rolle zu. Diese Möglichkeit wird im ersten Teil dieser Arbeit theoretisch untersucht. So werden beispielsweise systematische Substitutionen der metallorganischer Verbindungen dazu benutzt, die gewünschten elektronischen und magnetischen Eigenschaften in neuen und modifizierten Strukturen zu erreichen. Diese Studien erlauben ein graduelles Verständnis der Eigenschaften der niedrigdimensionalen Systeme und können als Anleitung für die systematische

Synthese im Labor dienen.

Die grosse Anzahl von Atomen in der Elementarzelle und die niedrige Symmetrie, die man in der Regel bei metallorganischen Verbindungen vorfindet, erschweren jedoch die numerische Untersuchung ihrer elektronischen und magnetischen Eigenschaften erheblich. Hinzu kommt, dass die Struktur häufig nur schlecht bestimmt ist, da eine genaue Bestimmung der Wasserstoffpositionen mit Röntgenstreuung sehr schwer ist. In einigen Fällen ist nicht einmal die Kristallstruktur bekannt, da es keine für die Röntgenanalyse geeigneten Kristalle gibt. Deswegen waren theoretische Untersuchen dieser Verbindungen zumeist Strukturuntersuchungen welche auf klassischen Ansätzen basierten. Die Art der organischen Komponente hat einen wichtigen Einfluss auf die Eigenschaften der metallischen Zentren, so dass diese bei der Untersuchung der Grundzustandseigenschaften berücksichtigt werden müssen. Eine Methode, die den Einfluss aller Konstituenten eines Materials berücksichtigt, ist die Dichtefunktionaltheorie (DFT). Um kontrollierte DFT-Rechnungen für solche Strukturen durchzuführen, wird in dieser Arbeit ein neuer Zwei-Schritt-Ansatz verfolgt, bei dem klassische und quantenmechanische Methoden dazu benutzt werden, um systematische Modellstrukturen für metallorganische oder polymerische Verbindungen herzustellen und zu ihrer Gleichgewichtsstruktur zu relaxieren. Diese Prozedur erlaubt es, nicht nur den Grundzustand von Verbindungen zu studieren, sondern auch ihre Konstituenten zu modifizieren. Es wird gezeigt, dass diese Prozedur sehr effektiv ist und zudem den Vorteil besitzt, quantenmechanische Effekte mit einzubeziehen. Eine Vernachlässigung der Quanteneffekte kann zur Unterdrückung interessanter Eigenschaften und falschen Schlussfolgerungen führen. Diese theoretische Prozedur wurde in dieser Arbeit erfolgreich auf verschiedene metallorganische Materialien angewandt.

In der Klasse der metallorganischen Verbindungen sind wir insbesondere an Hydrochinone-abgeleiteten Linkern, die Cu^{2+}-Ionen verbinden, interessiert. Der Vorteil ist, dass diese chemisch so modifiziert werden können, dass die Koordinationsgeometrie der Cu^{2+}-Ionen beeinflusst wird während die Stärke der magnetischen Austausch-Wechselwirkung moderat gehalten wird. Für zwei Repräsentanten der Familie der hydroquinone-basierten niedrigdimensionalen Quantenspinssysteme - Cu^{2+}-2,5-bis(pyrazol-1-yl)-1,4-dihydroxybenzene (CuCCP), das sich wie ein eindimensionales Spinkettensystem verhält, und das gekoppelte Dimersystem TK91 - wurde der Einfluß der organischen Linker auf die magnetische Korrelation der Metallzentren untersucht. Zusätzlich wurden systematische Änderungen der CuCCP Polymere theoretisch untersucht, um gewünschte elektronische und magnetische Eigenschaften in den neuen Strukturen zu erhalten. Diese Untersuchungen erlauben ein graduelles Verständnis der Eigenschaften dieser Systeme und geben eine Hilfestellung für die systematische Synthese im Labor.

Es wurden verschiedene chemische Modifikationen der Cu-basierten polymerischen Koordinationsverbindung CuCCP analysiert. Unser Ziel war es, die magnetischen Wechselwirkungen zwischen Cu-Zentren kontrolliert zu verändern und damit die Effizienz und Durchführbarkeit unseres kombinierten Ansatzes zu überprüfen. Dabei wurden zwei Wege verfolgt um die ursprüngliche CuCCP-Struktur zu verändern: i) durch unterschiedliche Substitutionen im Linker (hydrochinone) ii) durch Hinzufügen von Liganden zum System. Im Rahmen des ersten Schemas wurden zwei unterschiedliche H-Substitutionen im Hydrochinone-Ring untersucht, NH_2 (das Elektronen zur Verfügung stellt) und CN (das Elektronen entzieht). Im Rahmen des zweiten Schemas wurden Strukturen mit H_2O- und NH_3-Liganden untersucht. Das Ergebnis unserer Studie ist, dass NH_2-Substitution in Hydrochinone die effektivste Methode ist, um die Cu-Cu-Wechselwirkungen innerhalb der Kette im CuCCP zu erhöhen. Dagegen induziert oder verstärkt CN die Wechselwirkungen zwischen den Ketten, die in der ursprünglichen CuCCP-Verbindung nicht oder nur schwach vorhanden waren. Im Gegensatz dazu führt der Zusatz von H_2O und NH_3 zu einer Isolierung der Cu-Ionen. Die in dieser Untersuchung gefundenen Effekte sind sehr klein, hauptsächlich aufgrund der schwachen Kopplungskonstanten in dieser Art metallorganischer Materialien.

Wir haben gezeigt, dass die als TK91 bekannte Verbindung sich wie ein schwach gekoppeltes zweidimensionales Spin-1/2-Kettensystem verhält, mit der stärksten Cu-Cu-Wechselwirkung entlang den polymerischen Hydrochinone-basierten Ketten und einer schwachen Wechselwirkung entlang der c-Achse. Die Dimer-Einheit wird dabei nicht durch die direkt benachbarten Cu Atome, sondern durch die durch Hydroquinone-Linker verbundenen Cu-Ionen gebildet, die einen Abstand von 8 Å haben. Die mikroskopischen Parameter, die sich aus unseren Rechnungen ergeben, sind von der gleichen Grössenordnung wie diejenigen, die man aus Untersuchungen der experimentellen Kurven für die Suszeptibilität und für die spezifische Wärme bei verschwindendem Magnetfeld erhält. Die Analyse der elektronischen Eigenschaften dieser Verbindung zeigt, dass es in der Ebene der O-Cu-N-Atome innerhalb der Kette eine dd δ-Bindung gibt, die zu einer Verstärkung der Wechselwirkungen zwischen den Cu-Atomen entlang der Polymerkette führt. Diese Eigenschaften und die Existenz einer Lücke im Anregungsspekrum machen diese Verbindung zu einem möglichen Kandidaten für Untersuchungen quantenkritischer Phänomene. Zur Zeit der Fertigstellung dieser Dissertation wurde eine magnetfeldinduzierte Bose-Einstein-Kondensation von Magnonen oder ein Kosterlitz-Thouless-Szenario für diese Verbindung diskutiert. Es sind jedoch noch weitere experimentelle Untersuchungen notwendig, um diese Hypothesen zu bestätigen oder zu widerlegen. Solche Untersuchungen werden z.Z. durchgeführt.

Zusätzlich haben wir weiter den Einfluß der geometrischen Anordnung und das Wechselspiel verschiedener Energieskalen auf die magnetischen Phänomenen, wie sie in null-, ein- und zweidimensionalen Materialien beobachtet werden, untersucht. Hierfür wurden drei unterschiedliche Systeme mit $3d$ Übergangsmetall-Ionen betrachtet, in denen die magnetischen Wechselwirkungsparameter zwischen den magnetischen Zentren klein sind, und die im Magnetfeld oder unter Änderung des Drucks oder der Temperatur sehr interessante Eigenschaften zeigen.

Für den nulldimensionalen Fall wurde eine ausführliche Untersuchung von $Cu_4OCl_6L_4$ mit L=diallylcyanamide=N≡C-N-(CH_2-CH=CH_2)$_2$ ($Cu_4OCl_6daca_4$) durchgeführt. Im $Cu_4OCl_6daca_4$-System sind die durch Cu-Ionen gebildeten magnetischen Einheiten tetraedrisch angeordnet. Unsere Berechnungen zeigen, dass es sich um nahezu isolierte Cu^{2+} S=1/2 Tetraeder handelt. Das ungepaarte Elektron ist nur teilweise auf den Cu d-Zuständen lokalisiert und wird teilweise auf das Sauerstoffatom im Zentrum des Tetraeders und dann weiter auf die Atome im Molekül übertragen. Um das experimentell beobachtete anormale Verhalten des effektiven Moments zu erklären, gab es unterschiedliche Erklärungsversuche in der Literatur. Unsere Ergebnisse weisen diejenigen Szenarien zurück, bei denen die Verbindung als System mit gemischten Valenzen oder als isotropes Heisenberg System mit grosser Anisotropie und Orbitalentartung beschrieben wurde. Aufgrund der Geometrie des Clusters sind zwei Austauschpfade möglich. Zum einen ein antiferromagnetischer Cu-O-Cu-Austausch über das zentrale Sauerstoffatom, zum anderen ein ferromagnetischer Cu-Cl-Cu-Austausch über die Chloratome in der Peripherie. Dies, zusammen mit der Tatsache, dass Messungen der Bulkeigenschaften offensichtlich einen schwachen inter-tetraedrischen Austausch zwischen AFM/FM-Clustern zeigen, führte uns dazu, ein Modell mit AFM/FM und sehr schwachen AFM Inter-Cluster-Korrelationen vorzuschlagen. Unsere DFT-Rechnungen für ferro- und antiferromagnetische Intra-Cluster-Wechselwirkungen haben sich als relativ instabil bezüglich des Vorzeichens von J erwiesen, was auf ein hochfrustriertes Verhalten dieser Verbindung hindeutet. Die magnetische Frustration zusammen mit der schlechten Probenqualität und dem anisotropen Probenwachstum machen es schwierig, dieses Szenario experimentell zu bestätigen oder zurückzuweisen. Z.z. wird experimentell weiter versucht, Kristalle höherer Qualität zu erhalten und das Wechselspielzwischen elektronischer Delokalisierung und magnetischer Wechselwirkung genauer zu untersuchen.

Im eindimensionalen Fall haben wir die polymerischen Fe(II)-Triazol-Verbindungen untersucht, die von besonderer Bedeutung sind, da sich in ihnen möglicherweise ein Übergang zwischen einem Low- und High-Spin-Zustand (LS/HS) durch eine äussere Störung induzieren lässt. Nach einer zufriedenstellenden mikroskopischen Erklärung dieses kooperativen Phänomens wurde lange Zeit vergeblich gesucht. Einer der Gründe hierfür war der Mangel an Röntgendaten. In dieser Arbeit entwickeln wir einen neuen mikroskopischen Ansatz zur Klärung des Mechanismus des Spin-Crossovers in solchen Systemen und zeigen, dass in dieser Art von Verbindung der magnetische Austausch zwischen High-Spin Fe(II)-Zentren eine wichtige Rolle spielt. Für Fe(II)-triazole haben wir gezeigt, dass unter Verwendung sorgfältig präparierter Modellstrukturen der Übergang von einem LS zu einem HS Zustand simuliert werden kann. Ein Vorteil dieser Modellrechnungen ist, dass die Grundeinheiten dieser Polymerfamilie in den Rechnungen berücksichtigt werden, während die sich normalerweise ändernden Counterionen durch kleine Einheiten ersetzt wurden, die die Elementarzelle neutral halten. Unsere Berechnungen können daher auf beliebige polymerische Materialien übertragen werden. In unseren Rechnungen wurden die elastischen Freiheitsgrade eingefroren und wir haben uns auf die elektronischen und magnetischen Eigenschaften konzentriert, für die die entsprechenden Parameter quantifiziert wurden. Wir haben gezeigt, dass die magnetischen Wechselwirkungen eine wichtige Rolle im mikroskopischen Mechanismus des Spinübergangs spielen und damit eine mikroskopische Herleitung der Parameter gefunden, die den traditionellen theoretischen Ansätzen für polymerische Spin-Crossover-Materialien zugrunde liegen. Ein nächster Schritt für zukünftige Untersuchungen sollte die Gitterdynamik (Phononen) in den ab initio Berchnungen beinhalten.

Die korrekte Beschreibung der zugrunde liegenden Physik in vielen Materialien wird oft durch die Anwesenheit von Anisotropien erschwert. Um diese Schwierigkeit zu verdeutlichen, haben wir eine zweidimensionale verdünnte $K_2V_3O_8$-Verbindung untersucht, die einen ungewöhnlichen Spin-Reorientierungseffekt im Magnetfeld zeigt. Für $K_2V_3O_8$ haben wir gezeigt, dass man, ähnlich wie bei den metallorganischen Verbindungen, die atomaren Kräfte in den Strukturen relaxieren muss, um den korrekten Grundzustand zu erhalten. Aufgrund der hohen Symmetrie und der geringen Anzahl der Atome pro Elementarzelle, musste hier jedoch nicht die Zwei-Schritt-Prozedur angewandt werden. Es gibt zwar

Anisotropien in diesen Systemen, diese sind jedoch klein und beeinflussen die experimentell beobachteten Eigenschaften dieser Verbindungen nur im Magnetfeld. Unsere Berechnungen zeigen, dass diese Systeme gut durch einen antiferromagnetischen zweidimensionalen Heisenberg-Hamiltonoperator auf einem quadratischen Gitter beschrieben werden, mit einer nächsten-Nachbar-Wechselwirkung J $\sim$ 12 K und einem diagonalen Superaustauschterm J' $\sim$ 1.7 K. Dieser letzte Term wurde zuvor weder vorhergesagt noch beobachtet, beeinflusst aber die Grundzustandseigenschaften erheblich, wie durch unsere Berechnungen der Suszeptibiltät und der spezifischen Wärme gezeigt wird. Die Berücksichtung dieses Terms führt zu einer deutlich besseren Beschreibung der experimentellen Daten. Unser theoretischer Ansatz erlaubt eine bessere Beschreibung der Grundzustandseigenschaften dieser Verbindungen als solche Szenarien, die auf einer Orbitalentartung und einem Zwei-Spin-Modell basieren.

Curriculum vitae

Name: Lady-Andrea Salguero

Date of birth : January 12, 1981.

Place of birth : Ibague, Colombia.

Nationality : Colombian

Experience:

2005-2007: System Administrator
Institut für Theoretische Physik
Johann Wolfgang Goethe-Universität Frankfurt

2001: Summer research project in theoretical condensed matter
Centro Atómico Bariloche and Instituto Balseiro, Argentina
Project: *Conductance through a quantum wire side-coupled to a quantum dot*
Mentor: A.A. Aligia

August 2008: Summer research project in materials science
CAMD Technical University of Denmark
Project: *Computational materials design project on high energy-density materials*
Mentor: CAMD summer school organizers

Educational qualifications:

2005-2008: PhD Physics

Institut für Theoretische Physik

Johann Wolfgang Goethe-Universität Frankfurt

Advicer: Prof. Dr. M.R. Valentí

2002-2004: MSc. Physics

Special: theoretical solid state physics

National University of Colombia, Bogotá

Project: *FP-LAPW study of the structural and electronic properties of SrN and ZrN*

Advicer: Dr. J.A. Rodriguez and Dr. N. Takeuchi

Thesis awarded

1998-2002: Diploma in Physics

Special: theoretical solid state physics

National University of Colombia, Bogotá

Project:*Phase transitions of PbTe*

Advicer: Dr. J.A. Rodriguez

Acknowledgments

I would like to thank:

- Prof. Dr. Maria-Roser Valentí for giving me the opportunity to work on an interdisciplinary project, for her financial support and discussions about my work.
- Prof. Dr. Michael Lang, with whom we share a couple of projects, for his cooperativeness and for accepting to be the second referee of my thesis.
- Very specially to Prof. Dr. Martin Schmidt and his PhD student Christian Buchsbaum, with whom I shared some time building the structures with force-field techniques, and with whom I learned a lot about chemistry and for the very helpfull discussions and kindness.
- Dr. Tanusri Saha-Dasgupta and her PhD student Badiur Rahaman, with whom we share many projects, for useful discussions.
- Dr. Oksana Zaharko with whom I worked in a collaborative project. For the helpfull discussions, her motivation and entusiasm toward my work.
- Prof. Dr. Mattias Wagner and all forschergruppe members, where the main projects of my thesis were developed, both theoretically and experimentally. For the constant vivid discussions and support.
- Dr. Harald Jeschke for relaxing the atomic positions of Cu-hydroquinone and Fe-triazole compounds and for presenting some of my thesis projects in several conferences.
- Dr. Ivan Spremo, my friend, working partner and teacher in system administration during two years at the institute. His kindness, patiente and advices supported me and kept me motivated.
- Prof. Roger Berger, for introducing me to the quantum mechanics from the chemistry point of view. His availability to discuss and his kindness motivated me to see the problems I had to solve from different perspectives.
- Very specially to Dr. Jason L. Stuber for his inconditional help, for correcting my written english and giving me advices concerning my thesis and my work.
- Specially to Guido Laubender, system administrator of the Center for Super Computing, for his very nice, uninterested and very valuable help.

- To the Otto Stern School for allowing me to participate in their different workshops and activities.
- Dr. Ingo Opahle for discussions regarding the SO coupling and for translating the summary of the thesis, many many thanks.
- Dr. Yuzhong Zhang for the calculations of susceptibility with exact diagonalization and for discussions concerning spin Hamiltonians.
- Very specially to Dr. Tulika Maitra for her uninterested help and her kindness, her advices and discussions.
- Dr. Hem Kandpal for the useful discussions concerning my work and for teaching me to use the LMTO/NMTO Sttutgart code.
- To Prof. Peter Kopietz and the members of his group, for the nice times during lunch and coffee-ice cream times.
- To Joe Laperal Gomez for his cooperativeness and help regarding printers, mails
- To the secretaries Frau Maripola Kolokotsa and Frau Daniela Wirth-Pagano, for their help regarding documentation and administrative stuff, and also for their valuable advices and help in the difficult times.
- To Kateryna Foyevtsova and Niels Jackson, for the nice times we shared.
- To my collegues and friends Gregor Kaczor, Tejaswini Dalvi, Mauricio Martinez, Luis Mancera, Dr. Thomas Buernevich and Dr. Nils Hasselma. This work would not have finished without their trust, friendship and encourangement.
- Specially to my boyfriend Philipp Quenzer, his support, kindness and love helped me to acomplish this goal.
- Most of all to my family for their endless love and trust.